Multiscale experimental and theoretical investigation of the structure-property relationships in the myocardium

Nicole Tueni

Nicole Tueni. Multiscale experimental and theoretical investigation of the structure-property relationships in the myocardium. Biomechanics [physics.med-ph]. Ecole polytechnique, 2021. English. NNT : 2021IPPAX052 . tel-03330458v1

HAL Id: tel-03330458
https://theses.hal.science/tel-03330458v1
Submitted on 31 Aug 2021 (v1), last revised 13 Oct 2021 (v2)

INSTITUT
POLYTECHNIQUE
DE PARIS

NNT : 2021IPPAX052

Thèse de doctorat

Multiscale experimental and theoretical investigation of the structure-property relationships in the myocardium

Thèse de doctorat de l'Institut Polytechnique de Paris
préparée à l'École Polytechnique

École doctorale n°626 de l'Institut Polytechnique de Paris (EDIPP)
Spécialité de doctorat : Ingénierie Mécanique

Thèse présentée et soutenue à Palaiseau, le 1er Juillet 2021, par

NICOLE TUENI

Composition du jury :

Jacques Ohayon Professeur, UJF (TIMC-IMAG)	Président du jury
Sabine Bensamoun Directrice de recherche, UTC (BMBI)	Rapportrice
Karine Bruyère-Garnier Chercheuse, IFSTTAR (LBMC)	Rapportrice
Kostas Danas Chargé de recherche, CNRS (LMS)	Examinateur
Jean-Marc Allain Professeur, École Polytechnique (LMS)	Directeur de thèse
Martin Genet Professeur Assistant, École Polytechnique (LMS)	Co-directeur de thèse

Acknowledgements

J'ai eu la chance, au cours de ces trois années de thèse, de travailler sur un sujet passionant, dans un laboratoire de renommée internationale, entourée de personnes formidables que j'aimerais remercier chaleureusement.

Tout d'abord, je tiens à remercier mes deux encadrants de thèse, Jean-Marc Allain et Martin Genet, de m'avoir fait confiance, de m'avoir encouragée et de m'avoir guidée scientifiquement dans ce travail. Merci pour votre patience, votre disponibilité et vos judicieux conseils, qui ont contribué à alimenter ma réflexion. Merci à Jean-Marc pour toutes les discussions intéressants que nous avons eues, pour tes blagues et jeux de mots, et pour ton optimisme et ta bienveillance dans les moments difficiles. Merci à Martin de m'avoir initiée au monde des geeks, et pour ta patience face à mes compétences de "noob", sans oublier toutes nos conversations philosophiques et réflexions sur la vie.

J'aimerais aussi remercier Karine Bruyère-Garnier et Sabine Bensamoun qui m'ont fait l'honneur d'accepter d'être rapportrices de ce manuscrit pour avoir accepté de consacrer du temps à lire mon travail. Je remercie également chaleureusement les membres du jury: Jacques Ohayon et Kostas Danas qui ont gentiment accepté d'assister à ma soutenance malgré les conditions particulières dues aux conditions sanitaires et pour leur intérêt dans mon travail.

Je voudrais également remercier Andrei Costantinescu et Kostas Danas pour avoir suivi ma thèse pendant ces trois années, ainsi que Angelo Pierangelo et Jeremy Vizet pour notre collaboration.

Cette thèse n'est pas un accomplissement uniquement personnel mais le fruit des efforts du laboratoire. Je tiens donc à remercier très chaleuresement Vincent De Greef, Pascal Marie, Hakim Gharbi et Simon Hallais pour leur précieuse contribution à mon travail, leur disponibilité, mais également pour leur bonne humeur qui traduit l'ambiance au sein de ce laboratoire. Grand merci à Abdelfattah Halim, Anna Johnsson, Alexandra Joly pour tout le travail que vous fournissez pour assurer un excellent fonctionnement du laboratoire, pour votre disponibilité au quotidien.

Je souhaite remercier chaleureusement M. Abdul Barakat, qui a été mon tout premier contact dans ce monde de la recherche, et qui continue à m'encourager, 5 ans plus tard. No words can describe how grateful I am.

Cette aventure était non seulement scientifique, mais surtout humaine. Je souhaite remercier toutes les personnes qui contribuent à l'ambiance dynamique du LMS et de l'équipe MΞDISIM.

Merci à Philippe Moireau pour l'attention qu'il porte aux doctorants, les filtres de Kalman vont me manquer (ou pas...)! Merci à tous les membres de l'équipe, Patrick Le Tallec, Dominique Chapelle, Frédérique Clément, Sébastien Imperiale (mon confrère d'imprimante 3D), Fabrice Vallée (mon pull du temple sera toujours mon préféré), ce fut un plaisir de discuter avec vous autour de cafés et chouquettes. Ce fut un immense plaisir de partager cette expérience avec Federica Caforio. Merci pour ton soutien, ta bienveillance, ta grande disponibilité et tes nombreux conseils tout au long de ma thèse. Merci pour tes gâteaux, pour les séances de sport, ta recette de salade aux lentilles, et tout plein d'autres choses ! Merci à Jean-Sebastien Affagard d'avoir encadré mon stage de Master, d'avoir été patient lors de nos 7 km de courses, des matchs de foot, et surtout des dissections de coeur. Merci à Camille Declerck de m'avoir fait confiance pour encadrer ton stage, merci à Jessica Manganotti, tu m'as supportée au bureau et à la maison. Merci à Radek Chabiniok, pour ton optimisme contagieux, pour les soirées films, merci à Jérome Diaz et François Kimmig pour votre bonne humeur au quotidien, pour votre gentillesse et votre générosité.

Marija Gusseva, thank your friendship, your tolerance, your coolness. You definitely helped me stay (as) calm (as possible) during this adventure. Nikolai Khailov, Matthias Rambausek, Filippo Agnelli, thank you for all the unforgettable moments we shared together, parties, bars, camp, barbecues, picnics. Meeting you was one of the highlights of this adventure. Ezgi Berberoglu, thank you for all those trips we took together, for all the cheering and the moral boosting, for the cat talks and photos.

Je tiens à remercier tous les doctorants et post-doctorants que j'ai rencontré durant ma thèse, Arthur Le Gall, Florent Wijanto, Ustim Khristenko, Chloé Giraudet, Frédérique Robin, Cécile Patte, Jona Joachim, Francesco Regazzoni, Felipe Alvarez, Mahdi Manoochehrtayebi, Mathieu Barre, Tiphaine Delaunay, Hajer Methenni, Guillaume Balif, Marco Moscatelli, Kubra Sekmen, Ludovic Gil, Nicolas Hannappier, Alexandre Bleuset, Clément D'Hondt, Pierre Margerit, Sofia Sakout, Othmane Zerhouni, Vincenzo Zarra, Martin Avila Torrado, Lucas Benoit-Marechal, Camille Guévenoux, Jérémie Chichignoud, Nicolas Dimov, Zahra Hooshmand Ahoor, Nikhil Mohanan. Vous avez tous contribué à l'ambiance magnifique de ce laboratoire, à travers les soirées crêpes, raclettes, gualettes et pots de thèses.

Bien sûr, je ne serais pas là où je suis aujourd'hui sans mes proches. Pap, Mom, Céline, Ayo, Nounni, Dan, Charbel, Léna, Nicolli, Chacha, Rana, Roula, Karl, Kalyne, Roula Y., Jeff, Gina, Gilles, Grigor. Merci pour tout !

Marie Tueni, je te dédie ce travail.

Contents

Chapter I

Introduction (English)

1 General context

The heart is a beating muscular organ, located just behind and slightly left of the breastbone. It pumps blood, carrying oxygen and nutrients to the body, and metabolic waste such as carbon dioxide to the lungs. Cardiovascular diseases represent one of the main causes of death globally, accounting for an estimated 17.9 million lives each year [World Health Organization, 2017]. Early diagnosis of cardiac pathologies is crucial to reduce their severity and mortality. It is often performed by listening to the heart sounds using a stethoscope, by recording an electrocardiograph, by ultrasound, by blood pressure measurements, etc. These methods permit a rapid diagnosis of the heart condition, based on instantaneous global information.

One potential way of allowing a prediction of the heart condition is the development of models that take into account cardiac mechanics. Mechanical stresses play an important role in the development of cardiac diseases such as cardiomyopathy, hypertrophy, heart failure, etc.. Knowledge of the biomechanics of the heart is thus essential for understanding the causes and consequences of cardiac diseases. In addition to being used as prognosis tools, these models could be used for diagnosis and treatment. To do so, they require a detailed understanding of the mechanisms taking place at the small tissue scales. Indeed, studies have shown the existence of multiple spatial scales that govern the behavior of the cardiac tissue [Legrice et al., 2001], and have proved that cardiac structure and function are closely related [Horowitz et al., 1988]. Indeed, the cardiac structure evolves throughout life in response to alterations of the mechanical and chemical environments, either physiologically or pathologically. These phenomena are generally referred to as growth and remodeling, and consist in permanent alterations of the cardiac microstructure, leading to modifications in the cardiac function. An elucidation of these mechanisms and of their couplings would be very useful to design better prognosis and treatment of cardiac pathologies.

1.1 The heart

The heart consists of four chambers: The upper chambers are called the left and right atria, and the lower chambers are called the left and right ventricles. The inter-atrial septum separates the left and right atria and the inter-ventricular septum separates the left and right ventricles (see Figure I.1).

The left ventricle is the strongest chamber in the heart, and serves the purpose of distributing blood with higher pressure than the right ventricle. As a consequence, it is larger and thicker than the right ventricle. It has attracted a lot of scientific attention because it is affected by various physiological or pathological conditions that interfere with its proper functioning.

Four valves regulate blood flow through the heart and forbid the backflow: The tricuspid (between the right atrium and right ventricle), the pulmonary valve (between the right ventricle and the pulmonary artery), the mitral valve (between the left atrium and the left ventricle), and the aortic valve (between the left ventricle and the aorta).

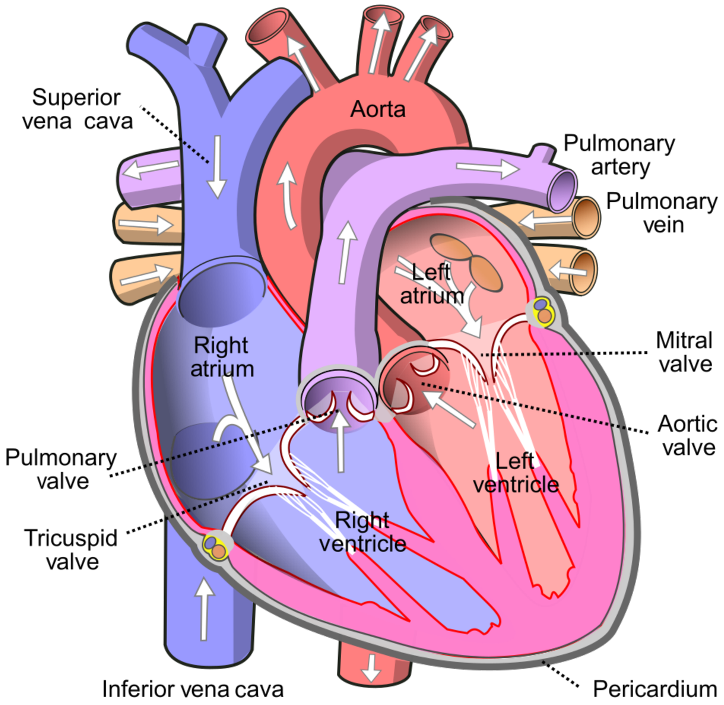

Figure I.1 – Schematic representation of the human heart showing the atria, ventricles, and the valves. Oxygenated blood is depicted in red and deoxygenated blood in blue. Illustration by Wapcaplet, licensed under CC BY-SA 3.0.

The cardiac cycle is a sequence of mechanical and electrical events consisting of two periods. One period during which the cardiac muscle relaxes and the ventricles refill with blood (blood flow from left and right atria into left and right ventricles respectively), called diastole, and one period of muscle contraction and pumping of blood (blood ejection from left and right ventricle into aorta and pulmonary arteries), called systole.

1.2 The myocardium

The heart wall is mainly composed of muscle tissue, also known as the myocardium. It contains the cardiomyocytes (cardiac cells, or cardiac fibers), which allow the cardiac contraction. It is approximately 15 mm thick, and sandwiched between a thin inner layer, the endocardium (0.5 µm thick), which wraps the cardiac chambers, and a thin outer layer, the epicardium, also known as visceral pericardium (2 mm thick), surrounding the heart. The parietal pericardium is a 0.8 µm layer that covers the pericardium (see Figure I.2).

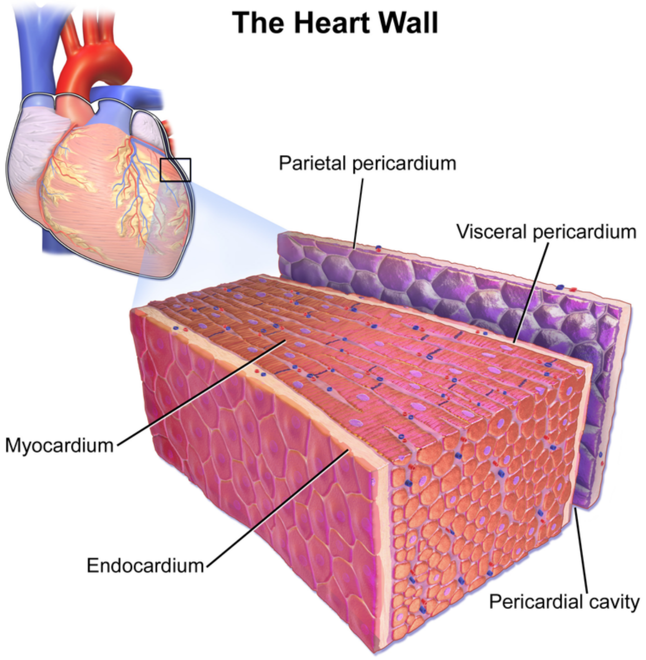

Figure I.2 – Schematic representation of the human heart wall, showing the myocardium, wrapped by the inner endocardium and the outer visceral pericardium. Illustration by BruceBlaus, licensed under CC BY 3.0.

Several animal models have been designed and used to conduct research. Pigs, in particular, show a vast range of similarities which makes them a well suited model to study cardiovascular diseases. They have an average heart rate of 90-110 beats per minute (bpm), mimicking a human's average heart rate of 70-100 bpm. In addition, their larger size provides a suitable choice for imaging and tissue engineering studies [Tsang et al., 2016].

1.2.1 Microstructure

The myocardium is made of structures organized into a hierarchical multiscale architecture. Figure I.3 shows a hierarchical organization of cardiomyocytes and connective tissue in the skeletal muscle, that is also observed in the cardiac muscle. We mainly notice four important scales: the sub-cellular scale, the cellular (fiber) scale, the fascicle scale and the tissue scale. Note that in the cardiac tissue, the fascicle scale is called the sheetlet scale, and its organization in the wall is different from that of the skeletal tissue.

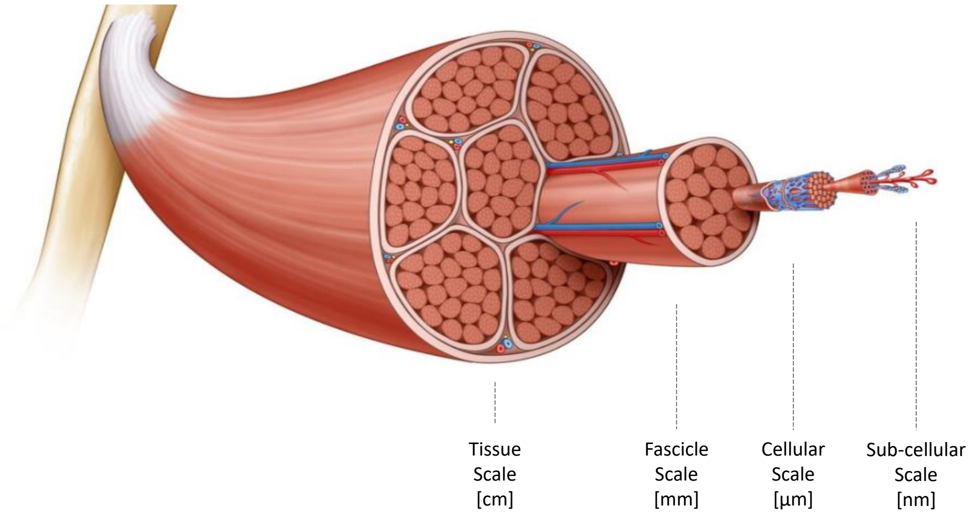

Figure I.3 – Skeletal muscle structure showing the hierarchical organization of the sub-cellular, the cellular (fiber), the fascicle and the tissue scales. Adapted from therobertslab.com.

Scale	Nomenclature	Dimension
Nanoscale	Subcellular scale	$<$1 µm
Microscale	Cellular/fiber/cardiomyocyte scale	1-10 µm
Mesoscale	Fascicle/sheetlet scale	100-500 µm
Macroscale	Tissue scale	$>$500 µm

Table I.1 – Glossary of the four scales, their different nomenclatures and dimensions.

Sub-cellular scale. At the sub-cellular scale, each cardiac fiber is primarily made of aligned sarcomeres. Each sarcomere consists of parallel actin (thin) and myosin (thick) filaments (see Figure I.4). The sarcomeres are responsible for the muscle striated appearance, obvious in Figure I.5 [Krueger et al., 1980; Roos, 1987; Kanzaki et al., 2010].

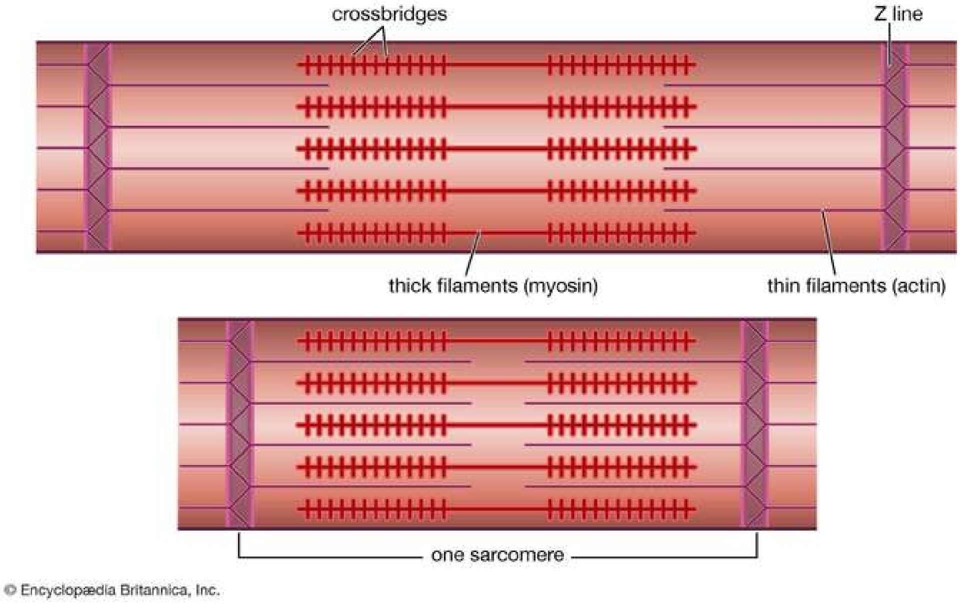

Figure I.4 – The arrangement of the sarcomeres, thick and thin filaments in a muscle fiber at the subcellular scale. The sarcomere is in relaxed (top) and contracted (bottom) positions. Extracted from *Encyclopedia Britannica, Inc.*

Cellular scale. The cardiomyocytes are roughly cylindrical, measuring 100-150 µm by 10-20 µm. They are extremely branched. Each cardiomyocyte is connected on average to 11 neighboring cells by intercalated discs (see Figure I.5, A) [Saffitz et al., 1994].

Each individual cardiac fiber is surrounded by a thin layer of connective tissue, called endomysial weave, and is connected to other myocytes by lateral endomysial struts [Robinson et al., 1988; Rossi et al., 1998; Kanzaki et al., 2009, 2010]. The endomysium has been shown to contain mainly collagen I and III components, and type IV and V in very minor amounts [Light and Champion, 1984]. Figure I.6 shows the myocardial connective tissue after removal of cardiomyocytes, where the endomysial collagen wraps each cardiomyocyte, for a normal subject (A) and for a subject with concentric hypertrophy (B). It shows that the pathological remodeling affects the endomysial extracellular matrix (ECM), with a thickening of the endomysium.

The cardiomyocytes are strongly altered by growth and remodeling. For instance, at the cellular scale, an elongation and thinning of the cardiomyocytes leads to a dilatation of the ventricles at the organ scale. This is known as eccentric hypertrophy. By contrast,

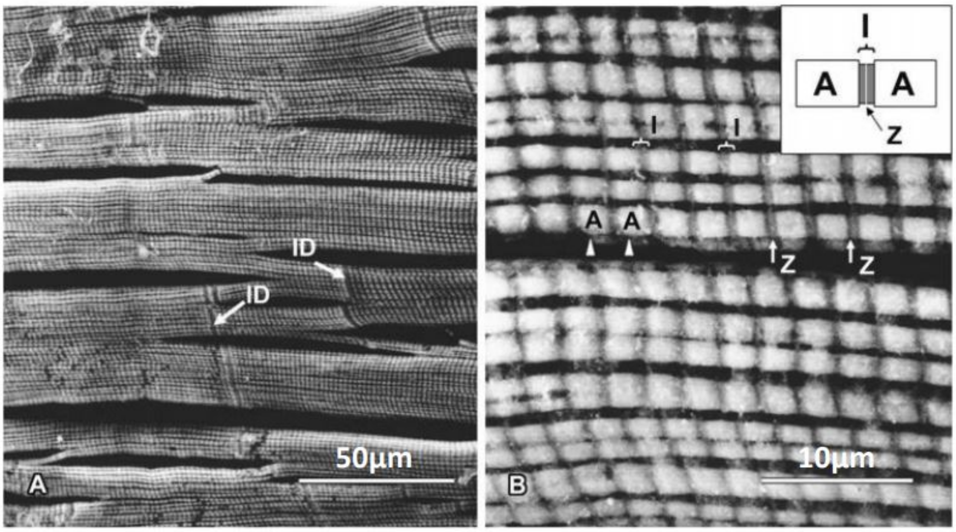

Figure I.5 – Scanning Electron Microscopy of normal human left ventricular cardiomyocytes. A: Intercalated discs (arrows) and sarcomere striations are clearly seen. B: Higher magnification of the sarcomeres. ID indicates intercalated disc; A, A band; I, I band; and Z, Z band. Extracted from [Kanzaki et al., 2010].

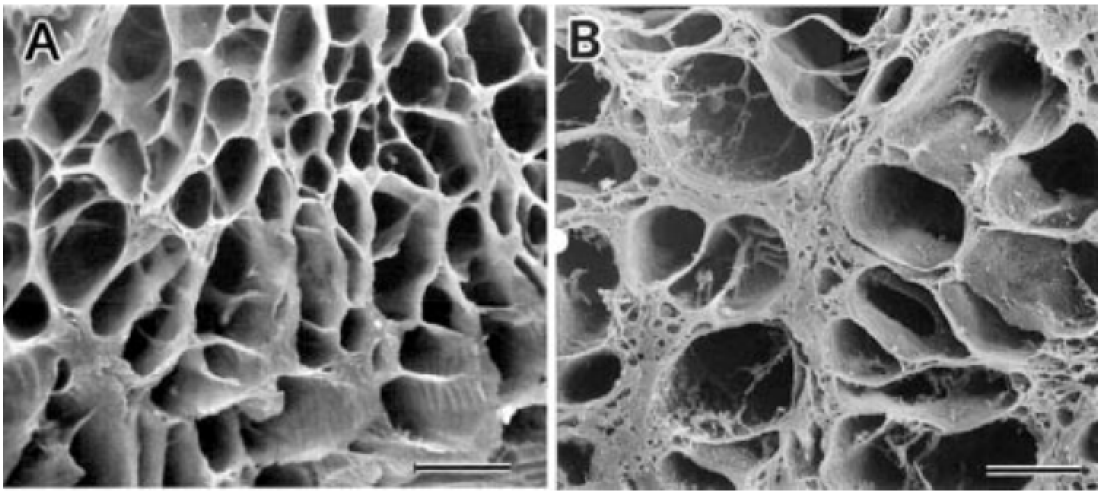

Figure I.6 – Scanning Electron Microscopy image showing the endomysial extracellular matrix surrounding each individual cardiac cell, for a normal subject (A), and a patient with concentric hypertrophy (B). Image shows the remodeling effect on the endomysium (Scale bar : 30 µm). Extracted from [Kanzaki et al., 2009].

a shortening and thickening of the cardiac cells leads to a thickening of the ventricular walls in the case of concentric hypertrophy [Hunter and Chien, 1999; Maillet et al., 2013] (see Figure I.7).

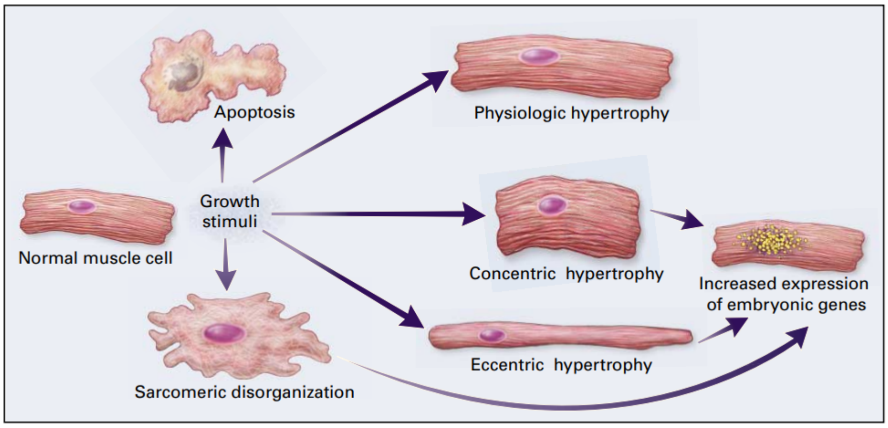

Figure I.7 – Phenotypically distinct changes in the morphology of the cardiomyocytes occur in response to various growth stimuli. Extracted from [Hunter and Chien, 1999].

Figure I.8 shows images of tissue samples obtained after removal of connective tissue for a normal subject (A), and a patient with concentric hyperthrophic cardiomyopathy (B and C). We notice a thickening of the cardiomyocytes in B and C, as well as a disarray in their organization.

Fascicle scale. The cardiomyocytes are locally parallel, arranged in bundles or fascicles of 5 to 10 cells, forming structures of 100-200 µm. These structures are wrapped by a layer of collageneous extracellular matrix, called perimysium [Legrice et al., 1997; Costa et al., 1997; Rossi et al., 1998; Young et al., 1998; Arts et al., 2001]. It is thicker than the endomysium, and can reach up to 10 µm in a healthy heart. It has been shown to contain mainly type I, III and V collagen [Light and Champion, 1984].

There is no consensus among the cardiac research community on the name of this structure. While some call it "bundle" or "fascicle" of cardiomyocytes, others call it "sheetlet" because it forms, locally in the tissue, sheet-like structures. We chose, in this research, to define the "sheetlet" as the group of cardiomyocytes wrapped by the perimysium layer. During our literature review, we encountered two coexistent theories that describe the sheetlet configuration in the tissue, the laminar and the globular configurations, that we are going to present in what follows.

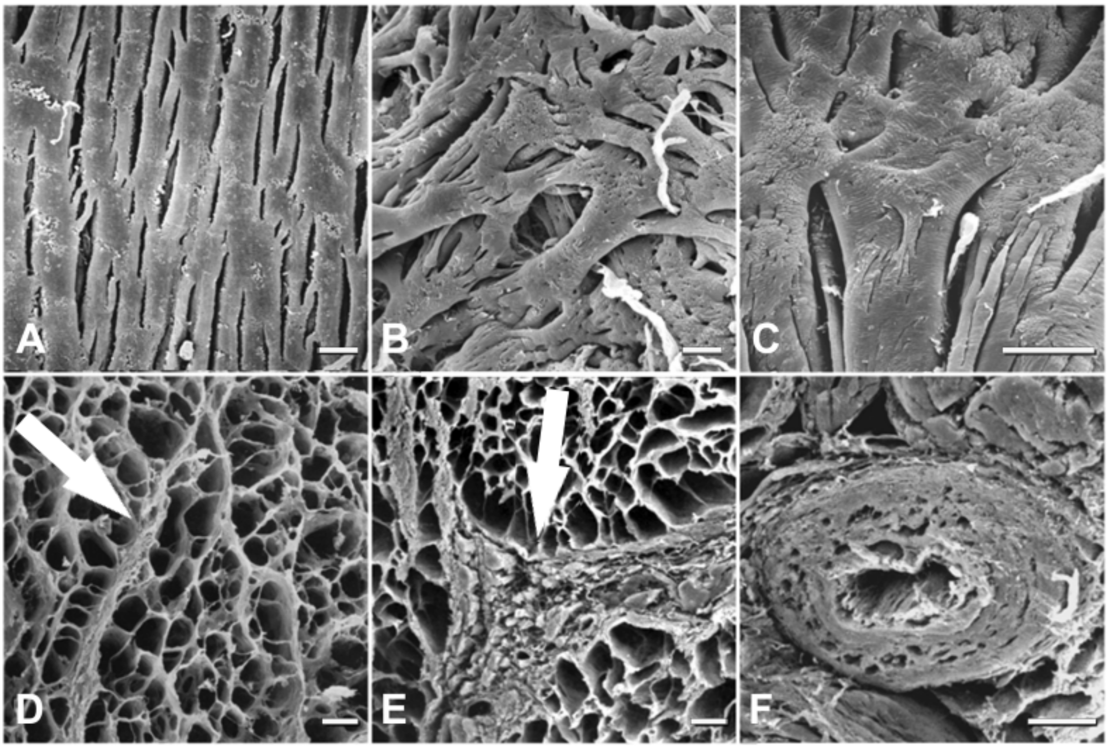

Figure I.8 – Scanning Electron Microscopy of cardiomyocytes. Tissue samples from normal subject (A, D) and a patient with hypertrophic cardiomyopathy (B, C, E, F) are shown. Images were obtained after the removal of either connective tissue (A, B, C) or non-fibrous tissue (D, E, F), (white arrows). In the heart sample from the patient with hypertrophic cardiomyopathy, myocardial disarray, abnormal branching are observed in B and C. E and F show an increased thickness of interstitial connective tissue and thickened small intramural vessels. (Scale bar: 20 µm). Extracted from [Kanzaki et al., 2012].

Laminar configuration. Longitudinal and radial sections in the heart wall showed flat sheets stacked adjacent to one another in the cardiac wall. These sheets run radially from endocardium to epicardium in transmural sections of the left ventricle, and are separated by appreciable spaces between layers, called cleavage planes [LeGrice et al., 1995; Young et al., 1998; Sands et al., 2005; Pope et al., 2008]. These planes are most probably caused by the tissue preparation (freezing, dehydration, slicing, clearing, etc.). Figure I.9 shows a three-dimensional representation of a registered stack volume of slices spanning the rat left ventricle wall from epicardium to endocardium, where the cleavage planes are obvious. The connective tissue (stained in white) covers the sides of the sheetlets, and its density increases near the epicardial and endocardial surfaces.

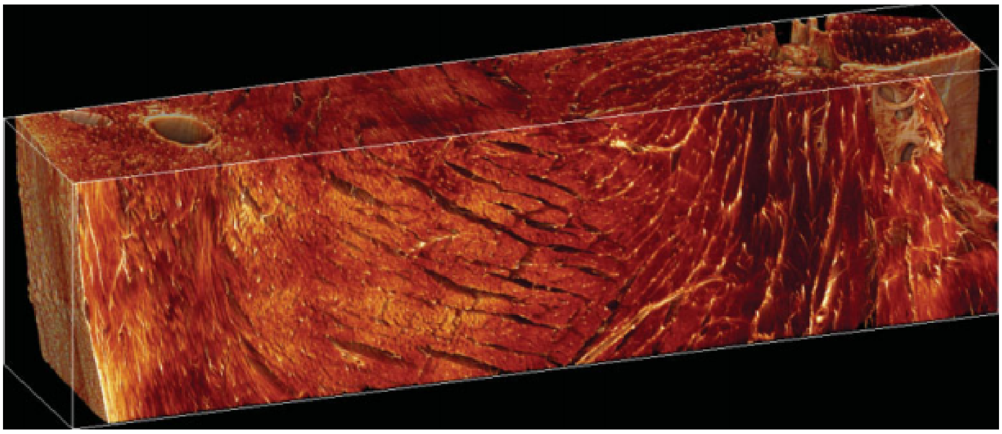

Figure I.9 – Three-dimensional representation of a transmural stack volume (4.25×1.12×0.88 mm) of slices imaged with confocal microscopy showing a laminar structure with sheets separated by elongated cleavage planes, and a dense collagen network near the endocardium and the epicardium. Extracted from [Sands et al., 2005].

Globular configuration. Images performed transversely to the cardiac cells show a globular arrangement of the cardiomyocyte bundles, encircled by a layer of perimysium [Kanzaki et al., 2010, 2012]. Cleavage planes are not observed in these images, instead, the tissue seems to be made of continuous adjacent globular clusters of different sizes, connected by the perimysium. Figure I.10 shows this globular arrangement, where bundles of cells (each wrapped by endomysium) are grouped together into ellipsoids and surrounded by perimysial collagen (thick arrow). To our knowledge, no study has investigated the organization and orientation of these globular structures in the wall thickness.

The sheetlet structure has attracted more and more attention, due to the fact that the

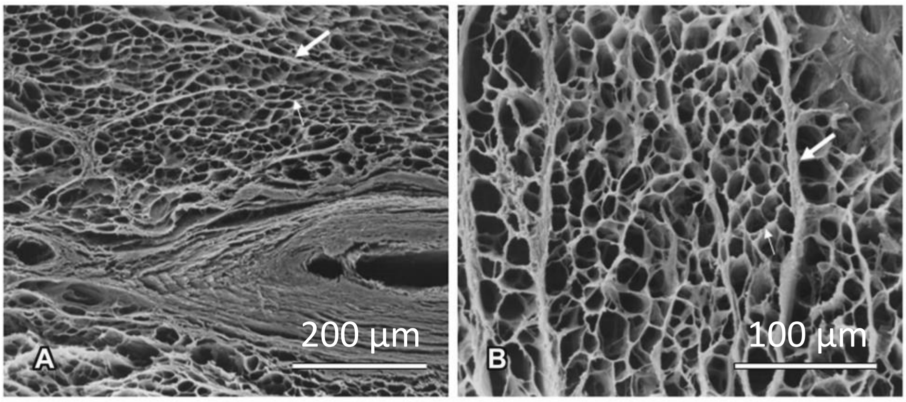

Figure I.10 – Connective tissue skeleton of human heart (transverse section). A: The globular sheetlet configuration, with perimysial collagen around cardiomyocytes and small vessels is clearly observed. (thick arrow, perimysium; thin arrow, endomysium). B: The interstitial connective tissue consisting of perimysial and endomysial components presents a honeycomb shape. The perimysium (thick arrow) surrounds groups of cardiomyocytes, and the endomysium (thin arrow) surrounds each cardiomyocyte. Extracted from [Kanzaki et al., 2010].

collageneous extracellular matrix, at this mesoscale, is strongly modified by heart remodeling. Figure I.8 shows images of tissue samples obtained after removal of cardiomyocytes for a normal subject (D), and a patient with concentric hypertrophy cardiomyopathy (E and F). We notice a thickening of the perimysial extracellular matrix in the case of the hypertrophied heart.

Tissue scale. At the tissue scale, the cardiomyocyte orientation has been widely studied. The myocardial fiber orientation is known to vary continuously and smoothly through the cardiac wall. Historically, it has been shown by performing measurements on circumferential sections of myocardium obtained from left ventricles, that the cardiac fiber angle varies from about 90° close to the endocardium to about -90° at the epicardium in pig [Streeter and Bassett, 1966], and ±60° in dogs [Streeter et al., 1969]. This arrangement was later confirmed and mapped using ex-vivo diffusion tensor magnetic resonance imaging (DT-MRI) [Scollan et al., 2000; Zhukov and Barr, 2003] (see Figure I.11), and more recently using in-vivo DT-MRI [von Deuster et al., 2016; Stoeck et al., 2016; Nielles-Vallespin et al., 2017].

The variation of the sheetlet orientation is less understood. It is still unclear how the sheetlet structures are organized through the myocardial thickness, and along its wall. While some studies support the predominance of a single laminar sheetlet popu-

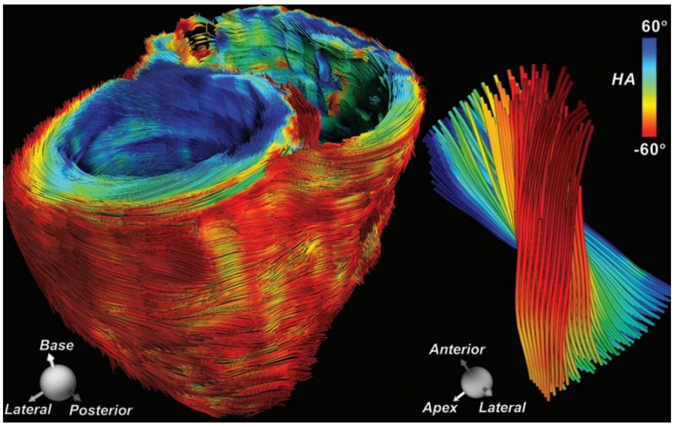

Figure I.11 – Image of DT-MRI on healthy patient showing the variation of the cardiomyocyte orientation through the thickness and along the heart wall. Extracted from [Mekkaoui et al., 2017].

lation, with an orientation that evolves linearly between endocardium and epicardium (see Figure I.12, left) [LeGrice et al., 1995; Ferreira et al., 2014; Nielles-Vallespin et al., 2017], other studies propose the coexistence of two local myocardial sheet populations (see Figure I.12, right) [Kung et al., 2011; Kilner et al., 2015].

1.2.2 Mechanical properties

The mechanical properties of the cardiac tissue can be split into two categories: an active behavior resulting from the muscle contraction via cross-bridge cycling [Huxley and Simmons, 1971; Lymn and Taylor, 1971], and a passive behavior arising from the other parts of the tissue.

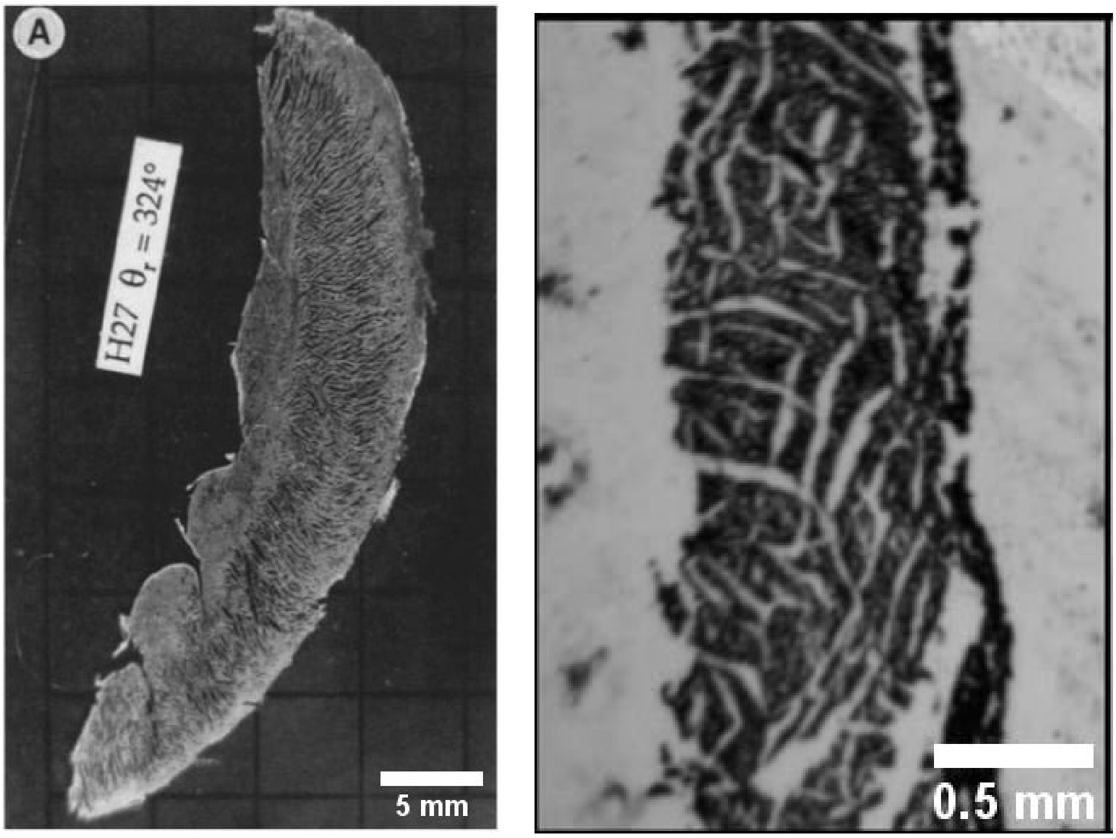

Figure I.12 – Longitudinal-transmural section of left ventricle showing: Left: a radial alignment of cardiomyocyte layers with a linearly varying orientation (extracted from [LeGrice et al., 1995]). Right: two distinct populations of sheetlets, extracted from [Kung et al., 2011].

Passive behavior. When subjected to uniaxial [Fung, 1967; Demer and Yin, 1983] or biaxial [Yin et al., 1987; Sommer et al., 2015] extension, the myocardial specimen experiences large, non linear deformations, with a stiffer behavior in the fiber direction than in the cross-fiber direction (see Figure I.13), and a pronounced hysteresis, indicating a significant energy dissipation during loading. When the traction is applied in the cardiac fiber direction, the cardiomyocytes are extended, and the distance between them decreases. The extracellular matrix fibers uncoil and contribute to the exponential increase in stress [MacKenna et al., 1994]. When load is lateral to the fibers, an exponential stiffening is also observed, due to the recruitment of the collagen network in the extracellular matrix.

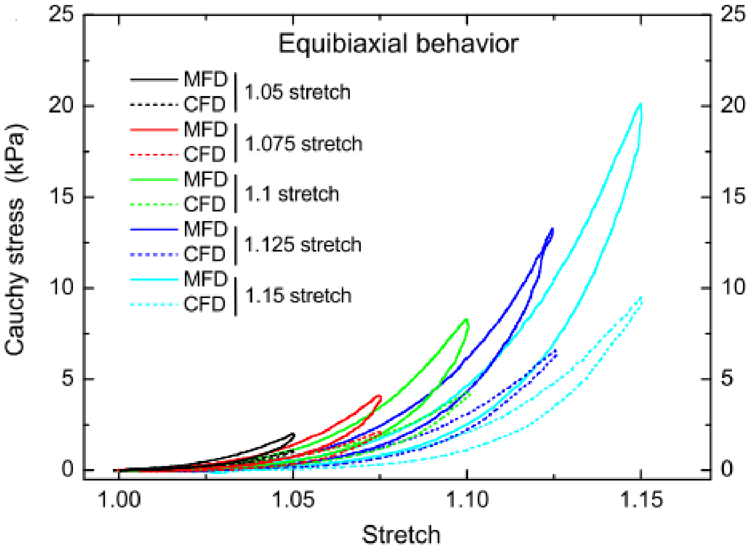

Figure I.13 – Stress vs. stretch behavior in the myofiber direction (MFD, solid curves) and cross-fiber direction (CFD, dashed curves) of human left ventricular free wall specimens showing a stiffer behavior in the MFD. Extracted from [Sommer et al., 2015].

Simple shear displacement was applied to myocardium samples with respect to three principal material axes (the fiber axis, the sheetlet axis and the normal to the fiber-sheetlet plane) in six modes, and resulted in six different shear stresses along the axes, highlighting the anisotropy in the tissue [Dokos et al., 2002; Sommer et al., 2015].

In most studies of the heart, the tissue has been assumed to be incompressible, primarily due to the fluid content within cells and interstitial components. Recently, studies have shown that the myocardial volume undergoes a dynamic change during the cardiac cycle, with up to 10% change, which cannot be fully accounted for by the movement of blood through the vasculature, or by the cardiac structure [Ashikaga et al., 2008].

Active behavior. In this work, the focus is put on the passive component of the muscle properties. Therefore, we will only briefly present the active properties. At the nanoscale, the sliding filament theory explains the mechanism of muscle contraction: the filaments slide past each other during contraction, and form a protein complex (called actomyosin), by attachment of a myosin head on the actin filament, forming a cross-bridge (see Figure I.14) [Huxley and Simmons, 1971; Lymn and Taylor, 1971]. The Lymn-Tylor cycle describes the crossbridge cycle in four steps, as shown in Figure I.14: First, a cross-bridge forms, with the binding of an activated myosin head to an actin, followed by a power stroke, where adenosine diphosphate (ADP) is released and the activated myosin head pivots, allowing the thin filament to slide toward the center of the sarcomere. Then, Adenosine triphosphate (ATP) binds to the myosin head, the link between the myosin head and actin weakens, and the myosin head detaches, and finally, ATP is hydrolyzed to ADP and inorganic phosphate. The energy released during hydrolisis reactivates the myosin head, returning it to its initial position. As this cycle repeats, the thick and thin myofilaments are pulled toward each other, and the sarcomere shortens, causing the muscle to contract.

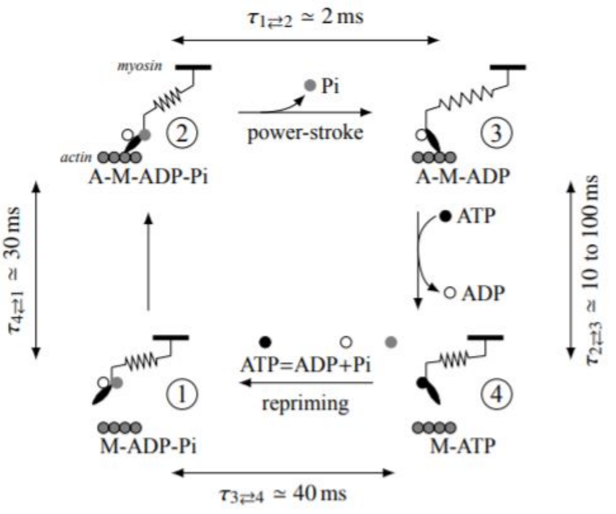

Figure I.14 – Representation of the four steps of the Lymn–Taylor cycle, leading to the sliding of the actin and myosin filaments, hence the muscle contraction. Extracted from [Caruel and Truskinovsky, 2018].

Existing continuum models at the organ scale can simulate the electromechanical activity of the heart during a cardiac cycle [Guccione et al., 1995; Hunter and Chien, 1999], even including detailed nanoscopic models of the active contraction [Chapelle et al., 2012; Caruel et al., 2019; Kimmig and Caruel, 2020]. At the macroscale, the muscle stiffness increases during contraction [Roos, 1987], which means that the contraction has an impact on the macroscopic mechanical properties of the myocardium.

2 Challenges

The complex, hierarchical 3D architecture of the myocardium is intriguing, and gives the tissue its intricate passive macroscopic mechanical properties. Moreover, alterations of the structure at the microscale deeply affect the behavior of the tissue. A thorough understanding of the mechanisms underlying the structure-properties relationships would be of great benefit for designing better diagnosis and treatment of cardiac pathologies.

Structural investigation, experimental testing and numerical modeling are essential and complementary for characterizing the multiscale mechanical properties of the cardiac tissue. The structural information creates a clear local image of the cardiac structure, which, coupled with experimental assays, is essential for developing multiscale numerical models [Schmid et al., 2014].

2.1 Experimental challenges

Structural studies have been able to give a clear view of the cardiomyocyte structure, and map its organization in the heart wall [Legrice et al., 2001]. The sheetlet scale, however, is less clearly defined. Its organization and orientation throughout the heart is not fully understood. This constitutes an obstacle in modeling this intermediate scale, which results in difficulties to investigate its mechanical properties and role in the tissue.

On another hand, experimental studies have been carried out at the macroscale, in order to quantify the stress-strain relationships. Experimental results differ from one study to another, which may be due to the sample preparation and experimental protocols such as tissue preconditioning, gripping, etc., and differences between tested hearts [Dokos et al., 2002; Sommer et al., 2015]. Thus, one of the major challenges remains in reproducing in-vivo experimental conditions when performing ex-vivo assays. Moreover, there is a lack of experimental studies linking the deformations at the macroscale with the deformations at the smaller scales. Such experiments would shed light on the micro-mechanisms in the tissue.

2.2 Modeling challenges

In parallel, existing continuum models can simulate the electro-mechanical activity of the heart during a cardiac cycle, even including detailed microscopic models of the active contraction [Chapelle et al., 2012]. However, in most models of the literature, the passive behavior is less finely described, being restricted to purely macroscopic models [Holzapfel and Ogden, 2009]. Although they have been able to fit the experimental data, the set of material parameters they employ is not unique, and differs, for the same model, depending on the mechanical assays. In addition, most of the models in the literature take into account the anisotropy of the tissue, however, its origin has not been studied yet. It is speculated that it arises from the structural arrangement in the tissue, however, to our knowledge, no study has tackled this question yet.

3 Structure of the thesis

In this thesis, we have investigated the relationship between the sheetlet structure and organization, and the passive macroscopic mechanical properties of the cardiac tissue. For this purpose, we used both experimental and computational approaches.

In Chapter II, an experimental setup is designed, in order to investigate the mesostructural deformation of the myocardium under stretch conditions. We observed separation lines that tended to form under traction. In Chapter III, using a fast imaging technique, and simple post processing, we attempted to observe the mesostructure organization and orientation throughout the thickness and all along the left ventricle wall. The obtained results allowed us to gain insight on the sheetlet orientation in 2D, but are not sufficient to reconstruct a 3D model. In Chapter IV, we developed a numerical model, in order to study the effect of the sheetlets and their organization on the macroscopic anisotropy. We found that both cardiomyocyte and sheetlet rotation in the cardiac wall are required to reproduce the anisotropy.

Bibliography

T. Arts, K. D. Costa, J. W. Covell, and A. D. McCulloch. Relating myocardial laminar architecture to shear strain and muscle fiber orientation. *American Journal of Physiology-Heart and Circulatory Physiology*, 280(5):H2222–H2229, 2001. doi: 10.1152/ajpheart.2001.280.5.H2222.

H. Ashikaga, B.A. Coppola, K.G. Yamazaki, F.J Villarreal, J.H. Omens, and J.W. Covell. Changes in regional myocardial volume during the cardiac cycle: implications for transmural blood flow and cardiac structure. *American Journal of Physiology-Heart and Circulatory Physiology*, 295(2):H610–H618, 2008. doi: 10.1152/ajpheart.00107.2008.

M. Caruel and L. Truskinovsky. Physics of muscle contraction. *Reports on Progress in Physics*, 81(3):036602, 2018. doi: 10.1088/1361-6633/aa7b9e.

M. Caruel, P. Moireau, and D. Chapelle. Stochastic modeling of chemical–mechanical coupling in striated muscles. *Biomechanics and Modeling in Mechanobiology*, 18(3): 563–587, 2019. doi: 10.1007/s10237-018-1102-z.

D. Chapelle, P. Le Tallec, P. Moireau, and M. Sorine. Energy-preserving muscle tissue model: formulation and compatible discretizations. *International Journal for Multiscale Computational Engineering*, 10(2):189–211, 2012. doi: 10.1615/intjmultcompeng.2011002360.

K.D. Costa, K. May-Newman, D. Farr, W.G. O'Dell, A.D. McCulloch, and J.H. Omens. Three-dimensional residual strain in midanterior canine left ventricle. *American Journal of Physiology-Heart and Circulatory Physiology*, 273(4):H1968–H1976, 1997. doi: 10.1152/ajpheart.1997.273.4.H1968.

L.L. Demer and F.C. Yin. Passive biaxial mechanical properties of isolated canine myocardium. *The Journal of Physiology*, 339(1):615–630, 1983. doi: 10.1113/jphysiol.1983.sp014738.

S. Dokos, B.H. Smaill, A.A. Young, and I.A. LeGrice. Shear properties of passive ventricular myocardium. *American Journal of Physiology-Heart and Circulatory Physiology*, 283(6):H2650–H2659, 2002. doi: 10.1152/ajpheart.00111.2002.

P.F. Ferreira, P.J. Kilner, L-A. McGill, S. Nielles-Vallespin, A.D. Scott, Siew Y Ho, Karen P McCarthy, Margarita M Haba, Tevfik F Ismail, Peter D Gatehouse, Ranil de Silva, Alexander R Lyon, Sanjay K Prasad, David N Firmin, and Dudley J Pennell. In vivo cardiovascular magnetic resonance diffusion tensor imaging shows evidence of abnormal myocardial laminar orientations and mobility in hypertrophic cardiomyopathy. *Journal of Cardiovascular Magnetic Resonance*, 16(1):87, 2014. doi: 10.1186/s12968-014-0087-8.

Y.C. Fung. Elasticity of soft tissues in simple elongation. *American Journal of Physiology-Legacy Content*, 213(6):1532–1544, 1967. doi: 10.1152/ajplegacy.1967.213.6.1532.

J.M. Guccione, K.D. Costa, and A.D. McCulloch. Finite element stress analysis of left ventricular mechanics in the beating dog heart. *Journal of Biomechanics*, 28(10): 1167–1177, 1995. doi: 10.1016/0021-9290(94)00174-3.

G.A. Holzapfel and R.W. Ogden. Constitutive modelling of passive myocardium: a structurally based framework for material characterization. *Philosophical Transactions of the Royal Society A: Mathematical, Physical and Engineering Sciences*, 367(1902): 3445–3475, 2009. doi: 10.1098/rsta.2009.0091.

A. Horowitz, Y. Lanir, F. C. P. Yin, M. Perl, I. Sheinman, and R. K. Strumpf. Structural Three-Dimensional Constitutive Law for the Passive Myocardium. *Journal of Biomechanical Engineering*, 110(3):200–207, 1988. doi: 10.1115/1.3108431.

J.J. Hunter and K.R. Chien. Signaling Pathways for Cardiac Hypertrophy and Failure. *New England Journal of Medicine*, 341(17):1276–1283, 1999. doi: 10.1056/nejm199910213411706.

A. F. Huxley and R. M. Simmons. Proposed Mechanism of Force Generation in Striated Muscle. *Nature*, 233(5321):533–538, 1971. doi: 10.1038/233533a0.

Y. Kanzaki, F. Terasaki, M. Okabe, and Y. Kitaura. Three-Dimensional Remodeling of Cardiomyocytes in a Patient With Aortic Stenosis: Scanning Electron Microscopy. *Circulation*, 119(2):e10, 2009. doi: 10.1161/circulationaha.108.809467.

Y. Kanzaki, F. Terasaki, M. Okabe, S. Fujita, T. Katashima, K. Otsuka, and N. Ishizaka. Three-Dimensional Architecture of Cardiomyocytes and Connective Tissue in Human Heart Revealed by Scanning Electron Microscopy. *Circulation*, 122(19):1973–1974, 2010. doi: 10.1161/circulationaha.110.979815.

Y. Kanzaki, Y. Yamauchi, M. Okabe, F. Terasaki, and N. Ishizaka. Three-Dimensional Architecture of Cardiomyocytes and Connective Tissues in Hypertrophic Cardiomyopathy: A Scanning Electron Microscopic Observation. *Circulation*, 125(5):738–739, 2012. doi: 10.1161/circulationaha.111.054668.

P.J. Kilner, K. McCarthy, M. Murillo, P. Ferreira, A.D. Scott, Laura-Ann McGill, Sonia Nielles-Vallespin, Ranil Silva, Dudley J Pennell, Siew Y Ho, and David Firmin. Histology of human myocardial laminar microstructure and consideration of its cyclic deformations with respect to interpretation of in vivo cardiac diffusion tensor imaging. *Journal of Cardiovascular Magnetic Resonance*, 17(S1):Q10, 2015. doi: 10.1186/1532-429x-17-s1-q10.

F. Kimmig and M. Caruel. Hierarchical modeling of force generation in cardiac muscle. *Biomechanics and Modeling in Mechanobiology*, 19(6):2567–2601, 2020. doi: 10.1007/s10237-020-01357-w.

J.W. Krueger, D. Forletti, and B.A. Wittenberg. Uniform sarcomere shortening behavior in isolated cardiac muscle cells. *The Journal of General Physiology*, 76(5):587–607, 1980. doi: 10.1085/jgp.76.5.587.

G.L. Kung, T.C. Nguyen, A. Itoh, S. Skare, N.B. Ingels, D.C. Miller, and D.B. Ennis. The presence of two local myocardial sheet populations confirmed by diffusion tensor MRI and histological validation. *Journal of Magnetic Resonance Imaging*, 34(5):1080–1091, 2011. doi: 10.1002/jmri.22725.

I. Legrice, P. Hunter, A. Young, and B. Smaill. The architecture of the heart: a data–based model. *Philosophical Transactions of the Royal Society of London. Series A: Mathematical, Physical and Engineering Sciences*, 359(1783):1217–1232, 2001. doi: 10.1098/rsta.2001.0827.

I. J. LeGrice, B. H. Smaill, L. Z. Chai, S. G. Edgar, J. B. Gavin, and P. J. Hunter. Laminar structure of the heart: ventricular myocyte arrangement and connective tissue architecture in the dog. *American Journal of Physiology-Heart and Circulatory Physiology*, 269(2):H571–H582, 1995. doi: 10.1152/ajpheart.1995.269.2.h571.

I. J. Legrice, P. J. Hunter, and B. H. Smaill. Laminar structure of the heart: a mathematical model. *American Journal of Physiology-Heart and Circulatory Physiology*, 272(5):H2466–H2476, 1997. doi: 10.1152/ajpheart.1997.272.5.h2466.

N. Light and A.E. Champion. Characterization of muscle epimysium, perimysium and endomysium coliagens. *Biochemical Journal*, 219:10, 1984. doi: 10.1042/bj2191017.

R. W. Lymn and E. W. Taylor. Mechanism of adenosine triphosphate hydrolysis by actomyosin. *Biochemistry*, 10(25):4617–4624, 1971. doi: 10.1021/bi00801a004.

D. A. MacKenna, J. H. Omens, A. D. McCulloch, and J. W. Covell. Contribution of collagen matrix to passive left ventricular mechanics in isolated rat hearts. *American Journal of Physiology-Heart and Circulatory Physiology*, 266(3):H1007–H1018, 1994. doi: 10.1152/ajpheart.1994.266.3.h1007.

M. Maillet, J.H. van Berlo, and J.D. Molkentin. Molecular basis of physiological heart growth: fundamental concepts and new players. *Nature Reviews Molecular Cell Biology*, 14(1):38–48, 2013. doi: 10.1038/nrm3495.

C. Mekkaoui, T.G. Reese, M.P. Jackowski, S.F. Cauley, K. Setsompop, H. Bhat, and D.E. Sosnovik. Diffusion Tractography of the Entire Left Ventricle by Using Free-breathing Accelerated Simultaneous Multisection Imaging. *Radiology*, 282(3):850–856, 2017. doi: 10.1148/radiol.2016152613.

S. Nielles-Vallespin, Z. Khalique, P.F. Ferreira, R. de Silva, A.D. Scott, P. Kilner, L.A. McGill, A. Giannakidis, P.D. Gatehouse, D. Ennis, E. Aliotta, M. Al-Khalil, P. Kellman, D. Mazilu, R.S. Balaban, D.N. Firmin, A.E. Arai, and D.J. Pennell. Assessment of Myocardial Microstructural Dynamics by In Vivo Diffusion Tensor Cardiac Magnetic Resonance. *Journal of the American College of Cardiology*, 69(6):661–676, 2017. doi: 10.1016/j.jacc.2016.11.051.

A.J. Pope, G.B. Sands, B.H. Smaill, and I.J. LeGrice. Three-dimensional transmural organization of perimysial collagen in the heart. *American Journal of Physiology-Heart and Circulatory Physiology*, 295(3):H1243–H1252, 2008. doi: 10.1152/ajpheart.00484.2008.

T.F. Robinson, M.A. Geraci, E.H. Sonnenblick, and S.M. Factor. Coiled perimysial fibers of papillary muscle in rat heart: morphology, distribution, and changes in configuration. *Circulation Research*, 63(3):577–592, 1988. doi: 10.1161/01.res.63.3.577.

K.P. Roos. Sarcomere length uniformity determined from three-dimensional reconstructions of resting isolated heart cell striation patterns. *Biophysical Journal*, 52(2):317–327, 1987. doi: 10.1016/s0006-3495(87)83219-8.

M.A. Rossi, M.A. Abreu, and L.B. Santoro. Connective Tissue Skeleton of the Human Heart: A Demonstration by Cell-Maceration Scanning Electron Microscope Method. *Circulation*, 97(9):934–935, 1998. doi: 10.1161/01.cir.97.9.934.

J.E. Saffitz, H.L. Kanter, K.G. Green, T.K. Tolley, and E.C. Beyer. Tissue-specific determinants of anisotropic conduction velocity in canine atrial and ventricular myocardium. *Circulation Research*, 74(6):1065–1070, 1994. doi: 10.1161/01.res.74.6.1065.

G.B. Sands, D.A. Gerneke, D.A. Hooks, C.R. Green, B.H. Smaill, and I.J. Legrice. Automated imaging of extended tissue volumes using confocal microscopy. *Microscopy Research and Technique*, 67(5):227–239, 2005. doi: 10.1002/jemt.20200.

H. Schmid, M.P. Nash, C. Walker, G.B. Sands, A. Pope, I.J. LeGrice, A.A. Young, P. Nielsen, and P.J. Hunter. A framework for multi-scale modeling of the myocardium. 2014.

D. F. Scollan, A. Holmes, J. Zhang, and R. L. Winslow. Reconstruction of Cardiac Ventricular Geometry and Fiber Orientation Using Magnetic Resonance Imaging. *Annals of Biomedical Engineering*, 28(8):934–944, 2000. doi: 10.1114/1.1312188.

G. Sommer, A..J. Schriefl, M. Andrä, M. Sacherer, C. Viertler, H. Wolinski, and G.A. Holzapfel. Biomechanical properties and microstructure of human ventricular myocardium. *Acta Biomaterialia*, 24:172–192, 2015. doi: 10.1016/j.actbio.2015.06.031.

C.T. Stoeck, C. von Deuster, and S. Kozerke. Second order motion compensated spin echo cardiac diffusion tensor imaging on clinical MR systems. *Journal of Cardiovascular Magnetic Resonance*, 18(1):61, 2016. doi: 10.1186/1532-429x-18-s1-p61.

D.D. Streeter and D.L. Bassett. An engineering analysis of myocardial fiber orientation in pig's left ventricle in systole. *The Anatomical Record*, 155(4):503–511, 1966. doi: 10.1002/ar.1091550403.

D.D. Streeter, H.M. Spotnitz, D.P. Patel, J. Ross, and E.H. Sonnenblick. Fiber Orientation in the Canine Left Ventricle during Diastole and Systole. *Circulation Research*, 24(3):339–347, 1969. doi: 10.1161/01.res.24.3.339.

H. G. Tsang, N. A. Rashdan, C. B. A. Whitelaw, B. M. Corcoran, K. M. Summers, and V. E. MacRae. Large animal models of cardiovascular disease: Cardiovascular Disease Models. *Cell Biochemistry and Function*, 34(3):113–132, 2016. doi: 10.1002/cbf.3173.

C. von Deuster, E. Sammut, L. Asner, D. Nordsletten, P. Lamata, Christian T. Stoeck, Sebastian Kozerke, and Reza Razavi. Studying Dynamic Myofiber Aggregate Reorientation in Dilated Cardiomyopathy Using In Vivo Magnetic Resonance Diffusion Tensor Imaging. *Circulation: Cardiovascular Imaging*, 9(10):e005018, 2016. doi: 10.1161/circimaging.116.005018.

World Health Organization. Cardiovascular diseases, 2017.

F.C.P. Yin, R.K. Strumpf, P.H. Chew, and S.L. Zeger. Quantification of the mechanical properties of noncontracting canine myocardium under simultaneous biaxial loading. *Journal of Biomechanics*, 20(6):577–589, 1987. doi: 10.1016/0021-9290(87)90279-x.

A.A. Young, I.J. Legrice, M.A. Young, and B.H. Smaill. Extended confocal microscopy of myocardial laminae and collagen network. *Journal of Microscopy*, 192(2):139–150, 1998. doi: 10.1046/j.1365-2818.1998.00414.x.

L. Zhukov and A.H. Barr. Heart-muscle fiber reconstruction from diffusion tensor MRI. In *IEEE Transactions on Ultrasonics, Ferroelectrics and Frequency Control*, pages 597–602, Seattle, WA, USA, 2003. IEEE. doi: 10.1109/visual.2003.1250425.

Introduction (Français)

1 Contexte général

Le cœur est un organe musculaire battant, situé juste derrière et légèrement à gauche du sternum. Il pompe le sang, transportant l'oxygène et les nutriments vers le corps, et les déchets métaboliques tels que le dioxyde de carbone vers les poumons. Les maladies cardiovasculaires représentent l'une des principales causes de décès dans le monde, avec un nombre de vies estimé à 17,9 millions par an [World Health Organization, 2017]. Le diagnostic précoce des pathologies cardiaques est crucial pour réduire leur gravité et leur mortalité. Il est souvent réalisé par l'écoute des bruits du cœur à l'aide d'un stéthoscope, par l'enregistrement d'un électrocardiographe, par l'échographie, par la mesure de la pression artérielle, etc. Ces méthodes permettent un diagnostic rapide de la condition cardiaque, basé sur des informations globales instantanées.

Une façon de permettre une meilleure prédiction de l'état du cœur est le développement de modèles qui prennent en compte la mécanique cardiaque. Les contraintes mécaniques jouent un rôle important dans le développement des maladies cardiaques telles que la cardiomyopathie, l'hypertrophie, l'insuffisance cardiaque, etc. La connaissance de la biomécanique du cœur est donc essentielle pour comprendre les causes et les conséquences des maladies cardiaques. En plus d'être utilisés comme outils de pronostic, ces modèles pourraient être utilisés pour le diagnostic et le traitement. Ils nécessitent alors une compréhension détaillée des mécanismes se déroulant aux petites échelles tissulaires. En effet, des études ont montré l'existence de multiples échelles spatiales qui régissent le comportement du tissu cardiaque et ont prouvé que la structure et la fonction cardiaques sont étroitement liées. En effet, la structure cardiaque évolue tout au long de la vie en réponse à des altérations de l'environnement mécanique et chimique, que ce soit sur le plan physiologique ou pathologique. Ces phénomènes sont généralement appelés croissance et remodelage, et consistent en des altérations permanentes de la microstructure cardiaque, entraînant des modifications de la fonction cardiaque. Une élucidation de ces mécanismes et de leurs couplages serait très utile pour concevoir un meilleur pronostic et traitement des pathologies cardiaques.

1.1 Le cœur

Le cœur est constitué de quatre cavités (voir Figure I.15) : les chambres supérieures sont appelées les oreillettes gauche et droite, et les chambres inférieures sont appelées les ventricules gauche et droit. Le septum inter-atrial sépare les oreillettes gauche et droite et le septum inter-ventriculaire sépare les ventricules gauche et droit.

Le ventricule gauche est la chambre la plus solide du cœur et a pour fonction de distribuer le sang avec une pression plus élevée que le ventricule droit. Par conséquent, il est plus grand et plus épais que le ventricule droit. Il a attiré beaucoup d'attention de la part des scientifiques car il est affecté par diverses conditions physiologiques ou pathologiques qui interfèrent avec son bon fonctionnement.

Quatre valves régulent le flux sanguin dans le cœur et interdisent le reflux : la tricuspide (entre l'oreillette droite et le ventricule droit), la valve pulmonaire (entre le ventricule droit et l'artère pulmonaire), la valve mitrale (entre l'oreillette gauche et le ventricule gauche) et la valve aortique (entre le ventricule gauche et l'aorte).

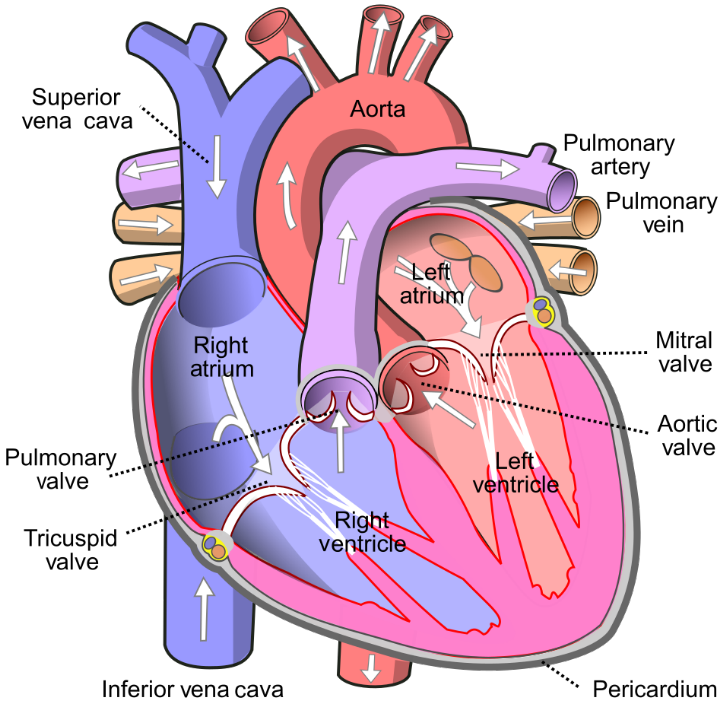

FIGURE I.15 – Représentation schématique du cœur humain montrant les oreillettes, les ventricules et les valves. Le sang oxygéné est représenté en rouge et le sang désoxygéné en bleu. Illustration de Wapcaplet, sous licence CC BY-SA 3.0.

Le cycle cardiaque est une séquence d'événements mécaniques et électriques, composée de deux périodes. Une période pendant laquelle le muscle cardiaque se relâche et les ventricules se remplissent à nouveau de sang (écoulement du sang des oreillettes gauche et droite dans les ventricules gauche et droit respectivement), appelée diastole, et une période de contraction musculaire et de pompage du sang (éjection du sang des ventricules gauche et droit dans l'aorte et les artères pulmonaires), appelée systole.

1.2 Le myocarde

La paroi du cœur est principalement composée de tissu musculaire, également appelé myocarde. Il contient les cardiomyocytes, qui permettent la contraction cardiaque. Elle mesure environ 15 mm d'épaisseur, et est prise en sandwich entre une fine couche interne, l'endocarde (0,5 µm d'épaisseur), qui enveloppe les chambres cardiaques, et une fine couche externe, l'épicarde, également appelé péricarde viscéral (2 mm d'épaisseur), qui entoure le cœur (voir Figure I.16). Le péricarde pariétal est une couche de 0,8 µm qui recouvre le péricarde.

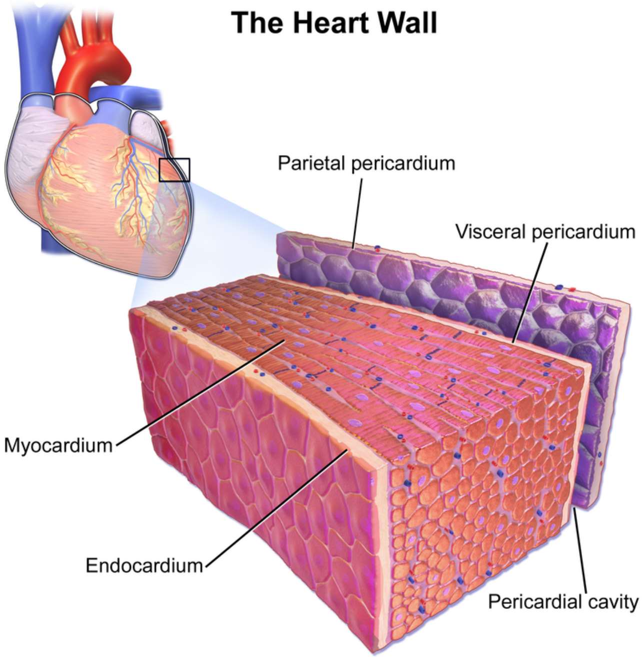

FIGURE I.16 – Représentation schématique de la paroi cardiaque humaine, montrant le myocarde, enveloppé par l'endocarde interne et le péricarde viscéral externe. Illustration de BruceBlaus, sous licence CC BY 3.0.

Plusieurs modèles animaux ont été conçus et utilisés pour mener des recherches. Les porcs, en particulier, présentent de nombreuses similitudes qui en font un modèle bien adapté à l'étude des maladies cardiovasculaires. Ils ont une fréquence cardiaque moyenne de 90-110 battements par minute (bpm), imitant la fréquence cardiaque moyenne de l'homme, qui est de 70-100 bpm. En outre, leur grande taille en fait un choix approprié pour l'imagerie et les études d'ingénierie tissulaire [Tsang et al., 2016].

1.2.1 Microstructure

Le myocarde est constitué de structures organisées selon une architecture hiérarchique multi-échelle. La figure I.17 montre une organisation hiérarchique des cardiomyocytes et du tissu conjonctif dans le muscle squelettique, qui est également observée dans le muscle cardiaque. On remarque principalement quatre échelles importantes : l'échelle sub-cellulaire, l'échelle cellulaire, l'échelle du fascicule et l'échelle du tissu. Notons que, dans le tissu cardiaque, l'échelle du fascicule est appelée échelle du feuillet, et son organisation dans la paroi est différente de celle du tissu squelettique.

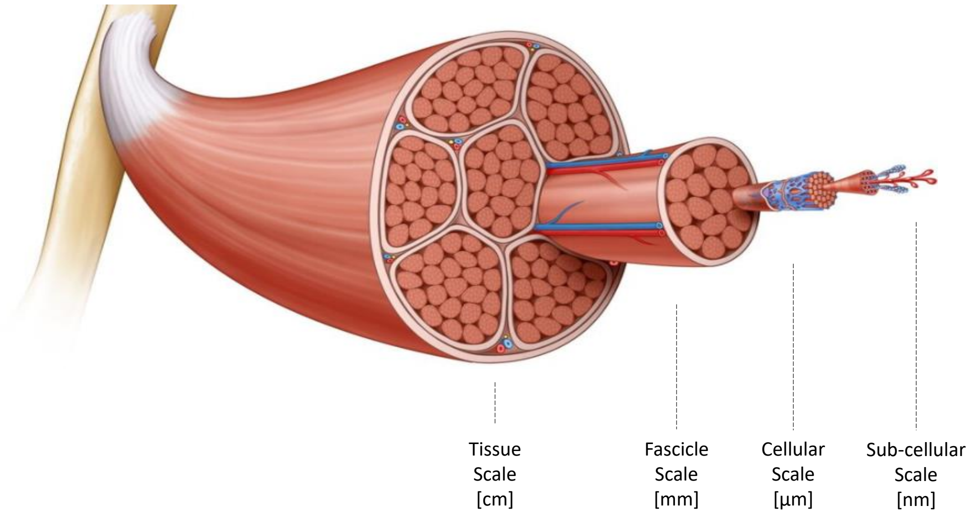

FIGURE I.17 – Structure musculaire squelettique montrant l'organisation hiérarchique des échelles sous-cellulaires, cellulaires, fasciculaires et tissulaires. Adapté de therobertslab.com

Echelle	**Nomenclature**	**Dimension**
Echelle nano	Échelle sub-cellulaire	<1 µm
Échelle micro	Échelle cellulaire	1-10 µm
Échelle meso	Échelle du feuillet	100-500 µm
Échelle macro	Échelle du tissu	>500 µm

TABLE I.2 – Glossaire des quatre echelles, leurs différentes nomenclatures et leurs dimensions.

Échelle sub-cellulaire. À l'échelle sub-cellulaire, chaque fibre cardiaque est principalement constituée de sarcomères alignés. Chaque sarcomère est constitué de filaments parallèles d'actine (fins) et de myosine (épais) (voir Figure I.18). Les sarcomères sont responsables de l'aspect strié du muscle, évident sur la figure I.19 [Krueger et al., 1980; Roos, 1987; Kanzaki et al., 2010].

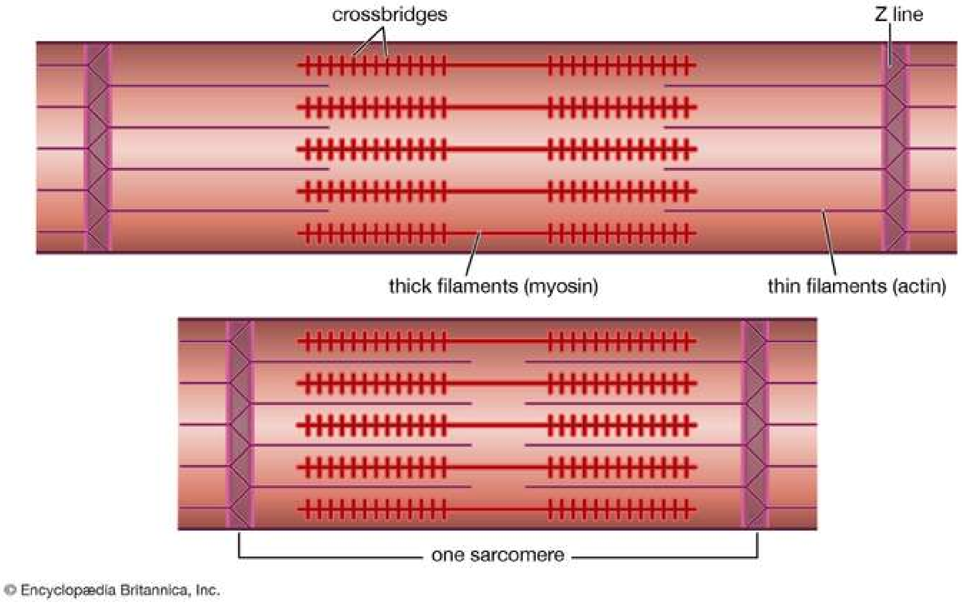

FIGURE I.18 – La disposition des sarcomères, filaments épais et fins dans une fibre musculaire. Le sarcomère est en position relâchée (en haut) et contractée (en bas). Extrait de *Encyclopedia Britannica, Inc.*

Échelle cellulaire. Les cardiomyocytes sont grossièrement cylindriques, mesurant 100-150 µm par 10-20 µm. Ils sont extrêmement ramifiés. Chaque cardiomyocyte est relié, en moyenne, à 11 cellules voisines par des disques intercalaires (voir Figure I.19, A) [Saffitz et al., 1994].

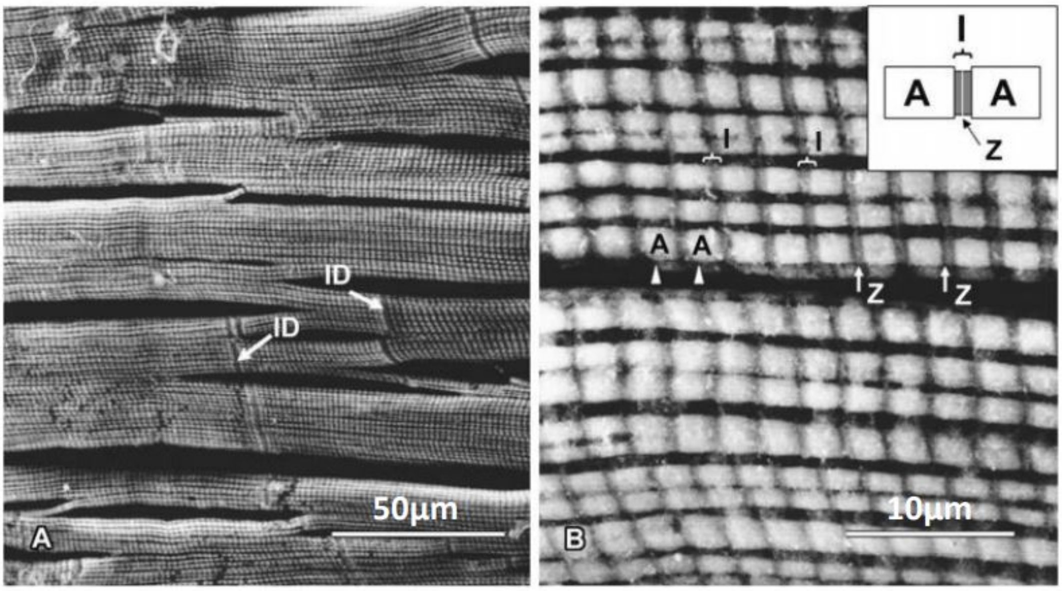

Figure I.19 – Microscopie électronique à balayage des cardiomyocytes du ventricule gauche humain. A : Les disques intercalés (flèches) et stries de sarcomère sont clairement visibles. B : Grossissement plus important des sarcomères. ID indique les disques intercalés ; A, les bandes A ; I, les bandes I ; et Z, les lignes Z. Extrait de [Kanzaki et al., 2010].

Chaque fibre cardiaque est entourée d'une fine couche de tissu conjonctif, appelée trame endomysiale, et est reliée à d'autres myocytes par du tissu endomysial latéral [Robinson et al., 1988; Rossi et al., 1998; Kanzaki et al., 2009, 2010]. Il a été démontré que l'endomysium contient principalement des composants de collagène I et III, et des types IV et V en quantités très mineures [Light and Champion, 1984].

La figure I.20 montre le tissu conjonctif du myocarde après élimination des cardiomyocytes, où le collagène endomysial enveloppe chaque cardiomyocyte, pour un sujet normal (A) et pour un sujet présentant une hypertrophie concentrique (B). Elle montre que le remodelage pathologique affecte la matrice extracellulaire endomysiale, avec un épaississement de l'endomysium.

Les cardiomyocytes sont fortement altérés par la croissance et le remodelage. Par exemple, à l'échelle cellulaire, un allongement et un amincissement des cardiomyocytes conduisent à une dilatation des ventricules à l'échelle de l'organe. Ce phénomène est

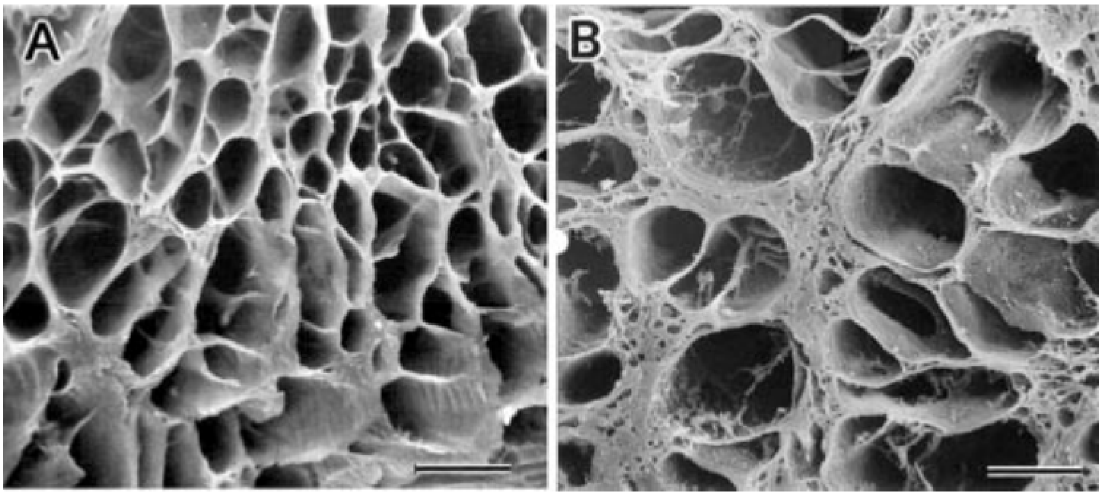

FIGURE I.20 – Image de microscopie électronique à balayage montrant la matrice extracellulaire endomysiale entourant chaque cellule cardiaque individuelle, pour un sujet normal (A), et un patient atteint d'hypertrophie concentrique (B). L'image montre l'effet de remodelage sur l'endomysium (barre d'échelle : 30 µm). Extrait de [Kanzaki et al., 2009].

connu sous le nom d'hypertrophie excentrique. A l'inverse, un raccourcissement et un épaississement des cellules cardiaques conduit à un épaississement des parois ventriculaires, dans le cas d'une hypertrophie concentrique [Hunter and Chien, 1999; Maillet et al., 2013] (see Figure I.21).

La figure I.22 montre des images d'échantillons de tissus obtenus après ablation du tissu conjonctif pour un sujet normal (A) et un patient atteint de cardiomyopathie hyperthrophique concentrique (B et C). On constate un épaississement des cardiomyocytes en B et C, ainsi qu'un désordre dans leur organisation.

Échelle du feuillet. Les cardiomyocytes sont localement parallèles, et sont disposés en fascicules de 5 à 10 cellules, formant des structures de 100-200 µm. Ces structures sont enveloppées par une couche de matrice extracellulaire collagénique, appelée perimysium [Legrice et al., 1997; Costa et al., 1997; Rossi et al., 1998; Young et al., 1998; Arts et al., 2001]. Le perimysium est plus épais que l'endomysium et peut atteindre jusqu'à 10 µm dans un cœur sain. Il a été démontré qu'il contient principalement du collagène de type I, III et V [Light and Champion, 1984].

Il n'existe pas de consensus au sein de la communauté de recherche cardiaque sur le nom de cette structure. Alors que certains l'appellent "fascicule" de cardiomyocytes, d'autres l'appellent "feuillet" car il forme, localement dans le tissu, des structures en forme de feuille. Nous avons choisi, dans cette recherche, de définir le "feuillet" comme

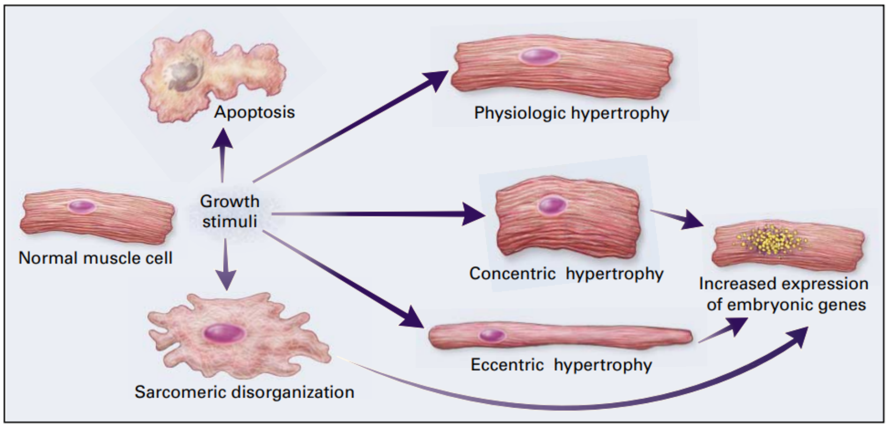

FIGURE I.21 – Des changements phénotypiquement distincts de la morphologie des cardiomyocytes se produisent en réponse à divers stimuli de croissance. Extrait de [Hunter and Chien, 1999].

le groupe de cardiomyocytes enveloppé par la couche de périmysium. Au cours de notre revue de la littérature, nous avons rencontré deux théories coexistantes qui décrivent la configuration des feuillets dans le tissu, la configuration laminaire et la configuration globulaire, que nous allons présenter.

Configuration laminaire. Les coupes radiales de la paroi cardiaque montrent des feuillets plats empilés les uns à côté des autres dans la paroi cardiaque. Ces feuillets s'étendent radialement de l'endocarde à l'épicarde dans les coupes transmurales du ventricule gauche, et sont séparés par des espaces appréciables entre les couches, appelés plans de clivage. Ces plans sont très probablement dus à la préparation du tissu (congélation, déshydratation, tranchage, défibrage, etc.) [LeGrice et al., 1995; Young et al., 1998; Sands et al., 2005; Pope et al., 2008]. La figure I.23 montre une représentation tridimensionnelle d'un volume de piles enregistrées de tranches couvrant la paroi du ventricule gauche de l'épicarde à l'endocarde, où les plans de clivage sont évidents. Le tissu conjonctif (coloré en blanc) couvre les côtés des feuillets, et sa densité augmente près des surfaces épicardiques et endocardiques.

Configuration globulaire. Les images réalisées transversalement aux cellules cardiaques montrent une disposition globulaire des faisceaux de cardiomyocytes, entourés d'une couche de périmysium [Kanzaki et al., 2010, 2012]. Les plans de clivage ne sont pas observés sur ces images, au contraire, le tissu semble être constitué d'amas globulaires adjacents continus de différentes tailles, reliés par le périmysium. La figure I.24 montre

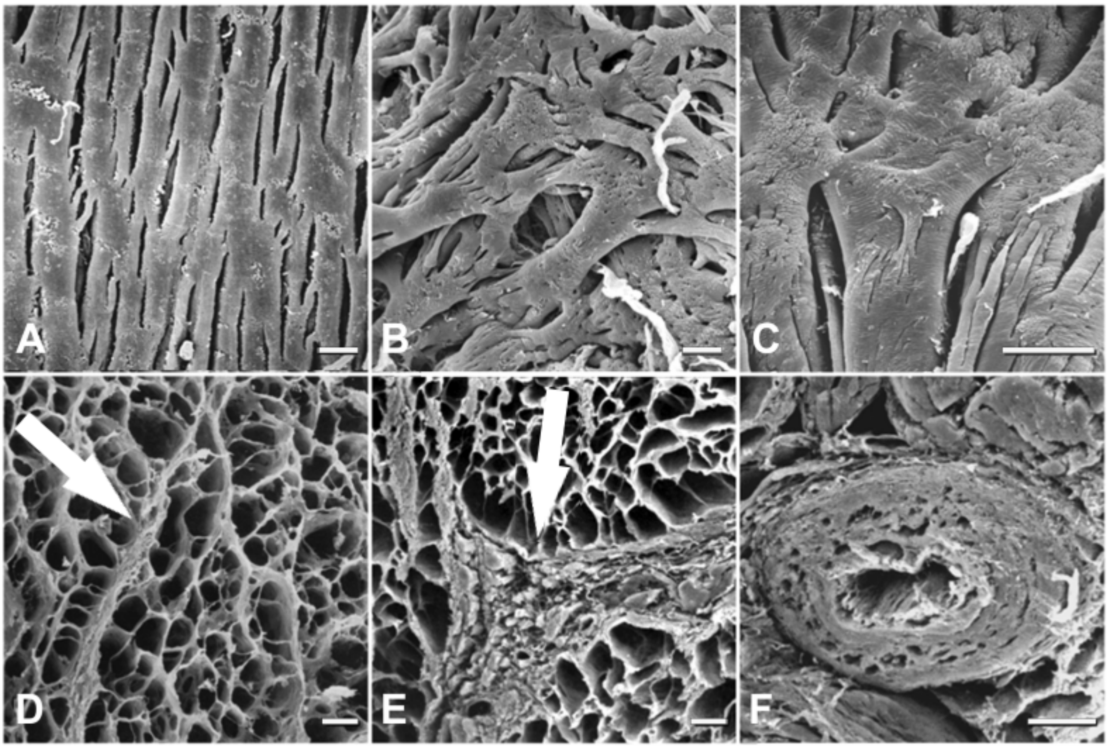

FIGURE I.22 – Microscopie électronique à balayage des cardiomyocytes. Des échantillons de tissus provenant d'un sujet normal (A, D) et d'un patient atteint de cardiomyopathie hypertrophique (B, C, E, F) sont présentés. Les images ont été obtenues après l'élimination du tissu conjonctif (A, B, C) ou du tissu non fibreux (D, E, F), (flèches blanches). Dans l'échantillon de cœur du patient atteint de cardiomyopathie hypertrophique, un désarroi myocardique et des ramifications anormales sont observés en B et C. E et F montrent une épaisseur accrue de tissu conjonctif interstitiel et des petits vaisseaux intramuraux épaissis. (barre d'échelle : 20 µm). Extrait de [Kanzaki et al., 2012].

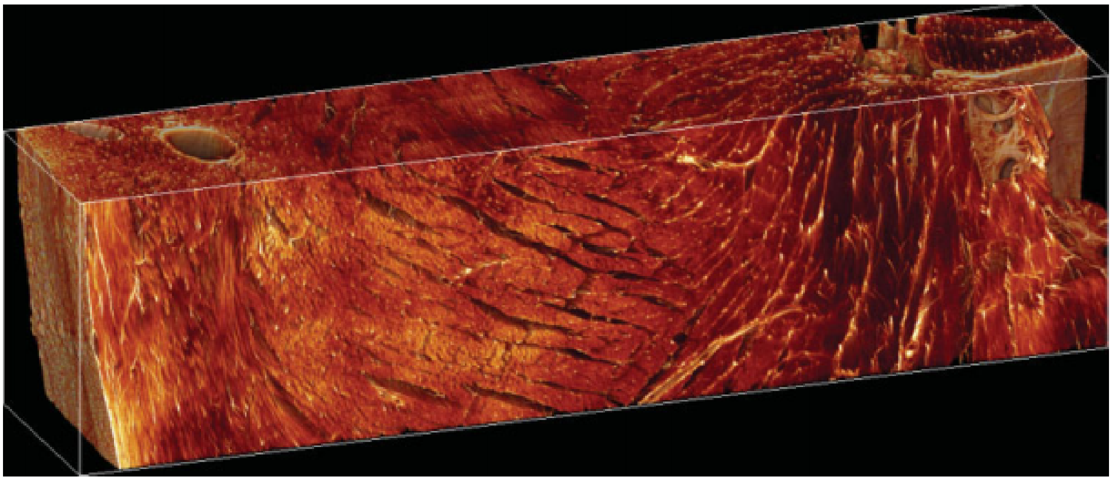

Figure I.23 – Représentation tridimensionnelle d'un volume d'empilement transmural (4,25×1,12×0,88 mm) de tranches imagées par microscopie confocale montrant une structure laminaire avec des feuillets séparés par des plans de clivage allongés et un réseau de collagène dense près de l'endocarde et de l'épicarde. Extrait de [Sands et al., 2005].

cet arrangement globulaire, où des faisceaux de cellules (chacune enveloppée par l'endomysium) sont regroupés en ellipsoïdes et entourés par le collagène périmysial (flèche épaisse). À notre connaissance, aucune étude n'a porté sur l'organisation et l'orientation de ces structures globulaires dans l'épaisseur de la paroi.

La structure en feuillets a attiré de plus en plus d'attention, du fait que la matrice extracellulaire de collagène, à cette méso-échelle, est fortement modifiée par le remodelage cardiaque. La figure I.22 montre des images d'échantillons de tissus obtenus après prélèvement de cardiomyocytes pour un sujet normal (D) et un patient atteint de cardiomyopathie d'hypertrophie concentrique (E et F). On remarque un épaississement de la matrice extra-cellulaire périmysiale dans le cas du cœur hypertrophié.

Échelle tissulaire. À l'échelle du tissu, l'orientation des cardiomyocytes a été largement étudiée. L'orientation des fibres myocardiques est connue pour varier de façon continue et régulière à travers la paroi cardiaque. Historiquement, il a été démontré en effectuant des mesures sur des sections circonférentielles de myocarde obtenues à partir de ventricules gauches, que l'angle des fibres cardiaques varie d'environ 90° près de l'endocarde à environ -90° à l'épicarde chez le porc [Streeter and Bassett, 1966], et de ±60° chez le chien [Streeter et al., 1969]. Cette disposition a ensuite été confirmée et cartographiée par imagerie par résonance magnétique à tenseur de diffusion (DT-MRI) [Scollan et al., 2000; Zhukov and Barr, 2003] (voir Figure I.25), et, plus récemment, in

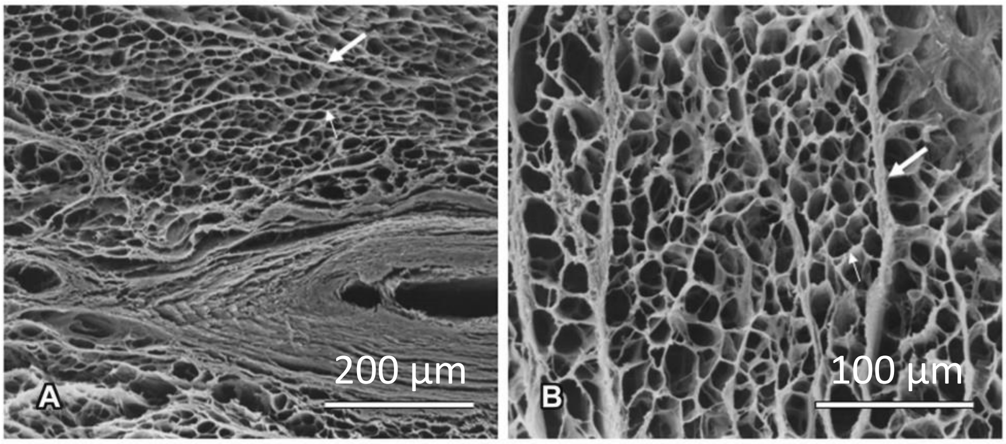

Figure I.24 – Squelette de tissu conjonctif du cœur humain (coupe transversale). A : On observe clairement la configuration en feuillets globulaires, avec du collagène périmysial autour des cardiomyocytes et des petits vaisseaux. (flèche épaisse, périmysium ; flèche fine, endomysium). B : Le tissu conjonctif interstitiel composé de composants périmysiaux et endomysiaux présente une forme en nid d'abeille. Le périmysium (flèche épaisse) entoure des groupes de cardiomyocytes, et l'endomysium (flèche fine) entoure chaque cardiomyocyte. Extrait de [Kanzaki et al., 2010].

vivo DT-MRI [von Deuster et al., 2016; Stoeck et al., 2016; Nielles-Vallespin et al., 2017].

La variation de l'orientation des feuillets est moins bien comprise. On ne sait toujours pas comment les structures des feuillets sont organisées dans l'épaisseur du myocarde et le long de sa paroi. Alors que certaines études ont soutenu la prédominance d'une seule population de feuillets laminaires, avec une orientation qui évolue linéairement entre l'endocarde et l'épicarde (voir Figure I.26, gauche) [LeGrice et al., 1995; Ferreira et al., 2014; Nielles-Vallespin et al., 2017], d'autres études ont montré la coexistence de deux populations locales de feuillets myocardiques (voir Figure I.26, droite) [Kung et al., 2011; Kilner et al., 2015].

1.2.2 Propriétés mécaniques

Les propriétés mécaniques du tissu cardiaque peuvent être divisées en deux catégories : un comportement actif résultant de la contraction musculaire via le cycle des ponts croisés [Huxley and Simmons, 1971; Lymn and Taylor, 1971], et un comportement passif résultant des autres parties du tissu.

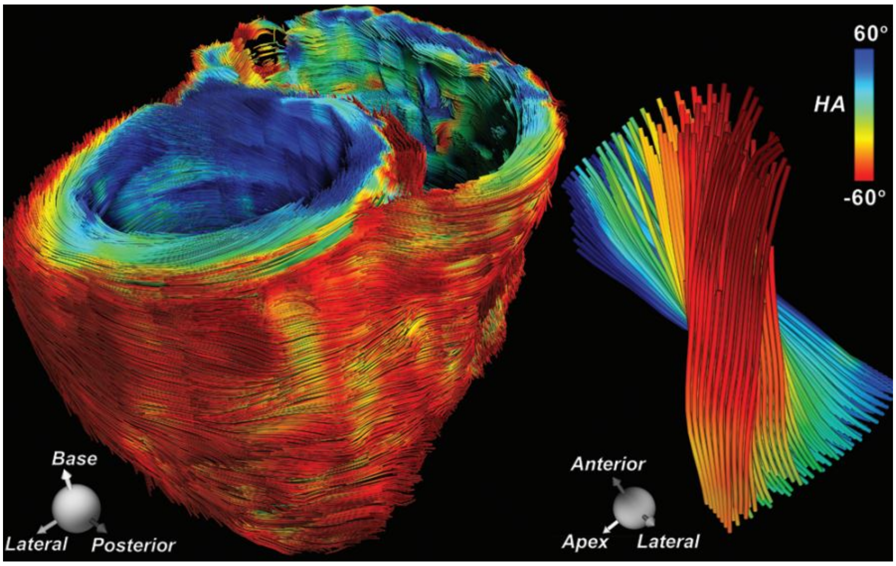

FIGURE I.25 – Image de DT-MRI sur un patient sain montrant la variation de l'orientation des cardiomyocytes à travers l'épaisseur et le long de la paroi cardiaque. Extrait de [Mekkaoui et al., 2017].

Comportement passif. Lorsqu'il est soumis à une extension uniaxiale, l'échantillon myocardique subit de grandes déformations non linéaires, avec un comportement plus rigide dans la direction des fibres que dans la direction des fibres transversales (voir Figure I.27), et une hystérésis prononcée indiquant une dissipation d'énergie importante lors du chargement [Fung, 1967; Demer and Yin, 1983] ou biaxiale [Yin et al., 1987; Sommer et al., 2015]. Lorsque la traction est appliquée dans le sens de la fibre cardiaque, les cardiomyocytes sont étendus et la distance entre eux diminue. Les fibres de la matrice extracellulaire se déroulent et contribuent à l'augmentation exponentielle de la contrainte [MacKenna et al., 1994]. Lorsque la charge est latérale aux fibres, on observe également un raidissement exponentiel, dû au recrutement du réseau de collagène dans la matrice extracellulaire.

Un cisaillement simple a été appliqué à des échantillons de myocarde par rapport à trois axes principaux du matériau (l'axe de la fibre, l'axe de la feuille et la normale au plan fibre-feuille) dans six modes, six contraintes de cisaillement différentes ont été mesurées le long des différents axes, mettant en évidence l'anisotropie du tissu [Dokos et al., 2002; Sommer et al., 2015].

Dans la plupart des études sur le cœur, le tissu a été supposé incompressible, principalement en raison du contenu fluide des cellules et des composants interstitiels. Récemment, des études ont montré que le volume du myocarde subit un changement dynamique

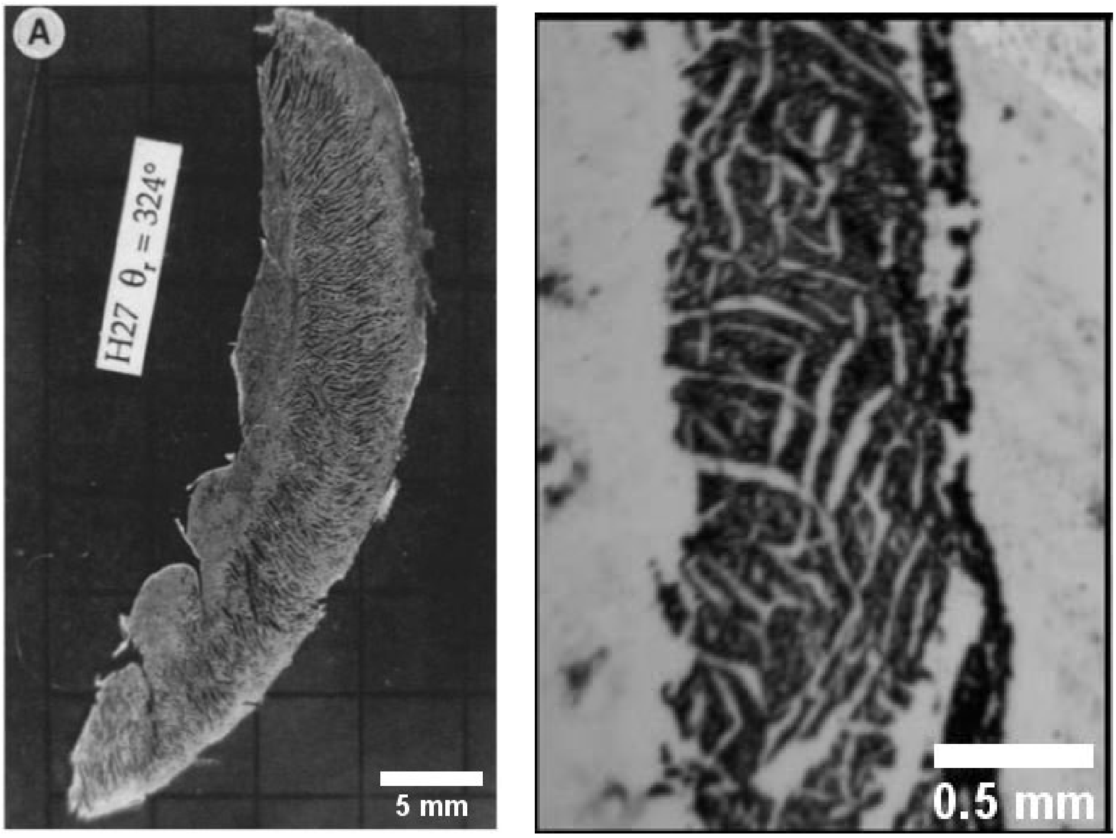

Figure I.26 – Coupe longitudinale-transmurale du ventricule gauche montrant : À gauche : un alignement radial des couches de myocytes avec une orientation linéairement variable (extrait de [Legrice et al., 2001]). À droite : deux populations distinctes de feuillets, extrait de [Kung et al., 2011].

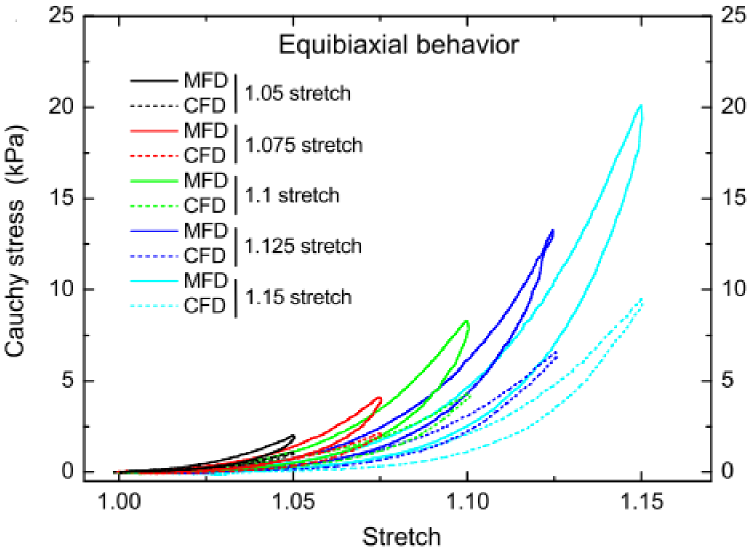

FIGURE I.27 – Comportement d'étirement des contraintes dans la direction de la myofibre (MFD, courbes pleines) et dans la direction des fibres transversales (CFD, courbes en pointillés) d'échantillons de paroi libre ventriculaire gauche humaine montrant un comportement plus rigide dans le MFD. Extrait de [Sommer et al., 2015].

au cours du cycle cardiaque, avec une variation pouvant atteindre 10%, qui ne peut pas être entièrement expliquée par le mouvement du sang dans le système vasculaire, ou par la structure cardiaque [Ashikaga et al., 2008].

Comportement actif. Dans ce travail, l'accent est mis sur la composante passive des propriétés musculaires. Par conséquent, nous ne présenterons que brièvement les propriétés actives. À l'échelle nanométrique, la théorie des filaments glissants explique le mécanisme de contraction musculaire : les filaments glissent les uns sur les autres lors de la contraction, et forment un complexe protéique (appelé actomyosine), par fixation d'une tête de myosine sur l'actine filament, formant un pont croisé (voir Figure I.28) [Huxley and Simmons, 1971; Lymn and Taylor, 1971]. Le cycle de Lymn-Tylor décrit le cycle du pont croisé en quatre étapes, comme le montre la figure I.28 : tout d'abord, un pont croisé se forme, avec la liaison d'une tête de myosine activée à une actine, suivie d'un coup de force, où l'adénosine diphosphate (ADP) est libérée et la tête de myosine activée pivote, permettant au filament fin de glisser vers le centre du sarcomère. Ensuite, l'adénosine triphosphate (ATP) se lie à la tête de myosine, le lien entre la tête de myosine et l'actine s'affaiblit, et la tête de myosine se détache. Enfin, l'ATP est hydrolysé en ADP et en phosphate inorganique. L'énergie libérée pendant l'hydrolyse réactive la tête de myosine, la ramenant à sa position initiale. Au fur et à mesure que ce cycle se répète, les myofilaments épais et fins sont rapprochés les uns des autres et le sarcomère se raccourcit, entraînant la contraction du muscle.

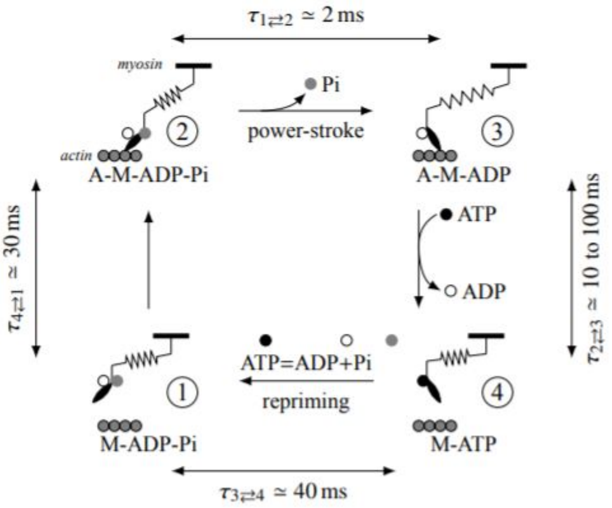

FIGURE I.28 – Représentation des quatre étapes du cycle Lymn-Taylor, conduisant au glissement des filaments d'actine et de myosine, donc à la contraction musculaire. Extrait de [Caruel and Truskinovsky, 2018].

Les modèles continus existants à l'échelle de l'organe peuvent simuler l'activité électromécanique du cœur pendant un cycle cardiaque [Guccione et al., 1995; Hunter and Chien, 1999], y compris même des modèles nanoscopiques détaillés de la contraction active [Chapelle et al., 2012; Caruel et al., 2019; Kimmig and Caruel, 2020]. À l'échelle macroscopique, la rigidité musculaire augmente lors de la contraction [Roos, 1987], ce qui signifie que la contraction a un impact sur les propriétés mécaniques macroscopiques du myocarde.

2 Enjeux

L'architecture 3D complexe et hiérarchique du myocarde est intrigante et confère au tissu ses propriétés mécaniques passives macroscopiques complexes. De plus, les altérations de la structure à l'échelle microscopique affectent profondément le comportement du tissu. Une compréhension approfondie des mécanismes sous-jacents aux relations structure-propriétés serait d'une grande utilité pour concevoir un meilleur diagnostic et traitement des pathologies cardiaques.

L'étude structurale, les tests expérimentaux et la modélisation numérique sont essentiels et complémentaires pour caractériser les propriétés mécaniques multi-échelles du tissu cardiaque. Les informations structurales créent une image locale claire de la structure cardiaque qui, couplée à des essais expérimentaux, est essentielle pour le développement de modèles numériques multi-échelles.

2.1 Enjeux éxperimentaux

Les études structurales ont permis de donner une vision claire de la structure du cardiomyocyte, et de cartographier son organisation dans la paroi cardiaque [Legrice et al., 2001]. L'échelle des feuillets, en revanche, est moins clairement définie. Son organisation et son orientation dans le cœur ne sont pas entièrement comprises. Cela constitue un obstacle à la modélisation de cette échelle intermédiaire, ce qui entraîne des difficultés pour étudier ses propriétés mécaniques et son rôle dans le tissu.

D'autre part, des études expérimentales ont été menées à l'échelle macroscopique, afin de quantifier les relations contrainte-déformation. Les résultats expérimentaux diffèrent d'une étude à l'autre, ce qui peut être dû à la préparation de l'échantillon et aux protocoles expérimentaux tels que le préconditionnement des tissus, la préhension, etc., et aux différences entre les cœurs testés [Dokos et al., 2002; Sommer et al., 2015]. Ainsi, l'un des principaux défis consiste à reproduire les conditions expérimentales in-vivo lors des essais ex-vivo. En outre, il y a un manque d'études expérimentales reliant les déformations à l'échelle macroscopique avec les déformations à des échelles plus petites. De telles expériences permettraient de faire la lumière sur les micro-mécanismes dans les tissus.

2.2 Enjeux de modélisation

En parallèle, les modèles continus existants peuvent simuler l'activité électromécanique du cœur pendant un cycle cardiaque et incluent même des modèles microscopiques détaillés de la contraction active [Chapelle et al., 2012]. Cependant, dans la plupart des modèles de la littérature, le comportement passif est moins finement décrit, se limitant à des modèles purement macroscopiques [Holzapfel and Ogden, 2009]. Bien qu'ils aient pu s'ajuster aux données expérimentales, l'ensemble des paramètres matériaux qu'ils emploient n'est pas unique et diffère, pour un même modèle, en fonction des essais mécaniques. En outre, la plupart des modèles de la littérature prennent en compte l'anisotropie du tissu, mais son origine n'a pas encore été étudiée. On suppose qu'elle provient de l'arrangement structurale du tissu, mais, à notre connaissance, aucune étude n'a encore abordé cette question.

3 Structure de la thèse

Dans cette thèse, nous avons étudié la relation entre la structure et l'organisation des feuillets, et les propriétés mécaniques macroscopiques passives du tissu cardiaque. Pour cela, nous avons utilisé des approches expérimentales et computationnelles.

Dans le Chapitre ch : :chapter1, un dispositif expérimental est conçu afin d'étudier la déformation mésostructurale du myocarde dans des conditions d'étirement. Nous avons observé des lignes de séparation qui ont tendance à se former sous traction. Dans le Chapitre ch : :chapter2, en utilisant une technique d'imagerie rapide et un post-traitement simple, nous avons tenté d'observer l'organisation et l'orientation de la mésostructure dans toute l'épaisseur et tout le long de la paroi du ventricule gauche. Les résultats obtenus nous ont permis d'avoir un aperçu de l'orientation des feuillets en 2D, mais ne sont pas suffisants pour reconstruire un modèle 3D. Dans le Chapitre ch : :chapter3, nous avons développé un modèle numérique, afin d'étudier l'effet des feuillets et de leur organisation sur l'anisotropie macroscopique. Nous avons trouvé que la rotation des cardiomyocytes et des feuillets dans la paroi cardiaque est nécessaire pour reproduire l'anisotropie.

Bibliographie

T. Arts, K. D. Costa, J. W. Covell, and A. D. McCulloch. Relating myocardial laminar architecture to shear strain and muscle fiber orientation. *American Journal of Physiology-Heart and Circulatory Physiology*, 280(5) :H2222–H2229, 2001. doi : 10.1152/ajpheart.2001.280.5.H2222.

H. Ashikaga, B.A. Coppola, K.G. Yamazaki, F.J Villarreal, J.H. Omens, and J.W. Covell. Changes in regional myocardial volume during the cardiac cycle : implications for transmural blood flow and cardiac structure. *American Journal of Physiology-Heart and Circulatory Physiology*, 295(2) :H610–H618, 2008. doi : 10.1152/ajpheart.00107.2008.

M. Caruel and L. Truskinovsky. Physics of muscle contraction. *Reports on Progress in Physics*, 81(3) :036602, 2018. doi : 10.1088/1361-6633/aa7b9e.

M. Caruel, P. Moireau, and D. Chapelle. Stochastic modeling of chemical–mechanical coupling in striated muscles. *Biomechanics and Modeling in Mechanobiology*, 18(3) : 563–587, 2019. doi : 10.1007/s10237-018-1102-z.

D. Chapelle, P. Le Tallec, P. Moireau, and M. Sorine. Energy-preserving muscle tissue model : formulation and compatible discretizations. *International Journal for Multiscale Computational Engineering*, 10(2) :189–211, 2012. doi : 10.1615/intjmultcompeng.2011002360.

K.D. Costa, K. May-Newman, D. Farr, W.G. O'Dell, A.D. McCulloch, and J.H. Omens. Three-dimensional residual strain in midanterior canine left ventricle. *American Journal of Physiology-Heart and Circulatory Physiology*, 273(4) :H1968–H1976, 1997. doi : 10.1152/ajpheart.1997.273.4.H1968.

L.L. Demer and F.C. Yin. Passive biaxial mechanical properties of isolated canine myocardium. *The Journal of Physiology*, 339(1) :615–630, 1983. doi : 10.1113/jphysiol.1983.sp014738.

S. Dokos, B.H. Smaill, A.A. Young, and I.A. LeGrice. Shear properties of passive ventricular myocardium. *American Journal of Physiology-Heart and Circulatory Physiology*, 283(6) :H2650–H2659, 2002. doi : 10.1152/ajpheart.00111.2002.

P.F. Ferreira, P.J. Kilner, L-A. McGill, S. Nielles-Vallespin, A.D. Scott, Siew Y Ho, Karen P McCarthy, Margarita M Haba, Tevfik F Ismail, Peter D Gatehouse, Ranil de Silva, Alexander R Lyon, Sanjay K Prasad, David N Firmin, and Dudley J Pennell. In vivo cardiovascular magnetic resonance diffusion tensor imaging shows evidence of abnormal myocardial laminar orientations and mobility in hypertrophic cardiomyopathy. *Journal of Cardiovascular Magnetic Resonance*, 16(1) :87, 2014. doi : 10.1186/s12968-014-0087-8.

Y.C. Fung. Elasticity of soft tissues in simple elongation. *American Journal of Physiology-Legacy Content*, 213(6) :1532–1544, 1967. doi : 10.1152/ajplegacy.1967.213.6.1532.

J.M. Guccione, K.D. Costa, and A.D. McCulloch. Finite element stress analysis of left ventricular mechanics in the beating dog heart. *Journal of Biomechanics*, 28(10) : 1167–1177, 1995. doi : 10.1016/0021-9290(94)00174-3.

G.A. Holzapfel and R.W. Ogden. Constitutive modelling of passive myocardium : a structurally based framework for material characterization. *Philosophical Transactions of the Royal Society A : Mathematical, Physical and Engineering Sciences*, 367(1902) : 3445–3475, 2009. doi : 10.1098/rsta.2009.0091.

J.J. Hunter and K.R. Chien. Signaling Pathways for Cardiac Hypertrophy and Failure. *New England Journal of Medicine*, 341(17) :1276–1283, 1999. doi : 10.1056/nejm199910213411706.

A. F. Huxley and R. M. Simmons. Proposed Mechanism of Force Generation in Striated Muscle. *Nature*, 233(5321) :533–538, 1971. doi : 10.1038/233533a0.

Y. Kanzaki, F. Terasaki, M. Okabe, and Y. Kitaura. Three-Dimensional Remodeling of Cardiomyocytes in a Patient With Aortic Stenosis : Scanning Electron Microscopy. *Circulation*, 119(2) :e10, 2009. doi : 10.1161/circulationaha.108.809467.

Y. Kanzaki, F. Terasaki, M. Okabe, S. Fujita, T. Katashima, K. Otsuka, and N. Ishizaka. Three-Dimensional Architecture of Cardiomyocytes and Connective Tissue in Human Heart Revealed by Scanning Electron Microscopy. *Circulation*, 122(19) :1973–1974, 2010. doi : 10.1161/circulationaha.110.979815.

Y. Kanzaki, Y. Yamauchi, M. Okabe, F. Terasaki, and N. Ishizaka. Three-Dimensional Architecture of Cardiomyocytes and Connective Tissues in Hypertrophic Cardiomyopathy : A Scanning Electron Microscopic Observation. *Circulation*, 125(5) :738–739, 2012. doi : 10.1161/circulationaha.111.054668.

P.J. Kilner, K. McCarthy, M. Murillo, P. Ferreira, A.D. Scott, Laura-Ann McGill, Sonia Nielles-Vallespin, Ranil Silva, Dudley J Pennell, Siew Y Ho, and David Firmin.

Histology of human myocardial laminar microstructure and consideration of its cyclic deformations with respect to interpretation of in vivo cardiac diffusion tensor imaging. *Journal of Cardiovascular Magnetic Resonance*, 17(S1) :Q10, 2015. doi : 10.1186/1532-429x-17-s1-q10.

F. Kimmig and M. Caruel. Hierarchical modeling of force generation in cardiac muscle. *Biomechanics and Modeling in Mechanobiology*, 19(6) :2567–2601, 2020. doi : 10.1007/s10237-020-01357-w.

J.W. Krueger, D. Forletti, and B.A. Wittenberg. Uniform sarcomere shortening behavior in isolated cardiac muscle cells. *The Journal of General Physiology*, 76(5) :587–607, 1980. doi : 10.1085/jgp.76.5.587.

G.L. Kung, T.C. Nguyen, A. Itoh, S. Skare, N.B. Ingels, D.C. Miller, and D.B. Ennis. The presence of two local myocardial sheet populations confirmed by diffusion tensor MRI and histological validation. *Journal of Magnetic Resonance Imaging*, 34(5) :1080–1091, 2011. doi : 10.1002/jmri.22725.

I. Legrice, P. Hunter, A. Young, and B. Smaill. The architecture of the heart : a data–based model. *Philosophical Transactions of the Royal Society of London. Series A : Mathematical, Physical and Engineering Sciences*, 359(1783) :1217–1232, 2001. doi : 10.1098/rsta.2001.0827.

I. J. LeGrice, B. H. Smaill, L. Z. Chai, S. G. Edgar, J. B. Gavin, and P. J. Hunter. Laminar structure of the heart : ventricular myocyte arrangement and connective tissue architecture in the dog. *American Journal of Physiology-Heart and Circulatory Physiology*, 269(2) :H571–H582, 1995. doi : 10.1152/ajpheart.1995.269.2.h571.

I. J. Legrice, P. J. Hunter, and B. H. Smaill. Laminar structure of the heart : a mathematical model. *American Journal of Physiology-Heart and Circulatory Physiology*, 272 (5) :H2466–H2476, 1997. doi : 10.1152/ajpheart.1997.272.5.h2466.

N. Light and A.E. Champion. Characterization of muscle epimysium, perimysium and endomysium coliagens. *Biochemical Journal*, 219 :10, 1984. doi : 10.1042/bj2191017.

R. W. Lymn and E. W. Taylor. Mechanism of adenosine triphosphate hydrolysis by actomyosin. *Biochemistry*, 10(25) :4617–4624, 1971. doi : 10.1021/bi00801a004.

D. A. MacKenna, J. H. Omens, A. D. McCulloch, and J. W. Covell. Contribution of collagen matrix to passive left ventricular mechanics in isolated rat hearts. *American*

Journal of Physiology-Heart and Circulatory Physiology, 266(3) :H1007–H1018, 1994. doi : 10.1152/ajpheart.1994.266.3.h1007.

M. Maillet, J.H. van Berlo, and J.D. Molkentin. Molecular basis of physiological heart growth : fundamental concepts and new players. *Nature Reviews Molecular Cell Biology*, 14(1) :38–48, 2013. doi : 10.1038/nrm3495.

C. Mekkaoui, T.G. Reese, M.P. Jackowski, S.F. Cauley, K. Setsompop, H. Bhat, and D.E. Sosnovik. Diffusion Tractography of the Entire Left Ventricle by Using Free-breathing Accelerated Simultaneous Multisection Imaging. *Radiology*, 282(3) :850–856, 2017. doi : 10.1148/radiol.2016152613.

S. Nielles-Vallespin, Z. Khalique, P.F. Ferreira, R. de Silva, A.D. Scott, P. Kilner, L.A. McGill, A. Giannakidis, P.D. Gatehouse, D. Ennis, E. Aliotta, M. Al-Khalil, P. Kellman, D. Mazilu, R.S. Balaban, D.N. Firmin, A.E. Arai, and D.J. Pennell. Assessment of Myocardial Microstructural Dynamics by In Vivo Diffusion Tensor Cardiac Magnetic Resonance. *Journal of the American College of Cardiology*, 69(6) :661–676, 2017. doi : 10.1016/j.jacc.2016.11.051.

A.J. Pope, G.B. Sands, B.H. Smaill, and I.J. LeGrice. Three-dimensional transmural organization of perimysial collagen in the heart. *American Journal of Physiology-Heart and Circulatory Physiology*, 295(3) :H1243–H1252, 2008. doi : 10.1152/ajpheart.00484.2008.

T.F. Robinson, M.A. Geraci, E.H. Sonnenblick, and S.M. Factor. Coiled perimysial fibers of papillary muscle in rat heart : morphology, distribution, and changes in configuration. *Circulation Research*, 63(3) :577–592, 1988. doi : 10.1161/01.res.63.3.577.

K.P. Roos. Sarcomere length uniformity determined from three-dimensional reconstructions of resting isolated heart cell striation patterns. *Biophysical Journal*, 52(2) : 317–327, 1987. doi : 10.1016/s0006-3495(87)83219-8.

M.A. Rossi, M.A. Abreu, and L.B. Santoro. Connective Tissue Skeleton of the Human Heart : A Demonstration by Cell-Maceration Scanning Electron Microscope Method. *Circulation*, 97(9) :934–935, 1998. doi : 10.1161/01.cir.97.9.934.

J.E. Saffitz, H.L. Kanter, K.G. Green, T.K. Tolley, and E.C. Beyer. Tissue-specific determinants of anisotropic conduction velocity in canine atrial and ventricular myocardium. *Circulation Research*, 74(6) :1065–1070, 1994. doi : 10.1161/01.res.74.6.1065.

G.B. Sands, D.A. Gerneke, D.A. Hooks, C.R. Green, B.H. Smaill, and I.J. Legrice. Automated imaging of extended tissue volumes using confocal microscopy. *Microscopy Research and Technique*, 67(5) :227–239, 2005. doi : 10.1002/jemt.20200.

D. F. Scollan, A. Holmes, J. Zhang, and R. L. Winslow. Reconstruction of Cardiac Ventricular Geometry and Fiber Orientation Using Magnetic Resonance Imaging. *Annals of Biomedical Engineering*, 28(8) :934–944, 2000. doi : 10.1114/1.1312188.

G. Sommer, A..J. Schriefl, M. Andrä, M. Sacherer, C. Viertler, H. Wolinski, and G.A. Holzapfel. Biomechanical properties and microstructure of human ventricular myocardium. *Acta Biomaterialia*, 24 :172–192, 2015. doi : 10.1016/j.actbio.2015.06.031.

C.T. Stoeck, C. von Deuster, and S. Kozerke. Second order motion compensated spin echo cardiac diffusion tensor imaging on clinical MR systems. *Journal of Cardiovascular Magnetic Resonance*, 18(1) :61, 2016. doi : 10.1186/1532-429x-18-s1-p61.

D.D. Streeter and D.L. Bassett. An engineering analysis of myocardial fiber orientation in pig's left ventricle in systole. *The Anatomical Record*, 155(4) :503–511, 1966. doi : 10.1002/ar.1091550403.

D.D. Streeter, H.M. Spotnitz, D.P. Patel, J. Ross, and E.H. Sonnenblick. Fiber Orientation in the Canine Left Ventricle during Diastole and Systole. *Circulation Research*, 24(3) :339–347, 1969. doi : 10.1161/01.res.24.3.339.

H. G. Tsang, N. A. Rashdan, C. B. A. Whitelaw, B. M. Corcoran, K. M. Summers, and V. E. MacRae. Large animal models of cardiovascular disease : Cardiovascular Disease Models. *Cell Biochemistry and Function*, 34(3) :113–132, 2016. doi : 10.1002/cbf.3173.

C. von Deuster, E. Sammut, L. Asner, D. Nordsletten, P. Lamata, Christian T. Stoeck, Sebastian Kozerke, and Reza Razavi. Studying Dynamic Myofiber Aggregate Reorientation in Dilated Cardiomyopathy Using In Vivo Magnetic Resonance Diffusion Tensor Imaging. *Circulation : Cardiovascular Imaging*, 9(10) :e005018, 2016. doi : 10.1161/circimaging.116.005018.

World Health Organization. Cardiovascular diseases, 2017.

F.C.P. Yin, R.K. Strumpf, P.H. Chew, and S.L. Zeger. Quantification of the mechanical properties of noncontracting canine myocardium under simultaneous biaxial loading. *Journal of Biomechanics*, 20(6) :577–589, 1987. doi : 10.1016/0021-9290(87)90279-x.

A.A. Young, I.J. Legrice, M.A. Young, and B.H. Smaill. Extended confocal microscopy of myocardial laminae and collagen network. *Journal of Microscopy*, 192(2) :139–150, 1998. doi : 10.1046/j.1365-2818.1998.00414.x.

L. Zhukov and A.H. Barr. Heart-muscle fiber reconstruction from diffusion tensor MRI. In *IEEE Transactions on Ultrasonics, Ferroelectrics and Frequency Control*, pages 597–602, Seattle, WA, USA, 2003. IEEE. doi : 10.1109/visual.2003.1250425.

Chapter II

Investigation of the mesoscale mechanical properties of the myocardium

Abstract

In this chapter, we propose a method to experimentally investigate the mechanical response of the mesostructure (sheetlet) by combining a full-field Mueller Polarimetric Imaging (MPI) system with an *in-situ* traction device. This chapter is in the form of an article coauthored by N. Tueni, J. Vizet, M. Genet, A. Pierangelo and JM. Allain, published in Sci. Rep, and completed by some additional elements on the Materials & Methods.

Contents

1 Introduction

As explained in Chapter I, the mesoscale structure of the myocardium is still debated. Moreover, its role in the cardiac mechanics has not been fully defined yet, and the relationship between this mesostructure and the macroscopic mechanical properties of the tissue are still undetermined. A critical aspect of understanding the underlying structure-function relationships in soft tissues is to clarify how the microstructure rotates and stretches as the tissue is loaded. Most constitutive models use the affine transformation assumption, which supposes that the local microscopic kinematics of each constituent in the tissue follows the local macroscopic deformation. Verifying this hypothesis experimentally raises technical challenges, since it requires a simultaneous observation of the macroscopic deformation and the microstructure orientation.

Several experimental studies have been performed on cardiac tissue at the macroscale: uniaxial tensile testing [Humphrey et al., 1990; Hassan et al., 2012], biaxial testing [Demer and Yin, 1983; Humphrey et al., 1990; Hunter and McCulloch, 1998; Sommer et al., 2015a], confined compression [McEvoy et al., 2018] and shear testing [Dokos et al., 2002; Sommer et al., 2015b]. These studies were essential in order to understand the macroscopic mechanical properties of the cardiac tissue. However, they do not yield to information about the tissue deformation at smaller scales. In order to do so, multiscale experiments where simultaneous observation of the macroscopic deformation and microstructure orientation are required. Such experimental setups have been developed to study the kinematics of collagen in collagen rich tissues [Jayyosi et al., 2017; Krasny et al., 2017].

To answer this question, we developed an experimental setup that allowed to investigate the kinematics of the microstructure in the cardiac tissue under uniaxial load, detailed in a published article [Tueni et al., 2020] which we now present. The polarimetric measurements presented in this study were performed by J. Vizet from the LPICM laboratory. We will also further explain some methods used for the study, but not fully detailed in the article.

2 Article

www.nature.com/scientificreports

scientific reports

OPEN

Microstructural deformation observed by Mueller polarimetry during traction assay on myocardium samples

Nicole Tueni[1,2,4], Jérémy Vizet[3,4], Martin Genet[1,2], Angelo Pierangelo[3]✉ & Jean-Marc Allain[1,2]✉

Despite recent advances, the myocardial microstructure remains imperfectly understood. In particular, bundles of cardiomyocytes have been observed but their three-dimensional organisation remains debated and the associated mechanical consequences unknown. One of the major challenges remains to perform multiscale observations of the mechanical response of the heart wall. For this purpose, in this study, a full-field Mueller polarimetric imager (MPI) was combined, for the first time, with an in-situ traction device. The full-field MPI enables to obtain a macroscopic image of the explored tissue, while providing detailed information about its structure on a microscopic scale. Specifically it exploits the polarization of the light to determine various biophysical quantities related to the tissue scattering or anisotropy properties. Combined with a mechanical traction device, the full-field MPI allows to measure the evolution of such biophysical quantities during tissue stretch. We observe separation lines on the tissue, which are associated with a fast variation of the fiber orientation, and have the size of cardiomyocyte bundles. Thus, we hypothesize that these lines are the perimysium, the collagen layer surrounding these bundles. During the mechanical traction, we observe two mechanisms simultaneously. On one hand, the azimuth shows an affine behavior, meaning the orientation changes according to the tissue deformation, and showing coherence in the tissue. On the other hand, the separation lines appear to be resistant in shear and compression but weak against traction, with a forming of gaps in the tissue.

Cardiac muscle has a complex, highly hierarchical organization composed of cardiomyocytes, extracellular collagenous matrix, vasculature, etc. This organization is deeply related to the macroscopic mechanical and morphological properties of the heart. The cardiac muscle or myocardium is mostly made of an assembly of cells, the cardiomyocytes, which are roughly cylindrical with a typical diameter around 10–20 µm, and a length around 100–150 µm[1]. Each cardiomyocyte is surrounded by a thin layer of extra-cellular matrix, the endomysium. This defines the smallest scale of the tissue. Cardiomyocytes are bundled together, creating aggregates of typically 5–10 cells. These bundles have a typical size of around 100 µm. These aggregates are themselves surrounded by a thick extra-cellular matrix layer, the perimysium. Both endomysium and perimysium are mostly made of collagen fibers[2]. At a larger scale, these aggregates are assembled to create the heart wall which is approximately one centimeter thick.

The cardiomyocytes are contractile cells, their main axis being the direction of contraction. These local preferential directions are thus the ones of the cardiac fibers[3]. It is now well established that the fiber orientation rotates in the thickness of the heart wall[4,5]. The spatial organization of the cell aggregates remains elusive. It is often considered that these structures create sheetlets, large layers of cardiomyocytes separated by a thick film of extra-cellular matrix[6,7]. However, this is not definitively proven and other organizations, such as globular clusters of dozens of cardiomyocytes, have also been proposed[8,9]. On top of this uncertainty on the mesoscopic organization of the myocardium, the physiological role of this mesostructure is not completely understood[10,11].

[1]LMS, CNRS, École polytechnique, Institut Polytechnique de Paris, Palaiseau, France. [2]Inria, Palaiseau, France. [3]LPICM, CNRS, École polytechnique, Institut Polytechnique de Paris, Palaiseau, France. [4]These authors contributed equally: Nicole Tueni and Jérémy Vizet. ✉email: angelo.pierangelo@polytechnique.edu; jean-marc.allain@polytechnique.edu

The primary reason for this lack of knowledge of the mesostructural organization of the cardiomyocytes comes from the experimental difficulties to observe it, in particular in association with their mechanical role. Different methods have been used so far to observe the microstructure. The most resolving method is probably the Scanning Electronic Microscopy (SEM), which enables to observe, for example, the cellular shape[9,12] or the organization of the perimysium and the endomysium[9], showing clusters of cardiomyocytes. In these images, the perimysium appears to be much thicker and denser than the endomysium[13]. However, SEM has the major drawbacks of having a limited field of view and of requiring invasive sample preparation. Conversely, the Magnetic Resonance Imaging (MRI) has been used to investigate the local orientation of sheetlets (or at least the local anisotropy of cardiomyocyte aggregates) by measuring the magnetic relaxation[14,15]. While the MRI has the capability to observe the whole heart *in vivo*, it cannot be used to observe directly its mesostructure, which can only be inferred through theoretical assumptions. Intermediate scales have been investigated through confocal microscopy[8,16,17]. Here the collagen is specifically dyed to distinguish the endomysium and the perimysium from the cardiomyocytes. Millimeter-long lateral surfaces of rectangular pieces of the heart wall have been observed with this approach. It provides specificity, high resolution and a large field of view, but requires very long scanning times, making it incompatible with mechanical assays. Confocal microscopy images show large lines of collagen on the lateral surfaces of the sample. While some lines seem dense and thin, others appear broad and sparse. Sparse layers will tend to behave like lines of weakness, strong in compression but weak under traction, whilst denser layers will behave like stiff sheets. These contrasts raise questions about the mechanical properties of the collagen walls.

These mechanical properties, which have attracted considerable attention, can be generally split between active and passive properties[18–20]. The active response is due to the contraction of the cardiomyocytes, whilst the passive response arises from the whole tissue. Our focus is set on the latter. Various mechanical assays have been performed, such as uniaxial traction[21–24], biaxial ones[25–27] or shear experiments[26,28] with the ultimate aim to determine the anisotropic mechanical response of the tissue. The anisotropy arises mainly from the cardiomyocyte orientation, but some experiments point towards a role of the cardiomyocyte bundles in the response[26,28]. However, to our best knowledge, no experiment has probed the mechanical response at the scale of the cardiomyocyte bundle (although this has been done on skeletal muscle[29]). These questions require new experimental approaches, that allow to obtain mesostructural information for a large field of view and at a rate comparable to that of the mechanical loading.

To tackle these questions and access structural information at the mesoscale, a full-field Mueller Polarimetric Imager (MPI) is used, for the first time, in this study. Over the past few years, Mueller polarimetric imaging has shown great potential for exploring the microstructure of biological tissues for different types of biomedical applications[30]. The great advantage of this technique is that it can be used to observe, in few seconds, a macroscopic field of view (several square centimeters), thus providing structural information on the explored tissue with a microscopic resolution (less than 100 μm, which is smaller than the size of the mesostructure). This technique can thus provide unique and complementary information with respect to the other imaging techniques, at a rate compatible with mechanical assays. It exploits the polarization of the light to determine various biophysical polarimetric quantities related to the tissue's scattering or anisotropy properties. Many studies have demonstrated that this technique provides unique enhanced contrasts which can considerably improve the detection of pathological areas on a large variety of tissues[31–33]. Recently, Mueller polarimetric imaging has been used to characterize the microstructure of healthy and infarcted myocardium[34,35].

In this study, we investigated the role of the myocardium mesoscale organization in its mechanical response, with a particular interest in the response of the perimysium—the collagen layer which surrounds cardiomyocyte bundles—as the role of this structure remains unclear. To do so, we used full-field MPI to investigate the microstructure of the myocardium under different stretch conditions. For this purpose, an original setup, combining a full-field MPI and a mechanical traction device was built in order to measure the evolution of the different polarimetric properties of myocardium during the stretching of strip samples of pig heart wall. The proposed approach enables to quantitatively investigate the structural modification of myocardial tissue on a mesoscopic scale, via the measurement of its polarimetric parameters, under different traction conditions. We observed an affine evolution of the tissue optical orientation, indicating that the mesostructure follows the local macroscopic deformation. However, the forming of gaps, perpendicular to the traction direction, indicated the presence of defect lines. These lines reflect weaknesses in the tissue, and are associated with a lower depolarization, denoting a less dense region which considerably reduces the light scattering. Our new imaging method gives a first evidence of the mechanical response of the collagen structure surrounding the sheetlet, which appears weak in response to traction, while being resistant to shear and compression.

Results

Nine samples of dimensions approximately $30 \times 10 \times 2.4$ mm^3 were analyzed by using the new proposed approach. They were extracted from porcine left ventricle, parallel to the heart wall. One side of these samples was marked with an ink speckle to measure the local deformation via Digital Image Correlation (DIC). The samples were then fixed at both extremities of a custom-made traction device[36] and were kept immersed in a physiological buffered saline solution (PBS) to prevent any drying of the tissue during measurements. The samples were subjected to traction, with pauses every 10% of stretch for MPI acquisition. Three types of data were collected for each sample: (1) the Mueller polarimetric matrix at every 10% of deformation, (2) the force and the displacement of the traction machine every second and (3) the local deformation every 3 s.

Mueller polarimetric imaging. The Mueller matrix is determined through a custom-made MPI designed and constructed at LPICM. The MPI is used to measure the sample's Mueller matrix. It consists in a 16-compo-

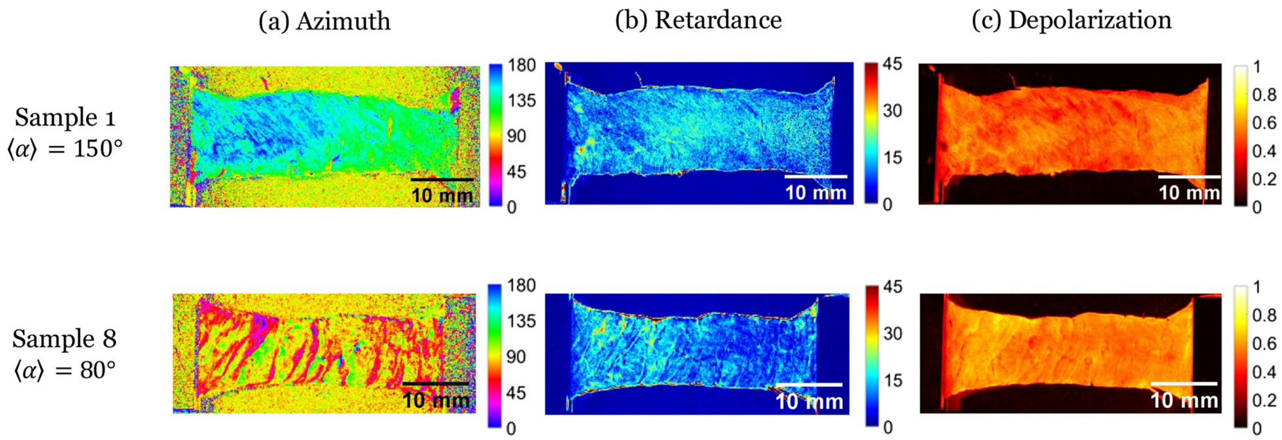

Figure 1. Maps of the Mueller polarimetry parameters [(**a**) Azimuth α (in °), (**b**) retardance R (in °), (**c**) depolarization Δ] for two of our 9 samples, chosen for their different initial mean azimuth $< \alpha >$ (top—Sample 1, $\langle\alpha\rangle \approx 150°$; bottom—sample 8, $\langle\alpha\rangle \approx 80°$; direction of traction 0°).

nents real valued matrix enabling the comprehensive polarimetric characterization of the explored sample. To retrieve the main polarimetric properties of the sample, the polar decomposition proposed by Lu and Chipman[37] is used to extract the birefringence, the depolarization and the dichroism matrices from measured Mueller Matrix. For the myocardium, the most relevant polarimetric parameters are the Depolarization (Δ), and the Linear birefringence, which is characterized by the Linear Phase Retardance (R) and the orientation of the fast axis, also named Azimuth (α). The parameters Δ, R and α are scalar and have been computed for each pixel of the image.

The parameter Δ quantifies the scattering properties of the explored sample (0 for non-depolarizing sample, 1 for a complete depolarization). Furthermore, the parameters α and R provide a complete information on the anisotropy of the explored tissue. Specifically α reflects the local optical orientation of the fiber structures in the tissue. The parameter R indicates the difference in optical phase shifts, between two polarization directions (respectively parallel and orthogonal to α), that the polarization of the light undergoes after reflections by the tissue.

Figure 1 shows the maps of α, R and Δ for two chosen samples of nine tested ones (samples numbered 1 and 8). These samples were chosen for their two different initial average value of α (indicated as $< \alpha >$ in the following text). Beside that they are representative of the other samples—which are all presented in supplementary data. Sample 1 has an initial value of $< \alpha > \approx 150°$, 0° being the traction direction (Fig. 1 top), whilst sample 8 presents a value of $< \alpha > \approx 80°$ (Fig. 1 down). For both samples, the azimuth maps reveal structural patterns, with higher contrasts observed for sample 8 (with pattern perpendicular to the traction direction). This pattern is due to lines on which the parameter α varies brutally, indicating a sudden change in the tissue microstructure orientation. We call these lines "separation lines". Linear retardance R and depolarization Δ maps are much less contrasted, even though they still show a pattern reflecting the separation lines.

Although the separation lines are observed on all samples, the contrast is stronger for samples with an average $< \alpha >$ perpendicular to the traction direction ($< \alpha > \approx 90°$). We explain it by the fact that, prior to loading, during their setting on the traction device, the gripping and the flattening of the samples is likely to cause a slight stretch, which induces a traction on the separation lines. However, for samples with an initial azimuth parallel to the traction direction, these lines were most likely sheared or compressed.

The precise microstructural origin of the measured macroscopic polarimetric signal in the myocardium has yet to be identified. However, a very interesting study performed on the skeletal muscle proposes a simplified optical model which can be relevant also to describe the polarimetric effects observed for the myocardium[38]. This model shows that the origin of the measured birefringence can be attributed to the presence of a high density of microscopic fiber structures (myofibrils). Specifically the orientation of these fibers can be visualized using the parameter α. Otherwise the measured depolarization Δ can be produced by the presence of a high density of beads (cellular organelles). By analogy it can be supposed that the birefringence observed on the myocardium is mainly generated by the presence of the cardiomyocytes, the orientation of which can be visualized by using the parameter α. In this case the observed depolarization can be mainly attributed to the organelles of the cardiomyocytes. The dense network of collagen fibers composing the extracellular matrix can contribute both to the birefringence and to the depolarization.

We compared classical white-light images and polarimetric images on the same side of the same sample (see Fig. 2). We observed on the white-light images well-ordered mesoscopic lines on the surface of the sample. We manually traced segments over the lines with the best contrast and measured the angle they make with the horizontal orientation using ImageJ. We observed a perfect agreement between this measure and the azimuth measured with the MPI, which confirms that α is a measure of local mesostructure orientation at the surface of the tissue. Our approach doesn't have the resolution of the azimuth measure and can be biased by the choice of the most contrasted lines. However, this manual measure has already been used in the literature to identify the tissue main orientation[26,28].

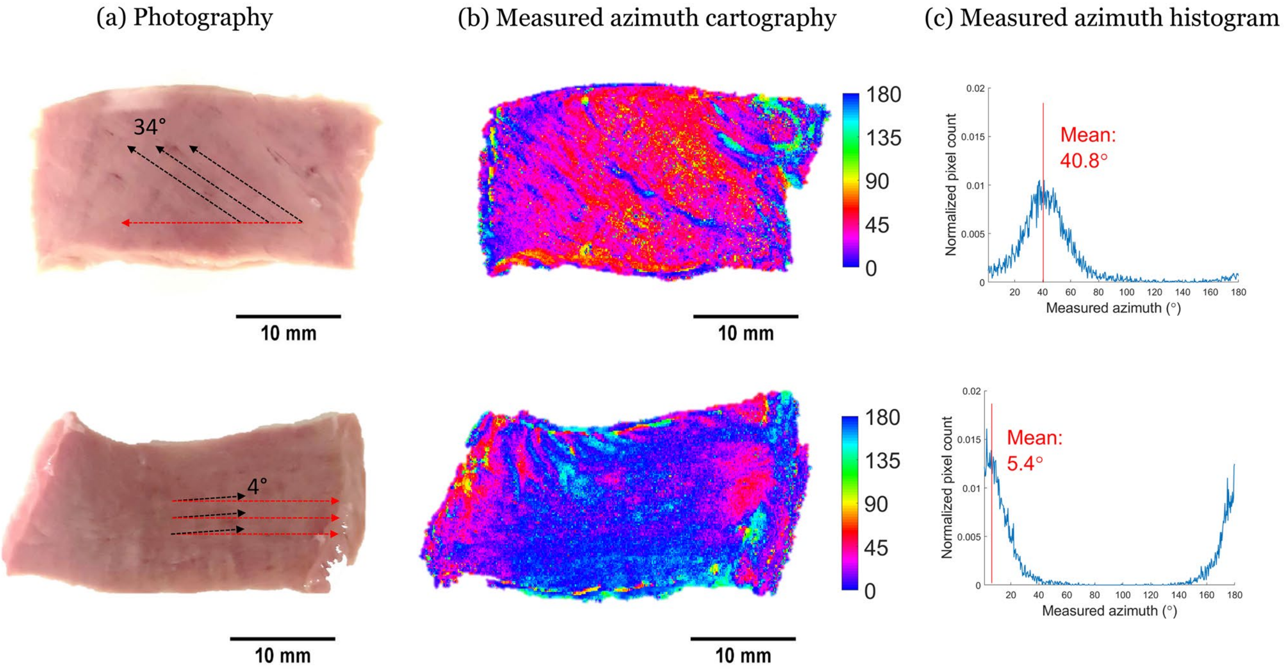

(a) Photography (b) Measured azimuth cartography (c) Measured azimuth histogram

Figure 2. Comparison between (**a**) white-light images and (**b**) azimuth (in °) maps. (**c**) α histogram of two samples.

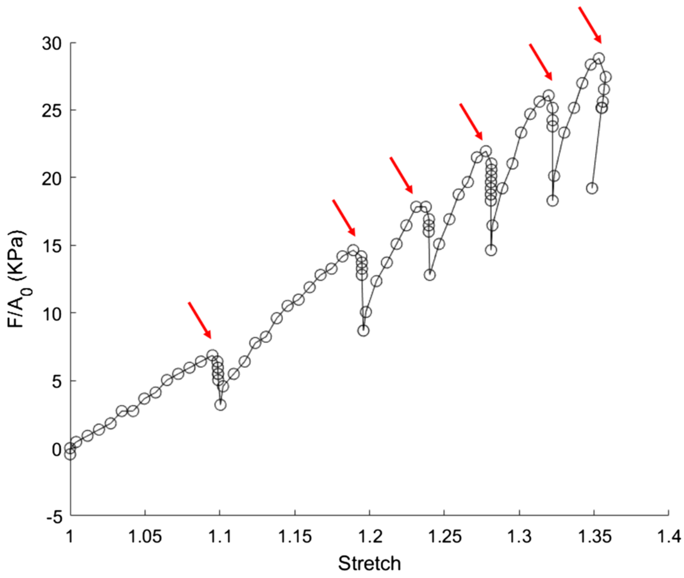

Figure 3. Nominal stress versus optically-measured stretch for sample 8. The relaxations are due to the pauses for MPI acquisition (red arrows).

Stress/stretch behavior. The macroscopic response of our myocardium samples is similar to what can be found in the literature[22–24]: after observing first a non-linear region, the curve becomes linear (see Fig. 3). An important relaxation occurs when the traction is paused for polarimetric acquisition (around 4 min per acquisition). In order to investigate the effect of the pauses on the global behaviour, we applied continuous stretches on 5 samples, without any pauses, and did not observe any significant differences in the mechanical response.

The heterogeneity of the stretch does not allow it to be simply approximated by the macroscopic one. As polarimetric and deformation measurements are done on two opposite sides of the sample, we investigated if the deformation measured on the lower side can be used to analyse the evolution of the polarimetric measures on the upper side. To do so, a test was done to verify that the stretch measurement gave similar results on both faces. 5 samples were subjected to continuous stretch. Each side was imaged using an optical camera, allowing the computation of a local stretch at a scale of 500 µm, using Digital Image Correlation. The deformation fields

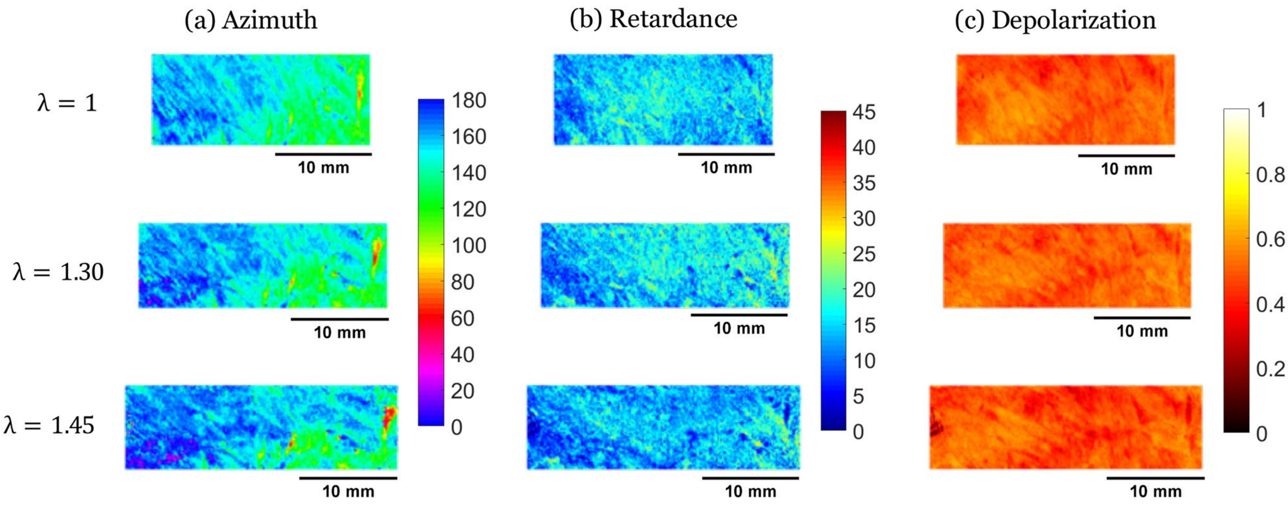

Figure 4. Maps of the Mueller polarimetry parameters [(**a**) Azimuth α (in °), (**b**) retardance R (in °), (**c**) depolarization Δ] measured on sample 1 at different imposed stretches ($\lambda = 1, \lambda = 1.30, \lambda = 1.45$).

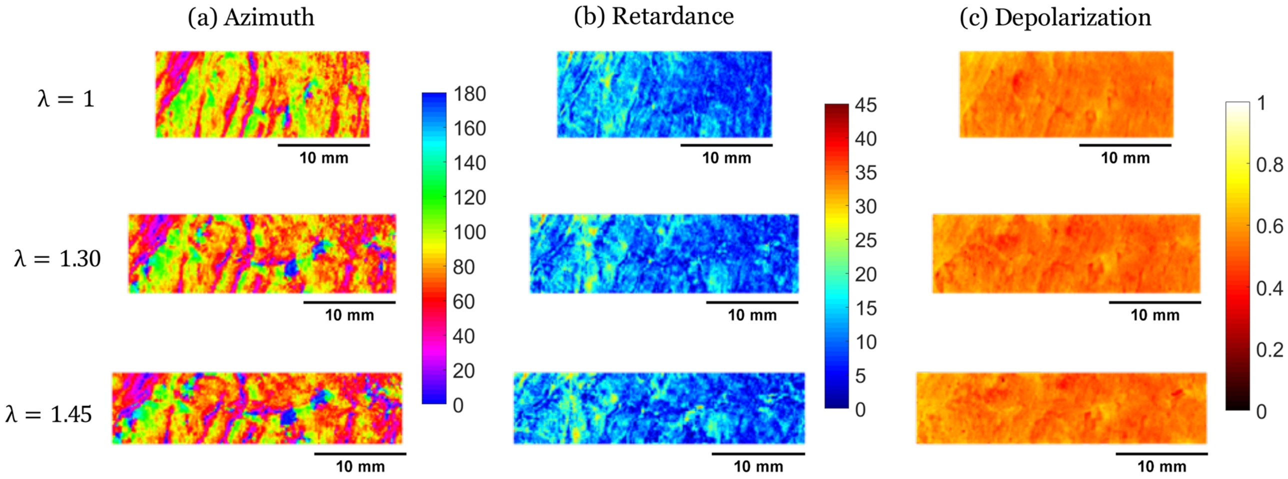

Figure 5. Maps of the Mueller polarimetry parameters [(**a**) Azimuth α (in °), (b) retardance R (in °), (**c**) depolarization Δ] measured on sample 8 at different imposed stretches ($\lambda = 1, \lambda = 1.30, \lambda = 1.45$).

on both sides were compared. We measured a typical stretch difference around 6% at 40% of applied stretch (see Supplementary Figure 1). As this difference was significantly much smaller than the applied stretch, we concluded that our stretch measure was a good (although non perfect) approximation of the one on the MPI side.

Polarimetric parameters evolution with traction. For each sample, three polarimetric images (of Azimuth α, Linear Phase Retardance R, and Depolarization Δ) were extracted from the Mueller Matrix, for different levels of stretch. In parallel, DIC was performed on regions of the images generated by the optical camera. To compare the same region of interest, we first registered the polarimetric and the DIC images to superimpose them and match the pixels. Then, we used DIC to deform the initial region, and finally, we cropped both images on the same region all along the traction. The Figs. 4 and 5 show the evolution of the polarimetric parameters at different stretch levels for the same 2 samples as Fig. 1 (see Supplementary Figure 2 for similar figures on all samples).

Azimuth. An evolution of the azimuth towards the angle of traction is observed. This is interpreted by the fact that the azimuth measures the microstructure orientation, which naturally tends to align with the traction direction.

The simplest way to link the motion of the fibers to the tissue deformation is by adopting the affine assumption, which assumes that the microstructure follows the motion of its surrounding volume[39]. This assumption is widely used in heart multiscale modeling[10,40–42]. It has the main advantage of being purely kinematic. Thus, it allowed us to predict the azimuth evolution, knowing the local stretch and the initial azimuth, and generate maps of the predicted α. The difference between the predicted maps and the MPI-measured azimuth maps were then computed. Figure 6a shows the histogram of the measured azimuth at different stretch levels for samples 1 and

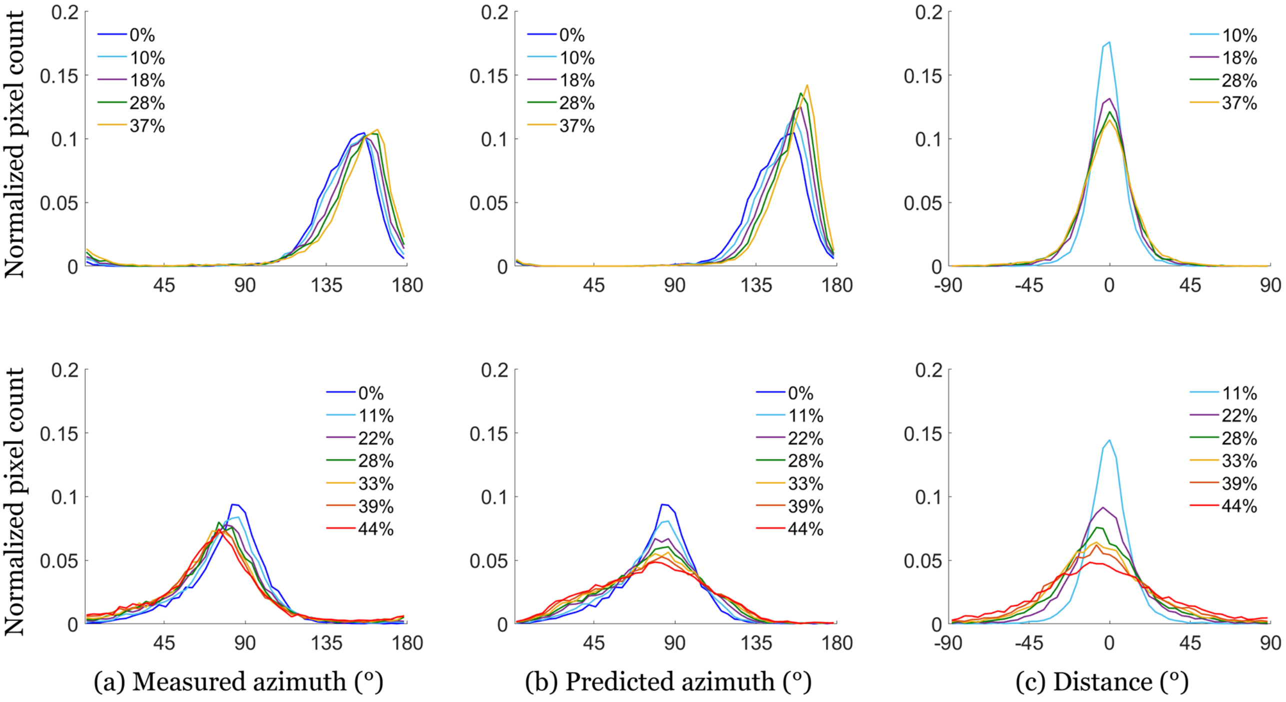

Figure 6. (**a**) Measured azimuth, (**b**) predicted azimuth, and (**c**) angular difference between measured and predicted azimuth distributions for sample 1 ($\langle\alpha\rangle \approx 150°$—top) and sample 8 ($\langle\alpha\rangle \approx 80°$—bottom), at different stretch levels. The predicted distributions are obtained using the affine assumption.

8. It also shows the computed histogram at the same stretch levels, using the affine assumption and the initial experimental histogram (Fig. 6b). Finally, the third histogram shows the difference between experimental and computed orientations at each stretch level (Fig. 6c). The results for all samples are available on Supplementary figure 3.

The samples with initial orientations close to the traction direction showed differences between computed and measured azimuth centered on 0 (see Fig. 6 top), indicating that the affine assumption leads to a good approximation of the azimuth evolution. We attribute the dispersion to the fact that we measure the deformation on the opposite side to the azimuth measure.

However, the samples with an initial azimuth perpendicular to the traction direction ($\langle\alpha\rangle \approx 80°$) showed non-centered distributions (see Fig. 6 bottom). The measured azimuth distribution remains almost unchanged during the stretch: as expected, fibers perpendicular to the traction do not rotate with the traction. However, the computed azimuth distribution evolves strongly towards the traction direction, leading to a significant difference between prediction and measure. This can be explained by the existence of separation lines, which open during traction (see Fig. 7), and create discontinuities in the tissue. As the resolution of the stretch measurement is larger than the size of separation line, the measured stretch includes a contribution of both the deformation of the cells and of the lines. When the lines open, they induce an increase in the deformation measure which is not representative of what is experienced by the tissue. This leads to an overestimation of the stretch applied on the cells and thus to errors in the azimuth variations.

Retardance. During traction, the retardance does not seem to vary significantly (see Figs. 4, 5, and Supplementary Figure 2) apart in some regions of strong non-affine behavior where it increases slightly with the line opening. It is likely that the imposed deformation is not sufficient to induce a significant modification of the fiber optical environment, but on the separation lines the traction opens gaps between cells, modifying the linear retardance.

Depolarization. Depolarization is interpreted as the result of multiple scattering events of the light by small organelles in the cells. During traction, the depolarization changes slightly (see Figs. 4, 5, and Supplementary Figure 2), probably because the organelles are not affected by the deformation. The only significant change is the depolarization decrease on the separation lines when they are perpendicular to the direction of traction. We explain this decrease by the opening of the separation lines, which creates a gap between cardiomyocytes and decreases the tissue density, decreasing the scattering.

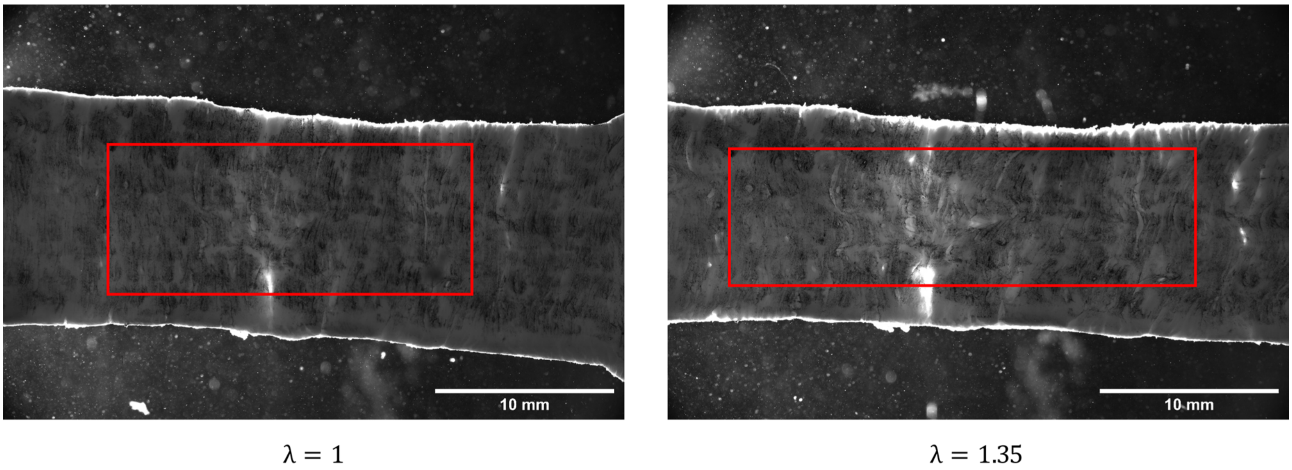

Figure 7. White-light images of the surface used for DIC (opposite to MPI) during the traction of sample 4. Left—prior stretch, $\lambda = 1$, Right—during stretch, $\lambda = 1.35$. We observe vertical lines of light grey which open during the traction, that we associate with the separation lines.

Discussion

In the recent years, the role of the myocardium mesostructure has attracted more and more attention. This is due to the fact that the physiological role of this spatial organization remains unclear[10,11]. However, as the collagen extracellular matrix is strongly modified during heart remodeling (such as infarction[13,17]), it may play a role in the heart remodeling capacities. Developed models in the literature include both the cardiomyocyte and the perimysium layer[20,43]. However, they rely on the affine transformation assumption, which states that local kinematics of each constituent follow the local macroscopic deformation. To our knowledge, this hypothesis has never been experimentally tested, as it requests a simultaneous observation of the macroscopic deformation and the microstructure orientation. In this study, we investigate the question of the cardiomyocyte bundle mechanical response in the myocardial tissue by combining for the first time a traction assay with Mueller polarimetry imaging. These cardiomyocyte bundles group together a few dozen cells, and are around a few hundred of micrometers in thickness. They are often considered as organized in sheetlets[6,7], although their spatial organization remains undetermined. Not surprisingly, their mechanical properties remain elusive as well[8].

Mueller Polarimetric Imaging explores the response of the tissue with respect to different polarization states of the illuminating light. Therefore, it probes the tissue organization. Three parameters appear to be of interest in the myocardium: the Azimuth, the Linear Phase Retardance, and the Depolarization. We associate the azimuth α with the cardiomyocyte orientation on the surface (see Fig. 2), and the depolarization Δ with the scattering events due to organelles and other small disorganized elements in the cardiomyocytes. During traction, azimuth tends to align with the traction direction, indicating that the fibers align with traction (see Fig. 6), for all samples except for those with an initial azimuth perpendicularly oriented to the traction. The motion of the fibers is well described by the affine assumption, which states that the fibers follow the deformation of the tissue they are embedded in. This emphasizes the cohesion of the cardiomyocytes together. The depolarization, as well as the retardance, do not appear to be modified by the traction. This indicates that the imposed deformations do not affect the optical anisotropy and thus are not sufficient to deform the cardiomyocytes at a perceptible level.

We observe "separation lines" in which the azimuth varies a lot on few micrometers, and in which the depolarization is smaller (see Fig. 1). These lines are initially separated by few hundreds of micrometers. We hypothesize that these lines are the perimysium, the collagen layer surrounding the border of the cell aggregates. They have the adequate size, and show a sudden change in the orientation. The lower depolarization indicates that the tissue is less dense or contains less diffusive elements. During traction, we observe that these lines become larger for samples with azimuth perpendicular to the traction direction. At the same time, the depolarization decreases in the line. Therefore, these lines appear to open under traction as observed on samples with azimuth near 90°, as well as on optical images (see Fig. 7). Samples with other orientations do not exhibit an opening of these separation lines, nor do they show a non-affine response. This supports that the perimysium is resistant against shear and compression, but weak against traction, as we may expect for a thin loosely-connected layer of collagen.

To confirm the mechanical role of these separation lines, it will be of interest to advance more complex mechanical loadings after having confirmed that they are really the borders of sheetlet. An improvement of the resolution of the Mueller polarimetric set-up will enable to achieve a more precise view of the microstructure. But most importantly, further developments will be strongly helped by an optical model of the signal including the cardiac microstructure, so that we can associate more precisely each element to a polarimetric parameter, as well as the size of probed volume.

The obtained results prove the feasibility to measure the mechanical properties of the myocardium mesostructure. These experimental measures can be used as inputs for the mathematical models to determine myocardial mechanical properties, although our results show that affine-based models are unlikely to reproduce correctly our observations. With such approach one can compare healthy and remodeled or pathological myocardium

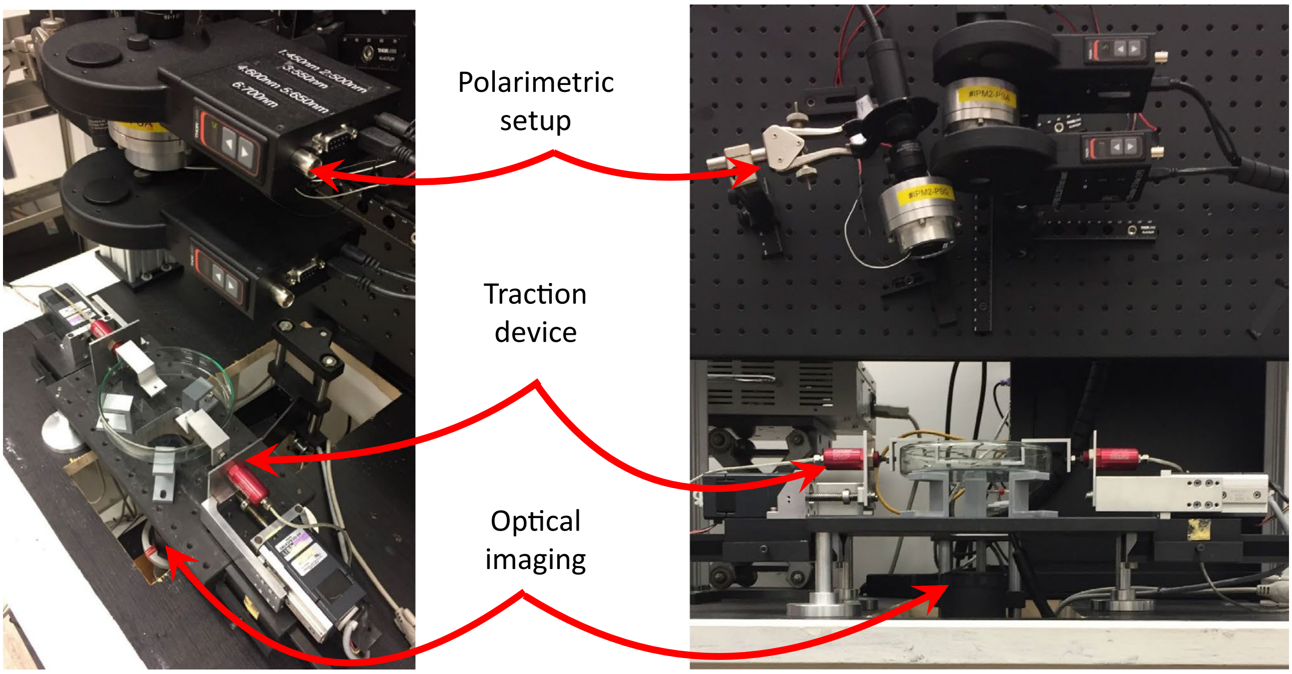

Figure 8. Global and close views of our experimental setup.

samples, and see how the mechanical response is modified at a mesoscale—a scale not investigated so far. However direct clinical applications will request further studies.

Methods

Sample preparation.

In total, 9 samples extracted from porcine left ventricles were studied. The hearts were purchased at the local butcher, stored in a cooling box during transportation, and tested the same day. The left ventricle was first isolated. Then, using a slicing machine, the pericardium and the myocardium were separated, and thin slices of myocardial tissue were cut (average thickness 2.4 ± 0.5 mm). From these slices, strips of 30 × 10 mm were cut with a scalpel. The dominant orientation of the microstructure on the upper surface of each slice was visually identified with respect to the strip length. To measure the displacement field, a speckle pattern was created on one of the surfaces of each sample by tapping a sponge sunk in Indian ink. The freshly cut samples were then mounted on a custom-made uniaxial traction machine[36] (see Fig. 8). The sample was then immersed in a solution of phosphate-buffered saline (PBS). In our setup, the upper surface of the sample was observed by MPI, while the lower surface (the stained one) was observed by a standard optical camera to measure the stretch field. Once the sample in place, its dimensions were measured using a digital caliper.

Mueller polarization.

A custom-made sequential multispectral Mueller polarimetric imager (MPI) in backscattering configuration, designed and constructed at LPICM, was used to analyze myocardial samples. It is an upgraded version of the one described in[32]. Briefly, a Polarization State Generator (PSG) temporally modulates the polarization of the light impinging on the sample to be explored by consecutively generating four independent probing polarization states which are described by four Stokes vectors and regrouped together as the columns of a modulation matrix called $\underline{\underline{W}}$. The light backscattered by the sample then passes through a Polarization State Analyzer (PSA) placed in front of the detector. Each of the four polarization states produced by the PSG, after interacting with the sample, is analyzed trough four independent consecutive configurations of the PSA which are described by four Stokes vectors and grouped together as the rows of an analysis matrix called $\underline{\underline{A}}$. Described procedure enables to acquire 16 intensity images which are stacked in a 4x4 matrix $\underline{\underline{B}}$ given by:

$$\underline{\underline{B}} = \underline{\underline{A}}.\underline{\underline{M}}.\underline{\underline{W}}, \tag{1}$$

where $\underline{\underline{M}}$ is the unknown Mueller matrix of the analyzed sample. If $\underline{\underline{W}}$ and $\underline{\underline{A}}$ have been previously accurately determined through a calibration process, the Mueller matrix $\underline{\underline{M}}$ of the sample can be obtained from Eq. (1).

The Eigenvalue Calibration Method, widely described in[44], has been used here to calibrate the system. The PSG and PSA have been constructed by using ferroelectric liquid crystals as explained in[45]. The light is delivered by a 150 Watt halogen source (Olympus CLH-CS, USA). and guided to the MPI by means of a liquid light guide (Thorlabs LLG0538-6, USA). Appropriate collimation optics was placed at the outlet of the liquid guide to produce a bright spot 6 cm in diameter at a working distance of about 30 cm corresponding to the sample position. A monochromatic CCD-camera (f080b Allied Vision, Germany, 512x386 pixels in binning mode) has been used as detector. It is provided with an electronics enabling to acquire 16-bit intensity images. The CCD-camera is provided of an objective of focal length f = 25mm and it has been positioned at a distance of about 20 cm from the sample in order to obtain a field of view of about $5 \times 4 \ \text{cm}^2$, corresponding to a nominal resolution of about

100 μm/pixel. A wheel containing several dichroic filters is placed in front of the CCD-camera, enabling to perform measurements between 450 and 700 nm with steps of 50 nm and a bandwidth of 40 nm for each selected wavelength. In particular, the wavelength at 550 nm has been selected for the experiments described in this study.

The Mueller matrix $\underline{\underline{M}}$ of a sample enables its comprehensive polarimetric characterization. Once the Mueller matrix has been measured, the sample's polarimetric properties can be retrieved by a number of algebraic procedures. In this study, we made the choice to interpret these images by applying the polar decomposition proposed by Lu and Chipman[37]. This decomposition enables to describe a Mueller matrix M as the product of three matrices:

$$\underline{\underline{M}} = \underline{\underline{M}}_{\Delta} \cdot \underline{\underline{M}}_{R} \cdot \underline{\underline{M}}_{D}, \tag{2}$$

where $\underline{\underline{M}}_{\Delta}$ is the Mueller matrix of a depolarizer, $\underline{\underline{M}}_{R}$ of a birefringent medium and $\underline{\underline{M}}_{D}$ of a diattenuator. In particular, the main polarimetric properties observed on myocardial tissue are the depolarization and the linear birefringence. This last can be quantified by two parameters which are the phase retardance and the orientation of its fast (or equivalently the slow) axis also named azimuth. Depolarization and linear phase retardance are linked to scattering and anisotropy of a tissue on a microscopic scale. The depolarization is expressed as:

$$\Delta = 1 - \frac{|a| + |b| + |c|}{3}, \tag{3}$$

where a, b and c are the eigenvalues of $\underline{\underline{M}}_{\Delta}$. Δ reflects the total depolarization power of the Mueller matrix, and includes the sample ability to depolarize both linear and circular polarization states. It ranges from 0 in the case of non-depolarizing to 1 for a pure depolarizing sample.

The phase retardance can be obtained by:

$$R = \arccos\left(\frac{tr\left(\underline{\underline{M}}_{R}\right)}{2} - 1\right). \tag{4}$$

It is measured in degrees and for biological tissues generally spans in the full range between 0 and 180°.

Finally the azimuth is given by:

$$\alpha = \frac{1}{2}\arctan\left(\frac{\underline{\underline{M}}_{R24}}{\underline{\underline{M}}_{R43}}\right). \tag{5}$$

With this formula, the azimuth varies in the range between 0 and 90°. To avoid recurring jumps and to facilitate the reading on macroscopic maps, we extended this range so that α spans between 0 and 180°[33].

Mechanical assay. The mechanical traction was done using a custom-made traction device made of two symmetric motors[36], equipped with load cells (LPM200, 2lb, Futek, USA), on which the sample was attached (see Fig. 8). After immersion in PBS, we slowly stretched the sample to flatten it, while keeping the force below the noise level. Once the sample was flat (seen with the naked eye), its size was measured using a digital caliper. Then a traction at 0.1 mm/s (around 0.3%.s^{-1}) was exerted. The force was recorded every second. At every 10% of the initial sample length, the motors were stopped for the acquisition of the polarimetric images.

In parallel, high definition images of the lower side of the sample were taken (0.33 fps), using a 8-bit CCD camera (Allied Vision GX6600, 6576 (H) × 4384 (V), Allied Vision, Germany) connected to a telecentric lens (Opto Engineering TC16M036, Opto Engineering, Italy). The camera has a field of view of 4384 × 6576 px, each pixel corresponding to a physical square of 5.5 × 5.5 μm. The lighting (and thus the optical acquisition) was interrupted during the polarimetric acquisition.

Using these images, local-based Digital Image Correlation (DIC) was performed (CorrelManuV 1.66, Michel Bornert[46]) to determine the displacement and stretch fields. The correlation was performed on positions separated by 100 px (500 μm), with local domains of 100 px. Thus, the displacement is measured on a grid of square pixels of a size of 100 px (550 μm in physical unit). The correlation was performed on the region of the sample which remained in the camera field of view during the whole traction (typically 30 × 15 displacement points).

Deformation on the upper surface. As the polarimetric and deformation measurements are done on two different surfaces of the sample, we also checked if our stretch measurement gave similar results on both sides. To do so, the polarimetric set-up was replaced by an optical camera (Allied Vision GX3300, 3296 (H) × 2472 (V), Allied Vision, Germany). 5 samples, extracted from porcine left ventricles and of dimensions approximately 30 × 10 × 2.5 mm^3, were tested as previously described, without the pauses for the polarimetric acquisition.

Images superposition. In order to compare mechanical and polarimetric data, the information obtained on the two sides had to be extrapolated on the same location. To do so, we first registered the two images so that both were aligned in the same coordinate system. The registration was done using a "feature-based" technique, consisting in finding a few matching features on both images, and then computing a transformation matrix $\underline{N}$ that matches points $\underline{X}$ from the first image and their corresponding points $\underline{X}'$ in the second image by a least-square minimization. The feature detection was done manually using Fiji, and the minimization was done in Matlab. The maximum residual obtained using the Matlab minimization was of 20 pixels, which represents a

4% error. The transformation matrix $\underline{\underline{N}}$ concatenates a translation $\underline{\underline{T}}$, a scaling ($\underline{\underline{S}}$), and a rotation of the plane $\underline{\underline{R}}$ such that:

$$\underline{\underline{N}} = \underline{\underline{T}} \cdot \underline{\underline{R}} \cdot \underline{\underline{S}}. \tag{6}$$

The scaling avoids the need to convert the pixel size into physical length: we preferred to work in pixel of the upper camera. The two images were cropped to observe only the same region of interest.

Once the images were registered, we determined the displacement $\underline{u}(\underline{X})$, and the associated deformation gradient $\underline{\underline{F}}(\underline{X})$ for each position X_i at which the polarimetric parameters were measured. As the DIC image has a lower resolution (10x larger) than the polarimetric image, we used a bilinear extrapolation between the nearest displacement measures to determine the deformation $\underline{\underline{F}}(X_j)$ in between.

Note that the positions X_j were in the initial polarimetric image (prior to loading), as the displacement field was defined in the sample reference configuration. Using the measured displacement, it was possible to determine the values of the mechanical parameters at each position x_j in the subsequent polarimetric image.

Received: 21 July 2020; Accepted: 26 October 2020

References

1. Olivetti, G. *et al.* Aging, cardiac hypertrophy and ischemic cardiomyopathy do not affect the proportion of mononucleated and multinucleated myocytes in the human heart. *J. Mol. Cell. Cardiol.* **28**, 1463–1477. https://doi.org/10.1006/jmcc.1996.0137 (1996).
2. Robinson, T. F., Geraci, M. A., Sonnenblick, E. H. & Factor, S. M. Coiled perimysial fibers of papillary muscle in rat heart: Morphology, distribution, and changes in configuration. *Circ. Res.* **63**, 577–592. https://doi.org/10.1161/01.RES.63.3.577 (1988).
3. Huxley, H. & Hanson, J. Changes in the cross-striations of muscle during contraction and stretch and their structural interpretation. *Nature* **173**, 973–976. https://doi.org/10.1038/173973a0 (1954).
4. Streeter, D. D. & Bassett, D. L. An engineering analysis of myocardial fiber orientation in pig's left ventricle in systole. *Anat. Rec.* **155**, 503–511. https://doi.org/10.1002/ar.1091550403 (1966).
5. Streeter, D. D., Spotnitz, H. M., Patel, D. P., Ross, J. & Sonnenblick, E. H. Fiber orientation in the canine left ventricle during diastole and systole. *Circ. Res.* **24**, 339–347. https://doi.org/10.1161/01.RES.24.3.339 (1969).
6. LeGrice, I. J. *et al.* Laminar structure of the heart: Ventricular myocyte arrangement and connective tissue architecture in the dog. *Am. J. Physiol.* **269**, H571-582. https://doi.org/10.1152/ajpheart.1995.269.2.H571 (1995).
7. Legrice, I. J., Hunter, P. J. & Smaill, B. H. Laminar structure of the heart: A mathematical model. *Am. J. Physiol.* **272**, H2466-2476. https://doi.org/10.1152/ajpheart.1997.272.5.H2466 (1997).
8. Young, L. & Young, S. Extended confocal microscopy of myocardial laminae and collagen network. *J. Microsc.* **192**, 139–150. https://doi.org/10.1046/j.1365-2818.1998.00414.x (1998).
9. Kanzaki, Y. *et al.* Three-dimensional architecture of cardiomyocytes and connective tissue in human heart revealed by scanning electron microscopy. *Circulation* **122**, 1973–1974. https://doi.org/10.1161/CIRCULATIONAHA.110.979815 (2010).
10. Holzapfel, G. A. & Ogden, R. W. Constitutive modelling of passive myocardium: A structurally based framework for material characterization. *Philos. Trans. R. Soc. A Math. Phys. Eng. Sci.* **367**, 3445–3475. https://doi.org/10.1098/rsta.2009.0091 (2009).
11. Stephenson, R. *et al.* Resolving the true ventricular mural architecture. *J. Cardiovasc. Dev. Dis.* **5**, 34. https://doi.org/10.3390/jcdd5020034 (2018).
12. Kanzaki, Y., Terasaki, F., Okabe, M. & Kitaura, Y. Three-dimensional remodeling of cardiomyocytes in a patient with aortic stenosis: Scanning electron microscopy. *Circulation*https://doi.org/10.1161/CIRCULATIONAHA.108.809467 *(2009).*
13. Kanzaki, Y., Yamauchi, Y., Okabe, M., Terasaki, F. & Ishizaka, N. Three-dimensional architecture of cardiomyocytes and connective tissues in hypertrophic cardiomyopathy: A scanning electron microscopic observation. *Circulation* **125**, 738–739. https://doi.org/10.1161/CIRCULATIONAHA.111.054668 (2012).
14. Toussaint, N. *et al.* In vivo human cardiac fibre architecture estimation using shape-based diffusion tensor processing. *Med. Image Anal.* **17**, 1243–1255. https://doi.org/10.1016/j.media.2013.02.008 (2013).
15. von Deuster, C., Stoeck, C. T., Genet, M., Atkinson, D. & Kozerke, S. Spin echo versus stimulated echo diffusion tensor imaging of the in vivo human heart: Spin echo versus stimulated echo cardiac dti. *Magn. Reson. Med.* **76**, 862–872. https://doi.org/10.1002/mrm.25998 (2016).
16. Sands, G. B. *et al.* Automated imaging of extended tissue volumes using confocal microscopy. *Microsc. Res. Tech.* **67**, 227–239. https://doi.org/10.1002/jemt.20200 (2005).
17. Seidel, T., Edelmann, J.-C. & Sachse, F. B. Analyzing remodeling of cardiac tissue: A comprehensive approach based on confocal microscopy and 3d reconstructions. *Ann. Biomed. Eng.* **44**, 1436–1448. https://doi.org/10.1007/s10439-015-1465-6 (2016).
18. Bol, M., Reese, S., Parker, K. K. & Kuhl, E. Computational modeling of muscular thin films for cardiac repair. *Comput. Mech.* **43**, 535–544. https://doi.org/10.1007/s00466-008-0328-5 (2009).
19. Xi, J. *et al.* Myocardial transversely isotropic material parameter estimation from in-silico measurements based on a reduced-order unscented Kalman filter. *J. Mech. Behav. Biomed. Mater.* **4**, 1090–1102. https://doi.org/10.1016/j.jmbbm.2011.03.018 (2011).
20. Avazmohammadi, R. *et al.* A contemporary look at biomechanical models of myocardium. *Annu. Rev. Biomed. Eng.* **21**, 417–442. https://doi.org/10.1146/annurev-bioeng-062117-121129 (2019).
21. Pinto, J. G. & Fung, Y. Mechanical properties of the heart muscle in the passive state. *J. Biomech* **6**, 597–616. https://doi.org/10.1016/0021-9290(73)90017-1 (1973).
22. Forsell, C. & Gasser, T. C. Numerical simulation of the failure of ventricular tissue due to deep penetration: The impact of constitutive properties. *J. Biomech.* **44**, 45–51. https://doi.org/10.1016/j.jbiomech.2010.08.022 (2011).
23. Roe, A. T. *et al.* Increased passive stiffness promotes diastolic dysfunction despite improved Ca2+ handling during left ventricular concentric hypertrophy. *Cardiovasc. Res.* **113**, 1161–1172. https://doi.org/10.1093/cvr/cvx087 (2017).
24. Chalon, A. *et al.* Contribution of computational model for assessment of heart tissue local stress caused by suture in LVAD implantation. *J. Mech. Behav. Biomed. Mater.* **82**, 291–298. https://doi.org/10.1016/j.jmbbm.2018.03.032 (2018).
25. Novak, V., Yin, F. & Humphrey, J. Regional mechanical properties of passive myocardium. *J. Biomech.* **27**, 403–412. https://doi.org/10.1016/0021-9290(94)90016-7 (1994).
26. Sommer, G. *et al.* Biomechanical properties and microstructure of human ventricular myocardium. *Acta Biomater.* **24**, 172–192. https://doi.org/10.1016/j.actbio.2015.06.031 (2015).
27. Abbasi, M., Barakat, M. S., Vahidkhah, K. & Azadani, A. N. Characterization of three-dimensional anisotropic heart valve tissue mechanical properties using inverse finite element analysis. *J. Mech. Behav. Biomed. Mater.* **62**, 33–44. https://doi.org/10.1016/j.jmbbm.2016.04.031 (2016).

28. Dokos, S., Smaill, B. H., Young, A. A. & LeGrice, I. J. Shear properties of passive ventricular myocardium. *Am. J. Physiol. Heart Circ. Physiol.* **283**, H2650–H2659. https://doi.org/10.1152/ajpheart.00111.2002 (2002).
29. Ehret, A. E., Böl, M. & Itskov, M. A continuum constitutive model for the active behaviour of skeletal muscle. *J. Mech. Phys. Solids* **59**, 625–636. https://doi.org/10.1016/j.jmps.2010.12.008 (2011).
30. Ghosh, N. Tissue polarimetry: Concepts, challenges, applications, and outlook. *J. Biomed. Opt.* **16**, 110801. https://doi.org/10.1117/1.3652896 (2011).
31. Smith, M. H., Burke, P. D., Lompado, A., Tanner, E. A. & Hillman, L. W. Mueller matrix imaging polarimetry in dermatology. In Vo-Dinh, T., M.D., W. S. G. & M.D., D. A. B. (eds.) *Biomedical Diagnostic, Guidance, and Surgical-Assist Systems II*, vol. 3911, 210 – 216, https://doi.org/10.1117/12.384904. International Society for Optics and Photonics (SPIE, 2000).
32. Pierangelo, A. *et al.* Multispectral Mueller polarimetric imaging detecting residual cancer and cancer regression after neoadjuvant treatment for colorectal carcinomas. *J. Biomed. Opt.* **18**, 046014. https://doi.org/10.1117/1.JBO.18.4.046014 (2013).
33. Vizet, J. *et al.* In vivo imaging of uterine cervix with a Mueller polarimetric colposcope. *Sci. Rep.* **7**, 2471. https://doi.org/10.1038/s41598-017-02645-9 (2017).
34. Ghosh, N. Polarization birefringence measurements for characterizing the myocardium, including healthy, infarcted, and stem-cell-regenerated tissues. *J. Biomed. Opt.* **15**, 047009. https://doi.org/10.1117/1.3469844 (2010).
35. Ahmad, I. *et al.* Polarization image segmentation of radiofrequency ablated porcine myocardial tissue. *PLoS ONE* **12**, e0175173. https://doi.org/10.1371/journal.pone.0175173 (2017).
36. Bancelin, S. *et al.* Ex vivo multiscale quantitation of skin biomechanics in wild-type and genetically-modified mice using multiphoton microscopy. *Sci. Rep.*https://doi.org/10.1038/srep17635 *(2015).*
37. Lu, S.-Y. & Chipman, R. A. Interpretation of Mueller matrices based on polar decomposition. *J. Opt. Soc. Am. A* **13**, 1106. https://doi.org/10.1364/JOSAA.13.001106 (1996).
38. He, H. *et al.* Application of sphere-cylinder scattering model to skeletal muscle. *Opt. Express* **18**, 15104. https://doi.org/10.1364/OE.18.015104 (2010).
39. Jayyosi, C. *et al.* Affine kinematics in planar fibrous connective tissues: An experimental investigation. *Biomech. Model. Mechanobiol.* **16**, 1459–1473. https://doi.org/10.1007/s10237-017-0899-1 (2017).
40. Bol, M. & Reese, S. Micromechanical modelling of skeletal muscles based on the finite element method. *Comput. Methods Biomech. Biomed. Eng.* **11**, 489–504. https://doi.org/10.1080/10255840701771750 (2008).
41. Caruel, M., Chabiniok, R., Moireau, P., Lecarpentier, Y. & Chapelle, D. Dimensional reductions of a cardiac model for effective validation and calibration. *Biomech. Model. Mechanobiol.* **13**, 897–914. https://doi.org/10.1007/s10237-013-0544-6 (2014).
42. Hasaballa, A. I. *et al.* Microstructurally motivated constitutive modeling of heart failure mechanics. *Biophys. J.* **117**, 2273–2286. https://doi.org/10.1016/j.bpj.2019.09.038 (2019).
43. McEvoy, E., Holzapfel, G. A. & McGarry, P. Compressibility and anisotropy of the ventricular myocardium: Experimental analysis and microstructural modeling. *J. Biomech. Eng.* **140**, 081004. https://doi.org/10.1115/1.4039947 (2018).
44. Compain, E., Poirier, S. & Drevillon, B. General and self-consistent method for the calibration of polarization modulators, polarimeters, and Mueller-matrix ellipsometers. *Appl. Opt.* **38**, 3490. https://doi.org/10.1364/AO.38.003490 (1999).
45. Lindberg, A. *et al.* Innovative integrated numerical-experimental method for high-performance multispectral Mueller polarimeters based on ferroelectric liquid crystals. *Appl. Opt.* **58**, 5187–5199. https://doi.org/10.1364/AO.58.005187 (2019).
46. Héripré, E. *et al.* Coupling between experimental measurements and polycrystal finite element calculations for micromechanical study of metallic materials. *Int. J. Plast.* **23**, 1512–1539. https://doi.org/10.1016/j.ijplas.2007.01.009 (2007).

Acknowledgements

We thank V. de Greef for his technical support. This work has benefited from a financial support of the Labex LaSIPS (ANR-10-LABX0040–LaSIPS).

Author contributions

M. G., A.P. and J.M.A. supervised the research. A.P. and J.M.A designed the experiment, N.T. and J.V. performed the experiment(s), J.V. analized the results on polarimetry, N.T. analysed the mechanical results. All authors discussed the results and commented about the manuscript. N.T. and J.M.A. wrote the manuscript.

Competing interests

The authors declare no competing interests.

Additional information

Supplementary information is available for this paper at https://doi.org/10.1038/s41598-020-76820-w.

Correspondence and requests for materials should be addressed to A.P. or J.-M.A.

Reprints and permissions information is available at www.nature.com/reprints.

Supporting Information

Microstructural deformation observed by Mueller Polarimetry during traction assay on myocardium samples

Nicole Tueni[1,2,+], *Jérémy Vizet*[3,+], *Martin Genet*[1,2], *Angelo Pierangelo*[3], *Jean-Marc Allain*[1,2,*]

*Corresponding Author: angelo.pierangelo@polytechnique.edu ;

jean-marc.allain@polytechnique.edu

+These authors contributed equally to this work.

[1] LMS, CNRS, École Polytechnique, Institut Polytechnique de Paris, Palaiseau, France

[2] Inria, Palaiseau, France

[3] LPICM, CNRS, École Polytechnique, Institut Polytechnique de Paris, Palaiseau, France

Supplementary figure 1:

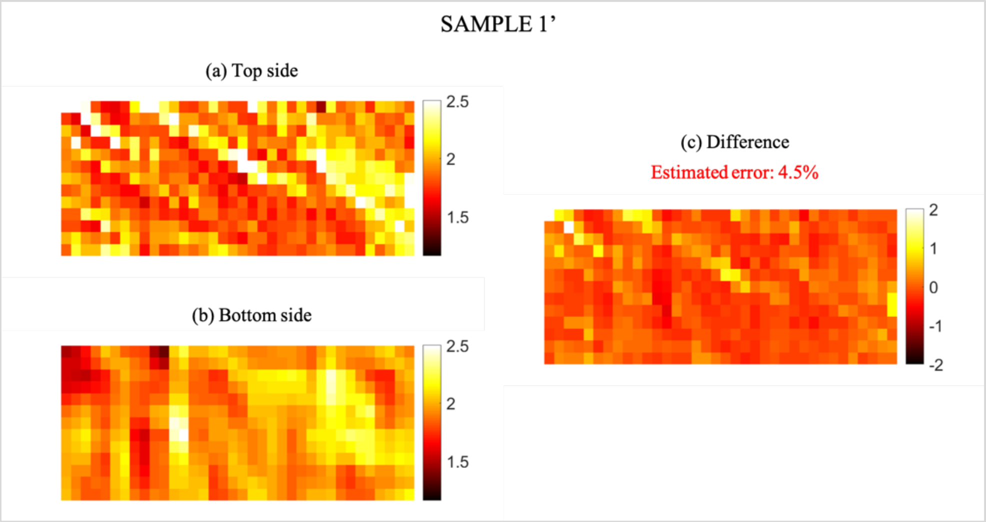

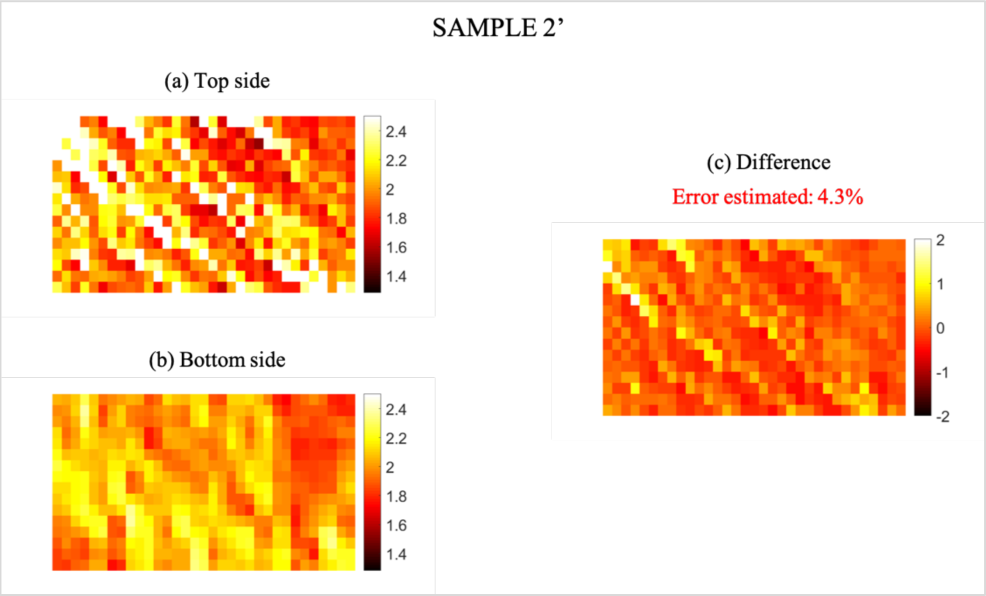

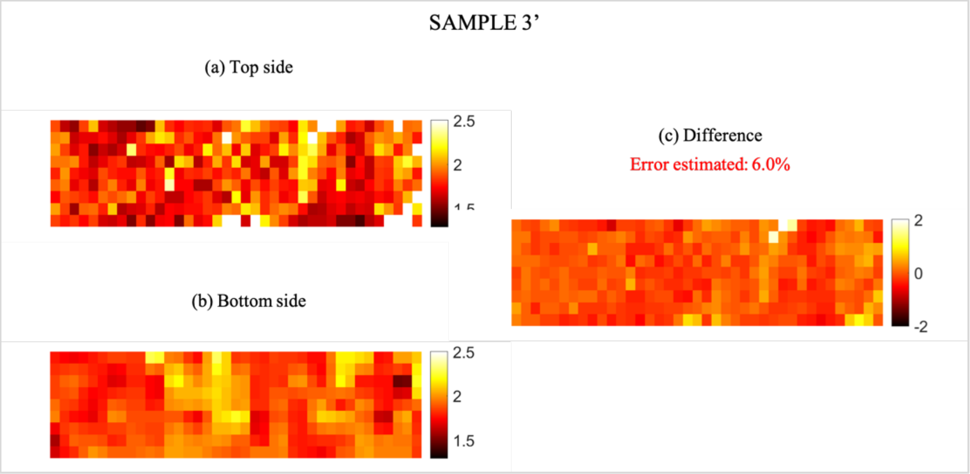

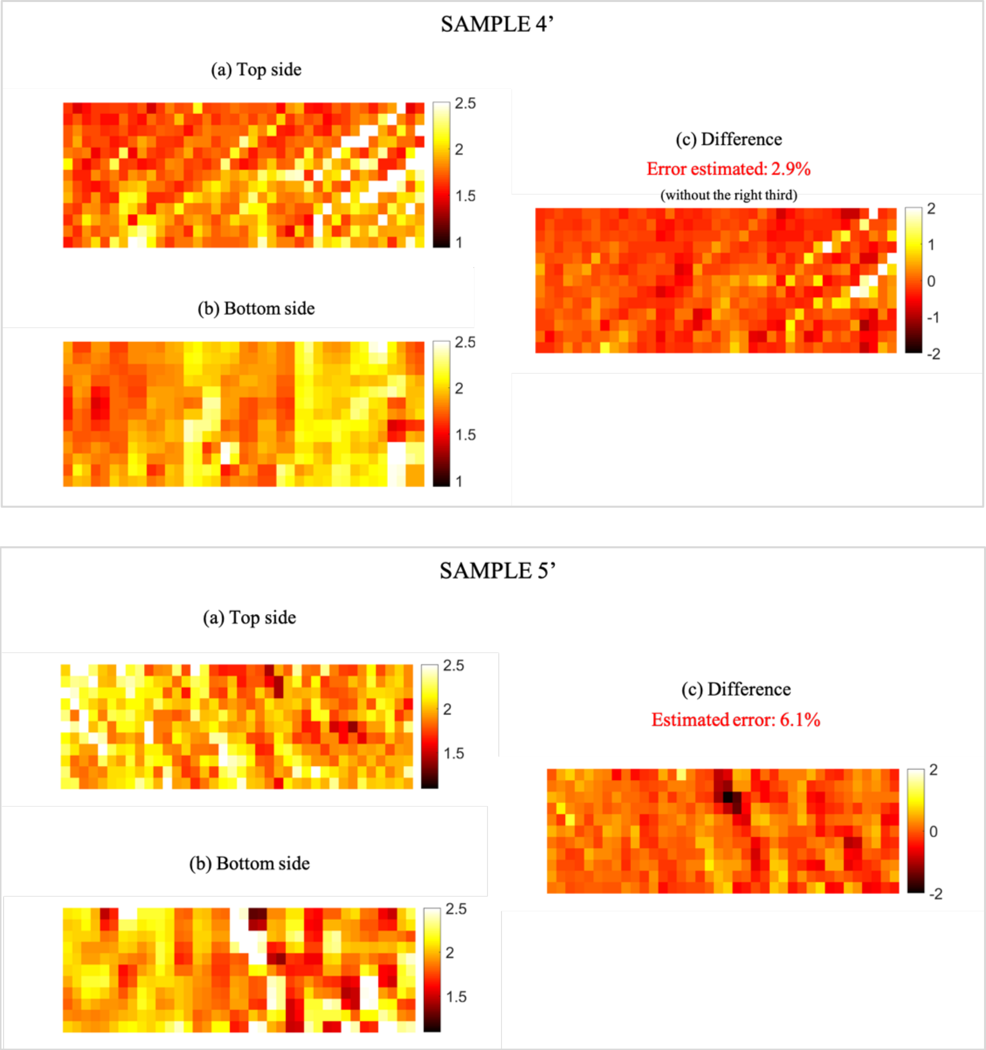

Figure S1. Comparison of the stretch measured by DIC on both sides of the same sample. (a) top and (b) bottom measures of each sample. (c) Difference $\boldsymbol{C_{top}} - \boldsymbol{C_{bottom}}$ of the two measures, as well as the estimation of error on the stretch based on the standard deviation of this difference.

Supplementary figure 2:

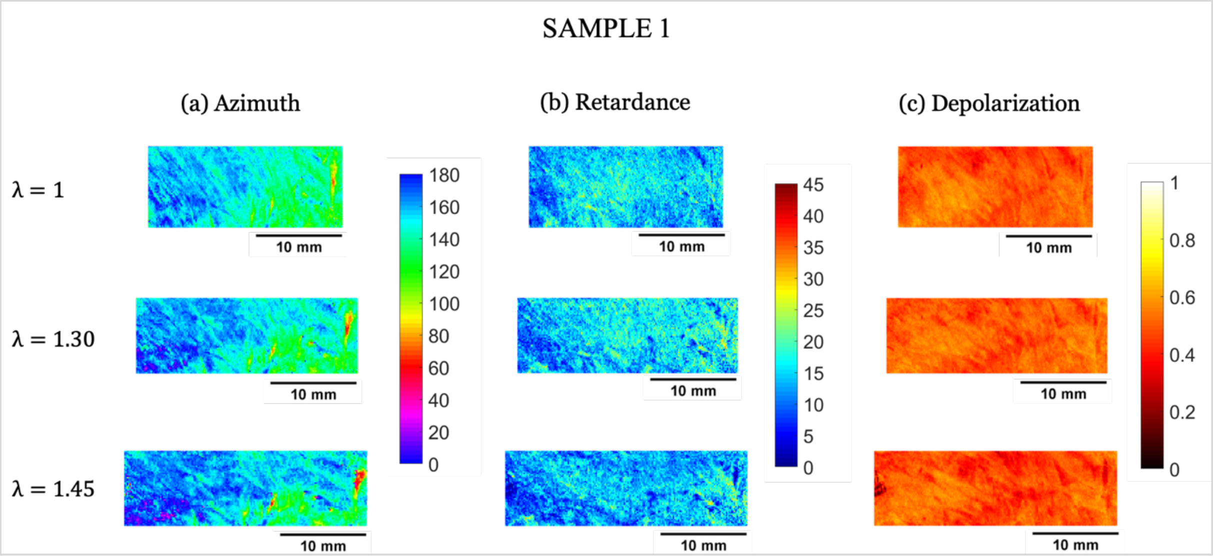

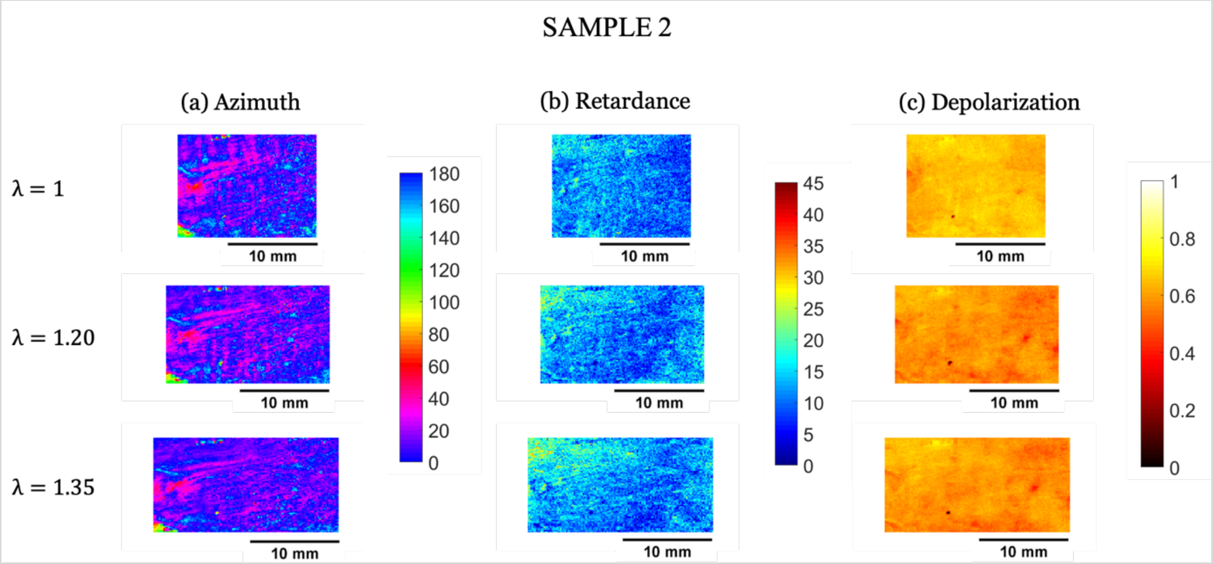

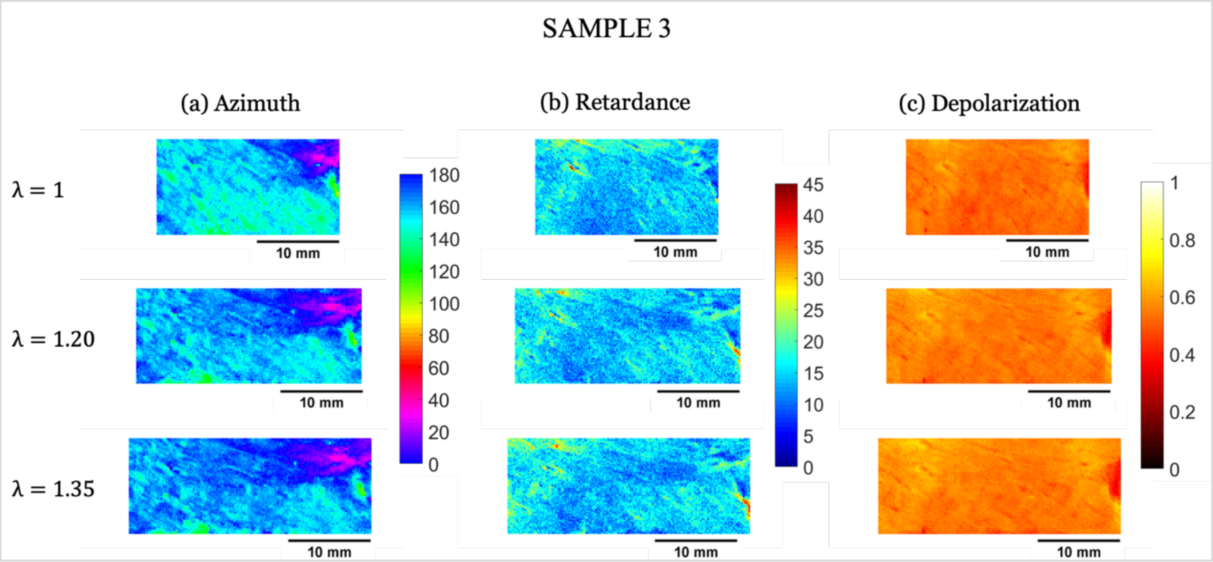

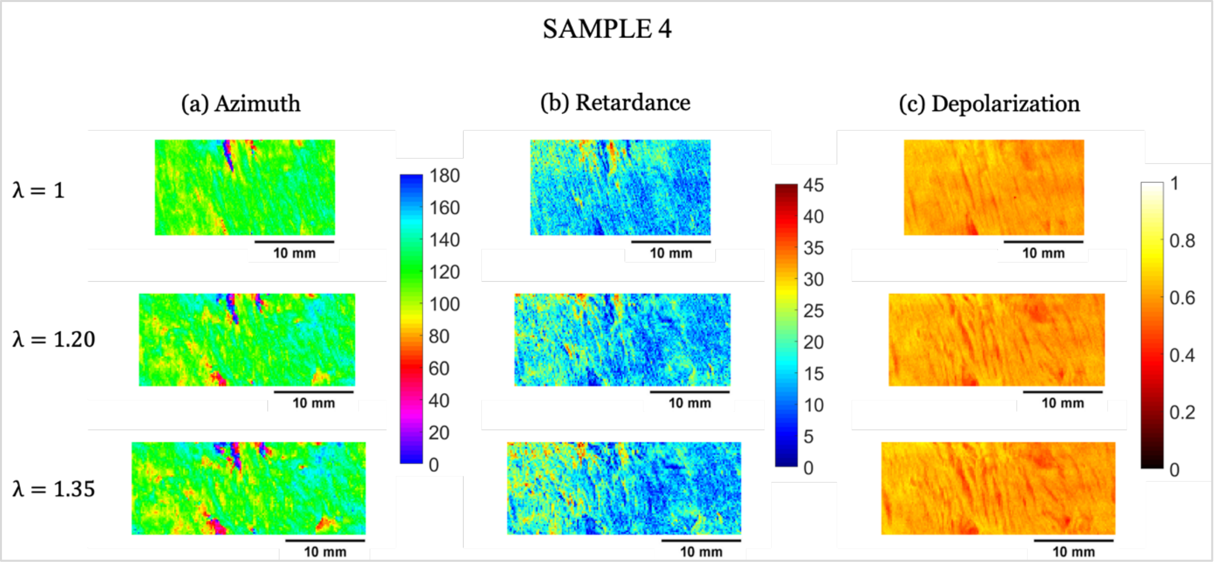
SAMPLE 4
(a) Azimuth
(b) Retardance
(c) Depolarization
λ = 1
λ = 1.20
λ = 1.35
10 mm
180
160
140
120
100
80
60
40
20
0
45
40
35
30
25
20
15
10
5
0
1
0.8
0.6
0.4
0.2
0

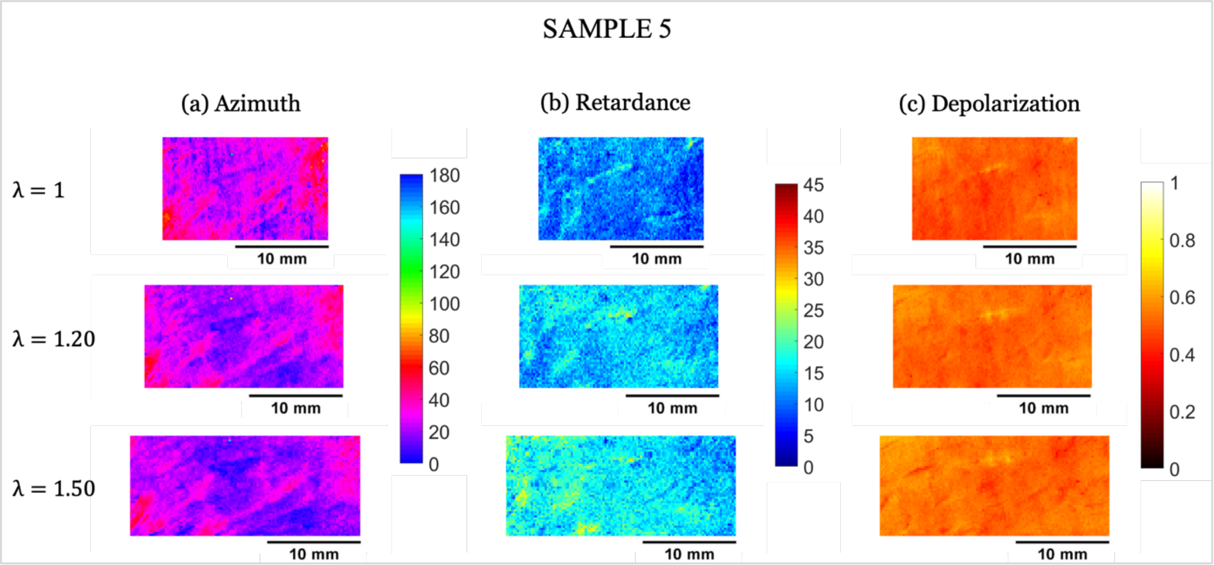
SAMPLE 5
(a) Azimuth
(b) Retardance
(c) Depolarization
λ = 1
λ = 1.20
λ = 1.50
10 mm
180
160
140
120
100
80
60
40
20
0
45
40
35
30
25
20
15
10
5
0
1
0.8
0.6
0.4
0.2
0

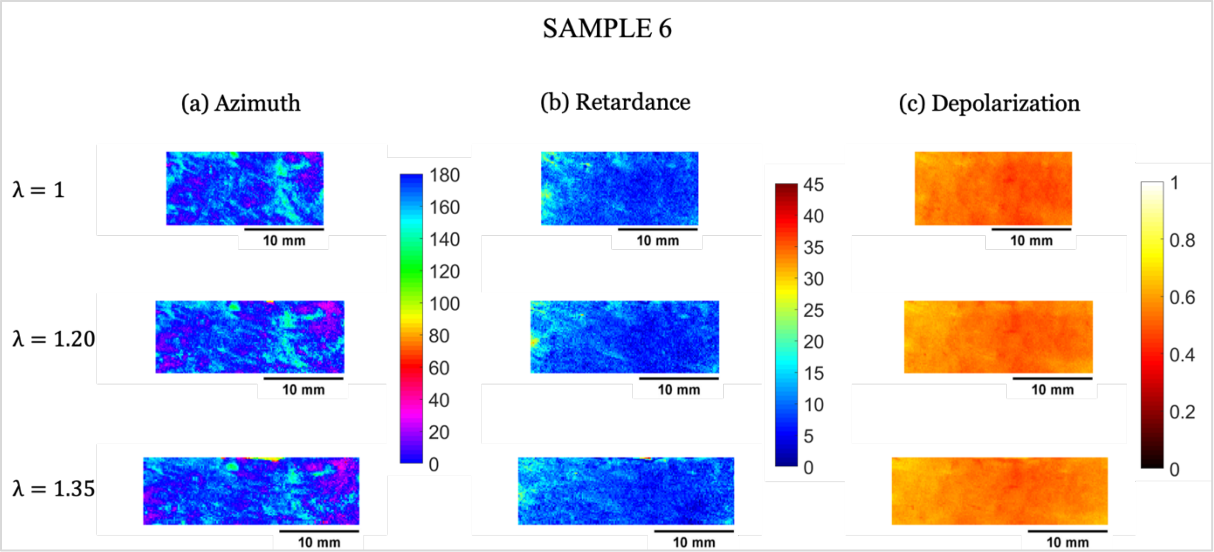
SAMPLE 6
(a) Azimuth
(b) Retardance
(c) Depolarization
λ = 1
λ = 1.20
λ = 1.35
10 mm
180
160
140
120
100
80
60
40
20
0
45
40
35
30
25
20
15
10
5
0
1
0.8
0.6
0.4
0.2
0

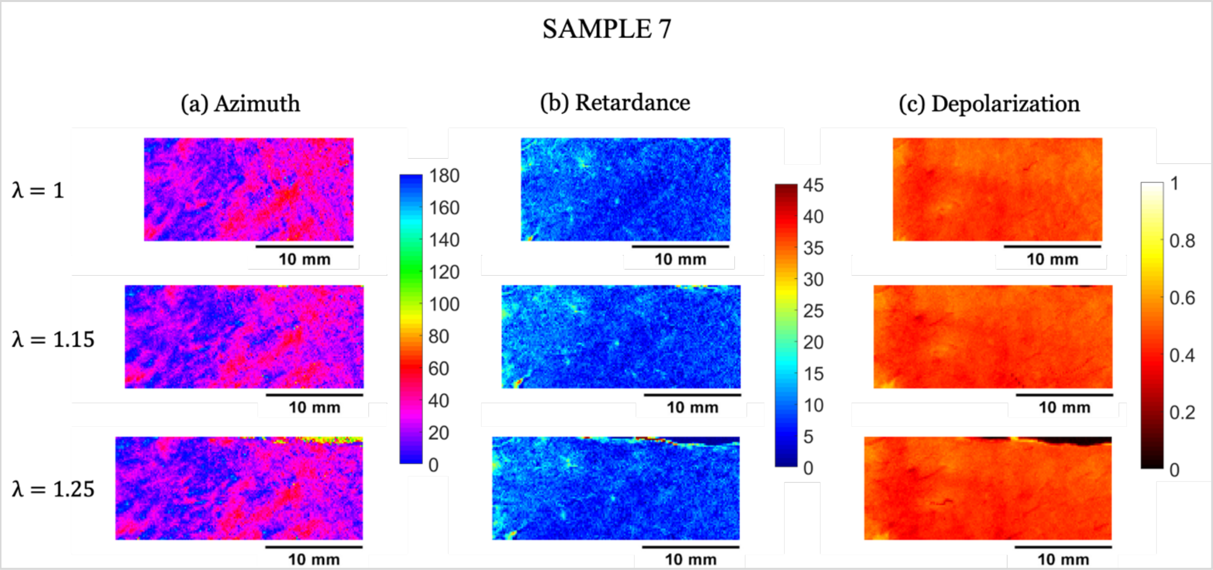
SAMPLE 7
(a) Azimuth
(b) Retardance
(c) Depolarization
λ = 1
λ = 1.15
λ = 1.25
10 mm
180
160
140
120
100
80
60
40
20
0
45
40
35
30
25
20
15
10
5
0
1
0.8
0.6
0.4
0.2
0

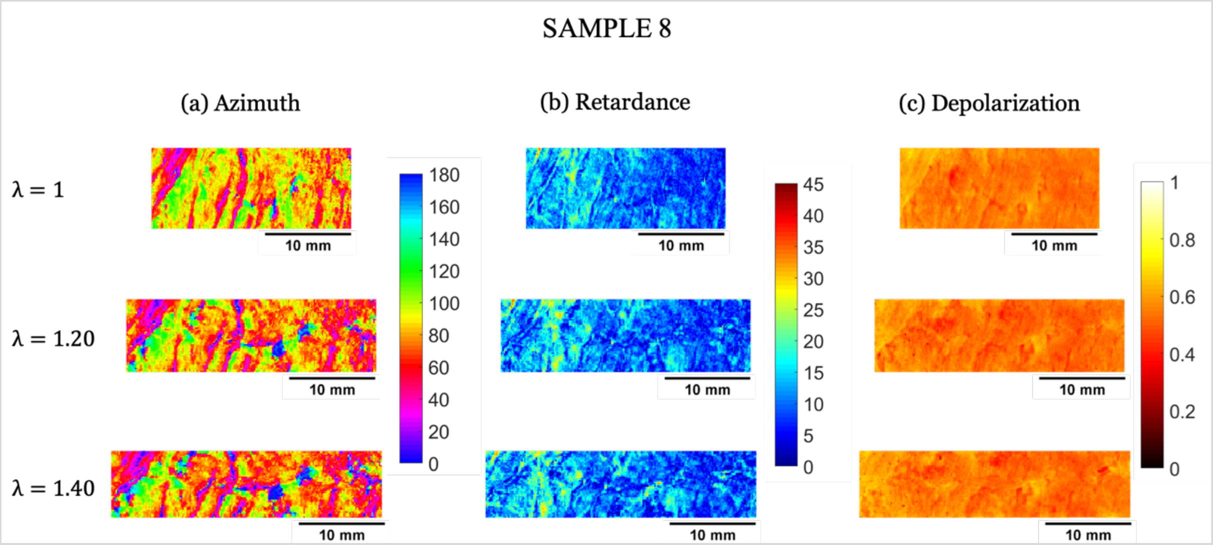
SAMPLE 8
(a) Azimuth
(b) Retardance
(c) Depolarization
λ = 1
λ = 1.20
λ = 1.40
10 mm
180
160
140
120
100
80
60
40
20
0
45
40
35
30
25
20
15
10
5
0
1
0.8
0.6
0.4
0.2
0

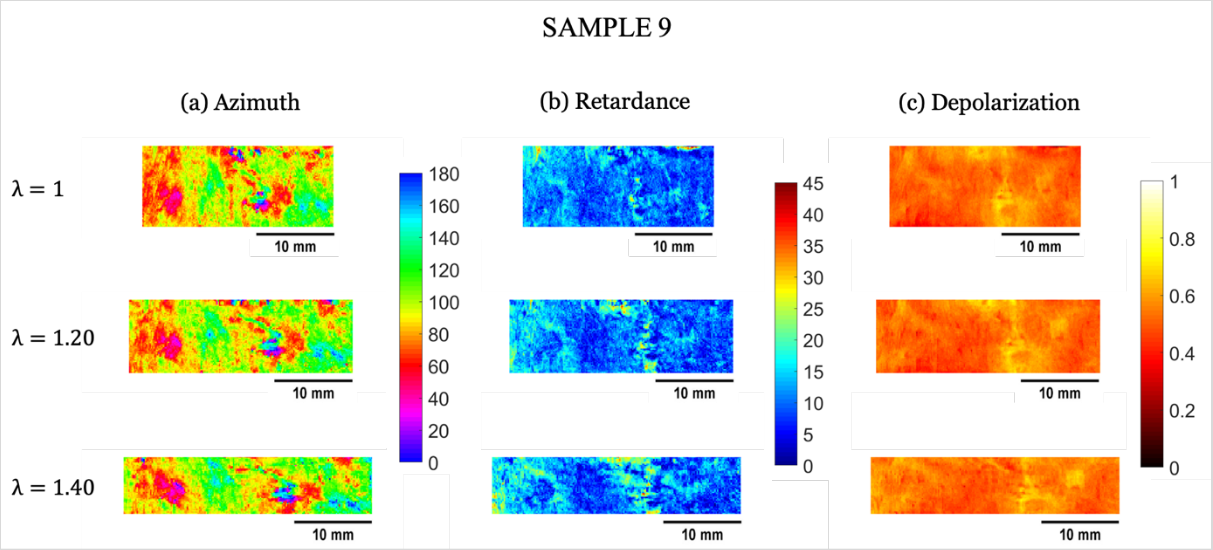
SAMPLE 9
(a) Azimuth
(b) Retardance
(c) Depolarization
λ = 1
λ = 1.20
λ = 1.40
10 mm
180
160
140
120
100
80
60
40
20
0
45
40
35
30
25
20
15
10
5
0
1
0.8
0.6
0.4
0.2
0

Figure S2. Maps of the Mueller polarimetry parameters (a - Azimuth (in °), b - Retardance (in °), c - Depolarization) measured at the different imposed stretches (indicated on the left), for all the samples.

Supplementary figure 3:

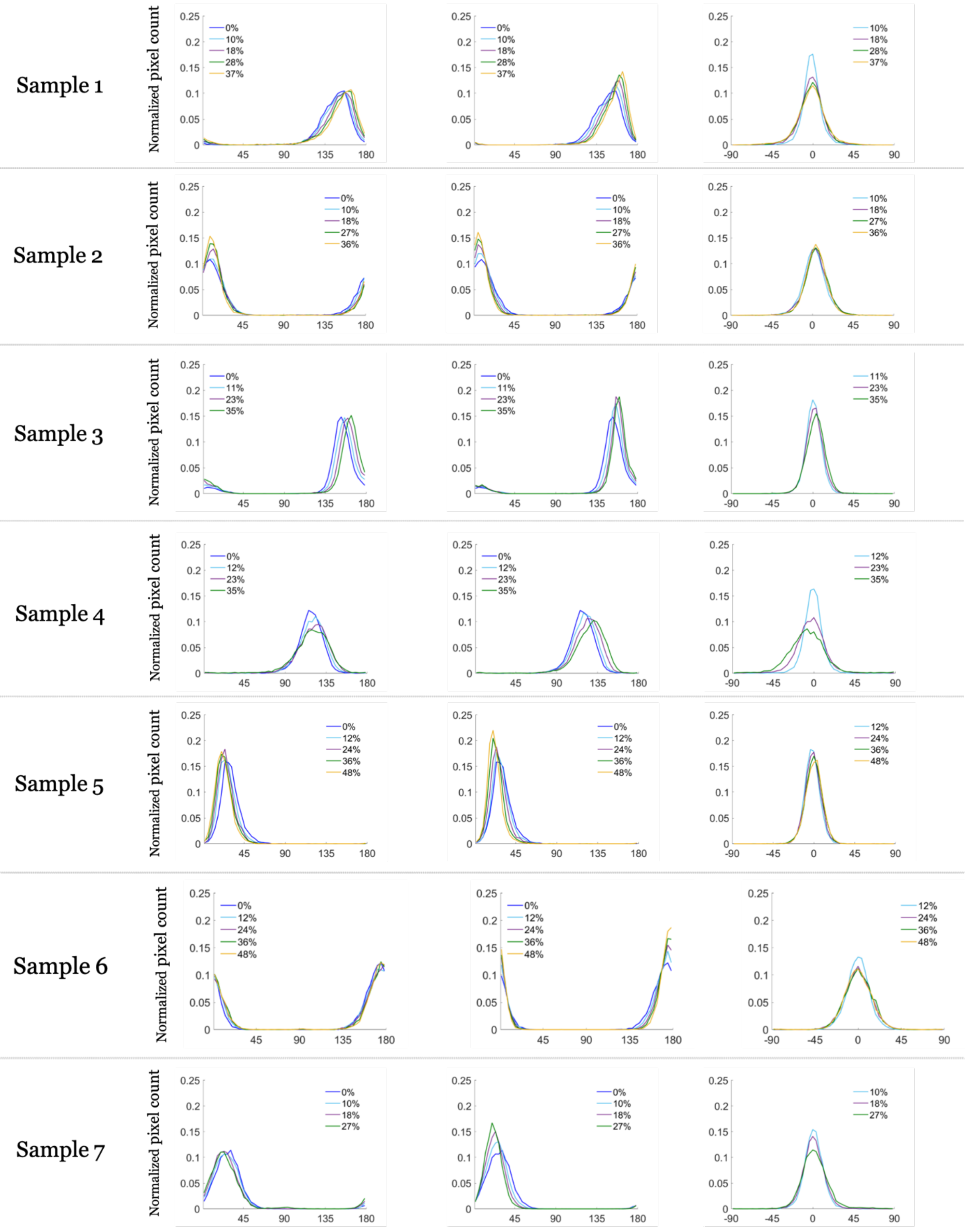

(a) Measured azimuth (°)

(b) Predicted azimuth (°)

(c) Distance (°)

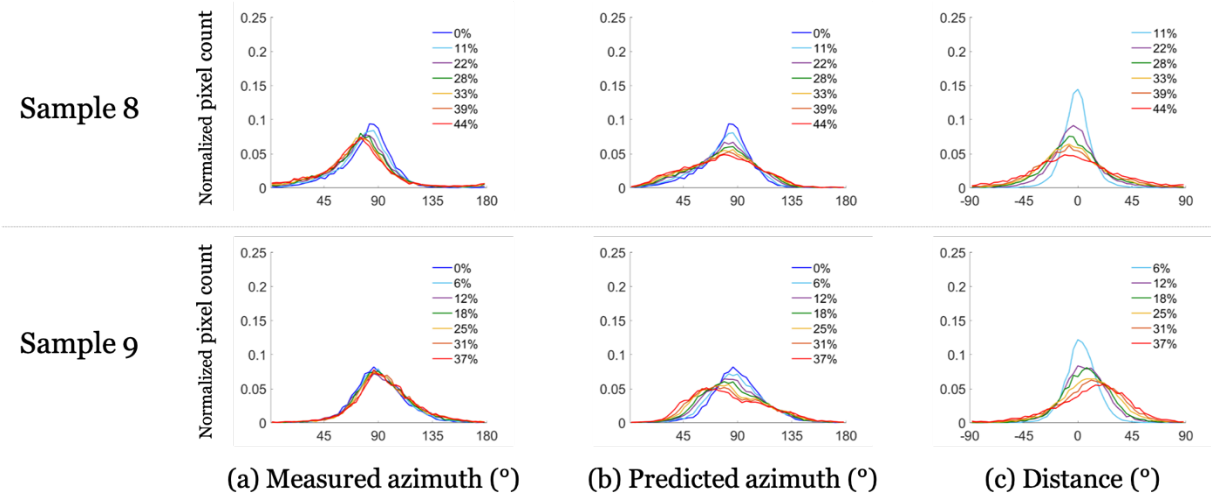

Figure S3. Histogram of the polarimetric parameters at different stretch level for each sample. a - Measured azimuth, b - Predicted azimuth, and c - Angular difference between measured and predicted azimuth distributions for each sample. The predicted distributions are obtained using the affine assumption.

3 Additional materials & methods

In the following, we will develop some of the methods that were used but not detailed in [Tueni et al., 2020]. First, we will describe the protocol used to prepare the samples in the study. Then, we will detail the post-processing of the obtained images and finally the computations used for the prediction of the mesostructure reorientation.

3.1 Sample preparation

This section completes the description of the sample preparation in the article by detailing the different methods tested for sample extraction and staining.

3.1.1 Extraction

Different techniques were tried to cut the samples. The first one consisted in using surgical scissors. However, it was impossible to slice the heart wall into thin layers. We tried a surgical scalpel. Although it was precise, it was very difficult to obtain smooth surfaces using this technique. In fact, given the tissue compliance, the obtained slices presented scratches and ripping. To obtain smooth surfaces, the section had to be done fast, and automatically.

We opted for using a meat slicing machine, which offered the most stability. The purchased machine was a Bosch Mas4201 slicer. It allowed a rapid clean cut through the heart wall, generating slices with a flat surface. We set the thickness to 2 mm. However, the obtained thickness was not homogeneous all along the slice as the gauge plate tended to move backwards as the ventricle was pushed on it (see Figure II.1).

The final protocol was: First, using the slicing machine, the epicardium was removed. Then, thin slices of thickness (2 mm) were cut parallel to the epicardium. From these slices, regions with homogeneous thickness were identified to extract the samples. Samples were extracted such that the visible orientation was 0°, 45° and 90°. We measured the sample thickness and the orientation of the mesostructure visible on its surface. Note that the mesostructure orientation varies in the thickness of the tissue, hence is different on both sides of the samples. We thus performed polarimetry imaging on both sides of test samples in order to assess the angular difference, and performed mechanical testing in order to compare the mechanical response. The samples were then placed it in a phosphate-buffered saline solution in the fridge for less than four hours, until testing. In total, 3 pig hearts were cut, and 3 samples from each heart were tested.

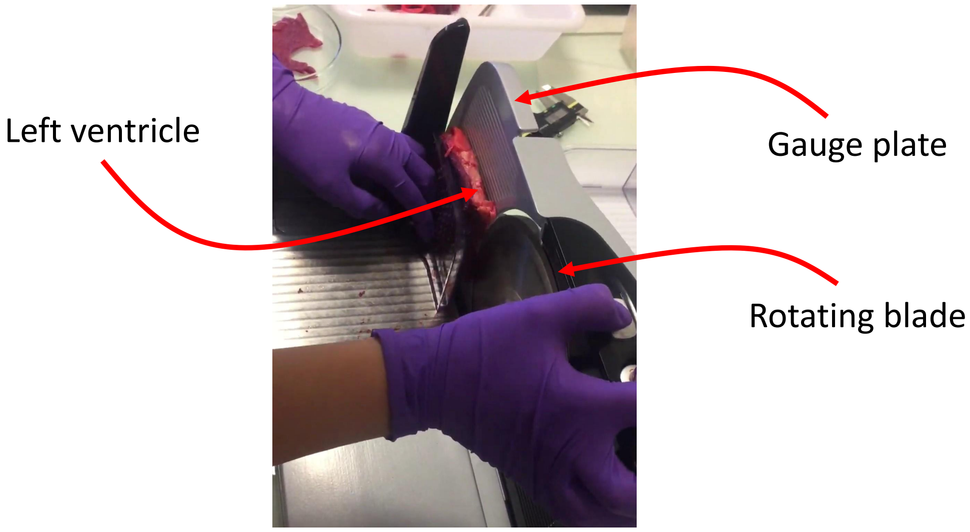

Figure II.1 – Photo of a pig left ventricle, pushed against the gauge plate of slicing machine. The gauge plate tends to move backwards, giving slices with heterogeneous thicknesses.

3.1.2 Staining

For each sample, the side used for digital image correlation was marked with an ink speckle, while the other side was left intact for polarimetric imaging. In order to mark the sample, different methods were tried.

The first method consisted in plotting a grid of dots on the sample, using a Uniball eye pen, in order to follow their displacement during stretching, as shown in Figure II.3. The precision in this method was not fine enough, and the dots too far apart to perform digital image correlation on a microscopic scale.

To compute the deformation on a smaller scale, we tried to glue micro-beads (20 µm in diameter) to the sample, using biological glue (M-coat Air drying polyurethane coating from Vishay). Although this method seemed precise enough to give a microscopic information about the displacement, it did not work as expected. In fact, the glue tended to form a thick, undeformable layer and to detach from the sample during stretching, as shown in Figure II.4.

Finally, the adopted method consisted in soaking a sponge in stamp pad ink [FIDOLINO Stamp pad ink, color black], and gently tapping it on the sample to transfer the ink on its surface, without it penetrating the tissue (see Figure II.5). We obtained a continuous ink pattern on the sample. The ink pattern presented enough contrast for digital image correlation on a microscopic scale.

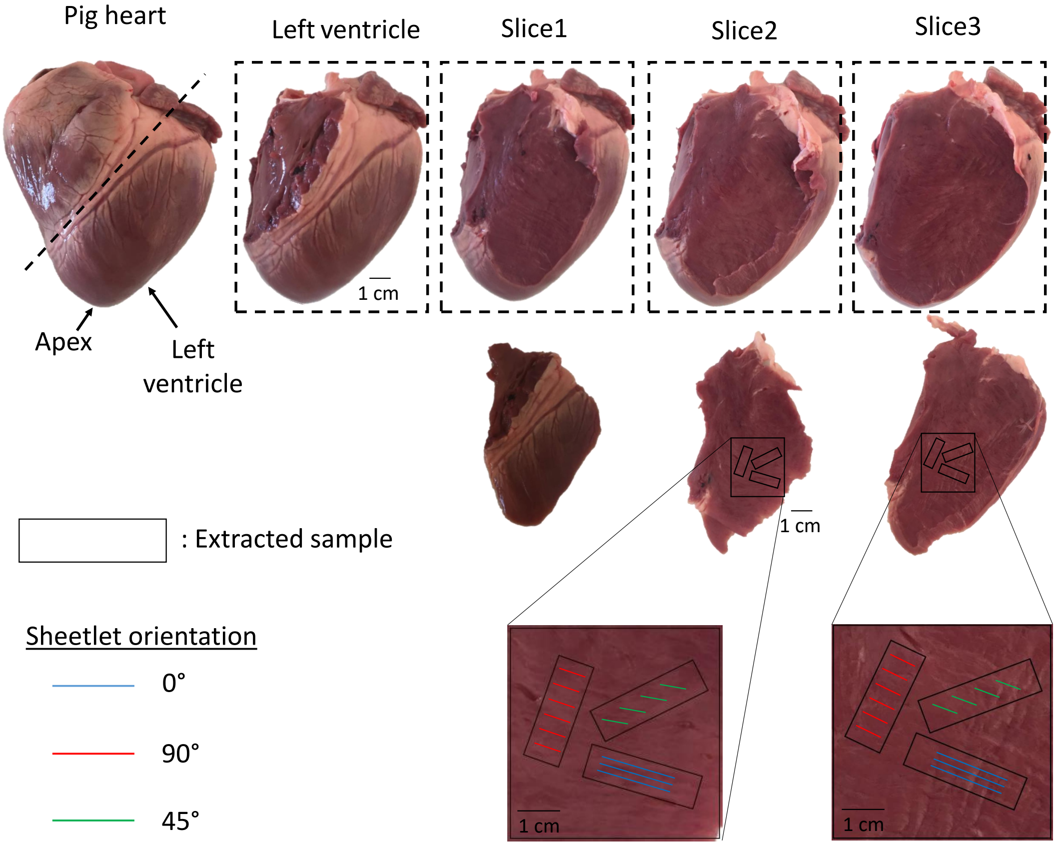

Figure II.2 – Photos of a sliced pig left ventricle, showing the slices and the orientations, allowing to extract samples with different orientations (0°, 45° and 90°).

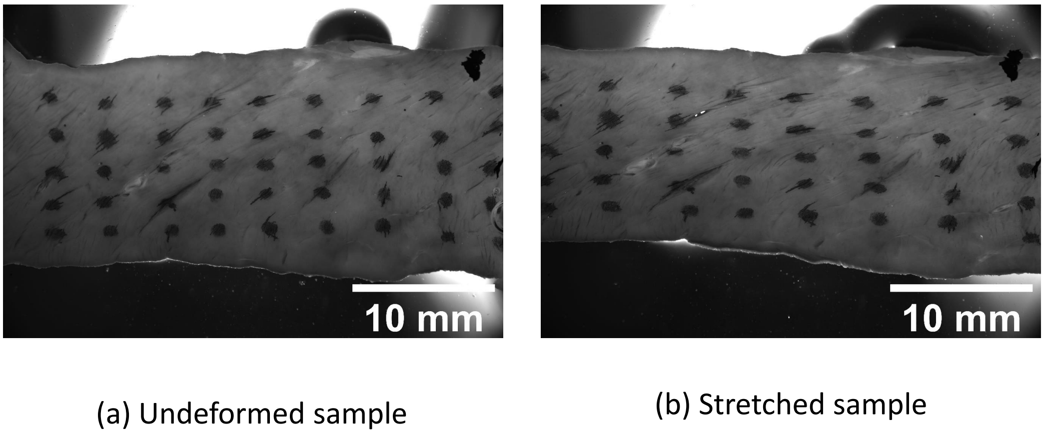

Figure II.3 – Marking method - macroscopic dots plotted on sample. As sample stretches, macroscopic deformation can be evaluated using dot displacement.

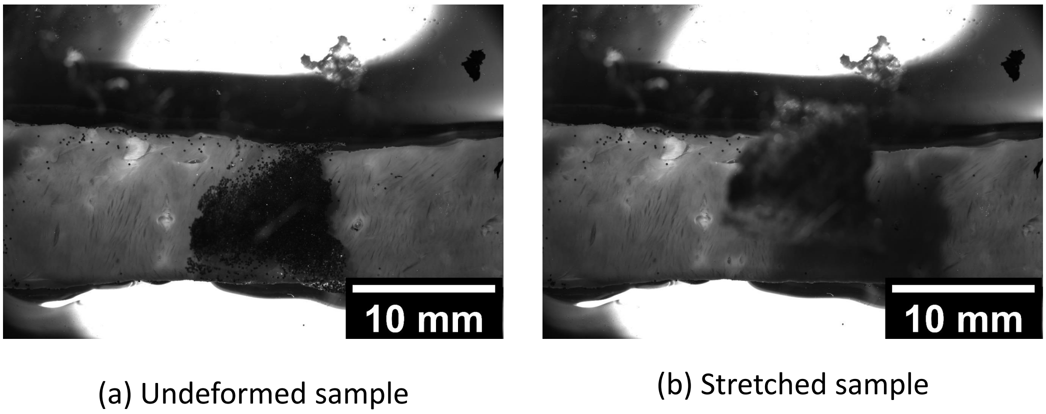

Figure II.4 – Marking method - The microscopic beads are glued on the sample in its undeformed configuration. As the sample is stretched, the glue detaches.

In order to verify that the speckle on one side did not alter the polarimetric response on the other side of the sample, one sample was imaged by the polarimeter twice: the first time, before marking the side, and the second time, after having added the ink speckle. The polarimetric response remained unchanged. We therefore concluded that this marking method was appropriate.

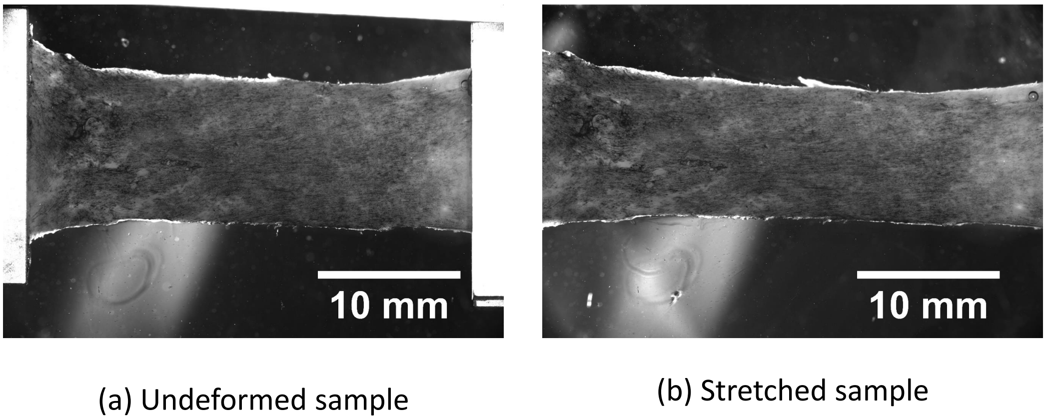

(a) Undeformed sample

(b) Stretched sample

Figure II.5 – Marking method - The ink speckle allowed to obtain a good contrast, and to compute the deformation at a fine scale.

3.2 Image post-processing

The images obtained from both sides of the samples were then processed in two steps: First, Digital Image Correlation (DIC) was performed on the images provided by the optical setup, generating maps of the samples local deformation. The images obtained with the optical setup and the Mueller matrices were then aligned. In the following, we will develop these steps, as they were not detailed in the published article.

3.2.1 Displacement field computation

DIC is an optical method that allows the computation of the displacement field using two images, consisting of a set of pixels with gray levels: the undeformed reference image and the deformed image. It aims at approximating at best the transformation $\underline{\Phi}(\underline{X})$ of a correlation domain in the neighborhood of $\underline{X}$ by measuring the similarity between the domain and its transform by $\underline{\Phi}$. The most used approaches for DIC are the local and the global approaches [Hild and Roux, 2012]. In the local approach [Lenoir et al., 2007], registration is performed on Zones Of Interest (ZOI), small correlation domains of the Region Of Interest (ROI). The mean displacement of each ZOI is computed. Whereas the global approach [Claire et al., 2004; Hild and Roux, 2006; Genet et al., 2018], discretizes the ROI into elements connected by nodes, and traces all these elements in the deformed image simultaneously, to evaluate all nodes displacements, hence enforcing the continuity of the displacement field.

The DIC software CorrelManuV 1.66, developed by M. Bornert [Allais et al., 1994; Héripré et al., 2007], was used to analyze the deformations of the studied samples. It uses a local approach to compute the displacements of a regular array of positions in a ROI defined by the user. We defined a ROI on the undeformed sample image by placing three points. The last point of the ROI was automatically added such that the ROI became a parallelogram (see Figure II.6, left, where the red border represents the ROI). We then set the size of the ZOI at 100 × 100 pixels, equivalent to 550 × 550 µm. This size was limited by the marker's resolution. The finer the marker, the smaller the domain size, and the finer the correlation. The ROI was then discretized into a selected number of ZOI (blue elements in Figure II.6).

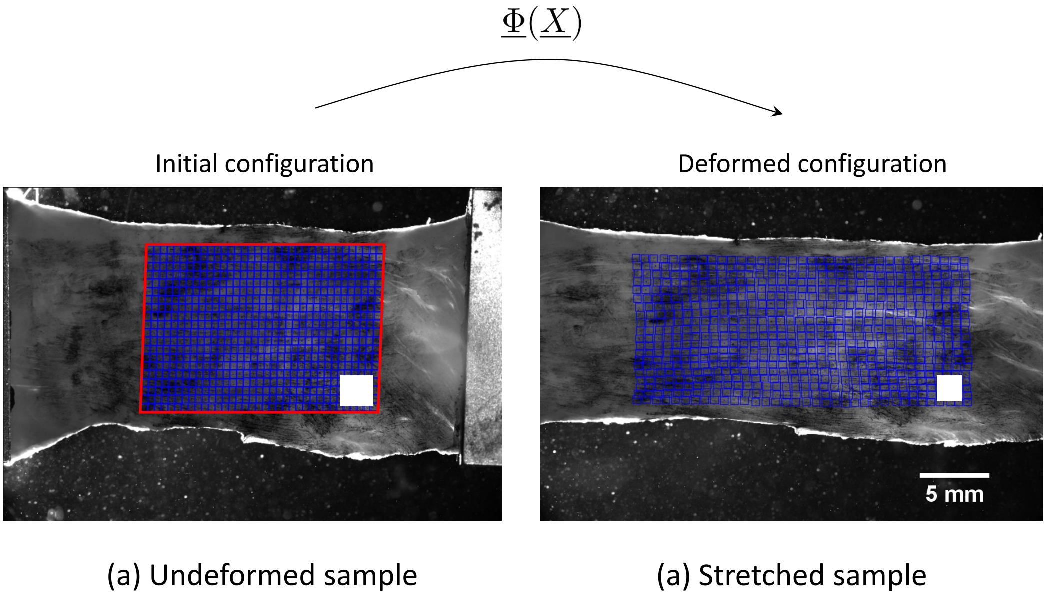

(a) Undeformed sample

(a) Stretched sample

Figure II.6 – Correlation grid for the undeformed (left) and deformed (right) sample. Red = ROI, Blue = ZOI.

3.2.2 Image alignment

This section details the *Image superposition* paragraph in *Methods* in the article. This step allowed us to align a set of two images of the same object (the myocardial sample here), taken by different devices (two imaging setups).

Image registration or image alignment algorithms can be classified into intensity-based and feature-based methods [Matl et al., 2017]: The intensity-based image alignment compares pixel intensity patterns in two images, while the feature-based method consists in finding matching features on the images to align.

In this study, we used the feature-based technique. We chose noticeable points on the edge of the sample. Once the correspondences between the features were found, we computed a transformation matrix $\underline{\underline{M}}$, that best matched points $\underline{X}$ from the first image and their corresponding points $\underline{x}$ in the second image (see Figure II.7). $\underline{\underline{M}}$ concatenates a set of affine transformations: $\underline{\underline{T}}$ (translation), $\underline{\underline{S}}$ (scaling) and $\underline{\underline{R}}$ (rotation), such that

$$\underline{\underline{M}} = \underline{\underline{T}} \cdot \underline{\underline{R}} \cdot \underline{\underline{S}}. \tag{II.1}$$

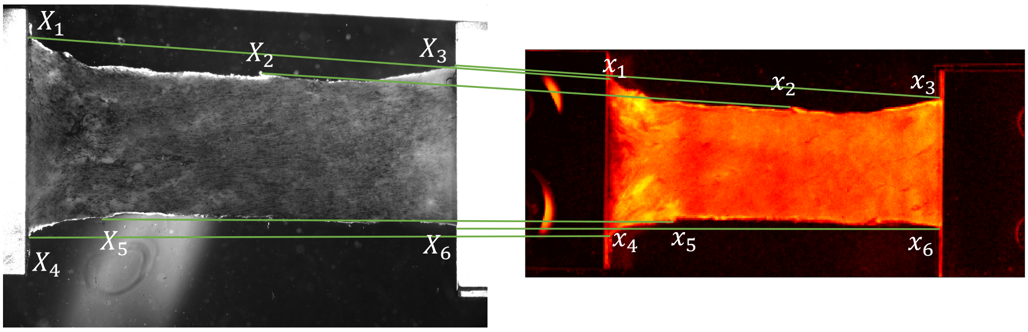

Figure II.7 – Matching features on optical image (left) and polarimetric image (right)

To represent the affine transformation with $\underline{\underline{\mathrm{M}}}$, we used the projective geometry instead of the Euclidean one, and introduced an extra dimension (W), called the "projective space". Coordinates in projective space are called "homogeneous coordinates" [Wikipedia, 2021]. With this method, we represented a 2D-vector $\underline{X} = (X, Y)$ by a 3-vector $\underline{X} = (X, Y, 1)$. Hence, for a rotation around the $\underline{e_z}$ axis,

$$\underline{\underline{S}} = \begin{bmatrix} S_x & 0 & 0 \\ 0 & S_y & 0 \\ 0 & 0 & 1 \end{bmatrix}, \quad \underline{\underline{R}} = \begin{bmatrix} \cos\theta & -\sin\theta & 0 \\ \sin\theta & \cos\theta & 0 \\ 0 & 0 & 1 \end{bmatrix}, \quad \text{and} \quad \underline{\underline{\mathrm{T}}} = \begin{bmatrix} 1 & 0 & T_x \\ 0 & 1 & T_y \\ 0 & 0 & 1 \end{bmatrix}.$$

Therefore,

$$\underline{\underline{M}} = \begin{bmatrix} S_x\cos\theta & -S_y\sin\theta & T_x \\ S_x\sin\theta & S_y\cos\theta & T_y \\ 0 & 0 & 1 \end{bmatrix} \quad \text{and} \quad \underline{\mathrm{x}} = \underline{\underline{\mathrm{M}}} \cdot \underline{\mathrm{X}}. \tag{II.2}$$

The parameter fitting was done in *Matlab* by solving a nonlinear least-squares problem of the form

$$\min_{\underline{p}} \left\{ f(\underline{p})^2 = \frac{1}{N_b} \sum_{k=1}^{N_b} \left\| \underline{\underline{M}}(\underline{p}) \cdot \underline{X}_k - \underline{x}_k \right\|_2^2 \right\}, \tag{II.3}$$

with N_b the number of matching points, and

$$\underline{p} = \{S_x, S_y, T_x, T_y, \theta\}. \tag{II.4}$$

Note that, by applying this method, we only had to align the reference undeformed images given by the two cameras for each sample. The obtained transformation matrix $\underline{\underline{M}}$ per sample was used to transform the remaining of the stretched images. In addition, the deformation being only measured on part of the sample, where DIC was performed, the image alignment method allowed us to match the corresponding zones where deformation was computed, hence correlate the information on the same region of interest in both images performed on two sides of the sample.

3.3 Prediction of mesostructure reorientation

Once the images were processed, we were able to proceed to the prediction of the microstructure reorientation, based on the initial measured fiber orientation (in the stress-free reference configuration), and on the computed local deformation.

The images generated by DIC on the lower side had a lower resolution than the polarimetric images of the upper side. In order to compare the mechanical and polarimetric data, the information obtained on both sides had to be extrapolated on the same location. In other words, we had to determine the displacement $\underline{u}(\underline{x})$ and its associated deformation gradient $\underline{\underline{F}}(\underline{X})$ at each point at which the polarimetric parameters were measured. Then, the computed deformation gradient was used to predict the reorientations of the MPI measured orientations.

3.3.1 Displacement field interpolation

Having the nodal positions for each deformation level, it was straightforward to compute the nodal displacements $\underline{u}^i$ (see Figure II.8), with

$$\underline{u}^i(\underline{X}) = \underline{x}^i - \underline{X}^i, \quad \forall\ i = 1, 2, 3, 4. \tag{II.5}$$

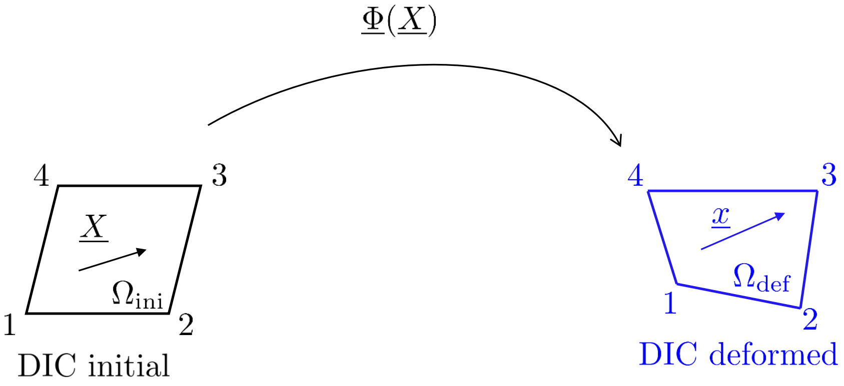

Figure II.8 – Elements with nodal positions in DIC and deformed configurations

In order to compute the deformation gradient at the positions where the polarimetric parameters were measured, we first chose to interpolate the measured displacement using bilinear interpolation. Bilinear interpolation aims at finding an approximate solution $\underline{u}(\underline{x})$ inside each element of the region of interest, by interpolating the nodal displacement $\underline{u}^i$ using bilinear shape functions Ψ^i. This is the same approach which is routinely used in the Finite Elements method with Q_1 elements. In the finite element method, shape functions are generally applied to isoparametric reference elements (square elements for quadrangles). However, in our study, the elements in the initial configuration, generated with DIC, were parallelograms. Given that there are no straightforward shape functions to interpolate a field from parallelogram element, a trick consisting in inserting an intermediate configuration of isoparametric square reference elements was adopted.

Figure II.9 shows the followed scheme: First, transformation $\underline{\Phi}_{\text{ini}}$ converts the refer-

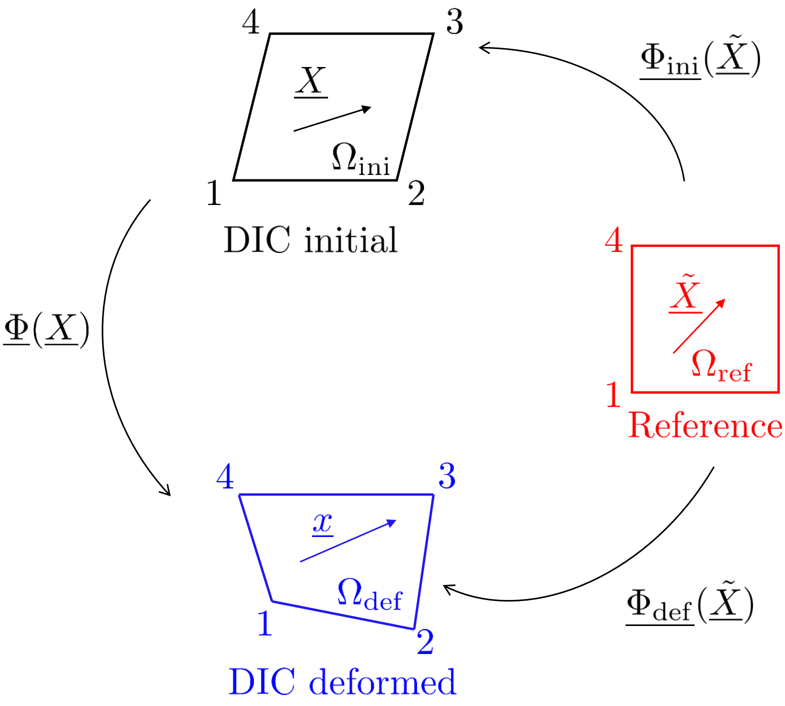

Figure II.9 – Element in the DIC, reference and deformed configuration, and the associated transformations.

ence element Ω_{ref} into the initial configuration element extracted from DIC Ω_{ini}. The reference element Ω_{ref} is also subject to transformation $\underline{\Phi_{\text{def}}}$ and leads to the deformed configuration element Ω_{def}.

The nodal positions X^i in the initial configuration, $\tilde{X}^i$ in the reference configuration, and x^i in the deformed configuration being known, the nodal displacements $\underline{u^i_{\text{ini}}}(\tilde{X})$ and $\underline{u^i_{\text{def}}}(\tilde{X})$ were computed such that:

$$\begin{cases} \underline{u^i_{\text{ini}}}(\underline{\tilde{X}}) = \underline{X^i} - \underline{\tilde{X}^i} \\ \underline{u^i_{\text{def}}}(\underline{\tilde{X}}) = \underline{x^i} - \underline{\tilde{X}^i} \end{cases} . \tag{II.6}$$

The transformations $\underline{\Phi_{\text{ini}}}$ and $\underline{\Phi_{\text{def}}}$ will first be presented separately.

Transformation $\underline{\Phi_{\mathrm{def}}}$. $\underline{\Phi_{\mathrm{def}}}$ transforms Ω_{ref} into Ω_{def}, as shown in Figure II.9. In order to obtain the displacement for all points of the elements, bilinear shape functions $\Psi^i(\underline{\tilde{X}})$ were used to interpolate the obtained nodal displacements, according to:

$$\underline{u_{\mathrm{def}}}(\underline{\tilde{X}}) = \sum_{i=1}^{4} \Psi^i(\underline{\tilde{X}})\underline{u^i_{\mathrm{def}}}, \quad \text{with} \quad \begin{cases} \Psi^1(\tilde{X}) = (1-\tilde{X})(1-\tilde{Y}) \\ \Psi^2(\tilde{X}) = \tilde{X}(1-\tilde{Y}) \\ \Psi^3(\tilde{X}) = \tilde{X}\tilde{Y} \\ \Psi^4(\tilde{X}) = \tilde{Y}(1-\tilde{X}) \end{cases} . \tag{II.7}$$

Knowing the displacement field $\underline{u_{\mathrm{def}}}(\underline{\tilde{X}})$, the deformation gradient $\underline{\underline{F_{\mathrm{def}}}}(\underline{\tilde{X}})$ was computed such that:

$$\underline{\underline{F_{\mathrm{def}}}}(\underline{\tilde{X}}) = \underline{\underline{\nabla}}\ \underline{u_{\mathrm{def}}}(\underline{\tilde{X}}) + \underline{\underline{1}}, \tag{II.8}$$

with

$$\begin{cases} F_{\mathrm{def,xx}}(\underline{\tilde{X}}) = -u^1_{\mathrm{def}} + u^2_{\mathrm{def}} + \tilde{Y}(u^1_{\mathrm{def}} - u^2_{\mathrm{def}} + u^3_{\mathrm{def}} - u^4_{\mathrm{def}}) + 1 \\ F_{\mathrm{def,xy}}(\underline{\tilde{X}}) = -u^1_{\mathrm{def}} + u^4_{\mathrm{def}} + \tilde{X}(u^1_{\mathrm{def}} - u^2_{\mathrm{def}} + u^3_{\mathrm{def}} - u^4_{\mathrm{def}}) \\ F_{\mathrm{def,yx}}(\underline{\tilde{X}}) = -v^1_{\mathrm{def}} + v^2_{\mathrm{def}} + \tilde{Y}(v^1_{\mathrm{def}} - v^2_{\mathrm{def}} + v^3_{\mathrm{def}} - v^4_{\mathrm{def}}) \\ F_{\mathrm{def,yy}}(\underline{\tilde{X}}) = -v^1_{\mathrm{def}} + v^4_{\mathrm{def}} + \tilde{X}(v^1_{\mathrm{def}} - v^2_{\mathrm{def}} + v^3_{\mathrm{def}} - v^4_{\mathrm{def}}) + 1 \end{cases} .$$

Transformation $\underline{\Phi_{\mathrm{ini}}}$. Similarly, for $\underline{\Phi_{\mathrm{ini}}}$, transforming the reference configuration Ω_{ref} into the initial configuration Ω_{ini}, as shown in Figure II.9, the displacement field $\underline{u_{\mathrm{ini}}}(\underline{\tilde{X}})$ and the deformation gradient $\underline{\underline{F_{\mathrm{ini}}}}(\underline{\tilde{X}})$ were obtained by interpolating the nodal displacement:

$$\underline{u_{\mathrm{ini}}}(\underline{\tilde{X}}) = \sum_{i=1}^{4} \Psi^i(\underline{\tilde{X}})\underline{u^i_{\mathrm{ini}}}. \tag{II.9}$$

This led to the expression of $\underline{\underline{F_{\mathrm{ini}}}}$ that links $\underline{X}$ to $\underline{\tilde{X}}$ via $\underline{X} = \underline{\underline{F_{\mathrm{ini}}}} \cdot \underline{\tilde{X}}$:

$$\underline{\underline{F_{\mathrm{ini}}}}(\underline{\tilde{X}}) = \underline{\underline{\nabla}}\ \underline{u_{\mathrm{ini}}}(\underline{\tilde{X}}) + \underline{\underline{1}} \tag{II.10}$$

with

$$\begin{cases} F_{\text{ini,xx}}(\underline{\tilde{X}}) = -u_{\text{ini}}^1 + u_{\text{ini}}^2 + \tilde{Y}(u_{\text{ini}}^1 - u_{\text{ini}}^2 + u_{\text{ini}}^3 - u_{\text{ini}}^4) + 1 \\ F_{\text{ini,xy}}(\underline{\tilde{X}}) = -u_{\text{ini}}^1 + u_{\text{ini}}^4 + \tilde{X}(u_{\text{ini}}^1 - u_{\text{ini}}^2 + u_{\text{ini}}^3 - u_{\text{ini}}^4) \\ F_{\text{ini,yx}}(\underline{\tilde{X}}) = -v_{\text{ini}}^1 + v_{\text{ini}}^2 + \tilde{Y}(v_{\text{ini}}^1 - v_{\text{ini}}^2 + v_{\text{ini}}^3 - v_{\text{ini}}^4) \\ F_{\text{ini,yy}}(\underline{\tilde{X}}) = -v_{\text{ini}}^1 + v_{\text{ini}}^4 + \tilde{X}(v_{\text{ini}}^1 - v_{\text{ini}}^2 + v_{\text{ini}}^3 - v_{\text{ini}}^4) + 1 \end{cases} . \tag{II.11}$$

In the case of a transformation from a square to a parallelogram, we have:

$$\begin{cases} u_{\text{ini}}^1 - u_{\text{ini}}^2 + u_{\text{ini}}^3 - u_{\text{ini}}^4 = 0 \\ v_{\text{ini}}^1 - v_{\text{ini}}^2 + v_{\text{ini}}^3 - v_{\text{ini}}^4 = 0 \end{cases} .$$

Hence, the expression of Equation (II.11) becomes independent of $\underline{\tilde{X}}$ and $\underline{\underline{F_{\text{ini}}}}(\underline{\tilde{X}})$ becomes easily invertible.

Transformation $\underline{\Phi}$. We were thus able to analytically link both initial (Ω_{ini}) and deformed (Ω_{def}) configurations to the reference configuration (Ω_{ref}) via: $\underline{X} = \underline{\underline{F_{\text{ini}}}}(\underline{\tilde{X}}) \cdot \underline{\tilde{X}}$, and $\underline{x} = \underline{\underline{F_{\text{def}}}}(\underline{\tilde{X}}) \cdot \underline{\tilde{X}}$. It was therefore possible to link them directly by inverting $\underline{\underline{F_{\text{ini}}}}(\underline{\tilde{X}})$, therefore obtaining

$$\underline{\tilde{X}} = \underline{\underline{F_{\text{ini}}}}^{-1}(\underline{X}) \cdot \underline{X} \tag{II.12}$$

and

$$\underline{x} = \underline{\underline{F_{\text{def}}}}(\underline{\tilde{X}}) \cdot \underline{\underline{F_{\text{ini}}}}^{-1}(\underline{X}) \cdot \underline{X} = \underline{\underline{F}}(\underline{X}) \cdot \underline{X}, \tag{II.13}$$

with

$$\underline{\underline{F}}(\underline{X}) = \underline{\underline{F_{\text{def}}}}(\underline{\tilde{X}}) \cdot \underline{\underline{F_{\text{ini}}}}^{-1}(\underline{X}). \tag{II.14}$$

This equation was used to transport all vectors in the initial configuration Ω_{ini} obtained with DIC to the deformed configuration Ω_{def}. Figure II.10 shows the displacement field measured using DIC (in green), and the interpolated displacement field (in red). The interpolation allowed to obtain the displacement information at the desired scale.

3.3.2 Angle transformation & comparison

The initial mesostructure orientation $\underline{e_{\text{m}}}$ was generated by the Mueller polarimetry setup in the form of an angle θ. To predict the mesostructure reorientation $\underline{e_{\text{m}}}'$, we used the Equation (II.13) to transport $\underline{e_{\text{m}}}$.

$$\underline{e_{\text{m}}}' = \underline{\underline{F}} \cdot \underline{e_{\text{m}}}, \tag{II.15}$$

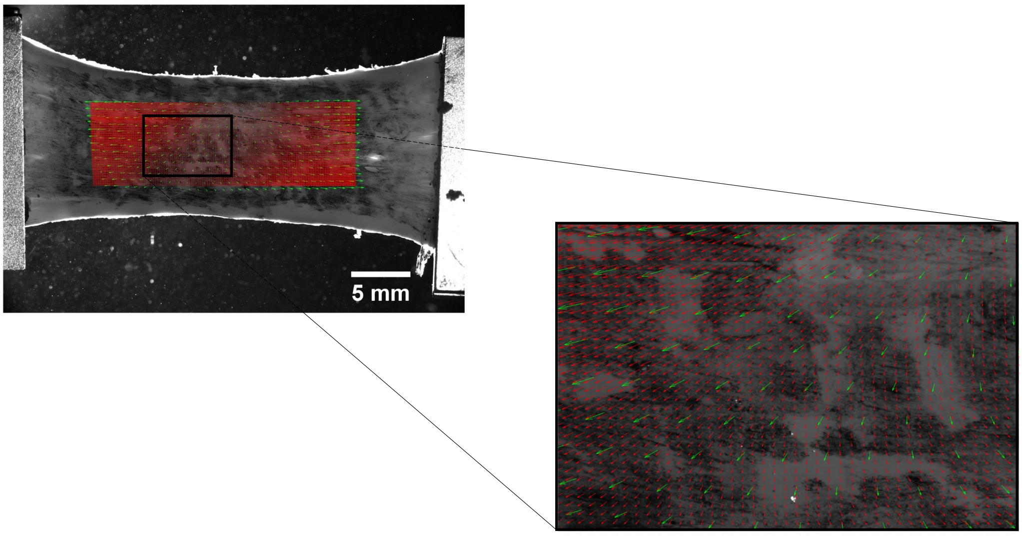

Figure II.10 – Map and zoom of the DIC measured displacement field (green) and interpolated displacement field (red) using the method detailed in Section 3.3. The interpolated field allows to obtain the local displacement at a finer scale.

with

$$\underline{e_{\mathrm{m}}} = \begin{bmatrix} \cos\theta \\ \sin\theta \end{bmatrix} \tag{II.16}$$

and

$$\theta' = \arctan\left(\frac{e'_{\mathrm{my}}}{e'_{\mathrm{mx}}}\right).$$

In order to compare the measured and predicted angles, we computed the angle between $\underline{e_{\mathrm{m}}}$ and $\underline{e_{\mathrm{m}}}'$. We point out that θ, generated by the polarimeter, and θ', computed based on θ were comprised between 0° and 180°, and that we wanted to obtain the smallest signed distance, comprised between $-90°$ and 90°.

Transforming the angles to radians, we first denoted $\Delta\theta$ the simple difference between both angles, which returned a signed angle between $\pm\pi$:

$$\Delta\theta = \theta - \theta'.$$

Then, we computed the distance d, between $\pm\frac{\pi}{2}$ such that:

$$d = \begin{cases} \Delta\theta & \text{if} \quad -\frac{\pi}{2} \leq \Delta\theta \leq \frac{\pi}{2} \\ \Delta\theta - \pi & \text{if} \quad \Delta\theta > \frac{\pi}{2} \\ \Delta\theta + \pi & \text{if} \quad \Delta\theta < -\frac{\pi}{2} \end{cases} . \tag{II.17}$$

Figure II.11 shows four maps of the Muller polarimetry imaging measured angles θ, predicted angles θ', the difference between them $\Delta\theta$ and the distance between them d for one sample, for a stretch $\lambda = 1.45$. As fully discussed in the paper, we notice important differences between θ and θ', which means that the predicted angles do not fully agree with the measured ones, therefore the affine assumption is not enough to describe the tissue behavior. Naturally, this leads to important differences between the θ and θ'. The $\Delta\theta$ map shows these differences, however it exhibits discrete patches of angular differences, that are corrected or smoothed by computing the distance between $\pm\frac{\pi}{2}$.

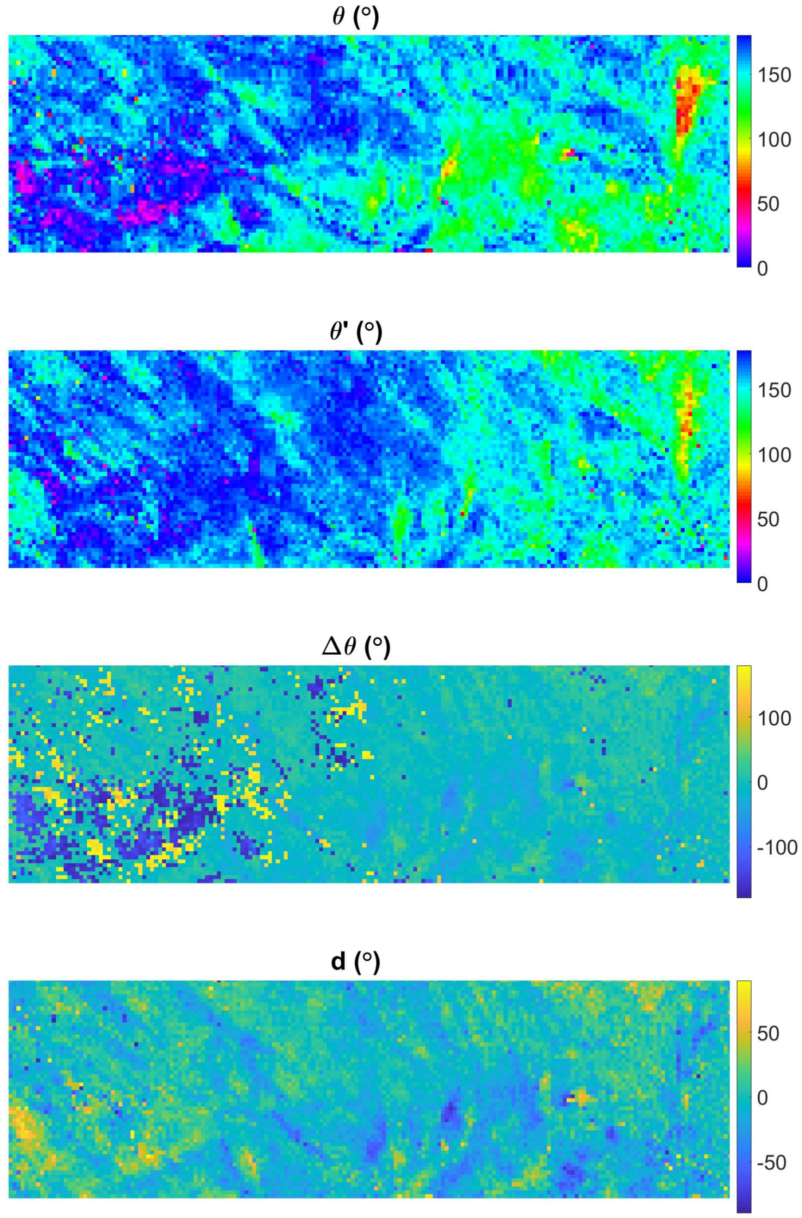

Figure II.11 – Maps of the MPI measured angles θ (top), predicted angles θ' (middle top), the difference between them $\Delta\theta$ (middle bottom) and the distance between them d (bottom). The differences $> \frac{\pi}{2}$ and $< -\frac{\pi}{2}$ seen in $\Delta\theta$ are corrected in the distance map d. Image size: 184×56 pixels, with 100 µm per pixel.

Bibliography

L. Allais, M. Bornert, T. Bretheau, and D. Caldemaison. Experimental characterization of the local strain field in a heterogeneous elastoplastic material. *Acta Metallurgica et Materialia*, 42(11):3865–3880, 1994. doi: 10.1016/0956-7151(94)90452-9.

D. Claire, F. Hild, and S. Roux. A finite element formulation to identify damage fields: the equilibrium gap method. *International Journal for Numerical Methods in Engineering*, 61(2):189–208, 2004. doi: 10.1002/nme.1057.

L.L. Demer and F.C. Yin. Passive biaxial mechanical properties of isolated canine myocardium. *The Journal of Physiology*, 339(1):615–630, 1983. doi: 10.1113/jphysiol.1983.sp014738.

S. Dokos, B.H. Smaill, A.A. Young, and I.A. LeGrice. Shear properties of passive ventricular myocardium. *American Journal of Physiology-Heart and Circulatory Physiology*, 283(6):H2650–H2659, 2002. doi: 10.1152/ajpheart.00111.2002.

M. Genet, C.T. Stoeck, C. von Deuster, L.C. Lee, and S. Kozerke. Equilibrated warping: Finite element image registration with finite strain equilibrium gap regularization. *Medical Image Analysis*, 50:1–22, 2018. doi: 10.1016/j.media.2018.07.007.

M.A. Hassan, M. Hamdi, and A. Noma. The nonlinear elastic and viscoelastic passive properties of left ventricular papillary muscle of a Guinea pig heart. *Journal of the Mechanical Behavior of Biomedical Materials*, 5(1):99–109, 2012. ISSN 17516161. doi: 10.1016/j.jmbbm.2011.08.011.

F. Hild and S. Roux. Digital Image Correlation: from Displacement Measurement to Identification of Elastic Properties - a Review. *Strain*, 42(2):69–80, 2006. doi: 10.1111/j.1475-1305.2006.00258.x.

F. Hild and S. Roux. Comparison of Local and Global Approaches to Digital Image Correlation. *Experimental Mechanics*, 52(9):1503–1519, 2012. doi: 10.1007/s11340-012-9603-7.

J. D. Humphrey, R. K. Strumpf, and F. C. Yin. Biaxial mechanical behavior of excised ventricular epicardium. *American Journal of Physiology-Heart and Circulatory Physiology*, 259(1):H101–H108, 1990. doi: 10.1152/ajpheart.1990.259.1.h101.

P.J. Hunter and A.D. McCulloch. Modelling the mechanical properties of cardiac muscle. *Molecular Biology*, 69:289 – 331, 1998.

E. Héripré, M. Dexet, J. Crépin, L. Gélébart, A. Roos, M. Bornert, and D. Caldemaison. Coupling between experimental measurements and polycrystal finite element calculations for micromechanical study of metallic materials. *International Journal of Plasticity*, 23(9):1512–1539, 2007. doi: 10.1016/j.ijplas.2007.01.009.

C. Jayyosi, J.-S. Affagard, G. Ducourthial, C. Bonod-Bidaud, B. Lynch, S. Bancelin, F. Ruggiero, M.-C. Schanne-Klein, J.-M. Allain, K. Bruyère-Garnier, and M. Coret. Affine kinematics in planar fibrous connective tissues: an experimental investigation. *Biomechanics and Modeling in Mechanobiology*, 16(4):1459–1473, 2017. doi: 10.1007/s10237-017-0899-1.

W. Krasny, C. Morin, H. Magoariec, and S. Avril. A comprehensive study of layer-specific morphological changes in the microstructure of carotid arteries under uniaxial load. *Acta Biomaterialia*, 57:342–351, 2017. doi: 10.1016/j.actbio.2017.04.033.

N. Lenoir, M. Bornert, J. Desrues, P. Bésuelle, and G. Viggiani. Volumetric Digital Image Correlation Applied to X-ray Microtomography Images from Triaxial Compression Tests on Argillaceous Rock. *Strain*, 43(3):193–205, 2007. doi: 10.1111/j.1475-1305.2007.00348.x.

S. Matl, R. Brosig, M. Baust, N. Navab, and S. Demirci. Vascular image registration techniques: A living review. *Medical Image Analysis*, 35:1–17, 2017. doi: 10.1016/j.media.2016.05.005.

E. McEvoy, G.A. Holzapfel, and P. McGarry. Compressibility and Anisotropy of the Ventricular Myocardium: Experimental Analysis and Microstructural Modeling. *Journal of Biomechanical Engineering*, 140(8):081004, 2018. doi: 10.1115/1.4039947.

G. Sommer, D.C. Haspinger, M. Andrä, M. Sacherer, C. Viertler, P. Regitnig, and G.A. Holzapfel. Quantification of Shear Deformations and Corresponding Stresses in the Biaxially Tested Human Myocardium. *Annals of Biomedical Engineering*, 43(10):2334–2348, 2015a. doi: 10.1007/s10439-015-1281-z.

G. Sommer, A..J. Schriefl, M. Andrä, M. Sacherer, C. Viertler, H. Wolinski, and G.A. Holzapfel. Biomechanical properties and microstructure of human ventricular myocardium. *Acta Biomaterialia*, 24:172–192, 2015b. doi: 10.1016/j.actbio.2015.06.031.

N. Tueni, J. Vizet, M. Genet, A. Pierangelo, and J.M. Allain. Microstructural deformation observed by Mueller polarimetry during traction assay on myocardium samples. *Scientific Reports*, 10(1):20531, 2020. doi: 10.1038/s41598-020-76820-w.

Wikipedia. Affine transformation, March 2021. Page Version ID: 1011191615.

Chapter III

Imaging the 3D mesostructure of the myocardium

Abstract

The cardiac tissue multiscale architecture has been investigated for a long time. While most of the studies have focused on the microscale architecture, that is to say the cardiomyocytes, their local organization, and their orientation throughout the ventricles, several studies have tackled the question of the sheetlet scale. This scale has been imaged in longitudinal and transversal sections, and appears to be made of bundles of locally parallel cardiomyocytes, wrapped by a layer of collageneous extra-cellular matrix called the perimysium. Although their structure is somewhat clear, their organization throughout the ventricle remains obscure, due to difficulties in observing them in 3D on the whole volume. In this chapter, we propose a simple optical method, combined with a controlled slicing of the heart to observe the sheetlets and to be able to reconstruct them in volume. This is a joint work with Camille Declerck as a part of her Masters' thesis.

Contents

1 Introduction

1.1 Context

As presented in the Chapter I, the cardiac tissue has a highly complex, multiscale architecture, that can be decomposed into four main scales. Figure III.1 shows three of them: the cell scale (10-100 µm), the sheetlet scale (100-1000 µm), and the tissue scale (1-10 mm). Advances in imaging techniques have allowed the scientific community to increasingly gather information about the cardiac tissue structure at several scales. While the microscale and the macroscale structures are well investigated, the sheetlet structure and organization are still not fully understood.

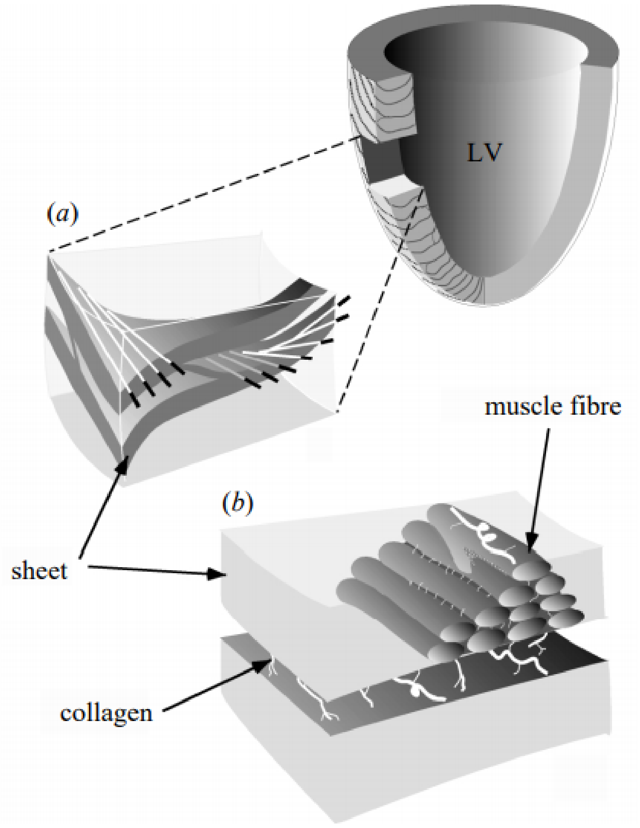

Figure III.1 – Schematic of cardiac microstructure. (a) A transmural block cut from the ventricular wall shows orientation of fibers. Note the transmural variation in fibre angle. (b) The muscle fibers are shown forming a layer three to four cells thick. Endomysial collagen is shown connecting adjacent cells within a sheet, while perimysial collagen links adjacent sheets. Extracted from [Legrice et al., 2001].

1.2 Literature review: imaging of the cardiac structure

In this section, we give a non exhaustive review of the imaging techniques used to image the myocardium at the different scales, with a special focus on their application to the sheetlet scale imaging.

1.2.1 Scanning Electron Microscopy

Scanning Electron Microscopy (SEM) is capable of scanning a surface with a resolution of 1-20 nm, allowing a visualization of the cardiac structure at the subcellular, cellular and sheetlet scale, as shown in Chapter I. It has been widely used to image the cardiac tissue because of its ability to exhibit the details of the microstructure [Legrice et al., 2001; Rossi et al., 1998; Kanzaki et al., 2009, 2010, 2012; Stephenson et al., 2016; Gálfiová et al., 2017; Stephenson et al., 2018].

Figure III.2 shows SEM images (approximately 1×1 mm) performed on decellularized human cardiac tissue. The panels show an intricate structure of endomysial extracellular matrix displaying a honeycomb pattern, wrapping each cardiomyocyte. This figure highlights the importance of the cutting procedure during sample preparation, with clearer information on the left image, as the right one presents sections that are "smashed" during cutting.

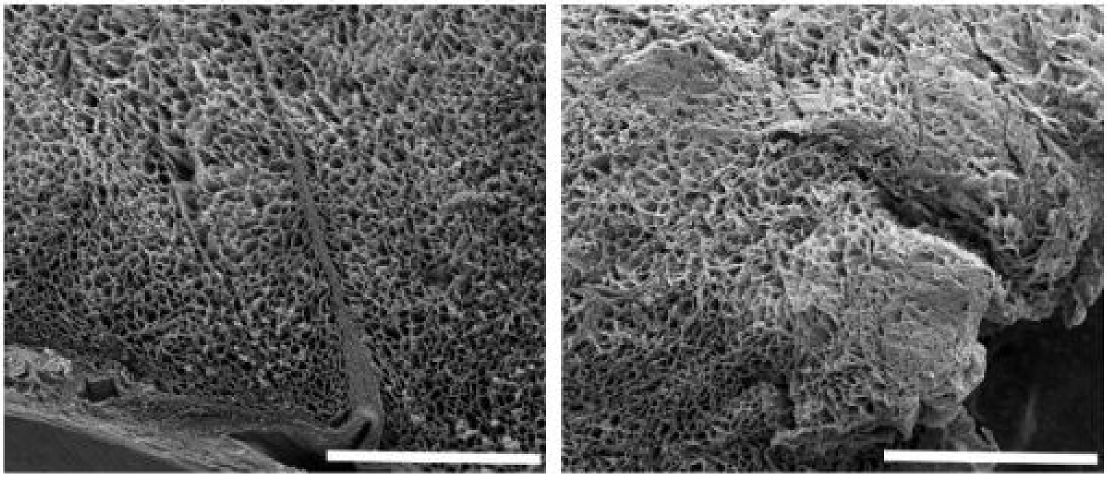

Figure III.2 – Scanning Electron Microscopic Images of the 3D arrangement of the extracellular matrix in a decellularized Human left ventricular tissue. It shows the matrix in cross-section at low magnification. Endomysium is clearly observed and presents a honeycomb shape. The perimysium in not seen (bars : 500 µm). Extracted from [Stephenson et al., 2016].

Figure III.3 also shows SEM images performed on decellularized left ventricle, but with a smaller field of view (approximately 150×150 µm), revealing the differences between the endomysium and the perimysium.

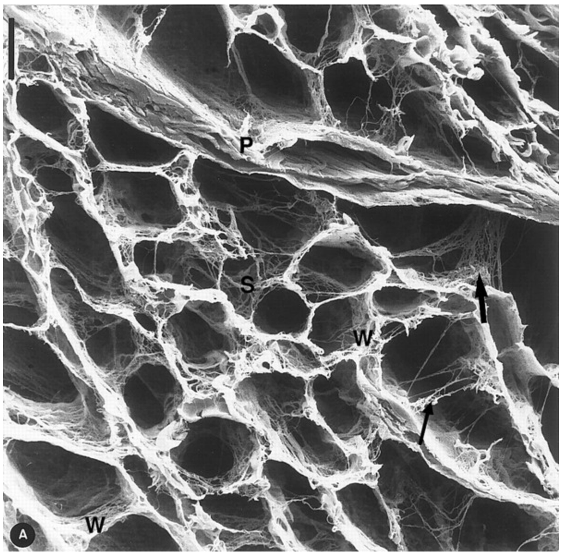

Figure III.3 – Connective tissue skeleton of human heart sectioned transversely. The perimysium (P) envelops groups of myocytes. The endomysium supports and connects individual cells. The endomysial weave (W) envelops each individual myocyte and is connected to adjacent myocytes by lateral endomysial struts (s) presenting branches of variable size and extension. A, Bar : 20 µm. Extracted from [Rossi et al., 1998].

The high-resolution images produced by SEM provide valuable information about the cardiac microstructure. However, this technique presents some disadvantages. The preparation of biological samples (fixation, clearing, etc.) is long, complex, and can result in artifacts. In addition, the images generated by SEM are 2D, they do not provide any information in volume, and have a limited field of view, that only allows a local imaging of the tissue, hence does not permit to grasp the sheetlet organization in the tissue.

1.2.2 Second Harmonic Generation

Second Harmonic Generation (SHG) has emerged as a useful imaging tool to evaluate collagen organization, because the hierarchical structure of collagen fibers produces strong signals. Ex-vivo studies on cardiac tissue were performed [Martin et al., 2013; Petra, 2018; Lopez and Larina, 2019]. In [Sommer et al., 2015], a sample of myocardium was optically cleared to allow a higher SHG penetration depth. It was then imaged, generating a 620×620 µm image, showing a parallel heart muscle fibers (see Figure III.4) in light green, separated by perimysial collagen layers in dark green.

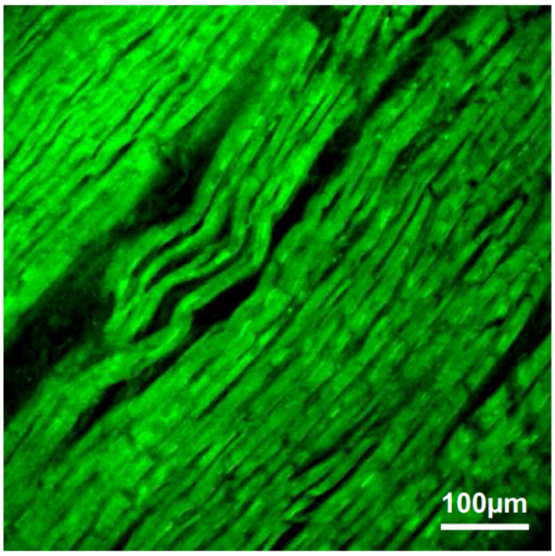

Figure III.4 – SHG image of heart muscle fibers. The cardiomyocytes (in light green) run parallel in the myocardium, surrounded by endomysial and perimysial collagen (in dark green). Gaps might be explained by defects due to cutting procedure. Bar : 100 µm Extracted from [Sommer et al., 2015].

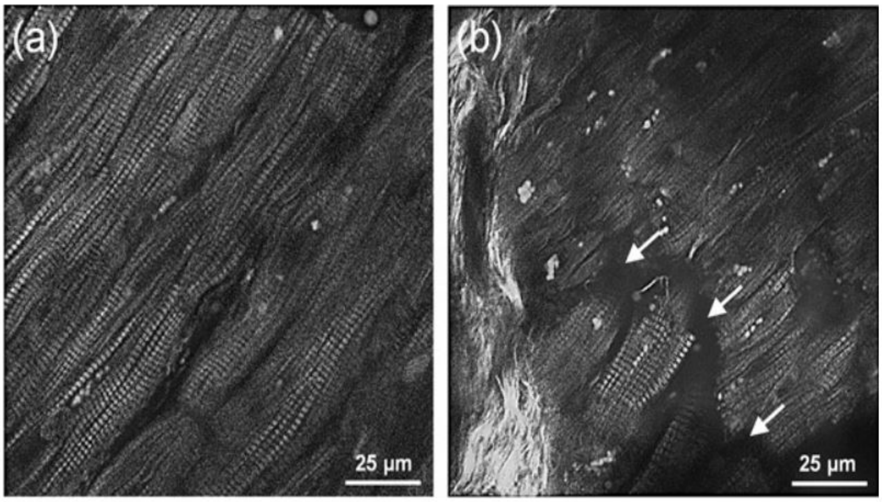

Figure III.5 – SHG image showing striated cardiomyocytes in a (a) physiological tissue, where cardiomyocytes have a well defined parallel orientation and a (b) pathological tissue with degenerative alterations (arrows) and collagen fiber bundles (bright white structures on the left side). Striations due to sarcomeres are observed in both images. Extracted from [Petra, 2018].

SHG has the advantage of imaging relatively large fields of view (1 mm^2 approximately), and of allowing a depth penetration of up to approximately 30 µm. It permits the visualization of the fibrillar structure of collagen as well as the cardiomyocytes and their striated appearance, as observed in Figure III.5, where SHG was performed on a physiological and a pathological tissue. Contrary to Figure III.4, the striated cardiomyocytes are obvious in Figure III.5. This might be due to the clearing performed on the sample prior to imaging in [Sommer et al., 2015]. SHG is time-consuming, and its field of view still not wide enough to image large sections of the heart wall, and to observe the sheetlet organization and orientation.

1.2.3 Confocal microscopy

Confocal microscopy has proved to be a very efficient technique for imaging large fields of cardiac tissue [Young et al., 1998; Sands et al., 2005; Pope et al., 2008]. Confocal images have allowed a quantitative assessment of the tissue components using segmentation, hence generating data on the microstructure of the cardiac tissue and its remodeling [Seidel et al., 2016; Hasaballa et al., 2017]. Figure III.6 shows the 3D organization of ventricular myocardium, achieved by stacking 2D confocal images performed on rat hearts, where the collagen was dyed specifically to distinguish the endomysium and the perimysium from the cardiomyocytes. The laminar structure is clearly visible. The figure shows large lines of collagen, very dense near the endocardium and the epicardium, and extensive gaps called cleavage planes in between.

This method is promising as it allows a 3D visualisation of relatively large blocs of cardiac wall, with detailed mesostructural information. Nonetheless, it requires tissue staining, in order to distinguish the different components. In addition, it necessitates a lot of image acquisition and significant post-processing duration.

1.2.4 Standard optical imaging

One study has attempted to quantify the sheetlet structure organization in the dog left ventricle [Legrice et al., 2001]. The hearts were fixed in a formaldehyde solution, and the ventricles were then divided into "wedge-shaped" segments circumferentially around the heart. The slices were imaged using a CCD camera and the mesostructure orientation was observed and measured.

Figure III.7 shows that the transmural variation of the muscle laminar structure varies between 30° and 90° close to the base, with a sudden increase in the orientations at the extremities (endo-epicardium). The equator and apex regions show a progressive change

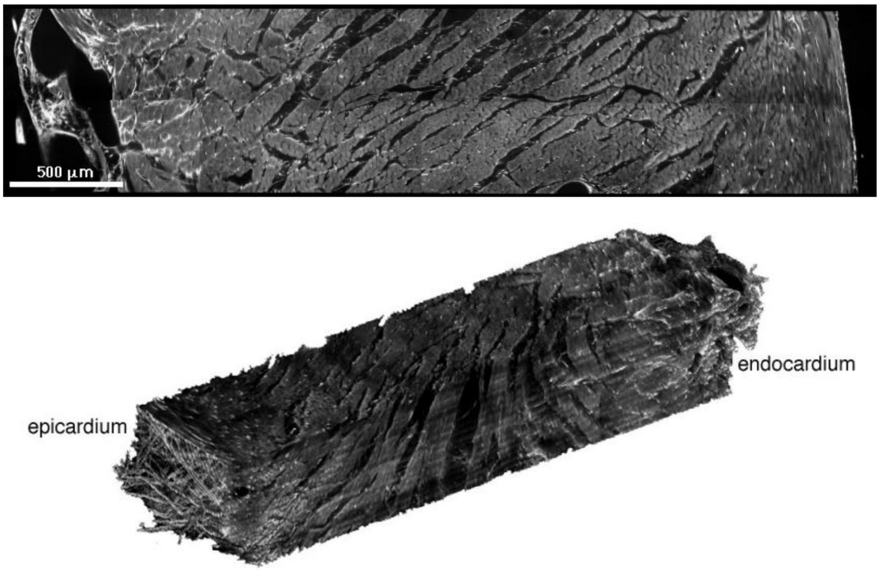

Figure III.6 – Up: Fully registered extended 2D image spanning the left ventricle wall from epicardium to endocardium. Down: Registered 3D projection showing the entire stack volume spanning 3600×800×800 µm. The images show the laminar shape of the sheetlets, and their organization through the wall thickness. Collagen (in white) is denser near endocardium and epicardium. Extracted from [Young et al., 1998].

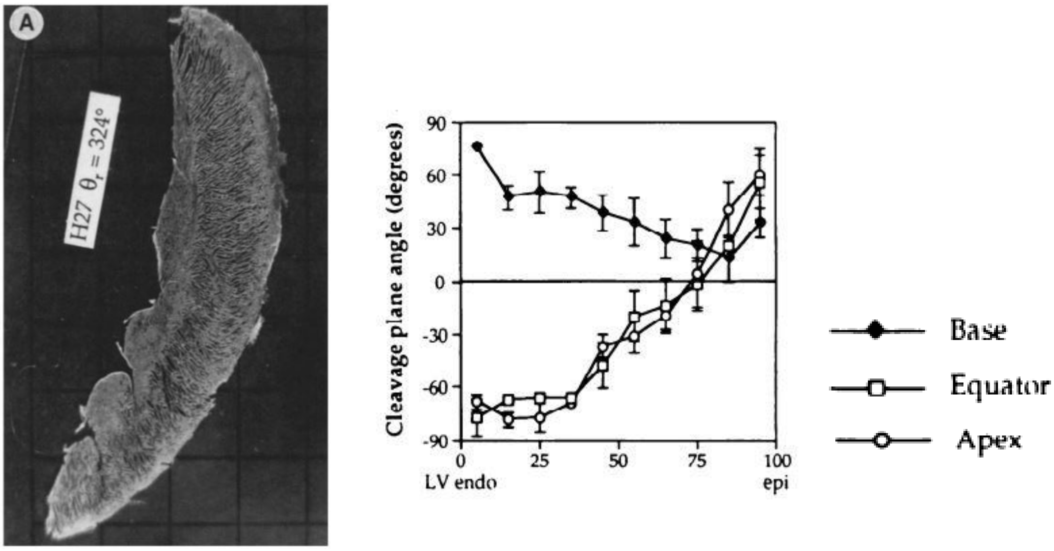

Figure III.7 – Left: Image of transmural section of left ventricle showing typical radial alignment of layers. Right: Transmural variation of structure orientation in left ventricle showing a slight transmural decrease of the laminar structure at the base of the heart, and a linear increase at the heart apex and equator. Extracted from [Legrice et al., 2001].

from around -90° at the endocardium to 30-60° at the epicardium.

1.2.5 Histology

Histology image analysis has been performed on formalin fixed ovine hearts [Kung et al., 2011] and formalin fixed human hearts [Kilner et al., 2015]. Figure III.8 shows histology images of slices cut parallel to the epicardial wall (below left), with parallel laminar structures, and perpendicular to wall sections with a dominant population and a sub-population of laminar structures (see Figure III.8 bottom right).

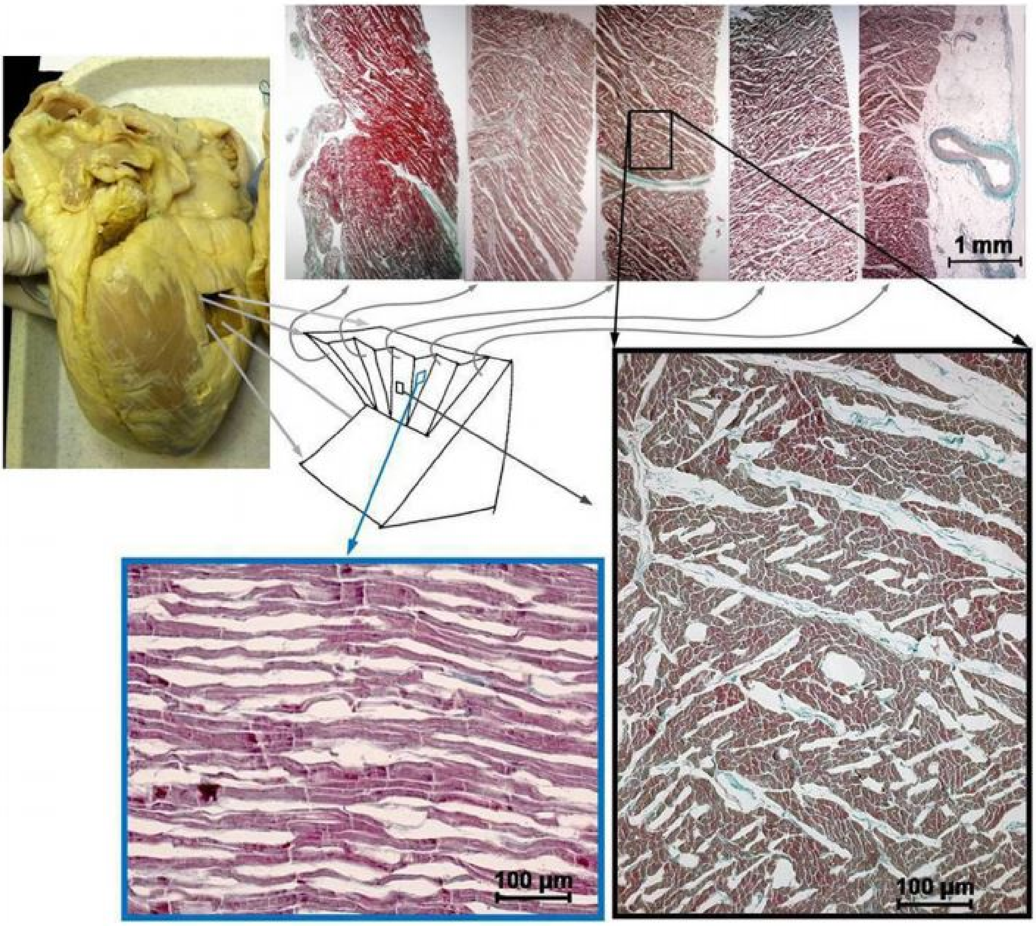

Figure III.8 – Images of human myocardial histology of five tangential slices of a mid lateral block were each sectioned perpendicular to the local myocytes (up). Slices parallel to wall sections show parallel laminar structures (bottom left). Slices perpendicular to wall sections show two populations of laminar structure (bottom right). Extracted from [Kilner et al., 2015].

Histology is efficient in visualizing the cardiac microstructure, and observing the local arrangement of cardiomyocytes and sheetlets. However, it is very invasive, and requires a considerable number of images to reconstitute the whole left ventricle.

1.2.6 Diffusion Tensor - Magnetic Resonance Imaging

Diffusion Tensor Magnetic Resonance Imaging (DT-MRI) is a non-invasive method for measurement of the cardiac architecture. It has a lower resolution than the previously mentioned techniques (300×300 µm), but has the capability to image larger fields. It has been widely used by the cardiac community to image the helical structure of the cardiac fibers, in ex-vivo studies [Scollan et al., 2000; Zhukov and Barr, 2003; Ferreira et al., 2014]. More recently, an in-vivo DT-MRI has been used to vizualise mesostructure [von Deuster et al., 2016]. Figure III.9 shows in-vivo DT-MRI images of the heart at end-systole and late diastole in a healthy patient. As expected, helix-angle distributions are observed, transitioning smoothly between ±70° in the cardiac wall thickness. In addition to its capability of mapping the microscale orientation, DT-MRI has also been used to identify the mesostructure organization in the heart [Rohmer et al., 2007; Nielles-Vallespin et al., 2017]. Figure III.10 shows the changes of sheetlet orientation, for a normal subject, between diastole, where sheetlets are parallel to heart wall, and systole, where they become roughly perpendicular. This technique has proven to be efficient in extracting the cell and sheetlet structure orientation at the tissue scale. It is however costly, and although it can map the sheetlet orientation in the tissue, it does not give any indication about its shape.

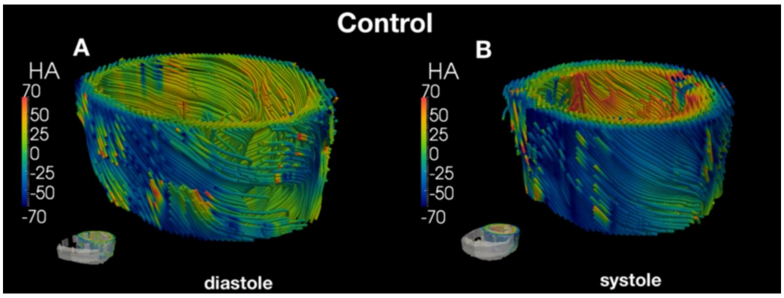

Figure III.9 – Three dimensional visualization of the principal cardiac fiber Helix Angle (HA) directions. Panels A and B show volume of HA for a control patient in late diastole and end systole respectively. Scale bars show color coding for helix angle. Extracted from [Ferreira et al., 2014].

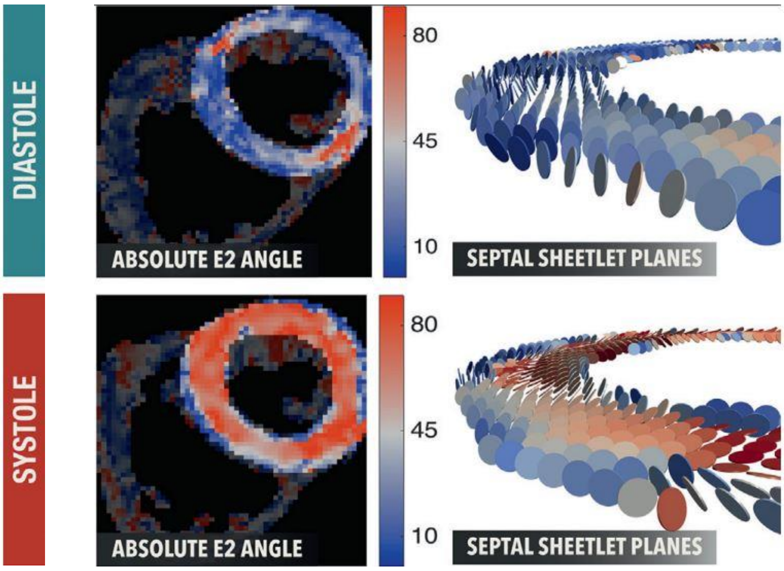

Figure III.10 – 3D glyphs of the sheetlet orientations for a normal subject. Change of orientation between diastole and systole is observed, with sheetlets parallel to heart wall in diastole, and perpendicular to heart wall during systole. Extracted from [Nielles-Vallespin et al., 2017].

1.3 Problematic

To better understand the structure-relationship properties of the cardiac tissue at the sheetlet scale, two important points have to be cleared: What is the shape of the sheetlet structure? How is it organized in the tissue?

In the following, assuming that the sheetlets are in fact locally laminar structures, we propose a protocol in order to investigate the second question, by using fast, high-resolution images of cardiac slices, with the aim of reconstructing a 3D model of the sheetlets at the left ventricular scale. This study was performed in the context of the Masters' thesis of C. Declerck, supervised by J·M. Allain and N. Tueni.

2 Materials & methods

We used 2D cross-section images in order to reconstruct the 3D structure. To do so, we first cut the left ventricles into longitudinal or transverse cross-sections and imaged them using a high definition optical camera. We then processed the images in order to extract the sheetlet orientation and attempted a 3D reconstruction.

2.1 Experimental protocol

The protocol for sample cutting is similar to the one explained in Chapter II. We purchased the hearts at the local butcher, stored them in a cooling box during transportation until we carried out the experiment.

2.1.1 Sample preparation

The left ventricle is approximately a cylindrical object with a local cylindrical coordinate system $(\underline{e_r}, \underline{e_\theta}, \underline{e_z})$. In order to characterize the 3D sheetlet orientation in the left ventricle, we propose to gather the information in the three local directions. Thus, we performed 3 types of sections, each on a different heart (see Figure III.11).

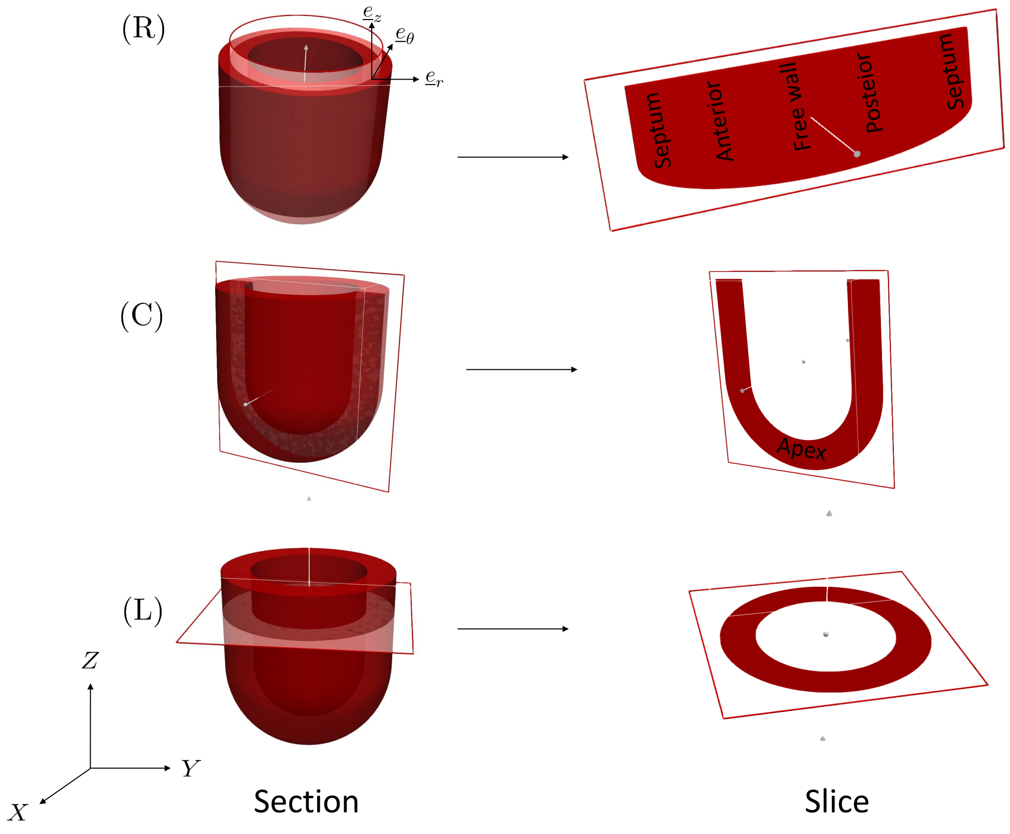

Figure III.11 – Three sections (left) and their corresponding slices (right) are shown: Section R (top) was performed at a fixed radial distance; Section C (middle), at a fixed tangential angle; Section L (bottom), at a fixed vertical distance.

1. Section R was made at a fixed radial distance, in the $(\underline{e_\theta}, \underline{e_z})$ plane, longitudinally to the heart wall (see Figure III.11 top). In order to make this section, the left ventricle was opened as if we are making a flat net of it.

2. Section C was made at a fixed circumferential or tangential angle in the $(\underline{e_r}, \underline{e_z})$ plane (see Figure III.11 middle).

3. Section L was made at a fixed longitudinal distance in the $(\underline{e_r}, \underline{e_\theta})$ plane (see Figure III.11 bottom).

In all three sections, we expected to observe the sheetlet orientation variation through the thickness of the myocardium. For each cross-section, 6 to 10 thin slices were made using the same meat slicing machine as Chapter II, with an average thickness of 1.4 ± 0.27 mm, measured using a digital caliper.

The slices were then marked with black ink, using the same method as in Chapter II Section 3.1.2. The black ink tended to concentrate in the lines that we assumed to be the laminar structures, hence increasing their contrast and visibility. The specimens were then kept in a water-based saline solution to help to maintain the pH and match the osmolarity and the ion concentrations of the pig body.

2.1.2 Imaging

Once the slices were cut and marked, they were imaged (still immerged) with an 8-bit CCD camera (Allied Vision GX 6600, 4384 × 6576 px) connected to a telecentric lens (Opto Engineering TC16M036), generating high definition images with pixels of 5.5 µm. The large field (36×24 mm) combined with the high definition allowed to discern the mesostructure at the tissue scale. The dimensions of the cardiac slices being superior to the field of the imaging system, multiple images of the samples were taken: the sample was positioned on a graph paper and manually translated such that the whole surface was imaged. Both sides of each slice were imaged.

2.2 Post-processing

We performed image stitching, then aligned the different slices, using image registration, in order to reconstruct the left ventricular volume. Finally, we extracted the mesostructure orientation on each of the stitched slices.

2.2.1 Image stitching

In order to reconstruct the entire image, image stitching was done using the *Grid/Collection Stitching* function of the *Image Stitching* plugin of *ImageJ* [Preibisch et al., 2009], that allows to stitch an arbitrary collection or grid of images, given an approximate layout of the tiles.

2.2.2 Image registration

Once the 2D cross-sectional tiles were stitched, image registration was undertaken in order to stack the different slices and reconstruct the volume. The same feature detection technique as in Chapter II Section 3.2.2 was used. Quickly, we selected matching features on each pair of consecutive slices and we used them to compute the transformation matrix $\underline{\underline{M}}$ to superimpose the slices. However, in this study, images of different slices generated by one camera were aligned. Therefore, the scaling parameters were taken equal to 1, and only three parameters, corresponding to the translation and the rotation, were optimized $\underline{p} = \{T_x, T_y, \theta\}$.

2.2.3 Image processing

Image correction. Image correction was achieved by first applying a flat field correction to improve the image quality by correcting the differences of illumination intensities in the field of view. The following operation is applied to each pixel of the raw image:

$$C = (R - D) \times G,$$

where C is the corrected pixel, R the raw pixel, D the offset or the dark field pixel, and G the gain. The *Offset* and *Gain* are evaluated, for each pixel, during a calibration procedure, the offset being the pixel value of the dark image (image captured in the dark), and the gain being the amount of signal given by the detector variation as a function of the amount of light. Once a detector has been appropriately flat-fielded, a uniform signal will create a uniform output image. For this, a flat-field ImageJ function *Pseudo flat field correction* from the *Biovoxxel* plugin [Brocher, 2014] is used.

Orientation extraction. Orientation extraction was performed using the function *OrientationJ Distribution* of the *OrientationJ* plugin in *ImageJ* [Rezakhaniha et al., 2012], to quantitatively analyze the orientations in a sample, by studying the evolution of the structure tensor in a local neighborhood of a point. For each point of the region of interest, a structure tensor is computed, encoding the local orientation, the energy of the tensor and the coherency. The orientation denotes the direction of the structure, or the direction along which the directional derivative is maximized.

3 Results & discussion

3.1 From slicing to orientation extraction

The left ventricles were not frozen nor fixed. Being a soft tissue, when it was pushed against the slicing machine wall, the ventricular wall tended to deform, which led to consecutive slices with very different shapes and sizes. Moreover, we noticed that the border of the layers tended to curl (see Figure III.12) due to residual stresses making it quasi-impossible to obtain clean-cut slices.

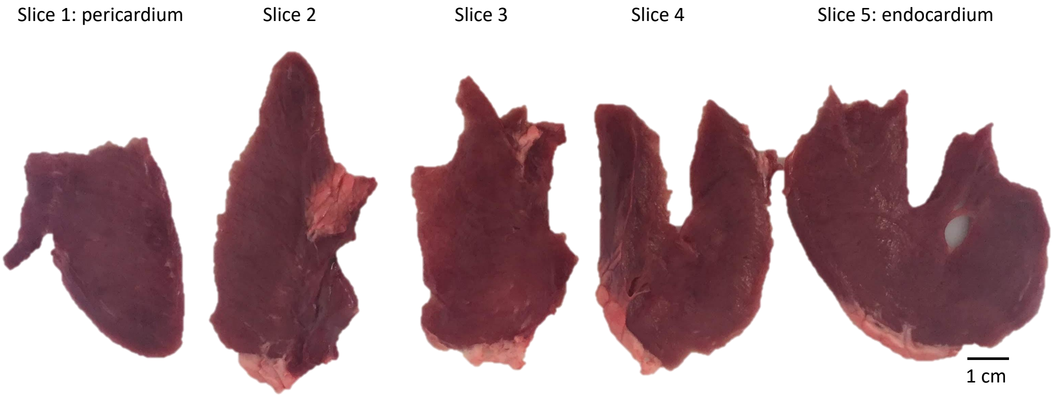

Figure III.12 – Slices obtained by cutting the left ventricle using slicing machine. Observed shapes are very different, due to post-cutting deformations resulting from residual stress.

Figure III.13 shows an image of one tile. The slice was cut longitudinally to the heart wall. Although the ink pattern is not homogeneous, the laminar organization is clearly seen, with the ink coalescing in the striations.

As the images were smaller than the sample, we stitched the adjacent images. Figure III.14 shows one stitched slice. The result shows contrast lines, where the tiles were fused, as well as brightness inhomogeneities. However, the image is clean, and the structures are well discernible. We can clearly observe the orientation variation on this slice.

We then applied a flat field and the orientation extraction filters on these images. Figure III.15 shows the result of the application of the filters on the image. On the left, the *flat-field* filter corrects the image, homogenizing the brightness, and highlighting the

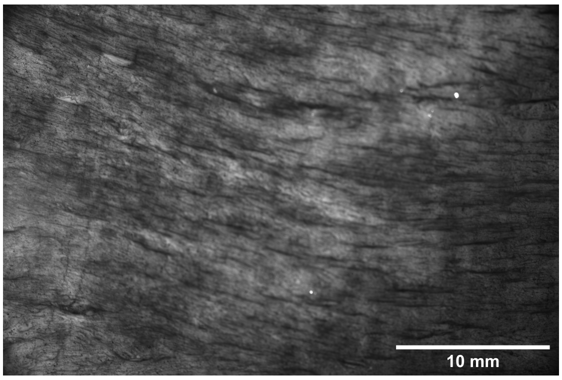

Figure III.13 – Image of one slice of the left ventricle. The ink pattern is very heterogeneous along the surface of the sample. Laminar structure with varying orientation is observed. Dimensions are 6576 × 4384 pixel, with 5.5 µm per pixel.

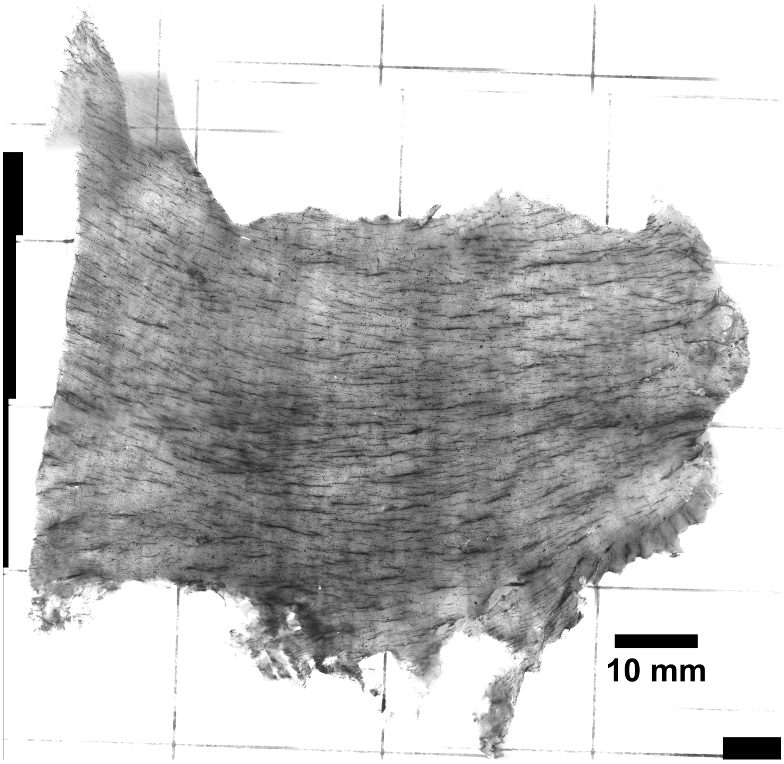

Figure III.14 – Image of a stitched slice. Structure orientation variation is obvious. Brightness inhomogeneities are due to image stitching. Dimensions are 15696 × 13456 pixels.

structures. On the right, the map shows the local orientation of the structures, going from -45° to +45° from left to right. Note that the orientation map has a transparent background and was superimposed on the flat-field image.

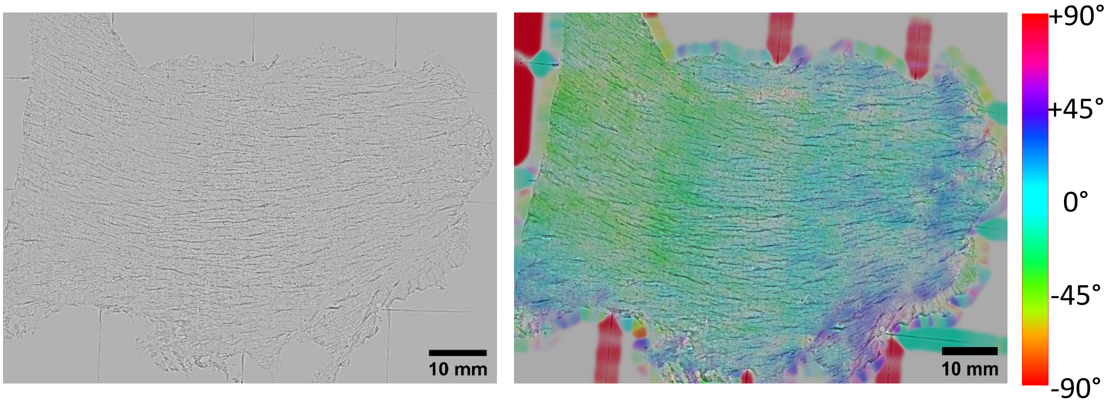

Figure III.15 – Sample image with (left) flat-field correction uniforming the image brightness and underlying structures, (right) orientation extraction map superimposed on left image, showing a dominant horizontal sheetlet orientation.

3.2 Image registration

Image registration was laborious as our slicing method, combined with the residual stress in the tissue, altered the features on the borders, making their identification very difficult. We tried imaging both sides of each slice, expecting that the image of the back of one slice would contain more matching features with the front side of the next, but this method did not help.

Still, a set of translation and rotation parameters T_x, T_y, θ was optimized for each slice. Figure III.16 shows the registration of two consecutive slices cut longitudinally to the cardiac wall. The slices were very deformed, and the matching features were quasi-impossible to find. We therefore aligned the left walls as a preferential feature. This lead to a transformation of a rotation $\theta = 3.4°$, and translation $T_x = 2400$ pixels and $T_y = 800$ pixels. In spite of these difficulties, this method gave promising results.

The problem of deformed samples was even more critical when performing the transversal cross-sections as the slices tended to curl towards the epicardial side due to residual stresses (see Figure III.17, left). We chose to manually straighten the slices, by rotating the curled sections, as a first approximation (see Figure III.17, right). One solution would have been to maintain the natural curvature of the heart by fixing it using a formalin solution, as explained in [Shi et al., 2019].

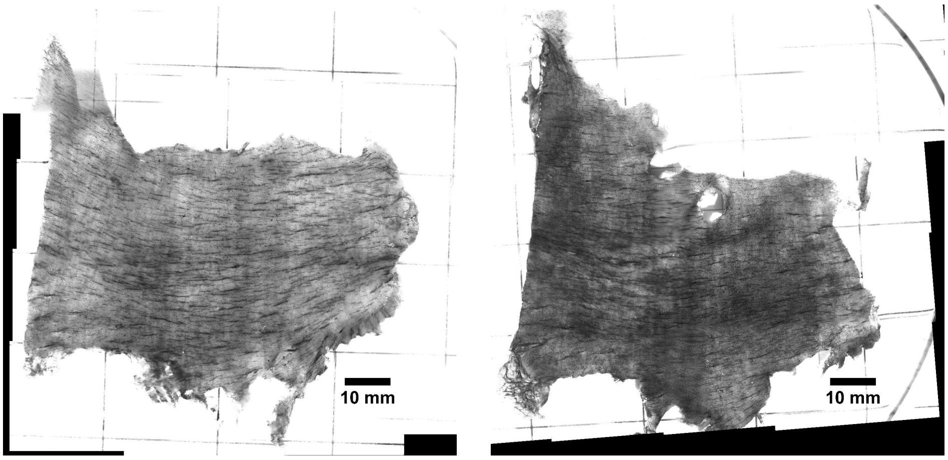

Slice 1

Slice 2

Figure III.16 – Image registration: alignment of two consecutive slices. The slices left wall are used for alignment. Slice 2 is rotated and translated to match Slice 1 (reference image).

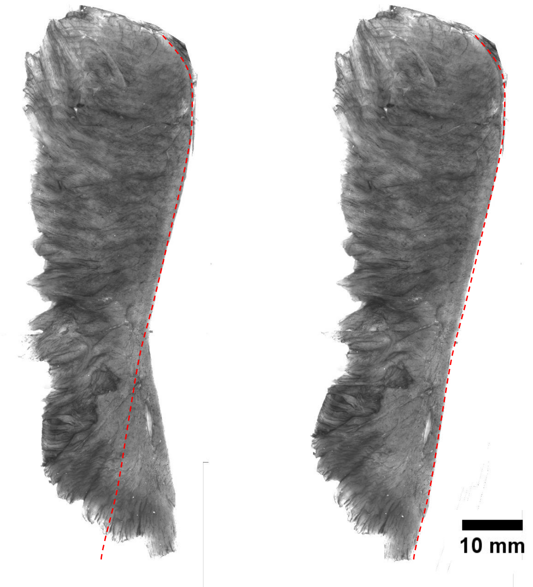

Original image

Straightened image

Figure III.17 – Images of one transversal slice. (left) The slice shows a curling towards the epicardium, due to residual stress. (right) The slice after being manually straightened.

3.3 Sheetlet orientations

Only two sections R and C (see Figure III.11) were analyzed.

3.3.1 Section at fixed radial distance

Figure III.18 shows the local orientations extracted on slices (R) cut at a fixed radial distance. Firstly, we observe a difference of orientations between the slices, with a predominance of blue and green colors close to the epicardium, hence horizontal structures, evolving towards a dominance of red in the slices close to the endocardium (vertical structures). Additionally, we notice that the orientation is quasi-constant for slices 1 and 2, with horizontal structures that gradually become vertical in slices 3, 4 and 5, especially near the base but does not vary much near the apex. Figure III.18 shows the histograms of the orientation distribution associated with each of the maps. As expected, histograms 1 and 2 show peaked distributions centered around 0°. The small peaks at 90° are due to epicardial layer, and are therefore not considered. The histograms flatten gradually, covering the whole range of orientations for slices 3 and 4, with a decrease of the distribution around 0°. This flattening could be due to irregularities in the slicing, causing disparities in the slice thickness homogeneity, and distorting the results, or due to the fact that we did not segment the images, causing a statistical noise in the histograms. However, a plausible cause for the dispersion could simply be the gradual variation of sheetlet orientation through the wall thickness, leading to the endocardium. We notice a slight peak around ±90° in slice 5, which could be explained by a rotation of the sheetlet orientations toward a 90° angle near the endocardium, or by an artifact caused by the slicing. These results are worth further investigations using more precise slicing and sample manipulation.

3.3.2 Section at fixed circumferential angle

Figure III.19 shows the local orientations for 5 slices cut at fixed circumferential angle (C). We first notice that all slices have approximately the same color pattern, which means that the orientations of the sheetlets, at a certain vertical or axial position, are roughly constant. Moreover, we observe important inhomogeneities in each slice. The upper regions of the slices, close to the base, present a slightly decreasing angle in the midwall, and a sudden variation close to the epicardium and the endocardium where the angles reach 45° and 60°. In the mid-region, we observe two populations of sheetlets with opposite orientations at $-45°$ and 45°. In the lower regions, near the base, the negative angles disappear, and the positive sheetlet population becomes dominant, with angles varying between 45° and 90°. Figure III.19 (right) shows the histograms of the orientation distribution associated with each of the maps. We notice that the curved cover all angle range for all of the slices, with a peaks at 90° due to noise on the sides.

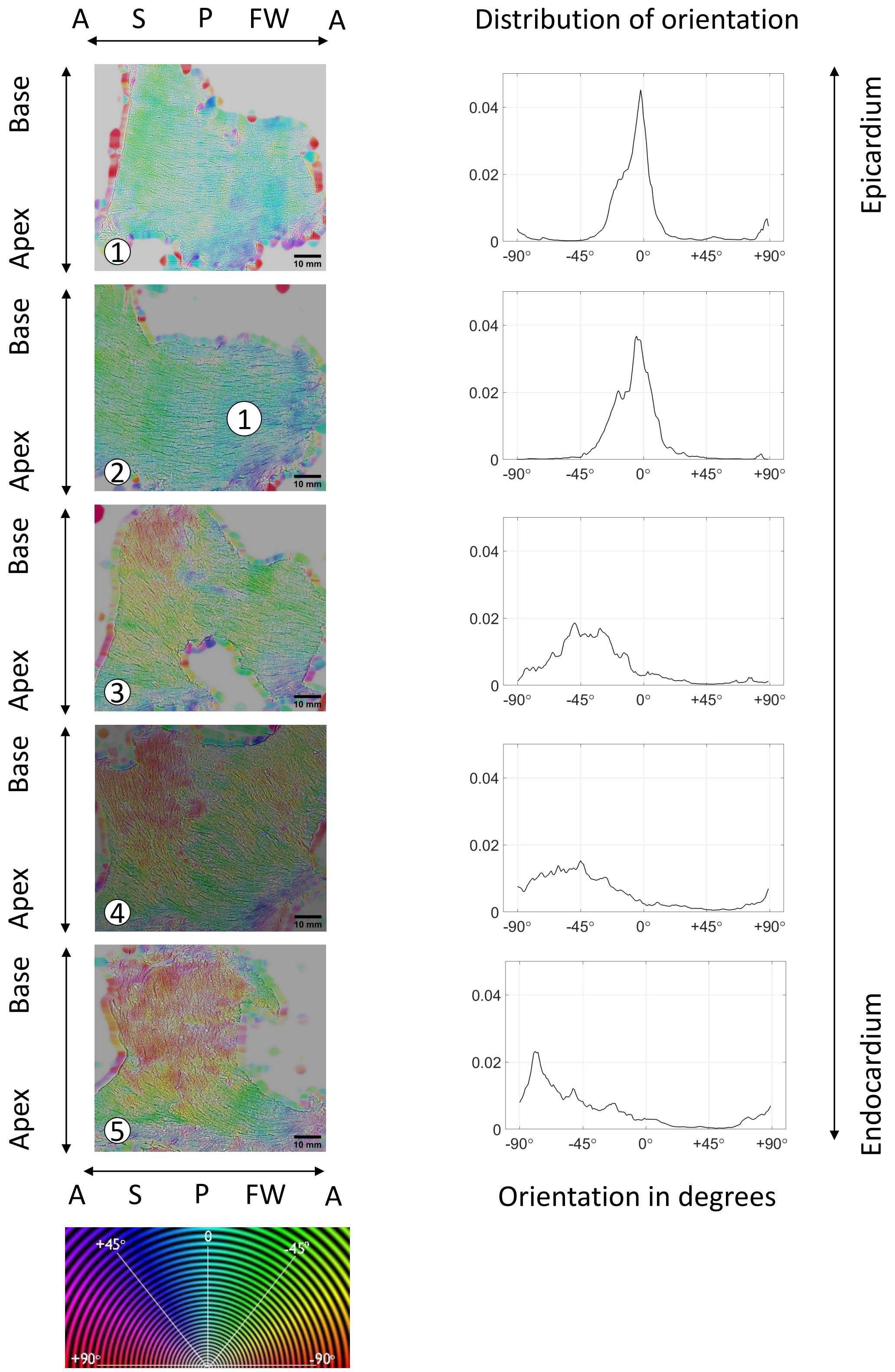

Figure III.18 – Left: Local structural orientations extracted on slices (R) through the heart wall, showing an evolution of the orientation, starting with quasi-horizontal structures near the epicardium, and vertical structures close to the basal endocardium. Right: Histograms showing the evolution of the local orientation distribution through the heart wall in slices (R). The distribution is centered around 0° for slices near the outer wall layer, and flattens as the slices get near to the endocardium. A indicates Anterior, S: Septum, P: Posterior, FW: Free Wall.

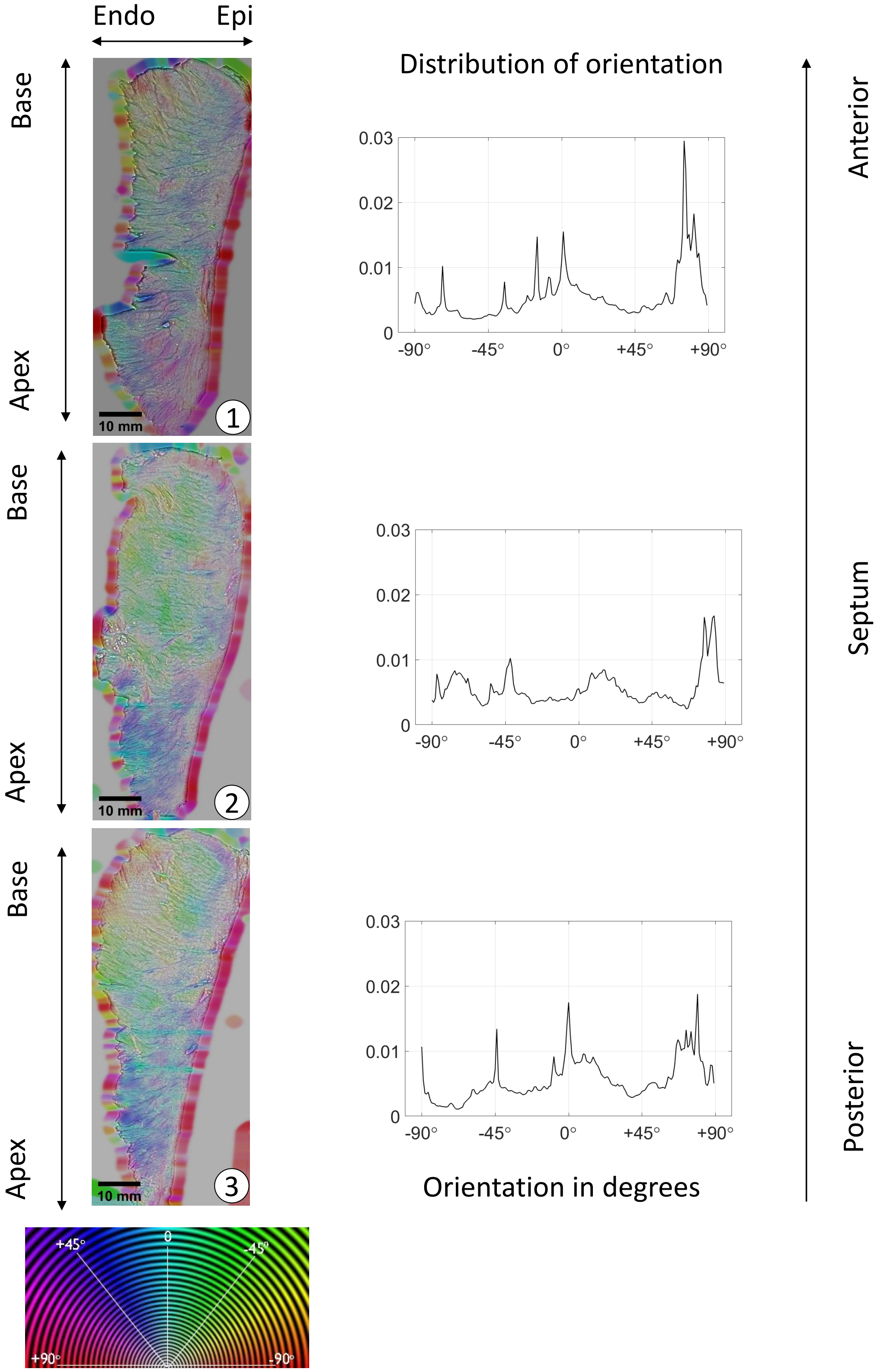
Endo
Epi
Distribution of orientation
Base
Apex
10 mm
1
0.03
0.02
0.01
0
-90°
-45°
0°
+45°
+90°
Anterior
Base
Apex
10 mm
2
Septum
Base
Apex
10 mm
3
Posterior
Orientation in degrees
+45°
0
-45°
+90°
-90°

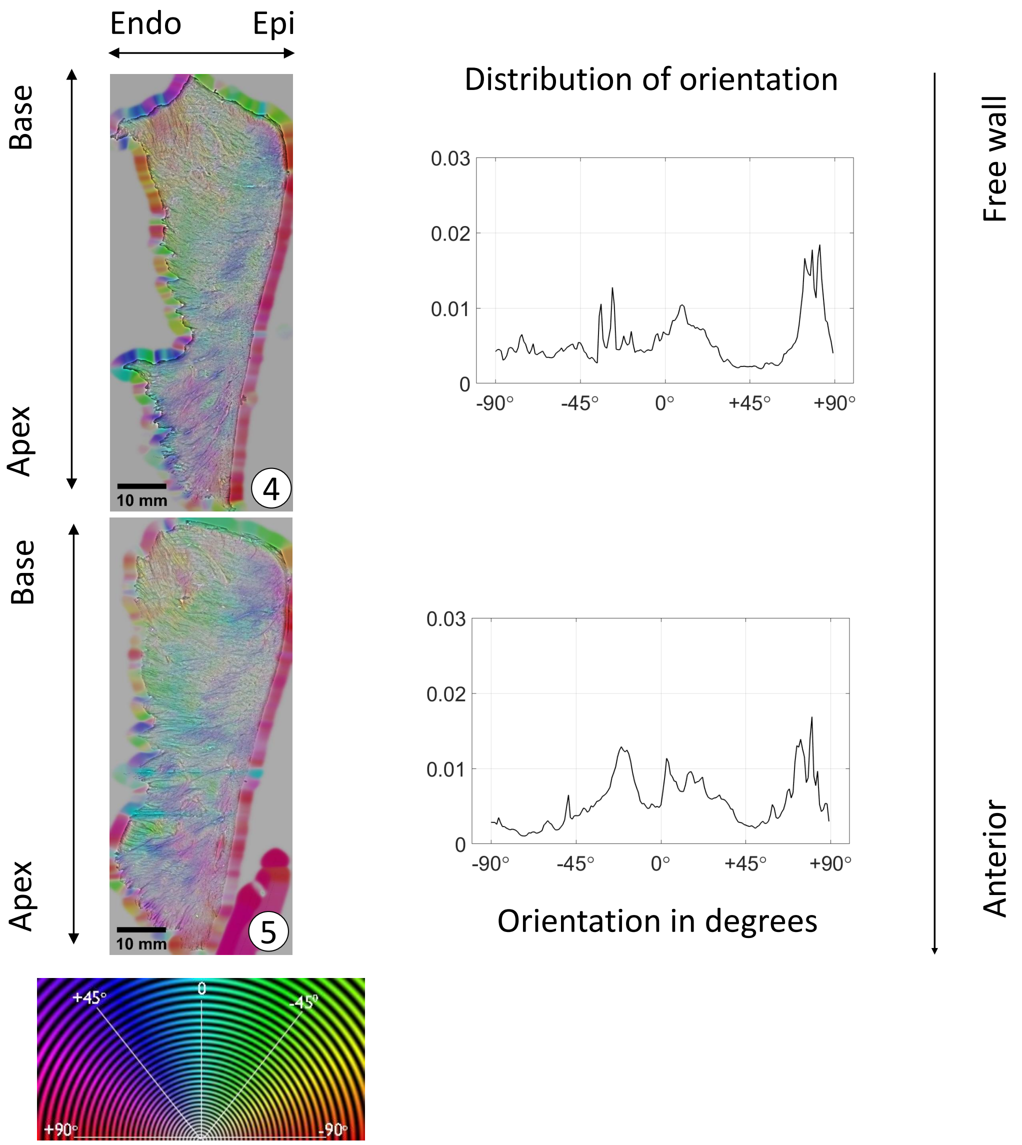

Figure III.19 – Left: Local orientations extracted on slices (C) show a roughly constant pattern for all slices, with a important heterogeneity of sheetlet orientations inside a slice. Right: Histograms showing the evolution of the local orientation distribution through the heart wall in section (C) slices. The peak at 90° is due to epicardial layer orientation, therefore is not considered. The distribution covers the whole angular interval.

3.3.3 Comparison to the literature

Previous studies have investigated this orientation of the sheetlets in the heart and have started to clarify their organization in the cardiac wall. However, as observed in Section 1.2, these methods are either time-consuming, or costly, or display small resolutions compared to other techniques. The main advantage of our method is that it combines a simple, rapid and high-resolution optical method. To our knowledge, this is the first study investigating the sheetlet orientation in slices cut parallel to the epicardium through the heart thickness cross-section (R). The obtained results are promising, and are worth further development by improving the sample preparation and slicing protocol in order to obtain less deformed slices for the registration. Cross-section (C), however, has already been investigated. Our results agree with the observations made by [Kung et al., 2011; Kilner et al., 2015] on the local presence of two populations of sheetlets in the left ventricle, with the presence of a dominant population and a sub-population. Quantitatively, the orientations of the dominant population at the base, equator and apex, are in accordance with the ones observed in [Legrice et al., 2001]. This study shows the feasibility and the limitations of our method, however, it is on no account concluded. Images in the cross-section (L) must be performed, and the information extracted from the three cross-sections should be used to reconstruct the sheetlet orientations in the left ventricle volume.

4 Conclusion

In this study, we suggested a method to investigate the organization of the sheetlets in the left ventricle. The protocol relies on slicing the ventricular wall in cross-sections in three orthogonal planes, marking the slices and imaging them using a high definition camera. An image processing is then performed on the images, in order to extract the local orientation of the structure. This approach allows to obtain stacks of images, containing information about the sheetlet orientation, in the three principal directions of the local coordinate system of the left ventricle $(\underline{e_r}, \underline{e_\theta}, \underline{e_z})$. We were able to carry out the study for two types of sections: the longitudinal one, and the transversal one, and to analyse the observed sheetlet orientations. This study shows interesting preliminary results about the mesostructure orientation in the left ventricle. However, in order to conclude it, the analysis in the vertical cross-sections has to be carried out, in order to obtain the necessary information that would allow to generate a 3D mesostructural model of the ventricle.

Bibliography

Jan Brocher. BioVoxxel Toolbox, 2014.

P.F. Ferreira, P.J. Kilner, L-A. McGill, S. Nielles-Vallespin, A.D. Scott, Siew Y Ho, Karen P McCarthy, Margarita M Haba, Tevfik F Ismail, Peter D Gatehouse, Ranil de Silva, Alexander R Lyon, Sanjay K Prasad, David N Firmin, and Dudley J Pennell. In vivo cardiovascular magnetic resonance diffusion tensor imaging shows evidence of abnormal myocardial laminar orientations and mobility in hypertrophic cardiomyopathy. *Journal of Cardiovascular Magnetic Resonance*, 16(1):87, 2014. doi: 10.1186/s12968-014-0087-8.

P. Gálfiová, S. Polák, R. Mikušová, A. Gažová, D. Kosnáč, T. Barczi, J. Kyselovič, and I. Varga. The three-dimensional fine structure of the human heart: a scanning electron microscopic atlas for research and education. *Biologia*, 72(12):1521–1528, 2017. doi: 10.1515/biolog-2017-0175.

A.I. Hasaballa, G.B. Sands, A.J. Wilson, A.A. Young, V.Y. Wang, Ian J. LeGrice, and Martyn P. Nash. Three-Dimensional Quantification of Myocardial Collagen Morphology from Confocal Images. In M. Pop and G.A. Wright, editors, *Functional Imaging and Modelling of the Heart*, volume 10263, pages 3–12. Springer International Publishing, Cham, 2017. doi: 10.1007/978-3-319-59448-4_1.

Y. Kanzaki, F. Terasaki, M. Okabe, and Y. Kitaura. Three-Dimensional Remodeling of Cardiomyocytes in a Patient With Aortic Stenosis: Scanning Electron Microscopy. *Circulation*, 119(2):e10, 2009. doi: 10.1161/circulationaha.108.809467.

Y. Kanzaki, F. Terasaki, M. Okabe, S. Fujita, T. Katashima, K. Otsuka, and N. Ishizaka. Three-Dimensional Architecture of Cardiomyocytes and Connective Tissue in Human Heart Revealed by Scanning Electron Microscopy. *Circulation*, 122(19):1973–1974, 2010. doi: 10.1161/circulationaha.110.979815.

Y. Kanzaki, Y. Yamauchi, M. Okabe, F. Terasaki, and N. Ishizaka. Three-Dimensional Architecture of Cardiomyocytes and Connective Tissues in Hypertrophic Cardiomyopathy: A Scanning Electron Microscopic Observation. *Circulation*, 125(5):738–739, 2012. doi: 10.1161/circulationaha.111.054668.

P.J. Kilner, K. McCarthy, M. Murillo, P. Ferreira, A.D. Scott, Laura-Ann McGill, Sonia Nielles-Vallespin, Ranil Silva, Dudley J Pennell, Siew Y Ho, and David Firmin.

Histology of human myocardial laminar microstructure and consideration of its cyclic deformations with respect to interpretation of in vivo cardiac diffusion tensor imaging. *Journal of Cardiovascular Magnetic Resonance*, 17(S1):Q10, 2015. doi: 10.1186/1532-429x-17-s1-q10.

G.L. Kung, T.C. Nguyen, A. Itoh, S. Skare, N.B. Ingels, D.C. Miller, and D.B. Ennis. The presence of two local myocardial sheet populations confirmed by diffusion tensor MRI and histological validation. *Journal of Magnetic Resonance Imaging*, 34(5):1080–1091, 2011. doi: 10.1002/jmri.22725.

I. Legrice, P. Hunter, A. Young, and B. Smaill. The architecture of the heart: a data–based model. *Philosophical Transactions of the Royal Society of London. Series A: Mathematical, Physical and Engineering Sciences*, 359(1783):1217–1232, 2001. doi: 10.1098/rsta.2001.0827.

A.L. Lopez and I.V. Larina. Second harmonic generation microscopy of early embryonic mouse hearts. *Biomedical Optics Express*, 10(6):2898, 2019. doi: 10.1364/boe.10.002898.

T.P. Martin, G. Norris, G. McConnell, and S. Currie. A novel approach for assessing cardiac fibrosis using label-free second harmonic generation. *The International Journal of Cardiovascular Imaging*, 29(8):1733–1740, 2013. doi: 10.1007/s10554-013-0270-2.

S. Nielles-Vallespin, Z. Khalique, P.F. Ferreira, R. de Silva, A.D. Scott, P. Kilner, L.A. McGill, A. Giannakidis, P.D. Gatehouse, D. Ennis, E. Aliotta, M. Al-Khalil, P. Kellman, D. Mazilu, R.S. Balaban, D.N. Firmin, A.E. Arai, and D.J. Pennell. Assessment of Myocardial Microstructural Dynamics by In Vivo Diffusion Tensor Cardiac Magnetic Resonance. *Journal of the American College of Cardiology*, 69(6):661–676, 2017. doi: 10.1016/j.jacc.2016.11.051.

B. Petra. Label-free Imaging of Myocardial Remodeling in Atrial Fibrillation Using Nonlinear Optical Microscopy: A Feasibility Study. *Journal of Atrial Fibrillation*, 10 (5):1644, 2018. doi: 10.4022/jafib.1644.

A.J. Pope, G.B. Sands, B.H. Smaill, and I.J. LeGrice. Three-dimensional transmural organization of perimysial collagen in the heart. *American Journal of Physiology-Heart and Circulatory Physiology*, 295(3):H1243–H1252, 2008. doi: 10.1152/ajpheart.00484.2008.

S. Preibisch, S. Saalfeld, and P. Tomancak. Globally optimal stitching of tiled 3D microscopic image acquisitions. *Bioinformatics*, 25(11):1463–1465, 2009. doi: 10.1093/bioinformatics/btp184.

R. Rezakhaniha, A. Agianniotis, J.T.C. Schrauwen, A. Griffa, D. Sage, and C.V.C. Bouten. Experimental investigation of collagen waviness and orientation in the arterial adventitia using confocal laser scanning microscopy. *Biomech Model Mechanobiol*, 11 (461–473):13, 2012. doi: 10.1007/s10237-011-0325-z.

D. Rohmer, A. Sitek, and G.T. Gullberg. Reconstruction and Visualization of Fiber and Laminar Structure in the Normal Human Heart from Ex Vivo Diffusion Tensor Magnetic Resonance Imaging (DTMRI) Data:. *Investigative Radiology*, 42(11):777–789, 2007. doi: 10.1097/rli.0b013e3181238330.

M.A. Rossi, M.A. Abreu, and L.B. Santoro. Connective Tissue Skeleton of the Human Heart: A Demonstration by Cell-Maceration Scanning Electron Microscope Method. *Circulation*, 97(9):934–935, 1998. doi: 10.1161/01.cir.97.9.934.

G.B. Sands, D.A. Gerneke, D.A. Hooks, C.R. Green, B.H. Smaill, and I.J. Legrice. Automated imaging of extended tissue volumes using confocal microscopy. *Microscopy Research and Technique*, 67(5):227–239, 2005. doi: 10.1002/jemt.20200.

D. F. Scollan, A. Holmes, J. Zhang, and R. L. Winslow. Reconstruction of Cardiac Ventricular Geometry and Fiber Orientation Using Magnetic Resonance Imaging. *Annals of Biomedical Engineering*, 28(8):934–944, 2000. doi: 10.1114/1.1312188.

T. Seidel, J.-C. Edelmann, and F.B. Sachse. Analyzing Remodeling of Cardiac Tissue: A Comprehensive Approach Based on Confocal Microscopy and 3D Reconstructions. *Annals of Biomedical Engineering*, 44(5):1436–1448, 2016. doi: 10.1007/s10439-015-1465-6.

X. Shi, Y. Liu, K.M. Copeland, S.R. McMahan, S. Zhang, J.R. Butler, Y. Hong, M. Cho, P. Bajona, H. Gao, and J. Liao. Epicardial prestrained confinement and residual stresses: a newly observed heart ventricle confinement interface. *Journal of The Royal Society Interface*, 16(152):20190028, 2019. doi: 10.1098/rsif.2019.0028.

G. Sommer, A..J. Schriefl, M. Andrä, M. Sacherer, C. Viertler, H. Wolinski, and G.A. Holzapfel. Biomechanical properties and microstructure of human ventricular myocardium. *Acta Biomaterialia*, 24:172–192, 2015. doi: 10.1016/j.actbio.2015.06.031.

M.K. Stephenson, S. Lenihan, R. Covarrubias, R.M. Huttinger, R.J. Gumina, D.B. Sawyer, and C.L. Galindo. Scanning Electron Microscopy of Macerated Tissue to Visualize the Extracellular Matrix. *Journal of Visualized Experiments*, 112:54005, 2016. doi: 10.3791/54005.

R.S. Stephenson, P. Agger, C. Omann, D. Sanchez-Quintana, J.C. Jarvis, and R.H. Anderson. Resolving the True Ventricular Mural Architecture. *J Cardiovasc Dev Dis.*, 5:14, 2018. doi: 10.3390/jcdd5020034.

C. von Deuster, E. Sammut, L. Asner, D. Nordsletten, P. Lamata, Christian T. Stoeck, Sebastian Kozerke, and Reza Razavi. Studying Dynamic Myofiber Aggregate Reorientation in Dilated Cardiomyopathy Using In Vivo Magnetic Resonance Diffusion Tensor Imaging. *Circulation: Cardiovascular Imaging*, 9(10):e005018, 2016. doi: 10.1161/circimaging.116.005018.

A.A. Young, I.J. Legrice, M.A. Young, and B.H. Smaill. Extended confocal microscopy of myocardial laminae and collagen network. *Journal of Microscopy*, 192(2):139–150, 1998. doi: 10.1046/j.1365-2818.1998.00414.x.

L. Zhukov and A.H. Barr. Heart-muscle fiber reconstruction from diffusion tensor MRI. In *IEEE Transactions on Ultrasonics, Ferroelectrics and Frequency Control*, pages 597–602, Seattle, WA, USA, 2003. IEEE. doi: 10.1109/visual.2003.1250425.

Chapter IV

Structural origin of the anisotropy in the myocardium

Abstract

The myocardium is a highly anisotropic material, due to structural inhomogeneities in the tissue. However, the link between the microstructure and the macroscopic mechanical properties is still not fully understood, and it is still not clear at which scale its anisotropy arises from. In order to shed light on this question, we decided to adopt a modeling approach and analyze the macroscopic mechanical behavior of cardiac tissue homogenized from different mesostructures consisting in cardiomyocytes and collagen layers. The anisotropic material behaviour induced by these microstructures was compared to available experimental data. This study confirmed the importance of collagen layers in assuring the tissue's anisotropic response and their organization was proven necessary in reproducing the experimental results.

Contents

1 Introduction

1.1 Context

Knowledge about the passive mechanical properties of the cardiac tissue has evolved over time. Several of the simplest models are based on isotropic elasticity [Demiray, 1976], or transversely isotropic elasticity [Humphrey and Yin, 1987; Costa et al., 2001]. More complex microstructural studies [LeGrice et al., 1995] have observed the cardiac micro and mesostructure, and concluded that the myocardium was made of a laminar hierarchy in which it is possible to identify three axes of symmetry, making it clear that it could not be a transversely isotropic material. Later on, [Dokos et al., 2002; Sommer et al., 2015] implemented a shear experiment to study the anisotropic response of the myocardium. Simple shear was applied to cubic myocardium samples with respect to the three principal material axes (the fiber axis (F), the sheetlet axis (S) and the normal to the fiber-sheetlet plane (N)) as shown in Figure IV.1 (left), in six shear modes. It resulted in six different forces, highlighting the anisotropy in the tissue (see Figure IV.1 (right)) [Dokos et al., 2002]. The deformation that produced an extension of the cardiac fibers (FS, FN) resulted in the highest resistance to shear, and the ones producing an extension in the normal to sheetlet direction (NF, NS) resulted in the lowest resistance to shear.

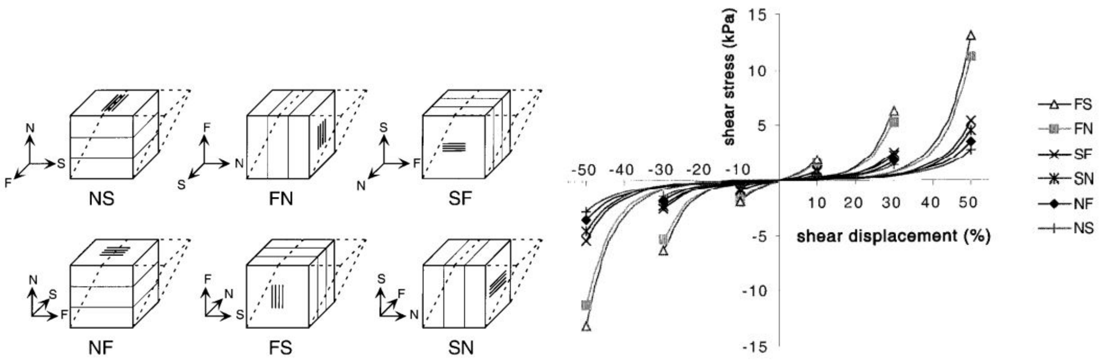

Figure IV.1 – Left: Six possible simple shear modes for an orthotropic myocardium cube defined with respect to the fiber, sheet, and sheet-normal direction. Right: Average shear stress vs. amount of shear behavior of myocardial specimens subjected to each shear mode. Highest shears are observed for modes FS and FS, while lowest shears are observed for modes NF and NS. Extracted from [Dokos et al., 2002].

The microstructural origin of these observations remains unclear, as it may arise either from the rotation of the cardiac fibers in the sample thickness (typically ±36°), or from the orthogonal sheetlets, or from both simultaneously. Experimental approaches will require to manipulate very small samples, and have not been performed up to now to our best knowledge.

1.2 Constitutive modeling of the sheetlet

Various constitutive models have been proposed in the past few decades. Here, we give a non-exhaustive review of the existing models that take into account the sheetlet scale or orientations in the tissue.

We can split the models of the passive properties of the myocardium into two categories:

- Macroscopic models, that comprise phenomenological models based on general observations of the material symmetries and orientations in the tissue, and structure-based models that take into account quantitative information about each constituent in the myocardium.
- Microstructure-based Representative Volumetric Element (RVE) models, where the RVE includes a sampling of all microstructural heterogeneities.

1.2.1 Macroscopic models

Phenomenological models. Phenomenological models of the myocardium are the most common in the literature. Being based on material symmetry in the tissue, they usually employ kinematic invariants. Early invariant-based macroscopic models suppose that the tissue is transversely isotropic, with one preferred direction in the myocardium, the fiber orientation [Humphrey and Yin, 1987], with

$$W = \Psi(I_1, I_4) = c[e^{b(I_1-3)} - 1] + A[e^{a(\sqrt{I_4}-1)^2} - 1],$$

with a, b, c and A material parameters to fit, I_1 is the principal invariant of the Cauchy-Green tensor $\underline{\underline{C}}$, and I_4, the invariant associated with the privileged direction $\underline{\tau}$, such that $I_4 = \underline{\tau} \cdot \underline{\underline{C}} \cdot \underline{\tau}$. The exponential form, used in this model, originally formulated by [Demiray, 1976] is an assumption made to capture the myocardium strong stiffening effect. Other models followed over the years, however, it became more and more clear that the passive behavior could not be fully described by a transversely isotropic model [Schmid et al., 2006, 2008]. Several macroscopic orthotropic models were also developed [Guccione et al., 1991; Costa et al., 2001; Schmid et al., 2006]. More recently, [Holzapfel and Ogden, 2009] proposed a model considering the fiber, the sheetlet and the sheet-normal directions in the tissue (see Figure IV.2). To do so, they used the invariant I_4 of each direction (I_{4f}, I_{4s} and I_{4n}), the coupling invariant I_8, and an isotropic term in I_1, representing a non-collageneous non-muscular matrix. The proposed energy function is given by:

$$\Psi = \frac{a}{2b}e^{b(I_1-3)} + \sum_{i=f,s} \frac{a_i}{2b_i}(e^{b_i(I_{4i}-1)^2} - 1) + \frac{a_{fs}}{2b_{fs}}(e^{b_{fs}I_8^2} - 1),$$

where the material parameters a, a_f, a_s and a_{fs} have the dimension of stress and b, b_f, b_s and b_{fs} are dimensionless. I_{4n} has been omitted because of its dependency on I_{4f} and I_{4s} due to the relation: $\sum_{i=f,s,n} I_{4i} = I_1$.

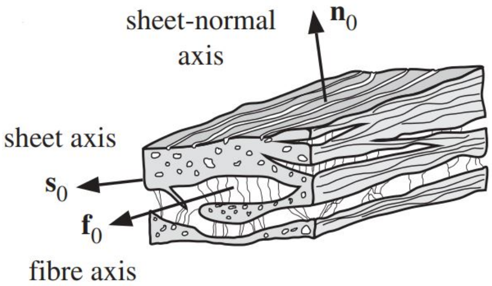

Figure IV.2 – The layered organization of myocytes and the collagen fibres between the sheets referred to a right-handed orthonormal coordinate system with fibre axis $\mathbf{f}_0$, sheet axis $\mathbf{s}_0$ and sheet-normal axis $\mathbf{n}_0$. Extracted from [Holzapfel and Ogden, 2009].

Although these models give a fairly good description of the macroscopic mechanical properties of the cardiac tissue, they lack microstructural information, hence cannot account for any changes occurring at the smaller scales. Invariants used to describe the sheetlet scale cannot explicitly take into consideration the extracellular matrix thickness or organization evolution. In order to do so, models containing quantitative information about the composition and microstructure of the myocardium.

Structure-based models. Structure-based models take into account detailed compositional and structural information about the tissue constituents, separating their mechanical contributions, and accounting for the interactions between them [Lanir, 1983; Horowitz et al., 1988; Humphrey and Yin, 1989]. Relatively recent structure-based models have been developed [Avazmohammadi et al., 2017]. They used histological images to quantify the orientation distributions and volume fraction ϕ of the cardiomyocytes, denoted m, collagen fibers, denoted c and amorphous ground matrix denoted g. The strain-energy density function is the sum of the contributions of each of the constituents m, c and g, and the interactions between them i. The energy contributions takes into account the orientation distribution of each of the constituents.

$$W = \phi^g \Psi^g(C) + \phi^m \Psi^m(C) + \phi^c \Psi^c(C) + \Psi^i(C).$$

Although promising, structure-based models are complex, as they contain a large number of parameters that require microstructural parameters difficult to obtain. Moreover, these models focus on the microstructure at the cellular scale, and do not straightforwardly represent the sheetlet scale at the moment.

1.2.2 Microstructural models

Microstructural modeling consists in identifying a heterogeneous RVE and determining its homogeneous mechanical properties from known characteristics of its constituents. This allows to generate the resulting properties of the material at the macroscale. Micro-models for the cardiac tissue are sparse, probably due to the complexity of the tissue organization, and to the difficulty in identifying a suitable RVE.

The work of [McEvoy et al., 2018] proposed a microstructural model of the myocardium, generating an RVE (see Figure IV.3) based on histological studies, containing layers of parallel cardiomyocytes, surrounded by a layer of endomysium (ECM 1) comprising vasculature. The layers are separated by perimysial collagen (ECM 2). Collagen and cardiomyocytes are represented by a compressible hyperelastic model [Nolan et al., 2014] that takes into account the collagen fiber dispersion. The presence of an underlying isotropic material is also supposed, and is described by a neo-hookean model. In order to investigate the compressibility of the myocardium, the RVE is subjected to confined compression and shows that at an applied strain of 0.05, the vasculature volume decreases by 6.2%, ECM 1 by 6.98%, ECM 2 by 6.2% and the cardiomyocytes by 0.5%. Moreover, under such loading, all the fibers shorten, and the stress is governed by the isotropic elastic behavior of the cardiomyocytes and extracellular matrix. Six modes of shear deformation are then applied to the RVE, such as shown in Figure IV.1. The obtained shear behavior corresponds to the ones obtained previously by [Dokos et al., 2002; Sommer et al., 2015], with both the shear stiffening and the good order in the stresses (FS>FN≥SF>SN>NF≅NS). The non-linear responses to shear in NS and NF are shown to be dependent on the endomysial and perimysial collagen dispersion. The shear responses in SN and SF are also due to the perimysial fibers aligned with the sheetlet direction, and the high stresses observed in FS and FN are caused by the cardiomyocytes, with a higher stress for FS due to the dispersion of the perimysial extracellular matrix.

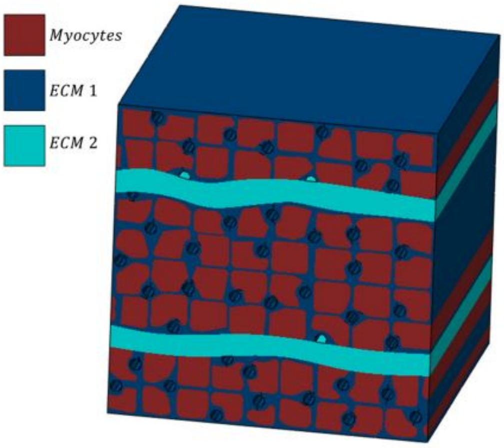

Figure IV.3 – Representative volumetric element of the myocardium with discrete regions for the cardiomyocytes, the matrix surrounding the cells (ECM 1), and the matrix surrounding the myocardial sheets (ECM 2). Capillaries are included as empty vessels. Extracted from [McEvoy et al., 2018].

To our knowledge, this is the only micro mechanical model to describe the cardiac tissue passive mechanical properties, maybe due to its high computational cost. Nonetheless, such models are essential for understanding the fundamental mechanisms underlying the complex multiscale properties of healthy and diseased cardiac tissue.

1.3 Problematic: origin of the anisotropy

One fundamental macroscopic property of the cardiac tissue is its anisotropy. Though it has been experimentally proven, and used in computational models, its structural origin has not been fully investigated yet, and the scale at which it is induced is unclear. Is the variation of the cardiomyocyte orientation sufficient to induce the observed anisotropy in [Dokos et al., 2002; Sommer et al., 2015]? If not, is the anisotropy achieved by the presence of mesoscopic extracellular matrix layers? On top of this uncertainty, the spatial organization, at the mesoscale, represents a structural complexity: it is often considered to be laminar, however, ellipsoidal clusters of cells, wrapped by perimysium, have been observed as well. To investigate these questions, we construct a mesoscale model, made of different configurations of cardiomyocytes and extracellular matrix. However, having only macroscopic experimental data, we perform linear homogenization given an initial set of parameters, and use the homogenized material properties at the macroscale, on which we performed macroscopic mechanical assays. Our main objective was to identify the mesostructure that best fits macroscopic experimental by optimizing the material parameters.

1.4 Recalls of periodic linear homogenization

The cardiac tissue being heterogeneous, made of different constituents with different material properties, its homogenized mechanical properties at the macroscale will depend on the coefficients of the constituents. Initially, homogenization techniques were based on the Hill-Mandel lemma which separates the material into two scales (a fast, periodic microscale, and a slow macroscale), and connects the mechanical energies of both scales [Hill, 1963; Mandel, 1972]. Later developments showed that the result can be recovered using a two-scale expansion method [Sanchez-Palencia, 1974; Michel et al., 1999].

When a macroscopic displacement $\underline{u} = \underline{\underline{\epsilon}} \cdot \underline{x}$ is imposed on the periodic mesostructure Ω, the strain and stress fields of the homogenized medium will be uniform:

$$\underline{\underline{\epsilon}} = \bar{\underline{\underline{\epsilon}}} \quad \text{and} \quad \underline{\underline{\sigma}} = \bar{\underline{\underline{\sigma}}}.$$

However, in the mesostructure with several phases, the fields are not homogeneous. They can be viewed as the superposition of the mean value and a periodic solution:

$$\underline{u}(\underline{x}) = \bar{\underline{\underline{\epsilon}}} \cdot \underline{x} + \underline{v}(\underline{x}), \qquad \underline{\underline{\epsilon}}(\underline{u}(\underline{x})) = \bar{\underline{\underline{\epsilon}}} + \underline{\underline{\epsilon}}(\underline{v}(\underline{x})), \qquad \underline{v}(\underline{x}) \quad \text{periodic}, \tag{IV.1}$$

where $\underline{\underline{\epsilon}}(\underline{u}(\underline{x}))$ is the local deformation field, composed of the imposed strain $\bar{\underline{\underline{\epsilon}}}$ and a fluctuating one $\underline{\underline{\epsilon}}(\underline{v}(\underline{x}))$. The periodicity of v implies that $\langle \underline{\underline{\epsilon}}(\underline{v}(\underline{x})) \rangle = \underline{0}$ and $\langle \underline{\underline{\epsilon}} \rangle = \bar{\underline{\underline{\epsilon}}}$, $\langle . \rangle$ being the volume average. In a linear elasticity setting, when the components have a stiffness matrix $\underline{\underline{\underline{\underline{C}}}}(\underline{x})$, this amounts to solving the following problem on Ω:

$$\text{Given } \bar{\underline{\underline{\epsilon}}}, \text{ find } \underline{v} \text{ such that : } \begin{cases} \underline{\mathrm{div}}(\underline{\underline{\sigma}}(\mathrm{x})) = \underline{0} & \text{in } \Omega, \\ \underline{\underline{\sigma}}(\underline{x}) = \underline{\underline{\underline{\underline{C}}}}(\underline{x}) : \underline{\underline{\epsilon}}(\underline{u}(\underline{x})) & \text{in } \Omega, \\ \underline{v}(\underline{x}) \quad \text{periodic.} \end{cases} \tag{IV.2}$$

This problem has a unique solution $\underline{v}$ for a given deformation $\bar{\underline{\underline{\epsilon}}}$. From the Hill-Mandel principle stating that the microscopic and macroscopic energies are equivalent, we obtain:

$$\frac{1}{2}\ \left\langle \underline{\underline{\epsilon}} : \underline{\underline{\underline{\underline{C}}}} : \underline{\underline{\epsilon}} \right\rangle = \frac{1}{2}\bar{\underline{\underline{\epsilon}}} : \left\langle \underline{\underline{\underline{\underline{C}}}} \right\rangle : \bar{\underline{\underline{\epsilon}}}, \tag{IV.3}$$

where $\left\langle \underline{\underline{\underline{\underline{C}}}} \right\rangle$ represents the homogenized elasticity tensor. Its components can be computed by solving the system (IV.2) for elementary load cases corresponding to the different components of $\bar{\underline{\underline{\epsilon}}}$.

1.5 Recalls of parameter bounds in linear elasticity

The stiffness matrix $\underline{\underline{\underline{\underline{C}}}}$ presented in the previous section is comprised of the material parameters associated with each of the constituents in the tissue. In order to identify these parameters, it is of the utmost importance to determine their bounds. In the following, we give a review on the parameter bounds in isotropic, transverse isotropic and orthotropic materials.

In the linear elastic setting, the material law can be written using the so called engineering notation [Cowin, 1989]:

$$\widehat{\underline{\sigma}} = \widehat{\underline{\underline{C}}} \cdot \widehat{\underline{\epsilon}} \qquad \text{or} \qquad \widehat{\underline{\epsilon}} = \widehat{\underline{\underline{\mathsf{S}}}} \cdot \widehat{\underline{\sigma}}, \tag{IV.4}$$

with $\widehat{\underline{\sigma}} \equiv \underline{\underline{\sigma}}$, $\widehat{\underline{\epsilon}} \equiv \underline{\underline{\epsilon}}$, $\widehat{\underline{\underline{C}}} \equiv \underline{\underline{\underline{\underline{C}}}}$, $\widehat{\underline{\underline{S}}} \equiv \underline{\underline{\underline{\underline{S}}}}$,

$$\widehat{\underline{\sigma}} = \begin{pmatrix} \sigma_{11} \\ \sigma_{22} \\ \sigma_{33} \\ \sqrt{2}\sigma_{23} \\ \sqrt{2}\sigma_{13} \\ \sqrt{2}\sigma_{12} \end{pmatrix}, \quad \widehat{\underline{\epsilon}} = \begin{pmatrix} \epsilon_{11} \\ \epsilon_{22} \\ \epsilon_{33} \\ \sqrt{2}\epsilon_{23} \\ \sqrt{2}\epsilon_{13} \\ \sqrt{2}\epsilon_{12} \end{pmatrix},$$

$$\widehat{\underline{\underline{S}}} = \begin{pmatrix} S_{1111} & S_{1122} & S_{1133} & 0 & 0 & 0 \\ S_{2211} & S_{2222} & S_{2233} & 0 & 0 & 0 \\ S_{3311} & S_{3322} & S_{3333} & 0 & 0 & 0 \\ 0 & 0 & 0 & 2S_{2323} & 0 & 0 \\ 0 & 0 & 0 & 0 & 2S_{3131} & 0 \\ 0 & 0 & 0 & 0 & 0 & 2S_{1212} \end{pmatrix}, \quad \text{and} \quad \widehat{\underline{\underline{C}}} = \widehat{\underline{\underline{S}}}^{-1},$$

where the compliance matrix $\underline{\underline{\widehat{S}}}$ and the stiffness matrix $\underline{\underline{\widehat{C}}}$ are symmetric, definite positive. This requires that the diagonal terms of the matrices are positive [Lempriere, 1968]. For an incompressible material, in addition to the previous conditions, the condition for incompressibility is a null trace of strain tensor [Loredo and Klöcker, 1997; Garcia et al., 1998].

1.5.1 Isotropic materials

For an isotropic material, a material with properties that are independent of the direction of examination,

$$\underline{\underline{\widehat{S}}} = \begin{pmatrix} \frac{1}{E} & \frac{-\nu}{E} & \frac{-\nu}{E} & 0 & 0 & 0 \\ \frac{-\nu}{E} & \frac{1}{E} & \frac{-\nu}{E} & 0 & 0 & 0 \\ \frac{-\nu}{E} & \frac{-\nu}{E} & \frac{1}{E} & 0 & 0 & 0 \\ 0 & 0 & 0 & \frac{1}{2G} & 0 & 0 \\ 0 & 0 & 0 & 0 & \frac{1}{2G} & 0 \\ 0 & 0 & 0 & 0 & 0 & \frac{1}{2G} \end{pmatrix},$$

with E the Young modulus, or the modulus of elasticity, ν the material's Poisson ratio and G the shear modulus such that $G = \frac{E}{2(1+\nu)}$. The eigenvalues of $\underline{\underline{\widehat{S}}}$ are

$$\lambda_{\underline{\underline{\widehat{S}}}} = \{\frac{1-2\nu}{E}, \frac{1+\nu}{E}, \frac{1+\nu}{E}, 2(1+\nu), 2(1+\nu), 2(1+\nu)\}. \tag{IV.5}$$

The positivity of $\underline{\underline{\widehat{S}}}$ in the isotropic case hence leads to conditions on E and ν, with

$$E > 0 \qquad \text{and} \qquad -1 < \nu < \frac{1}{2}. \tag{IV.6}$$

For an isotropic incompressible material in small strain, the condition for incompressibility is a null trace of the strain tensor [Loredo and Klöcker, 1997; Garcia et al., 1998] which translates into:

$$tr(\underline{\epsilon}) = 0 \quad \forall\, \underline{\sigma}, \tag{IV.7}$$

we thus obtain (no summation on i):

$$S_{11ii} + S_{22ii} + S_{33ii} = 0 \quad \forall\, i = 1, 2, 3, \tag{IV.8}$$

leading to

$$\frac{1}{E} - \frac{\nu}{E} - \frac{\nu}{E} = 0.$$

Hence, for an incompressible isotropic material,

$$\nu = 0.5. \tag{IV.9}$$

1.5.2 Transverse isotropic materials

A transverse isotropic material has the same properties in one plane, and different properties in the direction normal to this plane. In an orthogonal system $(\underline{e_1}, \underline{e_2}, \underline{e_3})$, with $\underline{e_1}$ symmetry axis, its compliance matrix is written such that:

$$\underline{\underline{\widehat{S}}} = \begin{pmatrix} \frac{1}{E_1} & \frac{-\nu_{12}}{E_1} & \frac{-\nu_{12}}{E_1} & 0 & 0 & 0 \\ \frac{-\nu_{21}}{E_2} & \frac{1}{E_2} & \frac{-\nu_{22}}{E_2} & 0 & 0 & 0 \\ \frac{-\nu_{21}}{E_2} & \frac{-\nu_{22}}{E_2} & \frac{1}{E_2} & 0 & 0 & 0 \\ 0 & 0 & 0 & \frac{1}{2G_{22}} & 0 & 0 \\ 0 & 0 & 0 & 0 & \frac{1}{2G_{12}} & 0 \\ 0 & 0 & 0 & 0 & 0 & \frac{1}{2G_{12}} \end{pmatrix},$$

where

$$G_{22} = \frac{E_2}{2(1+\nu_{22})} \tag{IV.10}$$

and, due to the symmetry of $\underline{\underline{\widehat{S}}}$,

$$\frac{-\nu_{12}}{E_1} = \frac{-\nu_{21}}{E_2}. \tag{IV.11}$$

Its stiffness matrix can be written such that:

$$\underline{\underline{\widehat{C}}} = \begin{pmatrix} \frac{1-\nu_{22}^2}{E_2^2\Delta} & \frac{\nu_{12}(1+\nu_{22})}{E_2^2\Delta} & \frac{\nu_{12}(1+\nu_{22})}{E_2^2\Delta} & 0 & 0 & 0 \\ \frac{\nu_{12}(1+\nu_{22})}{E_2^2\Delta} & \frac{1-\nu_{12}\nu_{21}}{E_1E_2\Delta} & \frac{\nu_{22}+\nu_{21}\nu_{12}}{E_1E_2\Delta} & 0 & 0 & 0 \\ \frac{\nu_{12}(1+\nu_{22})}{E_2^2\Delta} & \frac{\nu_{22}+\nu_{21}\nu_{12}}{E_1E_2\Delta} & \frac{1-\nu_{12}\nu_{21}}{E_1E_2\Delta} & 0 & 0 & 0 \\ 0 & 0 & 0 & 2G_{22} & 0 & 0 \\ 0 & 0 & 0 & 0 & 2G_{12} & 0 \\ 0 & 0 & 0 & 0 & 0 & 2G_{12} \end{pmatrix},$$

with

$$\Delta = (1 - \nu_{21}\nu_{12} - \nu_{22}^2 - \nu_{21}\nu_{12} - 2\nu_{21}\nu_{12}\nu_{22})/E_1E_2^2.$$

The positivity of the diagonal components of the stiffness matrix leads to:

$$(1-\nu_{22}^2), \quad (1-\nu_{12}\nu_{21}), \quad \Delta > 0. \tag{IV.12}$$

Using Equations (IV.11) and (IV.12), we obtain the following conditions on the Poisson ratios:

$$-\sqrt{\frac{E_1}{E_2}} < \nu_{12} < \sqrt{\frac{E_1}{E_2}}, \tag{IV.13}$$

and

$$-1 < \nu_{22} < 1 - 2\nu_{12}^2\frac{E_2}{E_1}. \tag{IV.14}$$

In addition to the conditions above, the condition for incompressibility is a null trace of the strain tensor. This leads to:

$$\frac{1}{E_1} - \frac{\nu_{12}}{E_1} - \frac{\nu_{12}}{E_1} = 0,$$

and

$$\frac{1}{E_2} + \frac{-\nu_{12}}{E_1} + \frac{-\nu_{22}}{E_2} = 0.$$

Therefore,

$$\nu_{12} = 0.5, \qquad \nu_{22} = 1 - \frac{E_2}{2E_1} \qquad \text{and} \qquad \mathrm{E}_1 > \frac{\mathrm{E}_2}{4}. \tag{IV.15}$$

The last condition comes from (IV.10). By replacing ν_{22} by $1-\frac{E_2}{2E_1}$ in (IV.10), we obtain

$$G_{22} = \frac{E_1E_2}{4E_1 - E_2} \qquad \text{and} \qquad \mathrm{E}_1 > \frac{\mathrm{E}_2}{4}.$$

1.5.3 Orthotropic materials

Orthotropic materials are a subset of anisotropic materials, having three planes and axes of symmetry. An orthotropic material compliance matrix is written such that:

$$\underline{\underline{\widehat{S}}} = \begin{pmatrix} \frac{1}{E_1} & \frac{-\nu_{12}}{E_2} & \frac{-\nu_{13}}{E_3} & 0 & 0 & 0 \\ \frac{-\nu_{21}}{E_1} & \frac{1}{E_2} & \frac{-\nu_{23}}{E_3} & 0 & 0 & 0 \\ \frac{-\nu_{31}}{E_1} & \frac{-\nu_{23}}{E_2} & \frac{1}{E_3} & 0 & 0 & 0 \\ 0 & 0 & 0 & \frac{1}{2G_4} & 0 & 0 \\ 0 & 0 & 0 & 0 & \frac{1}{2G_5} & 0 \\ 0 & 0 & 0 & 0 & 0 & \frac{1}{2G_6} \end{pmatrix},$$

and its stiffness matrix such that:

$$\underline{\underline{\widehat{C}}} = \begin{pmatrix} \frac{(1-\nu_{23}\nu_{32})}{E_2E_3\Delta} & \frac{(\nu_{12}+\nu_{13}\nu_{32})}{E_2E_3\Delta} & \frac{(\nu_{13}+\nu_{12}\nu_{32})}{E_2E_3\Delta} & 0 & 0 & 0 \\ \frac{(\nu_{21}+\nu_{23}\nu_{31})}{E_1E_3\Delta} & \frac{(1-\nu_{13}\nu_{31})}{E_1E_3\Delta} & \frac{(\nu_{23}+\nu_{31}\nu_{13})}{E_1E_3\Delta} & 0 & 0 & 0 \\ \frac{(\nu_{31}+\nu_{21}\nu_{32})}{E_1E_2\Delta} & \frac{(\nu_{32}+\nu_{12}\nu_{31})}{E_1E_2\Delta} & \frac{(1-\nu_{12}\nu_{21})}{E_1E_2\Delta} & 0 & 0 & 0 \\ 0 & 0 & 0 & 2G_4 & 0 & 0 \\ 0 & 0 & 0 & 0 & 2G_5 & 0 \\ 0 & 0 & 0 & 0 & 0 & 2G_6 \end{pmatrix},$$

with $\Delta = (1 - \nu_{12}\nu_{23} - \nu_{23}\nu_{32} - \nu_{31}\nu_{13}/E_1E_2E_3)$. The stiffness matrix symmetry and positivity impose bounds on the Poisson ratios:

$$|\nu_{ij}| < (E_j/E_i)^{1/2} \quad \text{for} \quad \text{i} = 1, 2, 3. \tag{IV.16}$$

In the case of an orthotropic incompressible material, when applying the incompressibility condition of Equation (IV.8), we obtain:

$$\begin{cases} \nu_{23} = \frac{1}{2}\frac{-E_2E_3+E_1E_3+E_1E_2}{E_1E_3} \\ \nu_{13} = \frac{1}{2}\frac{E_2E_3-E_1E_3+E_1E_2}{E_2E_3} \\ \nu_{12} = \frac{1}{2}\frac{E_2E_3+E_1E_3-E_1E_2}{E_2E_3} \end{cases}. \tag{IV.17}$$

2 Methods

We considered the tissue scale separation: At the mesoscopic scale (100-500 µm), we explored structures made of cardiac cells and extracellular matrix with homogeneous orientation of the fibers. At the macroscopic scale (>1 mm), we took into account the mesoscale change in orientation, by rotating the cardiac cells, and the perimysial extracellular matrix (sheetlet) layers.

2.1 Mesoscopic model

We explored three mesostructures: first, a homogeneous mesostructure (H), made only of cardiomyocytes, aligned with the direction $\underline{f}$ (see Figure IV.4, H). Then a second mesostructure (L), made of two blocks of cardiomyocytes aligned with $\underline{f}$, separated by a plane layer of extracellular matrix, and a third mesostructure, (E), made of cardiac cells aligned with $\underline{f}$, and the collagen layer formed an ellipsoid.

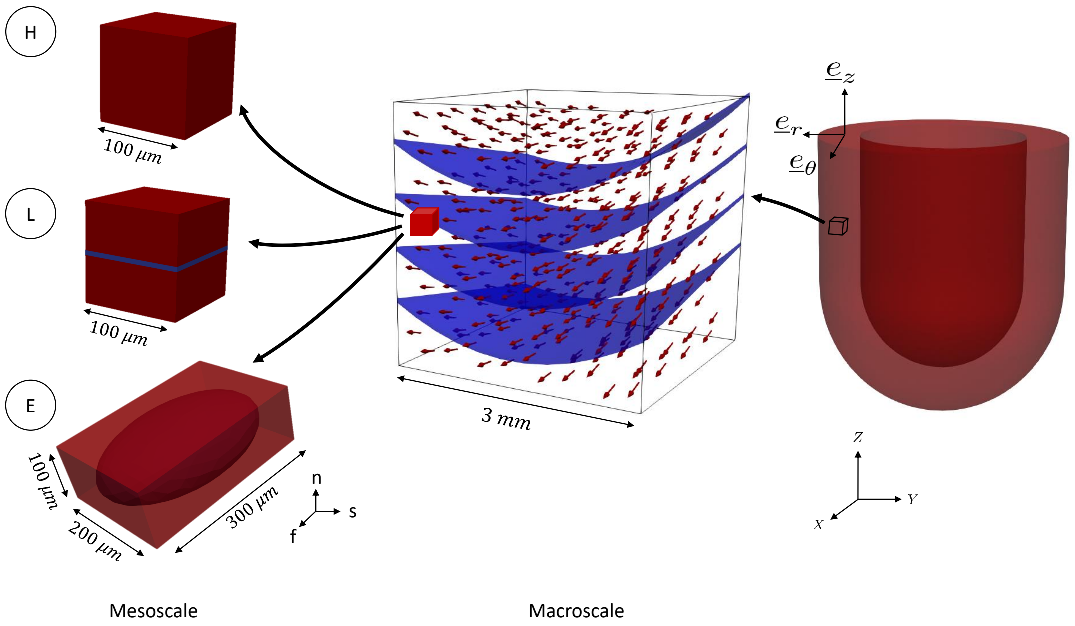

Figure IV.4 – Schematic showing the mesoscale with the different structures (H, L and E), and the macroscale with the change in orientation of the cardiac cells and sheetlets.

2.1.1 Mesoscopic structures

Structure H: Homogeneous. As mentioned, the first mesostructure is homogeneous, made of only cardiomyocytes. This structure was explored in order to investigate the role of the rotating cardiac fibers in the macroscopic orthotropy.

Structure L: Laminar. This mesostructure was explored in order to investigate the role of the laminar structure observed in the myocardium in the orthotropy [LeGrice et al., 1995; Young et al., 1998; Sands et al., 2005; Pope et al., 2008]. The structure was made of two blocks (50 µm) of parallel cardiac cells, separated by a layer of extracellular matrix. It has been shown that the collagen content of the heart evolves with age [Debessa et al., 2001]. While it is of 3.92 ± 0.8% in young subjects, it reaches 5.86 ± 0.81% in old hearts. We aimed at obtaining a volume fraction of approximately 5% of collagen in our model. We therefore fixed the collagen thickness layer to 5 µm, representing 4.75% of the total volume.

Structure E: Ellipsoidal. This structure was inspired by the ellipsoidal clusters observed in the transversal cross-sections of the cardiac wall [Kanzaki et al., 2010].

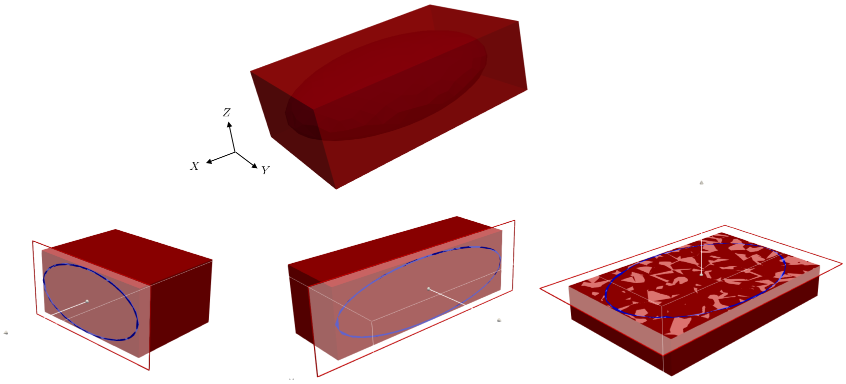

Section in (YZ) plane   Section in (XZ) plane   Section in (XY) plane

Figure IV.5 – Complete structure E and sections showing the different ellipse ratios on in three orthogonal planes, in order to create an orthotropic mesostructure.

We created an ellipsoid such that its axis ratio in the (YZ) plane (see Figure IV.5) was superior to 1, in order to avoid having a transverse isotropic structure. We chose the ratio to be 2. We supposed that the third direction, the cardiac cell direction, formed an elongated structure, and fixed its dimension such that the axis ratio in the (XZ plane) was equal to 3. Hence, our cell dimensions were 100×200×300 µm. The extracellular matrix layer thickness was 2.5 µm, representing 4.79% of the total volume. Note that this periodic structure does not allow to fill the space with ellipsoidal shaped sheetlets (see Figure IV.6).

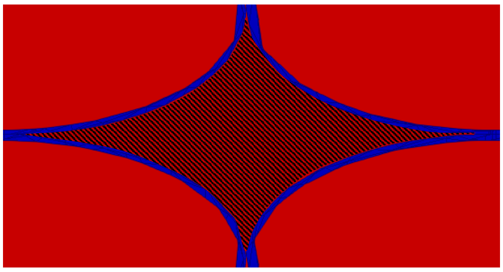

Figure IV.6 – 2D representation of the periodic ellipsoid shape showing a non ellipsoidal sheetlet (striped area) between four cells.

2.1.2 Material parameters

The material parameters are comprised in the stiffness matrix $\widehat{\underline{\underline{C}}}$ (see Section 1.5). In the following, we will introduce the material parameters for both cardiomyocytes and extracellular matrix, and present the elastic bounds, detailed in Section 1.5.

Cardiomyocytes. The cardiomyocytes being cylindrical elongated cells, it is thus only natural to model them as transverse isotropic materials, with physical properties symmetric about the cell axis, ($\underline{f}$, in our structures). The bundles being made of locally parallel cells, they are also transversely isotropic. Both compressible and quasi-incompressible cases for the cardiomyocytes were investigated in this study.

The material parameters for the cardiomyocytes are therefore: E_f, the longitudinal elastic modulus, E_t, the transversal or in plane elastic modulus, G_{tt} and ν_{tt}, the in-plane shear modulus and Poisson ratio and G_{ft} and ν_{ft}, the transversal shear modulus and the Poisson ratio. The myocardial volume change (up to 10%) during the cardiac cycle, is partly caused by the cardiac structure [Ashikaga et al., 2008]. We therefore considered two cases for the cardiomyocytes: compressible and quasi-incompressible. Their elastic bounds are summarized in Table IV.1.

Compressible material	Incompressible material
$E_f > 0$	$E_f > 0$
$E_t > 0$	$E_t > 0$
$G_{ft} > 0$	$G_{ft} > 0$
$G_{tt} = \frac{E_t}{2(1+\nu_{tt})}$	$G_{tt} = \frac{E_f E_t}{4E_f - E_t}$
$-\sqrt{\frac{E_f}{E_t}} < \nu_{ft} < \sqrt{\frac{E_f}{E_t}}$	$\nu_{ft} = 0.5$
$-1 < \nu_{tt} < 1 - 2\nu_{ft}^2 \frac{E_t}{E_f}$	$\nu_{tt} = 1 - \frac{E_t}{2E_f}$

Table IV.1 – Elastic bounds for a (left) compressible and (right) incompressible transverse isotropic material.

Extracellular matrix. The material symmetry for the extracellular matrix is not straightforward. In fact, it is a thin layer made mostly of interlocking collagen fibers arranged randomly. This structure hints at a transverse isotropic symmetry, with uniform parameters in the plane, and a symmetry axis orthogonal to the plane. However, supposing that it is a transversely isotropic material leads to six additional parameters, and considering the thinness of the layer, these parameters might not be identifiable. Thus, we chose to simplify the model by assigning an isotropic material to the extracellular matrix, with only two parameters to identify: the elastic modulus E_c (always > 0), and the Poisson ratio ν_c comprised between -1 and 0.5. In order to verify that our choice is pertinent, we performed a sensitivity analysis, that we will detail in Section 2.3.1. Additionally, recent studies hint towards a possible auxetic behavior in random fiber networks [Mauri et al., 2015; Domaschke et al., 2019]. Such networks with negative Poisson ratios do not contract, but expand transverse to the direction of extension when stretched.

2.1.3 Numerical linear homogenization

At the mesoscale, the periodic unit cells (Ω) (mesostructures L and E) are heterogeneous, made of two materials, cardiomyocytes and collageneous extracellular matrix. In order to obtain the material properties of the homogeneous medium associated with each of the mesostructures, linear homogenization was performed numerically. The method described in Section 1.4 was adopted.

2.2 Experimental data and associated macro-model

2.2.1 Shear experiments & anisotropy characterization

The detailed experimental data were sent to us by Prof. Socrates Dokos [Dokos et al., 2002]. Myocardial samples were extracted from six pig left ventricle mid walls. The experiment consisted in applying four cycles of sinusoidal simple shear, during which the maximum displacement was increased, at each cycle, to 10%, 20%, 30%, and 50%. The resulting shear forces were measured every 5% of deformation. The experiment was repeated on six samples for each of the the six shear modes NS, NF, FN, FS, SF, SN (see Figure IV.1, left).

The results are shown in Figure IV.1 (right). The graph shows the average shear stress-displacement loops over the tested samples. It reveals the material's anisotropy with the difference in the shear stresses along the six directions, with the highest values for the FS and FN modes, and the lowest ones for the NF and NS modes.

Similar results were also found in a more recent study done on human hearts [Sommer et al., 2015]. In Figure IV.7, we plotted the peak stress values at 50% deformation for both studies. The detailed data provided by Prof. Socrates Dokos allowed us to plot the dispersion, however, we did not have the data from the second study. We thus used the published experimental results. Although the peak shear stress values obtained for swine are higher than the ones obtained for humans, the ratios of the modes over SF are similar, with a slight difference in modes NS and NF (see Figure IV.7). However, these modes seem to be interchangeable in the literature, with no significant difference found between them [Dokos et al., 2002; Sommer et al., 2015; McEvoy et al., 2018].

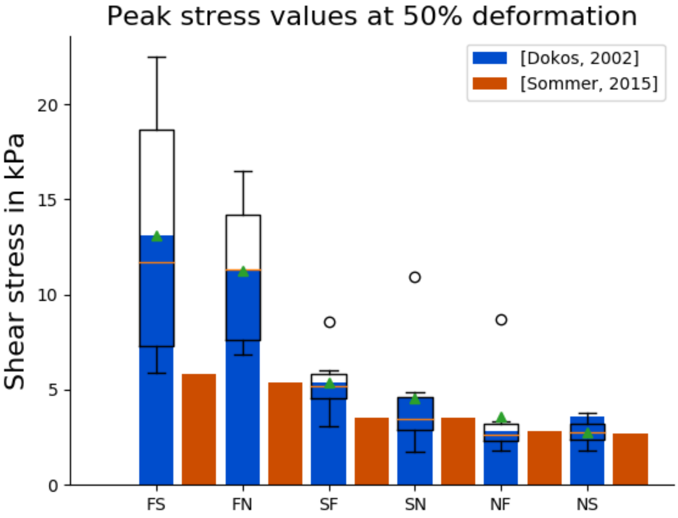

Figure IV.7 – Comparison of experimental data extracted from [Dokos et al., 2002] and [Sommer et al., 2015]. Bar plot of the peak shear stress values for 50% deformation for both studies. The stress values recorded in [Dokos et al., 2002], performed on swine hearts, are higher than the ones recorded in [Sommer et al., 2015], performed on human hearts. However, the order of the modes is similar, with FS>FN≥SF>SN>NF≅NS.

Using the data from [Dokos et al., 2002], we plotted the recorded peak stress of each mode, at 5% deformation for the four cycles (see Figure IV.8). At the first cycle, the anisotropy is evident, with high shear stresses for modes FS and FN (≅ 0.6 kPa), followed by SF and SN (≅ 0.3 Kpa), and low stresses for NS and NF (≅ 0.2 kPa). We noticed that the stresses tended to converge with the cycles, reaching ≅ 0.02 kPa for all modes. This means that the more cycles the tissue is subjected to, the more it is preconditioned, the more is loses of its anisotropy and becomes isotropic. We thus decided to study the small deformation anisotropy at the first cycle.

We then plotted, on Figure IV.9, the recorded stresses at 5%, 10%, 20%, 30%, 40% and 50% shear deformation for all modes. We noticed that the mode order stays consistent for all deformation levels, with the highest stresses recorded for FS, followed by FN, SF, SN, NF and finally NS. We therefore deduced that the anisotropy is inherent to the material, and not induced by large deformations. Thus, in order to investigate it, a linear elastic setting at small deformations is enough.

Given that our main objective was to compare the anisotropy, hence the order of

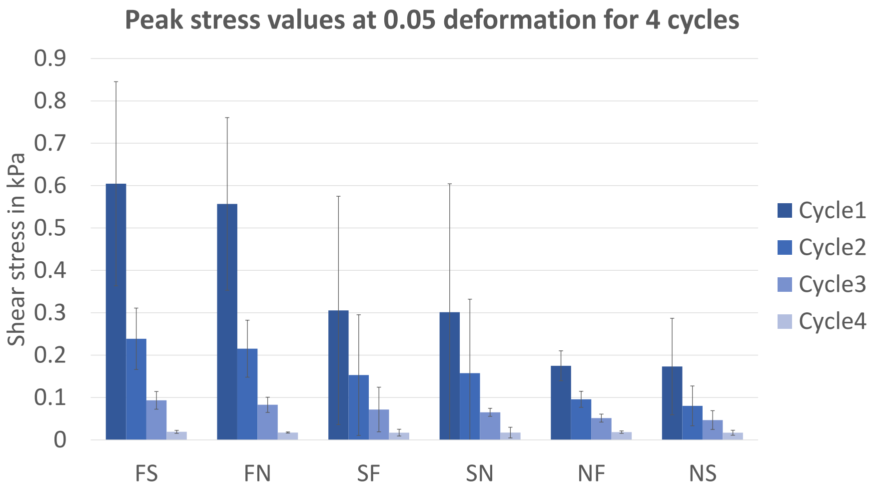

Figure IV.8 – Comparison of the peak shear stress recorded at 5% deformation for all cycles. Cycle 1 shows clear anisotropy with high shear stresses for modes FS and FN, and low stresses for NS and NF. Shear stress decreases with cycles, and reaches a same amplitude for all modes at cycle 4. Data extracted from [Dokos et al., 2002].

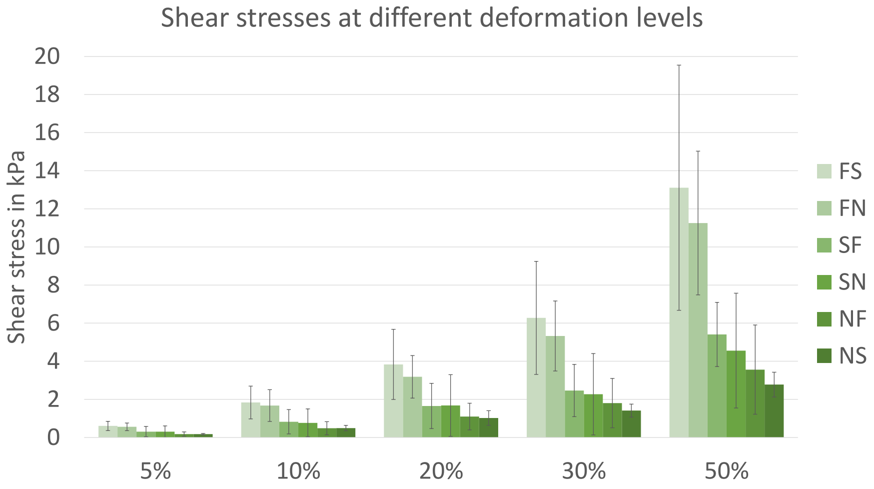

Figure IV.9 – Shear stress recorded at 5%, 10%, 20%, 30%, 40% and 50% deformation for all modes showing a conservation of the anisotropy for small and large deformations. Data extracted from [Dokos et al., 2002].

the shear stresses, we computed the experimental ratios over FS, FS corresponding to the mode with the highest recorded shear stresses. This also required to fix one of the material parameters, therefore reducing the number of parameters to optimize.

$$R = \{\frac{\sigma_{FN}}{\sigma_{FS}}, \frac{\sigma_{SF}}{\sigma_{FS}}, \frac{\sigma_{SN}}{\sigma_{FS}}, \frac{\sigma_{NS}}{\sigma_{FS}}, \frac{\sigma_{NF}}{\sigma_{FS}}\}. \tag{IV.18}$$

2.2.2 Associated macroscopic model

In order to numerically reproduce the simple shear experiment [Dokos et al., 2002], we simulated a 3×3×3 mm cube (see Figure IV.4, Macroscale).

Orientations in the tissue. The cardiac fibers and the sheetlets are known to rotate in the cardiac tissue. We therefore reproduced this rotation in our numerical cube. The cardiac fibers (originally aligned with $\underline{e_\theta}$) are known to rotate along $\underline{e_r}$ by an angle α, in the $(\underline{e_\theta}, \underline{e_z})$ plane. This leads to the rotation of $\underline{e_z}$ around $\underline{e_\theta}$ of an angle α as well, creating a new local system $(\underline{e_r}, \underline{e_f}, \underline{e'_z})$. In turn, the sheetlets (originally aligned with $\underline{e_r}$) rotate around $\underline{e_f}$ by an angle β in the $(\underline{e_r}, \underline{e'_z})$ plane, leading to a rotation of $\underline{e'_z}$ in this same plane, of an angle β. The new local coordinate system for fibers, sheetlets, and normal to fiber-sheetlets orientations becomes $(\underline{e_f}, \underline{e_s}, \underline{e_n})$, as illustrated in Figure IV.10.

Fiber orientation. Cardiomyocytes rotate in the cardiac wall, from endocardium to epicardium, such that they constitute a helical structure. Their orientation is called the Helix Angle (HA), and varies linearly between +90° to −90° [Streeter and Bassett, 1966] in pig heart walls (15 mm). Considering that the samples are extracted from mid wall, we assumed that the fiber orientation α varies linearly between +18° to −18°.

Sheetlet orientation. The sheetlet orientation distribution in the cardiac wall is not fully understood. Although this question has attracted more and more attention, disparities between the observations and the lack of a clear mapping of the sheetlets in the left ventricle leave this question partially unanswered [Rohmer et al., 2007; Kung et al., 2011; Nielles-Vallespin et al., 2017]. However, as seen in Chapter III, in the transversal section, orthogonal to the cardiomyocytes, an important variation of the sheetlet orientation was observed along the slice, ranging from -50° to +50° approximately. We therefore decided to conduct this study for several sheetlet orientations, ranging from ±0° to ±50° from endocardium to epicardium, hence analysing the effect of their orientation on the tissue's macroscopic behavior.

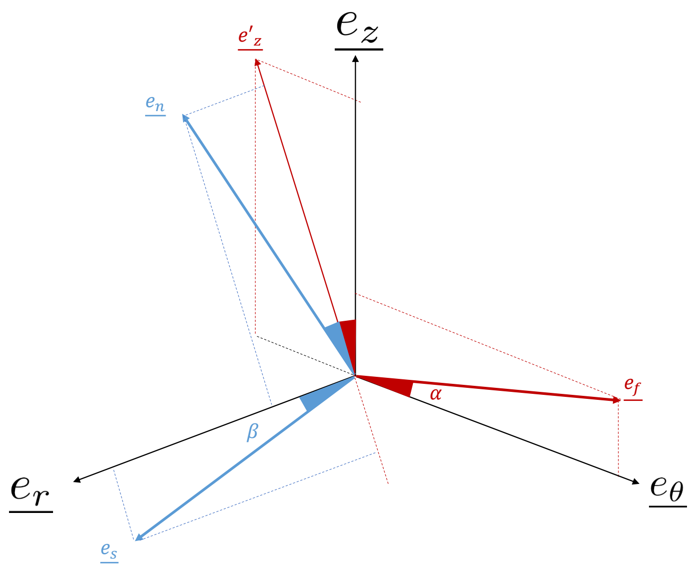

Figure IV.10 – Euler angles representing rotation of local fiber and sheetlet system. In red: rotation of $\underline{e_\theta}$ along $\underline{e_r}$ by angle α, in plane $(\underline{e_\theta}, \underline{e_z})$, leading to new system $(\underline{e_r}, \underline{e_f}, \underline{e'_z})$. In blue: rotation of $\underline{e_r}$ around $\underline{e_f}$ by angle β in $(\underline{e_r}, \underline{e'_z})$ plane, creating the new local system $(\underline{e_f}, \underline{e_s}, \underline{e_n})$. Cardiomyocytes are aligned with $\underline{e_f}$, and sheetlets are in the $(\underline{e_f}, \underline{e_s})$ plane.

Material parameters and simple shear. The previously obtained homogenized stiffness matrix $\left\langle \underline{\underline{\underline{\underline{C}}}} \right\rangle$ in Section 1.4 was used as an input material parameter at the macroscale. It was oriented with the $(\underline{e_f}, \underline{e_s}, \underline{e_n})$ basis at every point in the macrostructure. Simple shear tests were simulated: Dirichlet boundary conditions (see Table IV.2) were applied on two sides of the cube, as shown in Figure IV.1, in order to reproduce the experimental conditions. Linear elasticity was used to describe the material behavior. The problem here consisted in finding the displacement $\underline{u}(\underline{x})$ such that:

$$\begin{cases} \underline{\mathrm{div}}(\underline{\underline{\sigma}}) = \underline{0} & \text{in } \Omega \\ \underline{\underline{\sigma}} = \left\langle \underline{\underline{\underline{\underline{C}}}} \right\rangle : \underline{\underline{\epsilon}} & \text{in } \Omega \\ \underline{\underline{\epsilon}} = \frac{1}{2}(\underline{\underline{\nabla}}(\underline{u}) + (\underline{\underline{\nabla}}(\underline{u}))^T) & \text{in } \Omega \end{cases}$$

The solution $\underline{u}(\underline{x})$ to the problem allowed to compute the resultant shear stress $\underline{\underline{\sigma}}(\underline{u}(\underline{x}))$. To reproduce the six shear displacements shown in Figure IV.1, six different sets of Dirichlet boundary conditions were applied on the cube (see Table IV.2):

FN mode	$u(x_1 = 0) = [0, 0, 0]$	$u(x_1 = 3) = [0, 0, \bar{u}]$
FS mode	$u(x_1 = 0) = [0, 0, 0]$	$u(x_1 = 3) = [0, \bar{u}, 0]$
SF mode	$u(x_2 = 0) = [0, 0, 0]$	$u(x_2 = 3) = [\bar{u}, 0, 0]$
SN mode	$u(x_2 = 0) = [0, 0, 0]$	$u(x_2 = 3) = [0, 0, \bar{u}]$
NS mode	$u(x_3 = 0) = [0, 0, 0]$	$u(x_3 = 3) = [0, \bar{u}, 0]$
NF mode	$u(x_3 = 0) = [0, 0, 0]$	$u(x_3 = 3) = [\bar{u}, 0, 0]$

Table IV.2 – Dirichlet boundary conditions applied on the macroscopic cube in 6 modes

2.3 Parameter optimization

2.3.1 Material parameter sensitivity

The quality of the parameter estimation depends on the sensitivity of the output to the input parameters. A sensitivity analysis was thus performed to study the influence of changing input parameters on the system output at two scales. We studied the material parameters influence on the homogenized stiffness matrix at the mesoscale, and on the shear stress at the macroscale. This was done by evaluating a Hessian matrix using finite differences. In order to obtain a non-dimensional matrix, we introduced the non-dimensional parameter $\underline{\bar{x}}$ such that:

$$\underline{\bar{x}} = (\underline{x} - \underline{x_0}) \oslash \underline{x_0}, \tag{IV.19}$$

$\underline{x_0}$ being a reference value of the parameter, and $\oslash$ the Hadamard division.

The non-dimensional stiffness matrix error $\bar{J}$ is defined such that:

$$\bar{J}(\underline{\bar{x}}) = J(\underline{x} = \underline{x_0} \odot (\underline{1} + \underline{\bar{x}})), \tag{IV.20}$$

with $\odot$ the Hadamard product.

Using $\bar{J}(\bar{x})$, the first derivative $\nabla \bar{J}$ could thus be computed such that:

$$\nabla \bar{J}_i = \frac{\bar{J}(\underline{\bar{x}} + \bar{h}_i \underline{\bar{e}_i}) - \bar{J}(\underline{\bar{x}})}{\bar{h}_i}, \tag{IV.21}$$

and the hessian such that:

$$\nabla^2 \bar{J}_{ij} = \frac{\bar{J}(\underline{\bar{x}} + \bar{h}_i \underline{\bar{e}_i} + \bar{h}_j \underline{\bar{e}_j}) - \bar{f}(\underline{\bar{x}} + \bar{h}_i \underline{\bar{e}_i}) - \bar{f}(\underline{\bar{x}} + \bar{h}_j \underline{\bar{e}_j}) + \bar{f}(\underline{\bar{x}})}{\bar{h}_i \bar{h}_j}, \tag{IV.22}$$

where $\bar{h}_i$ and $\bar{h}_j$ are the introduced perturbations in the $\underline{\bar{e}_i}$ and $\underline{\bar{e}_j}$ directions.

Sensitivity of the homogenized material matrix to microscopic parameters. At the mesoscale, we used the material parameters as an input and computed a homogenized stiffness matrix. We therefore studied the sensitivity of the homogenized matrix on the material parameters $\underline{x}$, by evaluating the Hessian matrix in Equation (IV.22), with the error $\bar{J}(\underline{\bar{x}}) = \bar{J}_m(\underline{\bar{x}})$ computed such that:

$$\bar{J}_m = \sum_{n=1}^{N_\lambda} \frac{(\lambda_i - \lambda_i')^2}{\lambda_i^2}, \tag{IV.23}$$

with λ_i and λ_i' being respectively the eigenvalues of the stiffness matrix and the perturbed stiffness matrix and $N_\lambda = 6$.

The analysis was performed on mesostructures H, L and E, with compressible cardiomyocytes (presented first), and quasi-incompressible cardiomyocytes (presented next).

In the case of the compressible homogeneous mesostructure (H), with four parameters, E_f, G_{ft}, ν_{ft} and ν_{tt}, with $E_t = 1$ being fixed since only the ratios of the stresses are studied, Table IV.3 shows that parameters E_f, G_{ft} and ν_{tt} are associated with positive eigenvalues. The homogenized stiffness matrix is thus sensitive to these parameters. However, ν_{ft} is associated with a null eigenvalue. Therefore, at the mesoscale, ν_{ft} has no or little impact on the homogenized stiffness matrix.

EigenValues

4.00	2.00	0.06	**0.00**

EigenVectors

0.00	1.00	0.00	0.00	E_f
1.00	0.00	0.00	0.00	G_{ft}
0.00	0.00	0.00	-1.00	ν_{ft}
0.00	0.00	-1.00	0.00	ν_{tt}

Table IV.3 – Eigenvalues and associated eigenvectors of the Hessian computing the sensitivity of the homogenized material matrix to microscopic parameters in the isotropic compressible case.

For mesostructures L and E, six input parameters were investigated, considering a compressible transverse isotropic material for cardiomyocytes and an isotropic material for the perimysial extracellular matrix. The cardiomyocyte parameters are $\underline{p}_{cells} = \{E_f, E_t, G_{ft}, G_{tt}, \nu_{ft}, \nu_{tt}\}$, where $E_t = 1$ is fixed and $G_{tt} = \frac{E_t}{2(1+\nu tt)}$. The collagen parameters are $\underline{p}_{ECM} = \{E_c, G_{cp}, \nu_c\}$, where $G_{cp} = \frac{E_c}{2(1+\nu p)}$. The Hessian matrix eigenvalues and relative eigenvectors were computed. The primary directions of the eigenvectors relative to parameters ν_c, E_c and ν_{ft} (see Tables IV.4 and IV.5) are associated with null or small eigenvalues. A small variation of these parameters has therefore no or very little impact on the homogenized stiffness matrix. These parameters are associated with the perimysial extracellular matrix (except for ν_{ft}), which can be explained by the fact that the extracellular matrix layer is thin, and represents only 5% of the total volume. The choice of an isotropic material for the perimysial layer with less material parameters is thus suitable.

In the case of the homogeneous mesostructure (H) with quasi-incompressible cardiomyocytes, two parameters E_f and G_{ft} are investigated, $E_t = 1$ being fixed since the ratios are studied. At the mesoscale, Table IV.6 shows that both parameters E_f and G_{ft} have eigenvectors associated with positive eigenvalues. The homogenized material matrix is thus sensitive to both.

For the laminar (L) and elliptical (E) mesostructures with quasi-incompressible cardiomyocytes, two parameters E_f and G_{ft} corresponding to the cardiomyocytes, and parameters E_c and ν_{cp} corresponding to the perimysial extracellular matrix are investigated.

Table IV.7 shows that the homogenized stiffness matrix is sensitive to parameters E_f, G_{ft} and E_c.

EigenValues

18.50	3.63	1.96	0.01	**0.00**	**0.00**

EigenVectors

0.00	0.00	1.00	0.00	0.00	0.00	E_f
0.00	1.00	0.00	0.00	0.00	0.00	G_{ft}
0.00	0.00	0.00	0.00	0.00	-1.00	ν_{ft}
-1.00	0.00	0.00	0.00	0.00	0.00	ν_{tt}
0.00	0.00	0.00	1.00	0.00	0.00	E_c
0.00	0.00	0.00	0.08	1.00	0.00	ν_c

Table IV.4 – Eigenvalues and associated eigenvectors of the Hessian computing the sensitivity of the homogenized material matrix to microscopic parameters for mesostructure L with compressible cardiomyocytes.

EigenValues

60.20	3.57	0.16	0.01	**0.00**	**0.00**

EigenVectors

-0.11	0.00	0.79	-0.33	0.50	-0.04	E_f
0.00	1.00	0.00	0.00	0.00	0.00	G_{ft}
0.00	0.00	0.60	0.44	-0.67	-0.01	ν_{ft}
-0.99	0.00	-0.09	0.06	-0.04	0.00	ν_{tt}
-0.02	0.00	0.00	-0.83	-0.55	0.09	E_c
0.00	0.00	0.03	0.06	0.06	1.00	ν_c

Table IV.5 – Eigenvalues and associated eigenvectors of the Hessian computing the sensitivity of the homogenized material matrix to microscopic parameters for mesostructure E with compressible cardiomyocytes.

EigenValues

4.00	4.00

EigenVectors

1.00	0.00	E_f
0.00	1.00	G_{ft}

Table IV.6 – Eigenvalues and associated eigenvectors of the Hessian computing the sensitivity of the homogenized material matrix to microscopic parameters in the isotropic quasi-incompressible case.

EigenValues

3.71	2.08	0.83	**0.00**

EigenVectors

0.04	0.94	0.34	0.00	E_f
1.00	-0.06	0.07	0.01	G_{ft}
0.08	0.33	-0.94	-0.05	E_c
0.00	0.02	-0.05	1.00	ν_{cp}

Table IV.7 – Eigenvalues and associated eigenvectors of the Hessian computing the sensitivity of the homogenized material matrix to microscopic parameters for mesostructure L with incompressible cardiomyocytes.

EigenValues

3.29	1.90	0.56	**0.00**

EigenVectors

0.09	0.86	0.50	0.02	E_f
0.97	-0.19	0.14	0.02	G_{ft}
0.21	0.47	-0.85	-0.06	E_c
-0.01	0.02	-0.07	1.00	ν_{cp}

Table IV.8 – Eigenvalues and associated eigenvectors of the Hessian computing the sensitivity of the homogenized material matrix to microscopic parameters for mesostructure E with incompressible cardiomyocytes.

Mesostructure (E) shows the same parameter sensitivity results as mesostructure (L), with no sensitivity for parameter ν_{cp} at the mesoscale

Sensitivity of shear stress to microscopic parameters. At the macroscale, the input parameters were the homogenized stiffness matrix and the outputs were the shear stresses. We therefore studied the influence of small variations of material parameters on the resulting shear stress via the homogenized stiffness matrix, by evaluating the hessian matrix in Equation (IV.22), with $\bar{J}(\underline{\bar{x}}) = \bar{J}_M(\underline{\bar{x}})$ such that:

$$\bar{J}_M = \sum_{i=1}^{N_R} \frac{(R_i' - R_i)^2}{R_i^2} \tag{IV.24}$$

with $N_R = 5$, the number of ratios to optimize. R_i are the ratios of the exact problem, and R_i' the ratios resulting from the problem with the perturbed parameters. At this scale, the three mesostructures H, L and E were investigated.

For mesostructure H, with compressible cardiomyocytes, four parameters E_f, G_{ft}, ν_{ft} and ν_{tt} were analyzed. The sensitivity analysis at the macroscale showed that the macroscopic response is not affected by the parameter ν_{ft}, hence ν_{ft} is not identifiable (see Table IV.9). This result was expected given that ν_{ft} has no impact on the homogenized matrix, as seen in the previous section. The rest of the parameters were associated with positive eigenvalues.

EigenValues

1.80	0.47	0.03	**0.00**

EigenVectors

0.00	0.00	-1.00	0.00	E_f
-0.11	-0.99	0.00	0.00	G_{ft}
0.00	0.00	0.00	1.00	ν_{ft}
0.99	-0.11	0.00	0.00	ν_{tt}

Table IV.9 – Eigenvalues and associated eigenvectors of the Hessian computing the sensitivity of the shear stress to microscopic parameters in the isotropic compressible mesostructure.

For mesostructures L and E, we show here the sensitivity study for the case with compressible cardiomyocytes. The analysis shows, again, that the extracellular matrix parameters are not identifiable, with a quasi null sensitivity (see Tables IV.10 and IV.11). Thus, by performing simple shear assays at the macroscale, it is not possible to identify the non-sensitive parameters, mainly the extracellular matrix ones. This confirms our choice of reducing the number of parameters to identify for the extracellular matrix by choosing an isotropic material.

EigenValues

0.63	0.32	0.03	**0.00**	**0.00**	**0.00**

EigenVectors

0.08	0.03	0.99	-0.05	0.03	0.02	E_f
0.98	0.19	-0.09	0.04	-0.01	0.00	G_{ft}
0.00	0.00	-0.04	0.01	0.85	0.53	ν_{ft}
0.20	-0.98	0.02	-0.04	0.01	0.00	ν_{tt}
-0.03	-0.05	0.05	0.99	-0.05	0.08	E_c
0.00	0.00	0.00	-0.09	-0.53	0.84	ν_c

Table IV.10 – Eigenvalues and associated eigenvectors of the Hessian computing the sensitivity of the shear stress to microscopic parameters in mesostructure L with compressible cardiomyocytes.

EigenValues

0.54	0.27	0.02	**0.00**	**0.00**	**0.00**

EigenVectors

0.09	0.06	0.98	-0.17	0.04	0.01	E_f
0.97	0.20	-0.09	0.05	-0.01	0.00	G_{ft}
0.00	0.00	-0.04	0.01	0.91	0.41	ν_{ft}
0.21	-0.98	0.03	-0.06	0.01	0.00	ν_{tt}
-0.02	-0.06	0.17	0.98	-0.03	0.06	E_c
0.00	0.00	-0.01	-0.07	-0.41	0.91	ν_c

Table IV.11 – Eigenvalues and associated eigenvectors of the Hessian computing the sensitivity of the shear stress to microscopic parameters in mesostructure E with compressible cardiomyocytes.

In the case of incompressible cardiomyocytes, the macroscopic shear stress sensitivity to the microscopic material parameters is shown in Tables IV.12, IV.13 and IV.14.

At the macroscale, Table IV.12 shows that both parameters E_f and G_{ft} have eigenvectors associated with positive eigenvalues. The macroscopic shear stress is thus sensitive to both, in the case of the homogeneous mesostructure with incompressible cardiomyocytes.

At the macroscale, in the case of mesostructures (L) and (E) with incompressible transverse isotropic cardiomyocytes and isotropic collagen layer, Tables IV.13 and IV.14 show that only the cardiomyocyte parameters E_f and G_{ft} can be identified with macro-

EigenValues

0.96	0.16

EigenVectors

0.26	-0.97	E_f
-0.97	0.26	G_{ft}

Table IV.12 – Eigenvalues and associated eigenvectors of the Hessian computing the sensitivity of the shear stress to microscopic parameters in the isotropic quasi-incompressible mesostructure.

EigenValues

0.62	0.03	**0.00**	**0.00**

EigenVectors

0.00	-1.00	0.00	0.00	E_f
-1.00	0.00	-0.00	0.00	G_{ft}
0.00	-0.00	-1.00	0.00	E_c
0.00	0.01	0.00	1.00	ν_{cp}

Table IV.13 – Eigenvalues and associated eigenvectors of the Hessian computing the sensitivity of the shear stress to microscopic parameters in mesostructure L with incompressible cardiomyocytes.

EigenValues

0.54	0.02	**0.00**	**0.00**

EigenVectors

-0.08	-0.98	0.18	0.01	E_f
-1.00	0.07	-0.05	0.00	G_{ft}
0.03	-0.18	-0.98	0.04	E_c
0.00	0.01	0.04	1.00	ν_{cp}

Table IV.14 – Eigenvalues and associated eigenvectors of the Hessian computing the sensitivity of the shear stress to microscopic parameters in mesostructure E with incompressible cardiomyocytes.

scopic mechanical tests, E_c and ν_{cp} being associated with null eigenvalues.

2.3.2 Parameter estimation

The parameter estimation process is described in the flowchart of Figure IV.11: Given a mesostructure, and a set of material parameters $\underline{p}$, if the parameters respected the bounds detailed in Section 2.1.2, a linear homogenization was performed, generating the homogenized material properties of the resulting medium $\left\langle \underline{\underline{\underline{\underline{C}}}} \right\rangle$. These properties were then used, at the macroscale, to perform shear displacement in six modes on a cubic structure. We then obtained six values of numerical shear $\sigma_{num,i}$, $i = \{1..6\}$, that we compared to the experimental shear stresses obtained in [Dokos et al., 2002], via a cost function. However, instead of using the shear stress values in the cost function, and given that our main objective was to compare the anisotropy, hence the order of the shear stresses, we used experimental stress ratio $\tilde{R}$ and numerical R ratios (see Equation (IV.18)) in the optimization cost function J_{opt}, such that:

$$J_{opt} = \sum_{i=1}^{5} \frac{(R_i - \mu_{\tilde{R}_i})^2}{s^2_{\tilde{R}_i}}, \tag{IV.25}$$

μ being the mean value, and s the standard deviation, given that each experiment is repeated on six specimen. The parameter optimization was done using CMA-ES (Covariance Matrix Adaptation Evolution Strategy), which uses stochastic, derivative-free methods for numerical optimization [Igel et al., 2006].

3 Results

Our question was to determine whether the anisotropy arises from the cardiomyocytes rotation alone, or from the presence of the extracellular matrix layers at the mesoscale. In this section, we will present the main results obtained during our study, in order to identify the suggested mesostructure that best represents the mesoscale architecture.

3.1 Mesostructure H

Mesostructure H (see Figure IV.4) was made of aligned cardiomyocytes in the $\underline{f}$ direction. This cell did not require homogenization since it is already homogeneous. We therefore only simulated the simple shear displacement experiment on it. Two cases were studied for this configuration: quasi-incompressible and compressible. We recall that, for a transverse isotropic material, there are six parameters: $E_f, E_t, G_{ft}, G_{tt}, \nu_{ft}, \nu_{tt}$. Since

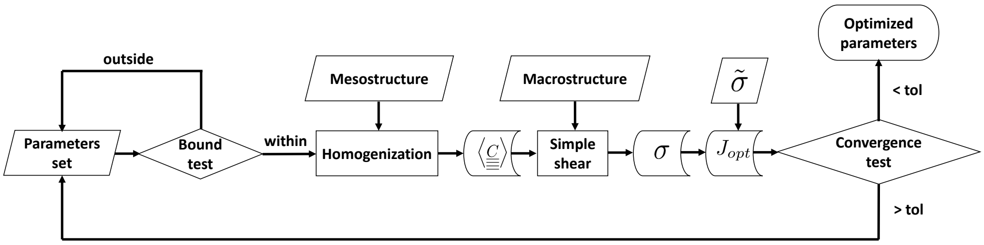

Legend	
$\langle \underline{\underline{\underline{\underline{C}}}} \rangle$	Homogenized stiffness matrix
σ	Numerical shear stress
$\tilde{\sigma}$	Experimental shear stress
J_{opt}	Cost function
tol	Tolerance

Figure IV.11 – Summarized schematic representation describing the parameter optimization process: given a mesostructure, and a set of material parameters respecting the elastic bounds, a linear homogenization is performed, generating the homogenized material properties of the resulting medium. These properties are used at the macroscale to perform shear displacement. The obtained numerical results are compared to experimental results via a cost function.

we decided to minimize the error over 5 mode ratios instead of 6 shear modes, we fixed one parameter, $E_t = 1$ for all the computations, which left us with two parameters to optimize in the quasi-incompressible cell (E_f and G_{ft}), and four in the compressible cell (E_f, G_{ft}, ν_{ft} and ν_{tt}) (see Table IV.1).

Figure IV.12 shows bar plots of the optimized shear stress modes, superimposed with box plots of the experimental shear stress modes for both compressible and quasi-incompressible cardiomyocytes. It is clear that, in both cases, the optimization could not reproduce the experimental data, even though the results are slightly better in the compressible case, which has more degrees of freedom. By varying the parameters in order to recover the experimental order in the compressible mesostructure, we found that an increase in mode $\frac{SN}{FS}$ (c), led to an increase in mode $\frac{NF}{FS}$ (e) as well, disarraying the order. Their CMA-ES optimized values are shown in Table IV.15.

Mesostructure H was not able to reproduce the anisotropy observed experimentally. This means that the cardiomyocyte rotation in the heart wall cannot, on its own, induce the level cardiac anisotropy observed experimentally. It therefore confirms the importance of collagen structure in assuring the orthotropic response.

3.2 Mesostructure L

For mesostructure L, two cases were investigated as well, consisting of quasi-incompressible or compressible transverse isotropic cardiomyocytes with an isotropic col-

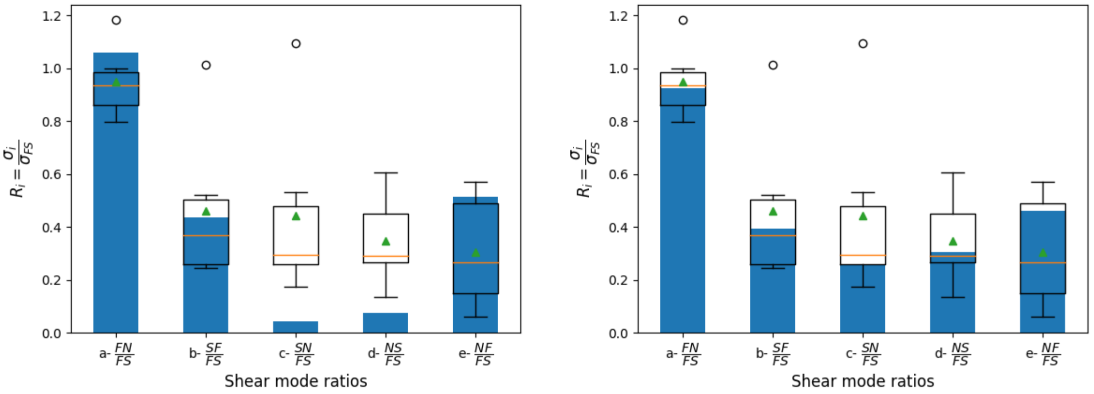

(a) Quasi-incompressible

(b) Compressible

Figure IV.12 – Quasi-incompressible (left) and compressible (right) transverse isotropic (Mesostructure H) - Experimental versus optimized shear stress ratios (Box plot of the experimental shear stress and bar plot of the numerical shear stress), for $\alpha = \pm 18°$.

	Quasi-incompressible	Compressible
Optimized	$E_f = 2.07$ $G_{ft} = 28.29$	$E_f = 10.72$ $G_{ft} = 6.11$ $\nu_{ft} = 2.82$ $\nu_{tt} = -0.84$
Computed	$G_{tt} = 0.28$ $\nu_{tt} = 0.76$	$G_{tt} = 3.12$
Fixed	$E_t = 1$ $\nu_{ft} = 0.49$	$E_t = 1$

Table IV.15 – Optimized cardiomyocyte material parameters in the quasi-incompressible and compressible cases for mesostructure H.

lagen layer.

3.2.1 Quasi-incompressible cardiomyocytes

In the first case, the experimental versus the numerical shear mode ratios are represented in Figure IV.13, for a laminar structure where the sheetlet angle $\beta = 0°, 12.5°, 25°$ and $50°$. The optimized parameters are shown in Table IV.16.

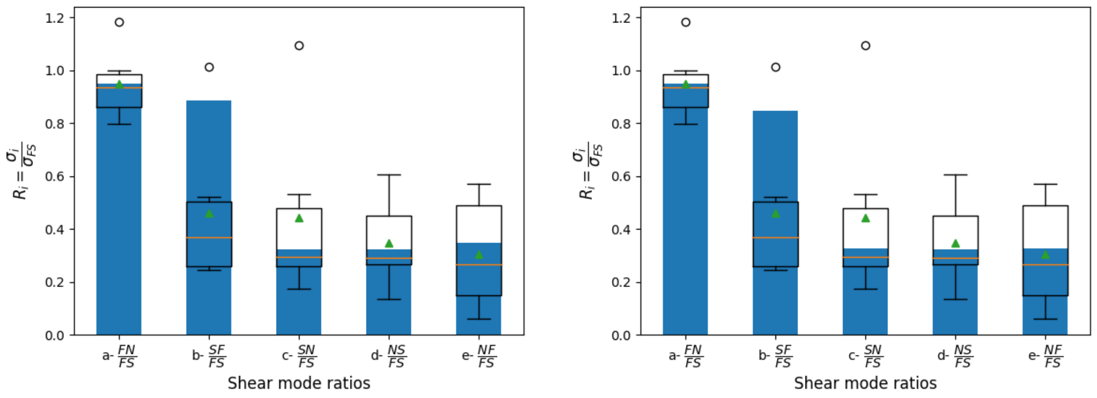

(a) $\beta = 0°$ (b) $\beta = 12.5°$

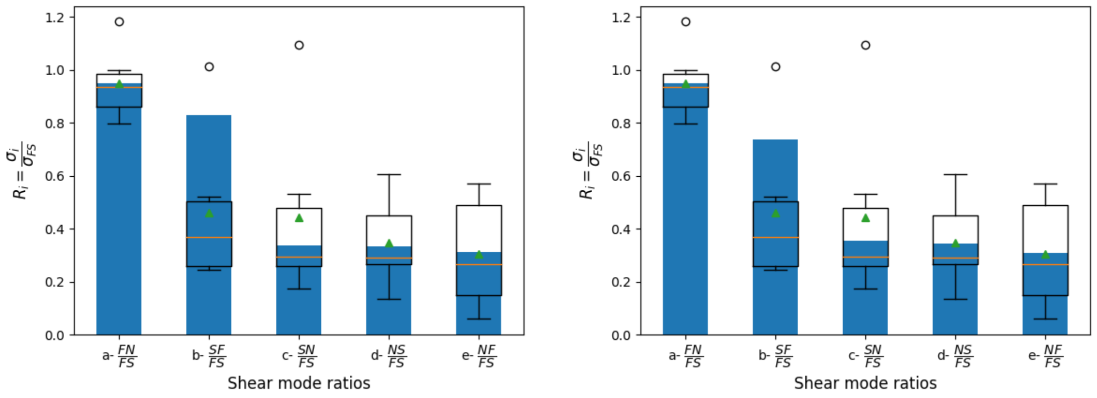

(c) $\beta = 25°$ (d) $\beta = 50°$

Figure IV.13 – Quasi-incompressible cardiomyocytes in the laminar mesostructure (L), for $\alpha = \pm 18°$, with $\beta = 0°, 12.5°, 25°, 50°$ - Experimental versus optimized shear stress ratios (Box plot of the experimental shear stress and bar plot of the numerical shear stress).

Even though the order of the optimized solutions agreed with the order of the experimental ratios, we were not able to find material parameters, within the bounds that

	0°	12.5°	25°	50°
Optimized	$E_f = 28.42$	$E_f = 28.73$	$E_f = 29.36$	$E_f = 28.8$
	$G_{ft} = 0.08$	$G_{ft} = 0.08$	$G_{ft} = 0.06$	$G_{ft} = 0.01$
	$E_c = 0.44$	$E_c = 0.45$	$E_c = 0.49$	$E_c = 0.7$
	$\nu_c = -0.99$	$\nu_c = -0.99$	$\nu_c = -0.99$	$\nu_c = -0.99$
Computed	$G_{tt} = 0.99$	$G_{tt} = 0.99$	$G_{tt} = 0.99$	$G_{tt} = 0.99$
	$G_c = 0.005$	$G_c = 0.005$	$G_c = 0.005$	$G_c = 0.005$
	$\nu_{tt} = 0.98$	$\nu_{tt} = 0.98$	$\nu_{tt} = 0.98$	$\nu_{tt} = 0.98$
Fixed	$E_t = 1$	$E_t = 1$	$E_t = 1$	$E_t = 1$
	$\nu_{ft} = 0.49$	$\nu_{ft} = 0.49$	$\nu_{ft} = 0.49$	$\nu_{ft} = 0.49$

Table IV.16 – Quasi-incompressible cardiomyocyte and collagen optimized material parameters in the laminar mesostructure (L), for $\beta = 0°, 12.5°, 25°$ and $50°$.

minimize the error (see Table IV.1). Optimized mode $\frac{SF}{FS}$ (b), was systematically too high compared to the experimental one for all values of β. We noticed, though, that the rotation of the sheetlets led to a closer solution. However, we concluded that four material parameters are not enough to reproduce the experimental data. We therefore expanded the compressible hypothesis to the cardiomyocytes.

3.2.2 Compressible cardiomyocytes

By relaxing the incompressibility assumption for the cardiomyocytes, we were able to reproduce the experimental results. Several optimal sets of parameters were obtained, meaning that the solution to this problem is not unique. This result indicates that it is not possible to identify the mesoscale parameters with simple shear assays at the macroscale.

Our study shows that the sheetlet orientation plays an important role in the anisotropy (see Figure IV.14). The higher the angle β (diastole), the more the numerical model reproduces the experimental results.

3.3 Mesostructure E

Our previous mesostructure has shown that, in order to fit the experimental data, cardiomyocytes, as well as the extracellular matrix, must be compressible. We therefore applied, for mesostructure E, compressible parameters for the materials, with transverse isotropic properties for the cardiomyocytes and isotropic properties for the collagen. The

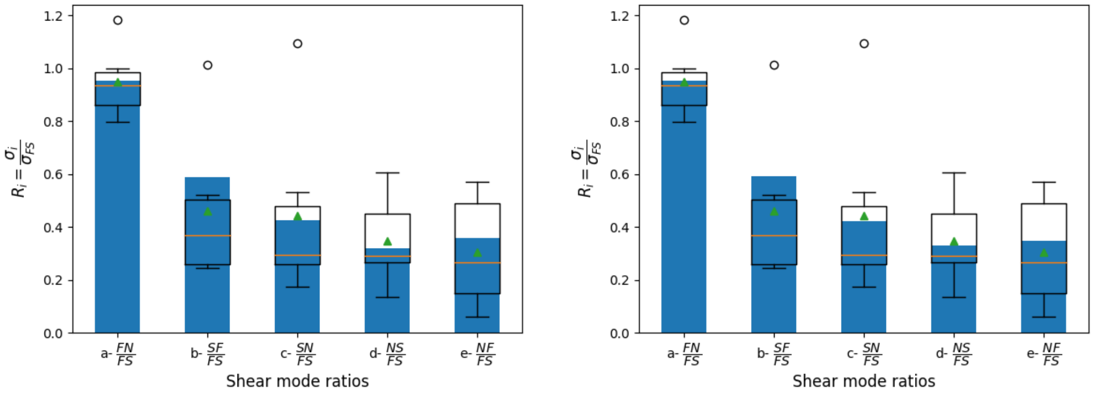

(a) $\beta = 0°$

(b) $\beta = 12.5°$

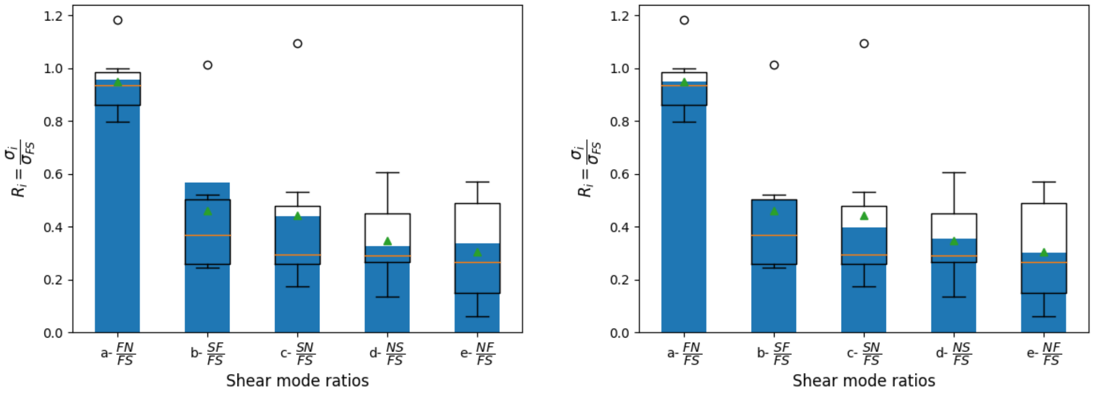

(c) $\beta = 25°$

(d) $\beta = 50°$

Figure IV.14 – Compressible cardiomyocytes in the laminar mesostructure (L), for $\alpha = \pm 18°$, with $\beta = 0°, 12.5°, 25°, 50°$ - Experimental versus optimized shear stress ratios (Box plot of the experimental shear stress and bar plot of the numerical shear stress).

optimization results are shown in Figure IV.15.

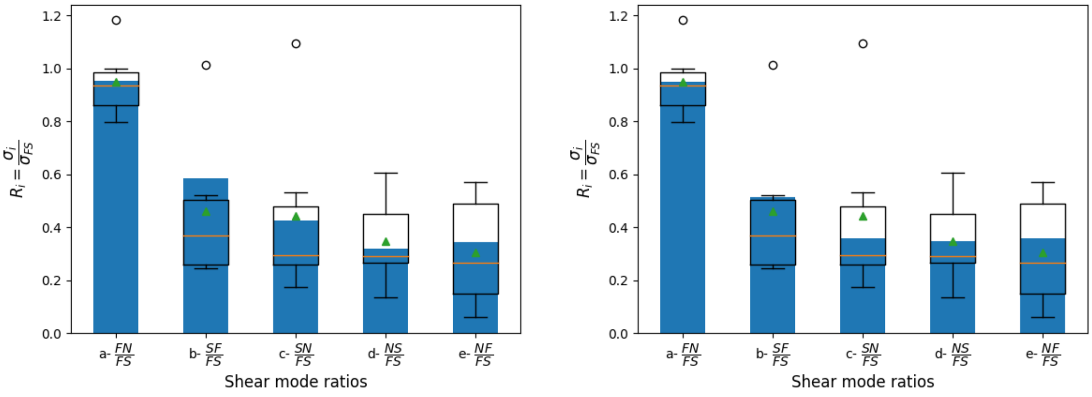

(a) $\beta = 0°$ (b) $\beta = 50°$

Figure IV.15 – Compressible cardiomyocyte in a circular cluster mesostructure (E), with $\beta = 0°$and$50°$ - Experimental versus numerical shear stress ratios (Box plot of the experimental shear stress and bar plot of the numerical shear stress).

The results observed for this mesostructure were similar to the results of mesostructure (L). The observed anisotropy was able to be reproduced by rotating the sheetlets, and the solution was not unique.

4 Discussion

In the recent years, the passive mechanical properties of the cardiac tissue have attracted a lot of attention. Several studies have been performed, aiming at determining the anisotropic mechanical response of the tissue [Dokos et al., 2002; Sommer et al., 2015; McEvoy et al., 2018]. They have shown that the material is clearly transverse isotropic and even slightly orthotropic. The anisotropy is often considered as due to the cardiomyocyte orientation change in the wall thickness. Moreover, some data point towards the role of the sheetlets in the anisotropy.

In this study, our main objective was to shed light on this anisotropy, and determine its origin. We analyzed the macroscopic behavior of the cardiac tissue composed of different mesostructural configurations consisting in altered organizations of cardiomyocytes and collagen planes. The orthotropic material behavior induced by these mesostructures was compared to available experimental data.

The cardiomyocyte orientation variation in the cardiac wall proved to be insufficient in inducing the observed anisotropy (see Figure IV.12). The addition of perimysial extracellular matrix allowed to recover the tissue anisotropy, but only under the assumption of compressible cardiomyocytes. Our study points towards important variations of the sheetlet angle in the wall, in order to reproduce the experimental data, in agreement with our observations in Chapter III. Surprisingly, we could not distinguish between the lamellar and elliptical perimysium mesostructure, even though they have different anisotropies.

Note that we do not have one single set of optimal parameters. This means that, in order to identify the microscopic parameters using macroscopic mechanical assays, simple shear displacement is insufficient. It should be combined with other macroscopic mechanical assays, such as pure shear, that allows to identify the shear parameters, and uniaxial and biaxial assays, to identify the Young moduli and the Poisson ratios. Another alternative would be to perform mechanical assays on mesostructural specimen of myocardial tissue to access more local measures.

Bibliography

H. Ashikaga, B.A. Coppola, K.G. Yamazaki, F.J Villarreal, J.H. Omens, and J.W. Covell. Changes in regional myocardial volume during the cardiac cycle: implications for transmural blood flow and cardiac structure. *American Journal of Physiology-Heart and Circulatory Physiology*, 295(2):H610–H618, 2008. doi: 10.1152/ajpheart.00107.2008.

R. Avazmohammadi, MR. Hill, MA. Simon, W. Zhang, and M Sacks. A novel constitutive model for passive right ventricular myocardium: evidence for myofiber–collagen fiber mechanical coupling. *Biomechanics and Modeling in Mechanobiology*, 16(2):561–581, 2017. doi: 10.1007/s10237-016-0837-7.

K.D. Costa, J. W. Holmes, and A. D. Mcculloch. Modelling cardiac mechanical properties in three dimensions. *Philosophical Transactions of the Royal Society of London. Series A: Mathematical, Physical and Engineering Sciences*, 359(1783):1233–1250, 2001. doi: 10.1098/rsta.2001.0828.

S.C. Cowin. Properties of the anisotropic elasticity tensor. *The Quarterly Journal of Mechanics and Applied Mathematics*, 42(2):249–266, 1989. doi: 10.1093/qjmam/42.2.249.

C.R.G. Debessa, L.B.M. Maifrino, and R.R. de Souza. Age related changes of the collagen network of the human heart. *Mechanisms of Ageing and Development*, pages 1049–1058, 2001. doi: 10.1016/s0047-6374(01)00238-x.

H. Demiray. Stresses in Ventricular Wall. *Journal of Applied Mechanics*, 43(2):194–197, 1976. doi: 10.1115/1.3423806.

S. Dokos, B.H. Smaill, A.A. Young, and I.A. LeGrice. Shear properties of passive ventricular myocardium. *American Journal of Physiology-Heart and Circulatory Physiology*, 283(6):H2650–H2659, 2002. doi: 10.1152/ajpheart.00111.2002.

S. Domaschke, A. Morel, G. Fortunato, and A. E. Ehret. Random auxetics from buckling fibre networks. *Nature Communications*, 10(1):4863, 2019. doi: 10.1038/s41467-019-12757-7.

J. J. Garcia, N. J. Altiero, and R. C. Haut. An Approach for the Stress Analysis of Transversely Isotropic Biphasic Cartilage Under Impact Load. *Journal of Biomechanical Engineering*, 120(5):608–613, 1998. doi: 10.1115/1.2834751.

J. M. Guccione, A. D. McCulloch, and L. K. Waldman. Passive Material Properties of Intact Ventricular Myocardium Determined From a Cylindrical Model. *Journal of Biomechanical Engineering*, 113(1):42–55, 1991. doi: 10.1115/1.2894084.

R. Hill. Elastic properties of reinforced solids: Some theoretical principles. *Journal of the Mechanics and Physics of Solids*, 11(5):357–372, September 1963. doi: 10.1016/0022-5096(63)90036-x.

G.A. Holzapfel and R.W. Ogden. Constitutive modelling of passive myocardium: a structurally based framework for material characterization. *Philosophical Transactions of the Royal Society A: Mathematical, Physical and Engineering Sciences*, 367(1902): 3445–3475, 2009. doi: 10.1098/rsta.2009.0091.

A. Horowitz, Y. Lanir, F. C. P. Yin, M. Perl, I. Sheinman, and R. K. Strumpf. Structural Three-Dimensional Constitutive Law for the Passive Myocardium. *Journal of Biomechanical Engineering*, 110(3):200–207, 1988. doi: 10.1115/1.3108431.

J. D. Humphrey and F. C. P. Yin. On Constitutive Relations and Finite Deformations of Passive Cardiac Tissue: I. A Pseudostrain-Energy Function. *Journal of Biomechanical Engineering*, 109(4):298–304, 1987. doi: 10.1115/1.3138684.

J.D. Humphrey and F.C.P. Yin. Biomechanical experiments on excised myocardium: Theoretical considerations. *Journal of Biomechanics*, 22(4):377–383, 1989. doi: 10.1016/0021-9290(89)90052-3.

C. Igel, T. Suttorp, and N. Hansen. A computational efficient covariance matrix update and a (1+1)-CMA for evolution strategies. In *Proceedings of the 8th annual conference on Genetic and evolutionary computation - GECCO '06*, page 453, Seattle, Washington, USA, 2006. ACM Press. doi: 10.1145/1143997.1144082.

Y. Kanzaki, F. Terasaki, M. Okabe, S. Fujita, T. Katashima, K. Otsuka, and N. Ishizaka. Three-Dimensional Architecture of Cardiomyocytes and Connective Tissue in Human Heart Revealed by Scanning Electron Microscopy. *Circulation*, 122(19):1973–1974, 2010. doi: 10.1161/circulationaha.110.979815.

G.L. Kung, T.C. Nguyen, A. Itoh, S. Skare, N.B. Ingels, D.C. Miller, and D.B. Ennis. The presence of two local myocardial sheet populations confirmed by diffusion tensor MRI and histological validation. *Journal of Magnetic Resonance Imaging*, 34(5):1080–1091, 2011. doi: 10.1002/jmri.22725.

Y. Lanir. Constitutive equations for fibrous connective tissues. *Journal of Biomechanics*, 16(1):1–12, 1983. doi: 10.1016/0021-9290(83)90041-6.

I. J. LeGrice, B. H. Smaill, L. Z. Chai, S. G. Edgar, J. B. Gavin, and P. J. Hunter. Laminar structure of the heart: ventricular myocyte arrangement and connective tissue architecture in the dog. *American Journal of Physiology-Heart and Circulatory Physiology*, 269(2):H571–H582, 1995. doi: 10.1152/ajpheart.1995.269.2.h571.

B. M. Lempriere. Poisson's ratio in orthotropic materials. *AIAA Journal*, 6(11):2226–2227, 1968. doi: 10.2514/3.4974.

A. Loredo and H. Klöcker. Generalized inverse of the compliance tensor, and behaviour of incompressible anisotropic materials — Application to damage. *Mechanics Research Communications*, 24(4):371–376, 1997. doi: 10.1016/S0093-6413(97)00038-4.

J. Mandel. Plasticité classique et viscoplasticité : course held at the Department of mechanics of solids, September-October 1971. Wien; New York, 1972. Springer. ISBN 3-211-81197-4 978-3-211-81197-9 0-387-81197-4 978-0-387-81197-0.

A. Mauri, A.E. Ehret, M. Perrini, C. Maake, N. Ochsenbein-Kölble, M. Ehrbar, M.L. Oyen, and E. Mazza. Deformation mechanisms of human amnion: Quantitative studies based on second harmonic generation microscopy. *Journal of Biomechanics*, 48(9): 1606–1613, 2015. doi: 10.1016/j.jbiomech.2015.01.045.

E. McEvoy, G.A. Holzapfel, and P. McGarry. Compressibility and Anisotropy of the Ventricular Myocardium: Experimental Analysis and Microstructural Modeling. *Journal of Biomechanical Engineering*, 140(8):081004, 2018. doi: 10.1115/1.4039947.

J.C. Michel, H. Moulinec, and P. Suquet. Effective properties of composite materials with periodic microstructure: a computational approach. *Computer Methods in Applied Mechanics and Engineering*, 172(1-4):109–143, 1999. doi: 10.1016/s0045-7825(98)00227-8.

S. Nielles-Vallespin, Z. Khalique, P.F. Ferreira, R. de Silva, A.D. Scott, P. Kilner, L.A. McGill, A. Giannakidis, P.D. Gatehouse, D. Ennis, E. Aliotta, M. Al-Khalil, P. Kellman, D. Mazilu, R.S. Balaban, D.N. Firmin, A.E. Arai, and D.J. Pennell. Assessment of Myocardial Microstructural Dynamics by In Vivo Diffusion Tensor Cardiac Magnetic Resonance. *Journal of the American College of Cardiology*, 69(6):661–676, 2017. doi: 10.1016/j.jacc.2016.11.051.

D.R. Nolan, A.L. Gower, M. Destrade, R.W. Ogden, and J.P. McGarry. A robust anisotropic hyperelastic formulation for the modelling of soft tissue. *Journal of the Mechanical Behavior of Biomedical Materials*, 39:48–60, 2014. doi: 10.1016/j.jmbbm.2014.06.016.

A.J. Pope, G.B. Sands, B.H. Smaill, and I.J. LeGrice. Three-dimensional transmural organization of perimysial collagen in the heart. *American Journal of Physiology-Heart and Circulatory Physiology*, 295(3):H1243–H1252, 2008. doi: 10.1152/ajpheart.00484.2008.

D. Rohmer, A. Sitek, and G.T. Gullberg. Reconstruction and Visualization of Fiber and Laminar Structure in the Normal Human Heart from Ex Vivo Diffusion Tensor Magnetic Resonance Imaging (DTMRI) Data:. *Investigative Radiology*, 42(11):777–789, 2007. doi: 10.1097/rli.0b013e3181238330.

E. Sanchez-Palencia. Comportements local et macroscopique d'un type de milieux physiques heterogenes. *International Journal of Engineering Science*, 12(4):331–351, 1974. doi: 10.1016/0020-7225(74)90062-7.

G.B. Sands, D.A. Gerneke, D.A. Hooks, C.R. Green, B.H. Smaill, and I.J. Legrice. Automated imaging of extended tissue volumes using confocal microscopy. *Microscopy Research and Technique*, 67(5):227–239, 2005. doi: 10.1002/jemt.20200.

H. Schmid, M. P. Nash, A. A. Young, and P. J. Hunter. Myocardial Material Parameter Estimation: A Comparative Study for Simple Shear. *Journal of Biomechanical Engineering*, 128(5):742–750, 2006. doi: 10.1115/1.2244576.

H. Schmid, P. O'Callaghan, M. P. Nash, W. Lin, I. J. LeGrice, B. H. Smaill, A. A. Young, and P. J. Hunter. Myocardial material parameter estimation: A non–homogeneous finite element study from simple shear tests. *Biomechanics and Modeling in Mechanobiology*, 7(3):161–173, 2008. doi: 10.1007/s10237-007-0083-0.

G. Sommer, A..J. Schriefl, M. Andrä, M. Sacherer, C. Viertler, H. Wolinski, and G.A. Holzapfel. Biomechanical properties and microstructure of human ventricular myocardium. *Acta Biomaterialia*, 24:172–192, 2015. doi: 10.1016/j.actbio.2015.06.031.

D.D. Streeter and D.L. Bassett. An engineering analysis of myocardial fiber orientation in pig's left ventricle in systole. *The Anatomical Record*, 155(4):503–511, 1966. doi: 10.1002/ar.1091550403.

A.A. Young, I.J. Legrice, M.A. Young, and B.H. Smaill. Extended confocal microscopy of myocardial laminae and collagen network. *Journal of Microscopy*, 192(2):139–150, 1998. doi: 10.1046/j.1365-2818.1998.00414.x.

Chapter V

Conclusion & perspectives

This thesis addresses some of the questions related to the passive properties of the cardiac tissue which has attracted less attention than the active part. In particular, it aimed at investigating the importance of the mesostructure on the tissue macroscopic mechanical properties. We first studied the evolution of this structure during a mechanical assay, highlighting the weakness of the collagen planes to traction, where they tend to open and create discontinuities, but not during compression and shear. We also studied this structure organization in 3D by mapping its orientation in the heart wall. Finally, we investigated the mesoscale structure role in the anisotropic response of the tissue scale. The main results and perspectives of this work are summarized in the following.

Evolution of the mesostructure during a mechanical assay

Summary. We have developed an experimental setup, combining a Mueller Polarimetry Imaging (MPI) device and an *in situ* mechanical traction device, in order to study the interaction between the mechanisms taking place at the mesoscale and the macroscale. The MPI generates information about the tissue orientation and structuring, and the traction device, coupled with a high definition camera, allows to measure the applied force and strain field.

Three parametric parameters were measured using the MPI on the same region of interest during stretch. The retardance and the depolarization, that we associate with subcellular elements, did not show a significant evolution. We think that it is due to the fact that the imposed deformation is not sufficient to induce alterations at the cell scale. The azimuth, that we associate with the cardiac fiber orientation, showed a significant evolution with stretch. Mesostructural planar structures were observed and associated with sheetlets. Two types of behaviors were distinguished. When the stretch was applied on samples with initial mesostructure orientations of 0° and 45°, the material tended to align smoothly with the traction direction, and its reorientation was well predicted by the affine assumption. When the stretch was applied on samples with initial mesostructure orientations of 90°, the mesostructure did not rotate towards the traction direction, and their orientation remained unchanged during stretch. Instead, gaps appeared, indicating that the collagen surrounding the sheetlets tended to separate. These samples show a non-affine response, which indicates that affine-based models are unlikely to reproduce correctly experimental observations.

Perspectives. To further complete this study, it would be advantageous to have better control of the specimen (shape, size, etc.), and to investigate the strain field at smaller scales to explore the multiscale affinity of the tissue. From a mechanical point of view, and in order to further understand the tissue behavior, it would be useful to compare the stress-stretch curves of samples with different initial mesostructural orientations, and confront them with the results obtained by [Dokos et al., 2002]. In addition, the application of multiple cycles on samples with different initial orientations would give more information on the tissue kinematics. Furthermore, it will be interesting to apply more complex mechanical loadings (biaxial, shear, etc.). This would give a better understanding of the mechanical response of the sheetlets at different scales. Furthermore, performing this study on decellularized and decollagenized myocardial samples would give more insight on the role of each of these constituents in the tissue macroscopic mechanical properties. Moreover, it would be interesting to compare healthy and remodeled cardiac samples, to have insight on the physiological role of the sheetlets. Finally, comparing models including the mesostructure to experimental data from uniaxial, biaxial and shear tests could help to obtain a quantitative mechanical description of the sheetlet.

Mesostructure orientation in the cardiac wall

Summary. We developed a fast and simple experimental protocol to observe the myocardium mesostructure organization in adjacent slices. We studied two different cross-sections: a longitudinal section, parallel to the epicardium, by performing circumferential-transmural cuts, and a transversal section, by performing radial-transmural cuts along the left ventricle. The longitudinal cross-sections showed a transmural evolution of the mesostructure orientation. The sheetlets are parallel and quasi-horizontal close to the epicardium. Near the apex, their orientation stays more or less constant, however, at the equator and base, their orientation varies gradually through the thickness, until they become vertical. The transversal cross-sections revealed that the sheetlet orientation remains quasi-unchanged around the ventricle, at the same latitude. However, the orientation varies in the wall thickness and along the slice. Near the base, we observe one family of parallel sheetlets, with a slightly decreasing angle from endocardium to epicardium. At the equator, this family remains dominant close to the endocardium, but a second family appears, with a slightly increasing angle, close to the epicardium. At the apex, the first family completely disappears, and the second family becomes dominant, with an increase of the sheetlet orientation angle. Our preliminary results agreed with the results found in the literature, therefore validates our experimental protocol.

Perspectives. This preliminary study is limited by the difficulty of the 3D reconstruction due to the tissue softness and the lack of identifiable matching features between two successive slices. The observed deformations could have been used to assess the residual stresses. The 3D reconstruction could be improved by fixing or freezing the tissue. In addition, thinner slices could be made, leading to a more accurate 3D reconstruction. The cross sections in the axial-transmural plane should be studied to obtain the information in all sections, and thus map a 3D model of the sheetlet orientation evolution. As an alternative to sample cutting, tomography imaging technique should be explored. The obtained 3D mesostructure combined with the cardiac fiber orientation can be used as a representative volume element to simulate the tissue mechanical response.

Mesostructure role in inducing the macroscale anisotropy

Summary. We developed a mesoscale model in a linear elastic setting, in order to understand the role of the mesostructure in the anisotropy of the tissue scale. We performed simple shear simulations that we compared the to the experimental data of [Dokos et al., 2002]. Our analysis showed that the cardiomyocyte rotation in the cardiac wall is not sufficient, on its own, to reproduce the experimentally observed anisotropy. The addition of a collageneous mesostructure enables to reproduce the experimental data but only if the cardiomyocytes are compressible. It is worth noting that the sheetlet rotation plays an essential role, as we needed a variation of at least ±25° of the sheetlet orientation to reproduce the experimental data. Surprisingly, both laminar and elliptical collageneous mesostructures give the same results, probably due to the lack of mesostructural experimental data.

Perspectives. To complete this study, it will be interesting to identify the actual material parameters, not only the ratios. To do so, first, constitutive laws for the cardiomyocytes and extracellular layer should be developed, and used in a non-linear elastic simulation. The stretch-stress curves of shear, but also uniaxial and biaxial experiments on samples of different sizes could be used for the identification. Finally, this model could be extended to investigate healthy and remodeled hearts. This could simply be done by varying the structural parameters of the components according to information extracted from imaging studies [Kanzaki et al., 2010; Seidel et al., 2016], and studying the impact of the alterations at the mesoscale on the macroscopic mechanical properties.

From a broader point of view, this work brings new mechanical and structural information about the interactions taking place at the mesoscale and the macroscale of the myocardium, using experimental, imaging and numerical techniques, and represents an important first step in the fundamental understanding of the coupled mechanisms at different spatial scales in the cardiac tissue. It takes part in a broad research project whose ultimate goal is to achieve a quantitative understanding of the structural and functional changes in diseased hearts, in order to improve the diagnosis and treatment of cardiac diseases. Moreover, it confirms the importance of mechanics in medical research, and reinforces the idea that the scientific and the medical communities should join forces and combine efforts to accelerate clinical research.

Bibliography

S. Dokos, B.H. Smaill, A.A. Young, and I.A. LeGrice. Shear properties of passive ventricular myocardium. *American Journal of Physiology-Heart and Circulatory Physiology*, 283(6):H2650–H2659, 2002. doi: 10.1152/ajpheart.00111.2002.

Y. Kanzaki, F. Terasaki, M. Okabe, S. Fujita, T. Katashima, K. Otsuka, and N. Ishizaka. Three-Dimensional Architecture of Cardiomyocytes and Connective Tissue in Human Heart Revealed by Scanning Electron Microscopy. *Circulation*, 122(19):1973–1974, 2010. doi: 10.1161/circulationaha.110.979815.

T. Seidel, J.-C. Edelmann, and F.B. Sachse. Analyzing Remodeling of Cardiac Tissue: A Comprehensive Approach Based on Confocal Microscopy and 3D Reconstructions. *Annals of Biomedical Engineering*, 44(5):1436–1448, 2016. doi: 10.1007/s10439-015-1465-6.

ECOLE DOCTORALE

Titre : Tissus cardiaques : étude du lien entre organisation du tissu et propriétés mécaniques

Mots clés : Biomécanique; Tissu cardiac; Etude multiéchelle; Microstructure; Propriétés mécaniques.

Résumé : Le myocarde est un tissu complexe, principalement constitué de cellules cardiaques et d'une matrice collagénique extracellulaire, disposées selon une microstructure hiérarchique. Cette microstructure évolue au cours du temps, de manière physiologique ou pathologique, altérant les propriétés mécaniques macroscopiques du cœur, et donc sa fonction. L'objectif de cette thèse est d'améliorer notre compréhension des relations structure-propriétés dans le tissu cardiaque en se focalisant sur le rôle de la mésostructure, appelée feuillet, sur les propriétés mécaniques macroscopiques. Dans une première partie, une revue de la littérature existante sur le rôle du sheetlet est réalisée. Dans le deuxième chapitre, je présente un dispositif expérimental que nous avons développé, combinant un imageur polarimétrique de Mueller plein champ et un dispositif de traction in-situ avec une mesure locale de la déformation pendant l'étirement de l'échantillon. Nous observons une cohésion globale du tissu séparé sur des lignes de séparation à la méso-échelle, qui ont tendance à s'ouvrir sous l'effet de la traction. Nous émettons l'hypothèse que ces lignes sont les couches collagènes séparant les feuillets, des faisceaux de cardiomyocytes entourés de couches de collagène périmysial. Dans le troisième chapitre, nous proposons une méthode optique simple combinée à une analyse d'image rapide pour extraire l'orientation locale des feuillets sur des tranches de ventricule gauche, afin de construire une cartographie 3D de l'organisation des feuillets dans le cœur. Dans la deuxième partie de la thèse (chapitre quatre), nous proposons un modèle multi-échelle du myocarde visant à déterminer l'origine structurelle de l'anisotropie mécanique observée à grande échelle. En effet, l'orthotropie observée peut être due soit à la rotation de l'orientation des cellules, soit à la présence de couches collagènes à méso-échelle. Nous concevons trois mésostructures constituées de différentes configurations de cardiomyocytes et de collagène. La réponse mécanique de ces mésostructures est homogénéisée par homogénéisation périodique numérique, et les paramètres matériels obtenus sont utilisés dans une simulation macroscopique d'une expérience de cisaillement. La comparaison entre nos résultats et les données expérimentales montre que les couches de collagène sont nécessaires pour reproduire l'orthotropie du matériau. Le dernier chapitre de ce manuscrit présente quelques perspectives de ce travail.

Title : Cardiac tissue: an investigation of the structure-properties relationships.

Keywords : Biomechanics; Cardiac tissue; Multiscale study; Microstructure; Mechanical properties.

Abstract : The myocardium is a complex tissue, primarily made of cardiac cells and extra-cellular collagenous matrix, arranged in a hierarchical microstructure. This microstructure evolves over time, either physiologically or pathologically, altering the macroscopic mechanical properties of heart, hence its function. The objective of this PhD thesis is to improve our understanding of the structure-properties relationships in the cardiac tissue by focusing on the role of mesostructure, called the sheetlet, on the macroscopic mechanical properties. In a first part, a literature review of the existing literature on the role of sheetlet is performed. In the second chapter, I present an experimental setup we developed, combining a full-field Mueller polarimetric imager and an in-situ traction device with a local measure of the deformation during sample stretch. We observe a global cohesion of the tissue apart on separation lines at the mesoscale, that tend to open under traction. We hypothesize that these lines are the collageneous layers separating the sheetles, bundles of cardiomyocytes surrounded by layers of perimysial collagen. In the third chapter, we propose a simple optical method combined with a fast image analysis to extract the sheetlet local orientation on left ventricle slices, in order to construct a 3D mapping of the sheetlet organization in the heart. In the second part of the PhD thesis (chapter four), we propose a multiscale model of the myocardium aiming at determining the structural origin of the observed macroscale mechanical anisotropy. Indeed, the observed orthotropy can be due either to the rotation of the cell orientation, or to the presence of the mesoscale collageneous layers. We design three mesostructures made of different configurations of cardiomyocytes and collagen. The mechanical response of these mesostructures are homogenized with numerical periodic homogenization, and the obtained material parameters are used in a macroscopic simulation of a shear experiment. The comparison between our results and the experimental data show that the collagen layers are necessary to reproduce the material orthotropy. The final chapter of this manuscript presents some perspectives of this work.

Institut Polytechnique de Paris
91120 Palaiseau, France